

**THE GENESIS OF THE QUARTZ-SERICITE SCHISTS OF THE
TOGGEKRY FORMATION, NONDWENI GREENSTONE BELT, SOUTH
AFRICA**

by

NKOSINATHI LUVUNO JELE

Submitted in fulfilment of the academic
requirements for the degree of
Master of Science in the
School of Agricultural, Earth and Environmental Sciences,
University of KwaZulu-Natal
Durban

December 2013

As the candidate's supervisor I have/have not approved this thesis/dissertation for submission.

Signed: _____ Name: _____ Date: _____

DECLARATION 1 - PLAGIARISM

I, Nkosinathi Luvuno Jele declare that:

1. The research reported in this thesis, except where otherwise indicated, is my original research.

2. This thesis has not been submitted for any degree or examination at any other university.

3. This thesis does not contain other persons' data, pictures, graphs or other information, unless specifically acknowledged as being sourced from other persons.

4. This thesis does not contain other persons' writing, unless specifically acknowledged as being sourced from other researchers. Where other written sources have been quoted, then:
 - a. Their words have been re-written but the general information attributed to them has been referenced
 - b. Where their exact words have been used, then their writing has been placed in italics and inside quotation marks, and referenced.

5. This thesis does not contain text, graphics or tables copied and pasted from the Internet, unless specifically acknowledged, and the source being detailed in the thesis and in the References sections.

Signed.....

DECLARATION 2 - PUBLICATIONS

Details of contribution to publications that form part and/or include research presented in this thesis:

Publication:

Saha, L., Hofmann, A., Jele, N., Harris, C., 2012. Palaeoarchaeoan sea-floor alteration and metamorphism of pillow basalts from the Nondweni Greenstone Belt, SE Kaapvaal Craton. *South African Journal of Geology*, **115**, 259-282.

Saha, L. – Mapping and sample collection, conducted the microprobe analyses, compiled the metamorphic section and metamorphic phase diagrams, analysed the polished sections and took photomicrographs. Co-writer of the paper.

Hofmann, A. – Mapping and sample collection, compiled the geochemistry and isotope section. Co-writer of the paper.

Jele, N. - Mapping and sample collection, prepared samples for XRF, ICP-MS and polished section, conducted SEM and microprobe analysis, analysed the polished sections and took photomicrographs, compiled part of the geochemistry and metamorphic petrology sections. Co-writer of the paper.

Harris, C. – Conducted the Oxygen isotope analysis, compiled part of the isotope geology section. Co-writer of the paper.

Signed:.....

ABSTRACT

The aim of this study was to investigate the origin of sulphide-bearing quartz sericite-schists of the Toggekry Formation in the Archaean Nondweni greenstone belt (NGB) in the SE Kaapvaal craton, and to compare them with similar units in the Barberton greenstone belt (BGB). Geochemical studies reveal that the quartz-sericite schists had a rhyolite protolith. These rocks were subjected to two major deformation phases. D₁ involved thrusting and stacking of the greenstone stratigraphy while D₂ formed the large syncline structure of the greenstone belt. Within the study area, the F₂ buckling mechanism seems to have been tangential longitudinal strain. Peak metamorphism occurred after D₂ at 3230 Ma when the Mvunyana granodiorite intruded. The extensive alteration of the schists is interpreted as being partially due to the deformation and metamorphism but mainly because of the position of the schists in the contact metamorphic aureole of the Mvunyana granodiorite.

The tholeiitic and calc-alkaline signatures of both the mafic and felsic rocks of the Toggekry Formation indicate that they formed in a back-arc setting. The enrichment in LREE relative to HREE that the rocks display is characteristic of crustal contamination and/or subduction zone magmas, enriched mantle source or small degrees of melting. The positive Pb anomalies and negative Nb-Ta are characteristic of subduction zone processes and indicate crustal involvement in the magma process. Epsilon Hf data suggests derivation either from a depleted mantle source with contamination by older continental crust or from a depleted mantle at an earlier age followed by re-melting.

The Toggekry Formation has an age of 3.54 Ga and is indistinguishable in age to the Theespruit Complex of BGB. Both sequences are lithologically similar and interpreted as forming in back-arc settings. However significant geochemical differences indicate that they formed in coeval but separate basins. Four models are proposed to account for this. The peak metamorphic event at ca. 3.2 Ga in both areas is considered to reflect an accretionary event during the formation of the Kaapvaal craton.

TABLE OF CONTENTS

CHAPTER 1: INTRODUCTION.....	1
1.1 Location of the study area.....	1
1.2 Objective of the study.....	1
1.3 Previous work.....	3
1.4 Regional geology.....	4
CHAPTER 2: GEOLOGY OF THE NONDWENI GREENSTONE BELT.....	9
2.1 Introduction.....	9
2.2 Stratigraphy of the Nondweni Group.....	9
2.2.1 <i>The Magongolzi Formation</i>	9
2.2.2 <i>The Toggekry Formation</i>	11
2.2.3 <i>The Witkop Formation</i>	36
2.3 Intrusions into the Nondweni Group.....	36
2.3.2 <i>Serpentinite</i>	38
2.3.3 <i>Mvunyana Granodiorite</i>	42
2.3.4 <i>Undeformed mafic dykes, sills and stocks</i>	43
2.4 Metamorphism of the Nondweni Group.....	43
2.4.1 <i>Sea-floor hydrothermal processes: veins and silicification of the Toggekry Formation</i>	43
2.4.2 <i>Regional metamorphism</i>	45
2.4.3 <i>Contact metamorphism</i>	45
2.5 Structural Geology.....	46
2.5.1 <i>Previous structural studies</i>	46
2.5.2 <i>Structure of the Toggekry Formation</i>	48
2.5.3 <i>Interpretation of the tectonic history of the Toggekry Formation</i>	58

CHAPTER 3: GEOCHRONOLOGY	62
3.1 Introduction	62
3.2 Rhyolite (NJ-10-L5A)	62
3.3 Andesite (NG 3A)	64
3.4 Andesite (NG 15)	64
3.5 Quartz-feldspar porphyry (NG 13).....	68
3.6 Quartz-sericite schist (NG 3B)	70
3.7 Discussion	72
CHAPTER 4: GEOCHEMISTRY	74
4.1 Introduction	74
4.2 Geochemical classification diagrams	74
4.3 Major and trace element geochemistry	76
4.4 Magma series.....	87
4.5 Normalized trace element diagrams	87
4.6 Element mobility (isocron diagrams)	98
4.7 Tectonic discrimination diagrams	100
4.8 Petrogenesis of the magma.....	101
CHAPTER 5. COMPARISON OF THE TOGGEKRY FORMATION WITH THE THEESPRUIT FORMATION, BARBERTON GREENSTONE BELT (BGB).....	104
5.1 Introduction	104
5.2 Summary of the Toggekry Formation	104
5.3 Theespruit Complex Geology	105
5.3.1 Geochronology	105
5.3.2 Lithologies.....	105
5.3.3 Structure and metamorphism	106

5.3.4 Geochemistry.....	106
5.4 Summary of the evolution of the Nondweni and Barberton greenstone belts	108
CHAPTER 6: CONCLUSIONS.....	115
ACKNOWLEDGEMENTS.....	119
REFERENCES.....	120
GEOCHEMISTRY LEGEND	129
APPENDIX 1: ANALYTICAL METHODS.....	130
APPENDIX 2: SAMPLE LOCALITIES AND TYPE OF ANALYSIS DONE	142
APPENDIX 3: MAJOR AND TRACE ELEMENT DATA	145
APPENDIX 4: ISOTOPE GEOCHEMISTRY	151
APPENDIX 5: MAPS.....	158
APPENDIX 6: PUBLICATION	160

CHAPTER 1: INTRODUCTION

1.1 Location of the study area

The study area is located in northern KwaZulu-Natal, about 56 km south of Vryheid and about 91 km north-west of Melmoth (Fig 1.1). The township of Nondweni (S28°11'02, 14"; E030°50'15.62") lies in the south-western part of the area while the confluence of the Nondweni and Mvunyana rivers occurs close to the eastern boundary of the study area.

1.2 Objective of the study

The objective of this research was to study a sequence of Archaean quartz-feldspar-sericite schists, which crops out in the Nondweni greenstone belt, northern KwaZulu-Natal on the south-eastern Kaapvaal craton. These rocks have been interpreted as originally being felsic volcanic rocks and have been dated to be about 3.53 Ga (Xie et al., 2012). If this extrusive origin is correct, then these schists are one of the oldest supracrustal sequences in southern Africa. If, however, they prove to have originally been intrusive in origin, then the surrounding units must be even older. These schists form part of the Toggekry Formation, which also includes bodies of stratiform volcanogenic sulphide mineralization. Such mineralization is very rare in 3.5 Ga greenstone belts, being almost exclusively confined to sequences younger than about 2.8 Ga.

The key questions to be answered are:

- What is the origin of the protolith to the quartz-feldspar-sericite schists in the Toggekry Formation?
- How do they compare with units of similar age and composition in the Barberton greenstone belt, South Africa?
- What are the implications for correlations between the greenstone belts of the Kaapvaal craton and the geological evolution of this region in the Archaean?

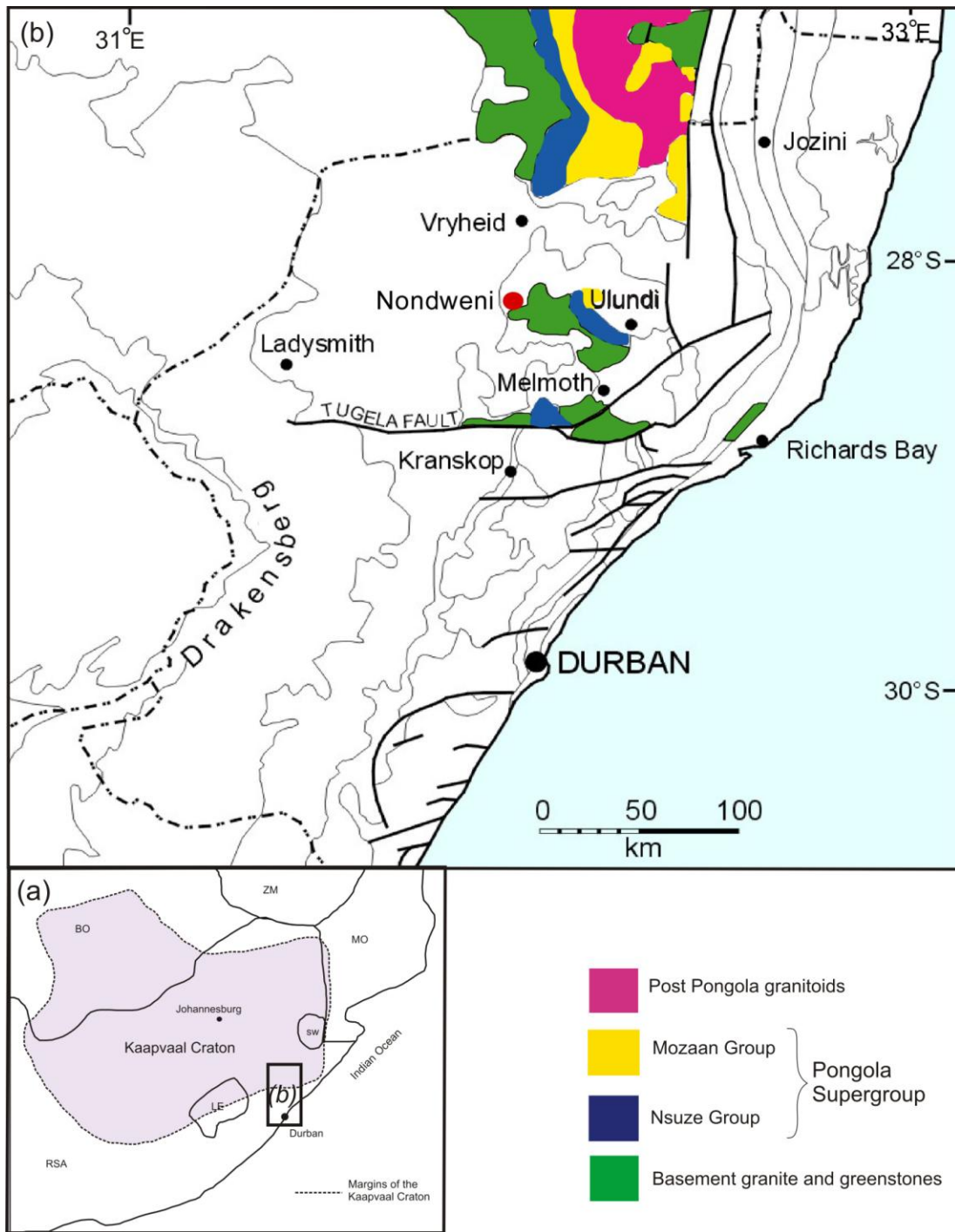


Figure 1.1 Location of the study area with simplified basement geology shown for reference. Insert map (a) shows outline of the Kaapvaal craton (after Wilson and Versfeld, 1994a) and the position of the study area relative to the SE part of the craton. Abbreviations: ZM = Zimbabwe; BO = Botswana; MO = Mozambique; SW = Swaziland; LE = Lesotho; RSA = South Africa

1.3 Previous work

The earliest studies on the Nondweni greenstone were carried out in the 1890's driven by the exploration for gold and copper. Hatch (1910) reported on the copper-zinc prospecting in Nondweni. Du Toit (1931) was the first to name and describe the Nondweni greenstone belt, subdividing the basement to the Pongola Supergroup into the Nkandla, Nondweni, Mfongosi and Tugela Series. Truter (1950) correlated the rocks of the Nondweni greenstone belt with the Onverwacht Group of the Barberton greenstone belt, while Truter (1950) and Matthews (1959) argued that the Nondweni and Mfongosi Series were part of the same stratigraphic succession. In 1987 the Nondweni "series" was accredited Group status by the Geological Survey of South Africa following the recommendations of the South African Committee for Stratigraphy (Linstrom, 1987; Versfeld and Wilson, 1992a).

Watkeys (1981) undertook a structural study of the northern part of the Nondweni greenstone belt as part of an Anglo-American exploration project for massive sulphide deposits. The main portion of this project was the study by Versfeld (1988) involving the first detailed investigation of the whole Nondweni greenstone belt. His work encompassed mapping of the entire greenstone belt and a comprehensive geochemical investigation of the volcanic rocks. He subdivided the Nondweni Group into the basal Magongolozi Formation, the Toggekry Formation and the upper Witkop Formation. Some of the results were published in two posthumous papers (Wilson and Versfeld, 1994a, b).

Matthews et al. (1989) obtained a minimum age of 3.29 Ga for the Nondweni greenstone belt by dating (Rb-Sr and Pb-Pb method) the Mvunyana granodiorites that are intrusive into the greenstones. Wilson and Carlson (1989) carried out Sm-Nd and Pb isotope studies on greenstone belts in the south-east Kaapvaal craton, including the Nondweni greenstone belt.

Riganti and Wilson (1995) presented a study on the geochemistry of the mafic-ultramafic lavas, while Riganti (1996) carried out a more extensive study of the field relations, petrography and geochemistry of the Magongolozi Formation. She also focused on a sequence of quartzites that was further studied by Van Den Kerkhof et al. (2004).

More recently Hofmann and Wilson (2007) studied the silicification of the volcanic rocks with the aim of understanding what sea-floor processes may have been responsible for the silicification phenomenon that is common in greenstone belts. Xie et al. (2012) used zircon SHRIMP dating to obtain an age 3.53 Ga for the felsic volcanic rocks of the Toggekry Formation. The most recent work was a metamorphic study on the pillow basalts of the Witkop Formation involving the author (Saha et al., 2012). Using geothermobarometry, peak metamorphic conditions of ~6.5 kbar and 600-650°C were calculated for the Nondweni greenstone belt

1.4 Regional geology

Archaean greenstone belts represent some of the oldest preserved rocks on the Earth's surface. They comprise variable amounts of volcanic and sedimentary rocks, deformed and usually at low to medium grades of metamorphism, enclosed by a variety of gneisses and granites. Not only are they vital sources of information about the early Earth's geological history but they also host a considerable portion of ore deposits worldwide. There are as many as 260 individual Archaean greenstone belts exposed in small areas all over the World (De Wit and Ashwal, 1997) (Fig 1.2). No doubt there are others yet to be discovered in poorly exposed areas such as the Amazon, Congo craton and in Antarctica.

The study area lies in the south-eastern Kaapvaal craton, the whole craton covering an area of about $1.2 \times 10^6 \text{ km}^2$ across Swaziland, South Africa and Botswana (Brandl and De Wit., 1997; De Wit and Hart., 1993) (Fig.1.3). The formation of the Kaapvaal craton commenced about 3.7 Ga ago by a process of intraoceanic obduction and stabilized after about 1000 million years (De Wit et al., 1992; Poujol et al., 2003).

This craton contains a number of greenstone belts, most notably the Barberton greenstone belt that lies about 250 km north of Nondweni, while further north are the Murichison, Pietersburg, and Giyana greenstone belts. The greenstone remnants closest to Nondweni are the Ilangwe greenstone belt (Mathe, 1997) to the south and the Comondale, De Kraalen, Assegai and Dwalile greenstone belts (Saha et al., 2010) to the north.

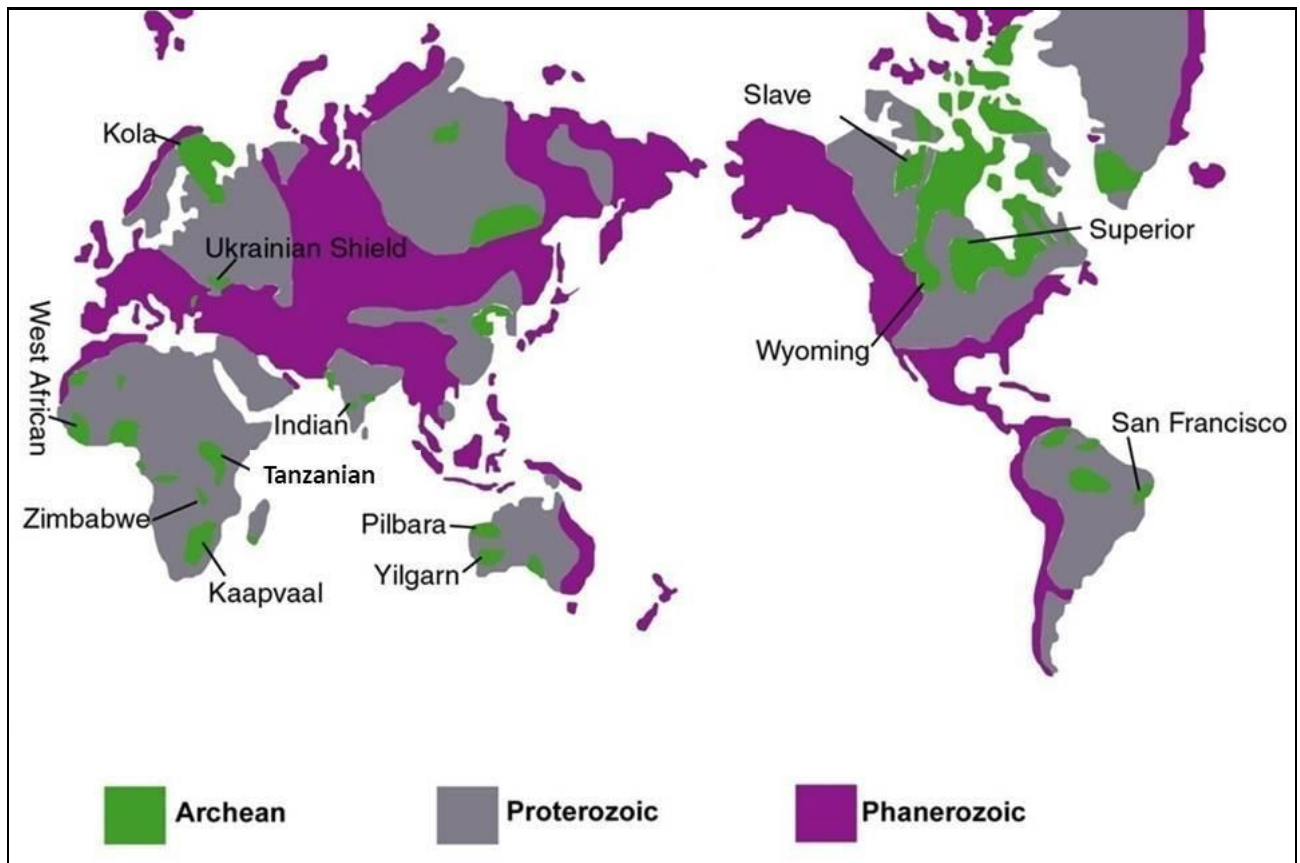


Figure 1.2 Distribution of Archean, Proterozoic and Phanerozoic rocks worldwide. The labeled areas are cratons that contain granite-greenstone terrains (modified after Condie, 1981; Rollinson, 2009).

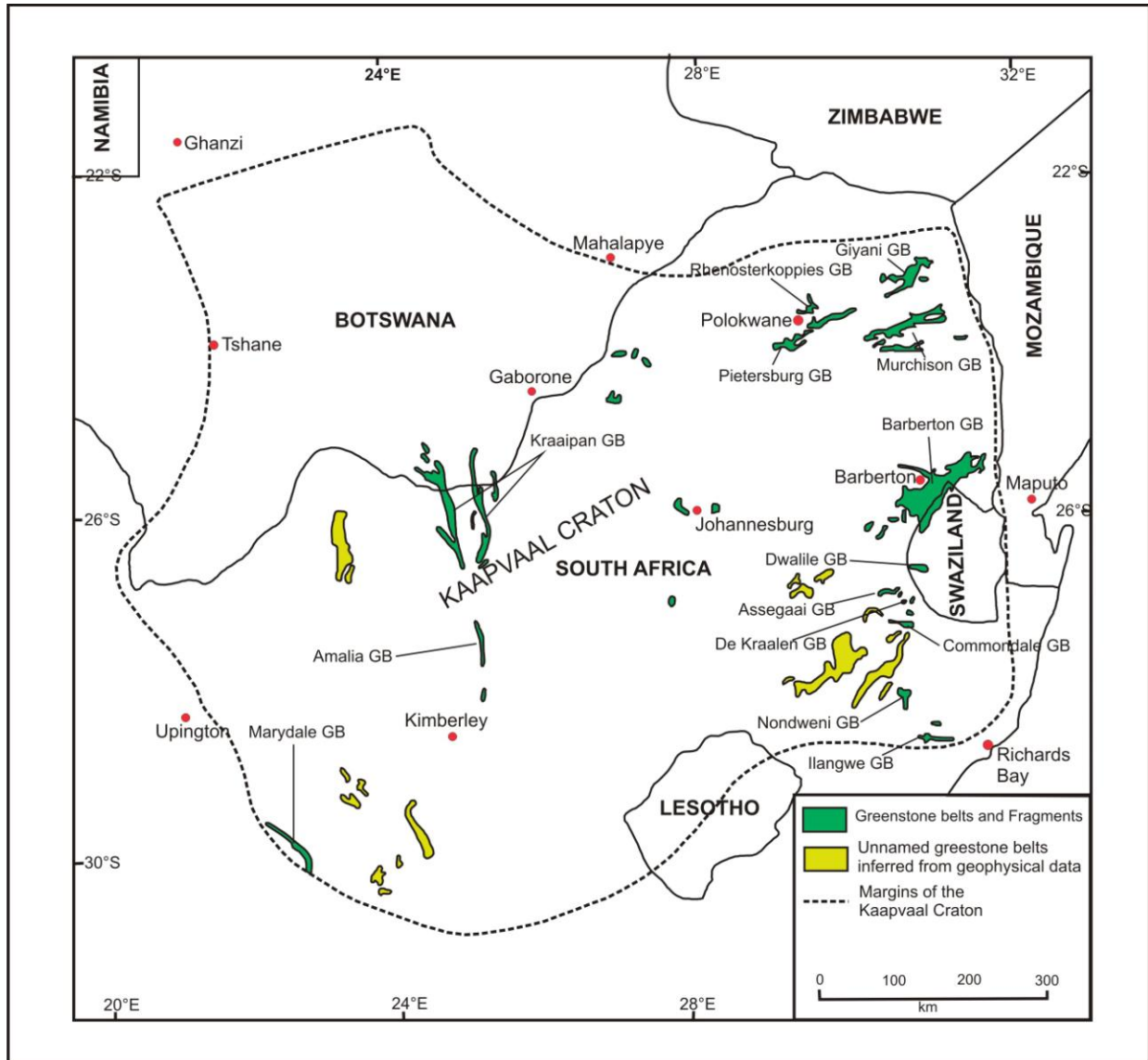


Figure 1.3 Geological map of the Kaapvaal craton showing distribution of greenstone belts on the Kaapvaal craton (modified after Brandl et al., 2006). Abbreviations: GB = greenstone belt.

The oldest rocks in the south-east Kaapvaal craton belong to the Ancient Gneiss Complex of Swaziland and known formally as the Ngwane gneiss and shown as NG in Figure 1.4 (Compston and Kröner, 1988; Kröner et al., 1989; Kröner and Tegtmeier, 1994) leading to a debate as to whether they could represent a granitic basement to the greenstone belts. Potassic granitoids intrude the greenstones (Robb et al., 2006) both as stock-like plutons and as sill-like batholiths.

In the south-east Kaapvaal craton the granite-greenstone basement is unconformably overlain by the Pongola Supergroup that consists of the lower dominantly volcanic Nsuze Group and the upper sedimentary Mozaan Group (Gold, 2006). The Nsuze volcanics yielded a U-Pb age of 2940 ± 22 Ma (Hegner et al., 1994). Fragments of the Nsuze Group overlie the eastern part of Nondweni greenstone belt (Versfeld, 1988; Riganti, 1996). The minimum age of the Mozaan Group is 2837 ± 5 Ma as established by dating of a pre-tectonic quartz porphyry sill, which was, folded with the host Mozaan sedimentary rocks (Gutzmer et al., 1999). The late Archaean Ushushwana Complex and post-Pongola granitoids as well as Proterozoic diabase dykes intrude the Pongola Supergroup.

Much of the south-east Kaapvaal craton region is covered by the Karoo Supergroup that is Carboniferous to Jurassic in age. This comprises a lower sedimentary sequence (Johnson et al., 2006) overlain by Jurassic volcanics with associated dolerite dykes and sills (Duncan and Marsh, 2006). In the study area only poorly exposed Permo-Carboniferous Dwyka Group diamictites and other related glacial sedimentary rocks are preserved. The Archaean basement of the Nondweni area is exposed as a window through this cover due to erosion during the Tertiary and Quaternary.

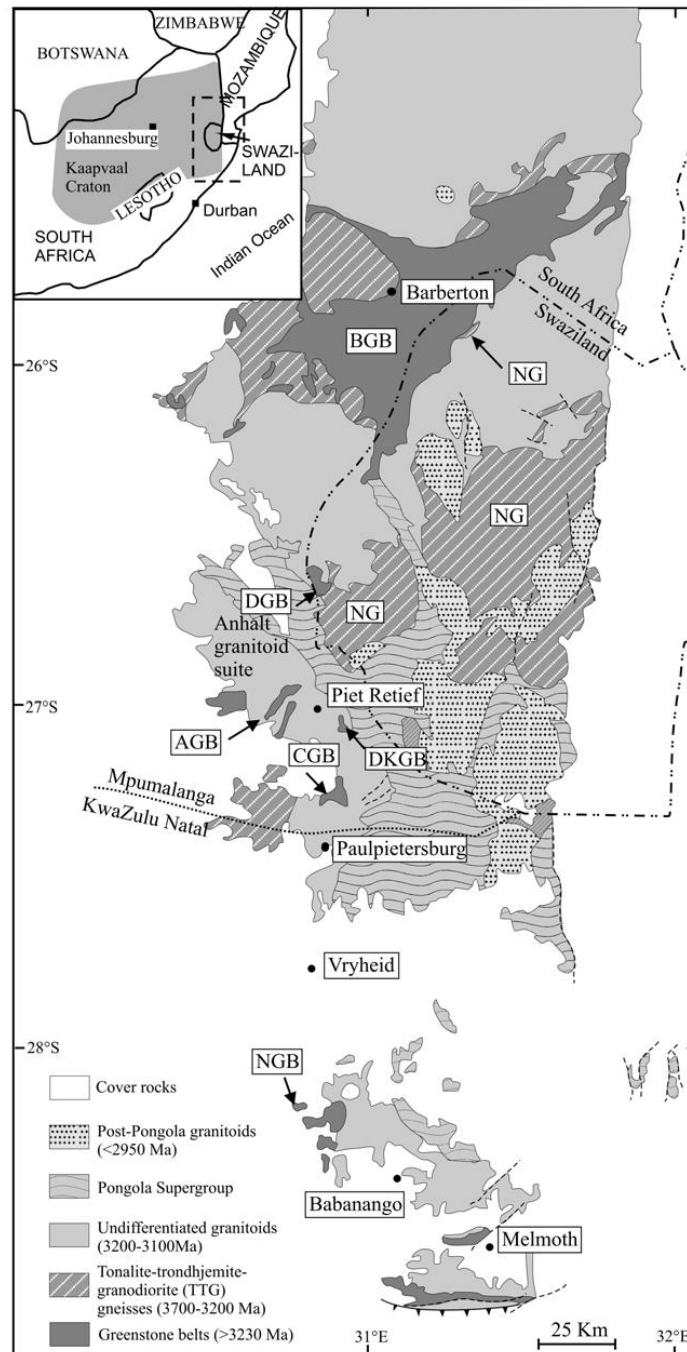


Figure 1.4 Geological map of the southeast Kaapvaal craton from Saha et al. (2012). Abbreviations: BGB = Barberton greenstone belt; DGB = Dwalile greenstone belt; AGB= Assegai greenstone belt; DKGB = De Kraalen greenstone belt; CGB = Comondale greenstone belt; NGB = Nondweni greenstone belt; NG = Ngwane Gneiss.

CHAPTER 2: GEOLOGY OF THE NONDWENI GREENSTONE BELT

2.1 Introduction

The Nondweni Group comprises three formations, namely the Magongolozi Formation, the Toggekry Formation and Witkop Formation (Versfeld, 1988). These are exposed as a north-east to south-west trending syncline (Fig 2.1). The Magongolozi and Toggekry Formations are exposed along the northern limb while the Witkop Formation is exposed along the northern limb, in the core of the fold and along the south-eastern limb. The eastern part of this syncline is intruded by the Mvunyana granodiorite whilst the Karoo Supergroup covers large portions.

Different aspects of the geology of the Nondweni group have been documented by Versfeld (1988), Wilson and Versfeld (1994a,b), Hofmann and Wilson (2007), Saha et al., (2012) and during the present study. Relevant aspects of these published studies are incorporated in the sections that follow

2.2 Stratigraphy of the Nondweni Group

2.2.1 The Magongolozi Formation

The Magongolozi Formation is the lowermost unit of the Nondweni Group. The formation is considered to be 7000 m thick, but structural duplication is inferred (Wilson and Versfeld, 1994a). It is exposed over a strike length of 13.5 km and the units in most of the area have constant sub-vertical dip and approximately east-west strike. Younging direction is regarded to be southwards based on indicators such as pillow structures, spinifex textures and graded accretionary lapilli bands. The lowermost boundary of the formation is not exposed due to the Karoo cover while the upper boundary is poorly exposed due to weathering and masked by granitic and dolerite intrusions but it is inferred to lie in contact with the Toggekry Formation (Wilson and Versfeld, 1994b).

Pillowed volcanic rocks comprise about half of the formation. They range from basalts to basaltic andesites and komatiitic andesites. The pillows are well-preserved in terms of original mineralogy and the pillow shapes are undeformed and up to 4m in diameter. Wilson and

Versfeld (1994b) attributed the large size of the pillows in the formation to the composition of the magma.

A thick succession of coarse-grained, pyroxene spinifex-textured mafic and intermediate igneous rocks comprises about a third of the formation (Wilson and Versfeld, 1994b).

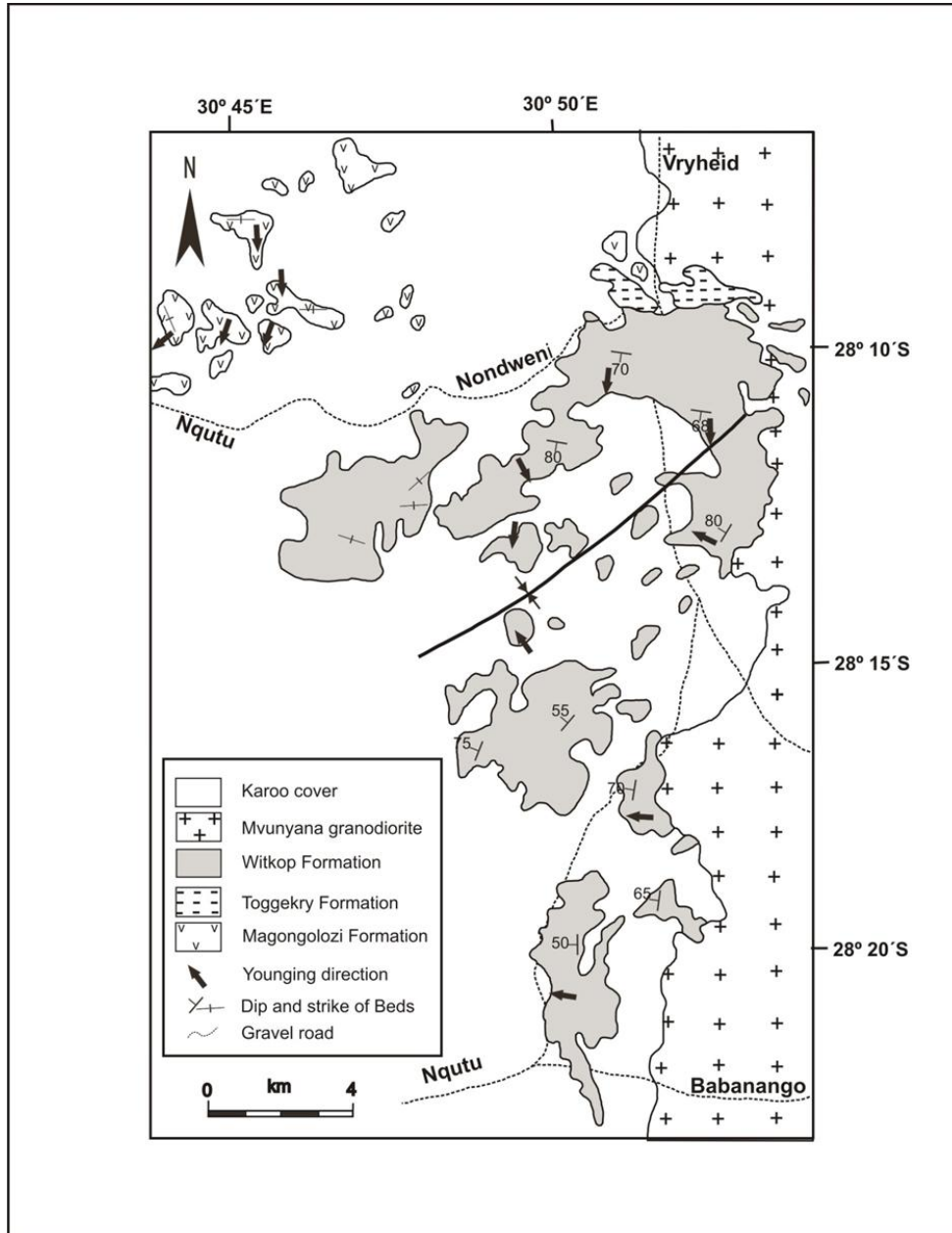


Figure 2.1 Geological map of the Nondweni greenstone belt showing the distribution of the Magongolozi, Toggekry and Witkop Formation (modified after Versfeld, 1988).

The way-up of the spinifex textures is consistent with the pillow lava way-up indicators. Structureless fine-grained mafic to intermediate volcanic rocks, which are similar in mineralogy and composition to the pillow lavas, constitute 15% of the formation. Diorite, pyroxenites, chert and fuchsitic quartzite constitute about 15% of the formation, with the cherts comprising about 5% and possessing relict textures of accretionary lapilli (Wilson and Versfeld, 1994b). The spinifex-cumulate in units is as thick as 150 m and is associated with ponding of the viscous lava.

According to Wilson and Versfeld (1994b) extreme heat loss from the top surface of the lava flows gave rise to spinifex textures while crystal accumulation was taking place at the base of the unit where cooling was relatively slow. The lateral variation in thickness within a single unit is attributed to either topographic control or lava ponding against lava. The thin chert layers found at base and top of units are due to accumulation of ash during a period of no volcanic activity.

2.2.2 The Toggekry Formation

The Toggekry Formation is exposed along a strike length of approximately 5 km and a maximum width of 1.2 km, the total outcrop area being about 4.4 km² (Versfeld, 1988). The succession is steeply dipping and regional strike is east-west (Wilson and Versfeld, 1994b). According to Wilson and Versfeld (1994a) way-up is to the south as deduced from overlying and underlying Witkop and Magongolzi Formations respectively. Riganti and Wilson (1995) interpret the 2000m thick Toggekry Formation to represent a locally developed felsic eruptive centre.

The Toggekry Formation comprises, in order of decreasing abundance, quartz-sericite schists, mafic schists, rhyolites, basaltic andesite flows, andesites, quartzites, graphitic schist and feldspar porphyry (Versfeld, 1988). Intrusive into the formation are small serpentinite bodies, granites, gabbros and dolerites. The rocks of the Toggekry Formation are generally more deformed and metamorphosed than the underlying and overlying rocks of the Mangongolzi and Witkop Formations, respectively. Hofmann and Wilson (2007) attributed this to the close proximity of the sequence to a syn-tectonic intrusive granite (Mvunyana granodiorite) and to the hinge of the synclinal fold closure south of the formation.

2.2.2.1 Quartz-sericite schists

Quartz-sericite schists constitute a major component of the Toggekry Formation. The quartz-sericite schists are reddish brown in colour where highly altered (Fig 2.2a) and silver grey when fresh (Fig 2.2b) and have no primary sedimentary or igneous structures. Wilson and Versfeld (1994a) interpreted the sericite schists as partially reworked tuffs. The quartz-sericite schists of the Toggekry Formation host small Cu-Zn massive sulphide bodies of volcanogenic origin (Wilson and Versfeld, 1994a).



Figure 2.2(a) Photograph of the quartz-sericite schist with its characteristic reddish brown colour in the central zone area (E 030°53'11, 4"; S 28°09'43, 5".)



Figure 2.2 (b) Hand specimen of quartz-sericite schist from St. James mine.

In thin section, the rock contains quartz, sericite, muscovite, chlorite and biotite. The quartz ranges from fine to coarse-grained and exhibits sutured grain boundaries (Fig 2.3 and 2.4) indicative of recrystallisation. The quartz occurs as porphyroclasts in a matrix of quartz, sericite and biotite (Fig 2.5) and displays undulose extinction indicating the rock was subjected to strain. The presence of quartz porphyroblasts, sutured grain boundaries and undulose extinction suggest that the rock underwent both static and dynamic recrystallisation. The rock is compositionally and texturally laminated with coarse-grained quartz laminae alternating with fine-grained sericite zones.

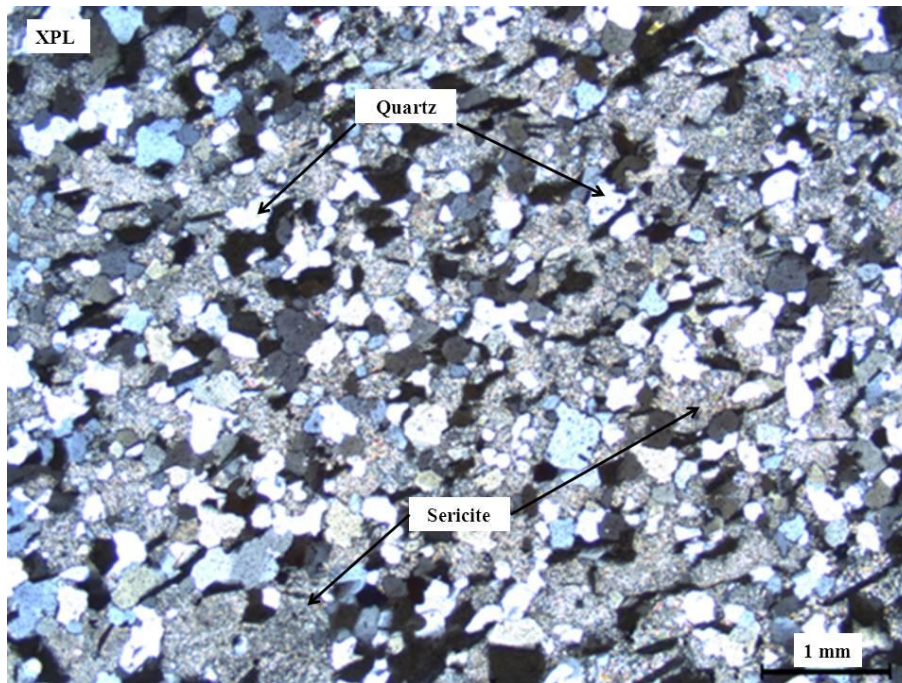


Figure 2.3 Photomicrograph of quartz-sericite schist (NG 20) showing quartz and sericite. (See Map 3 in Appendix 5 for locality)

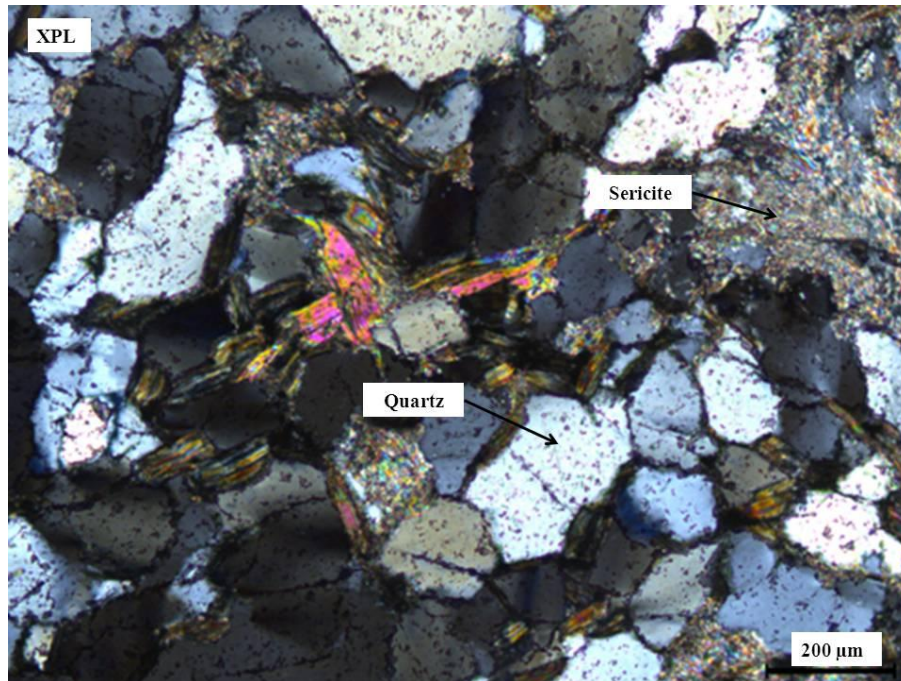


Figure 2.4 Photomicrograph of quartz-sericite schist (NG 4) showing quartz with sutured grain boundaries. Quartz crystals are partially surrounded by sericite. (See Map 3 in Appendix 5 for locality)

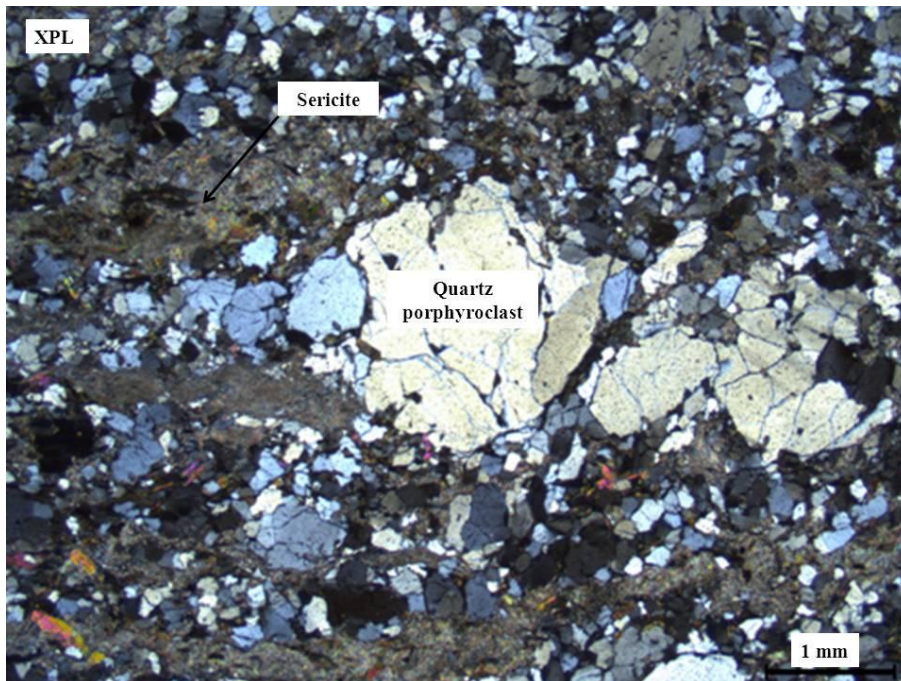


Figure 2.5 Photomicrograph of quartz-sericite schist (NG 4) showing quartz porphyroblast surrounded by sericite and quartz. (See Map 3 in Appendix 5 for locality)

2.2.2.2 Mafic schists

A significant portion of the mafic rocks of the Toggekry Formation have been deformed and metamorphosed to mafic schists. A minor portion of the mafic schists was further subjected to alteration following deformation and metamorphism resulting in chlorite schists (Fig 2.6). The mafic schists described in this section are interpreted to have been derived from basaltic andesites as the geochemistry indicates in the following chapters. Thus the mafic schists will be termed according to their geochemical composition i.e. basaltic andesites. Where alteration of the mafic rocks is not pervasive, deformed pillow structures have been preserved in the basaltic andesites. In the Scheelite Stream, basaltic andesites interlayered with massive structure-less units show clear progressive deformation from undeformed pillows (Fig 2.7a) to deformed pillows (Fig 2.7b). The massive and structure-less units (Fig 2.7b) are of similar composition to the basaltic andesites and were deduced by Versfeld (1988) to represent penecontemporaneous sills into the basaltic andesites before the rocks were subjected to strain.

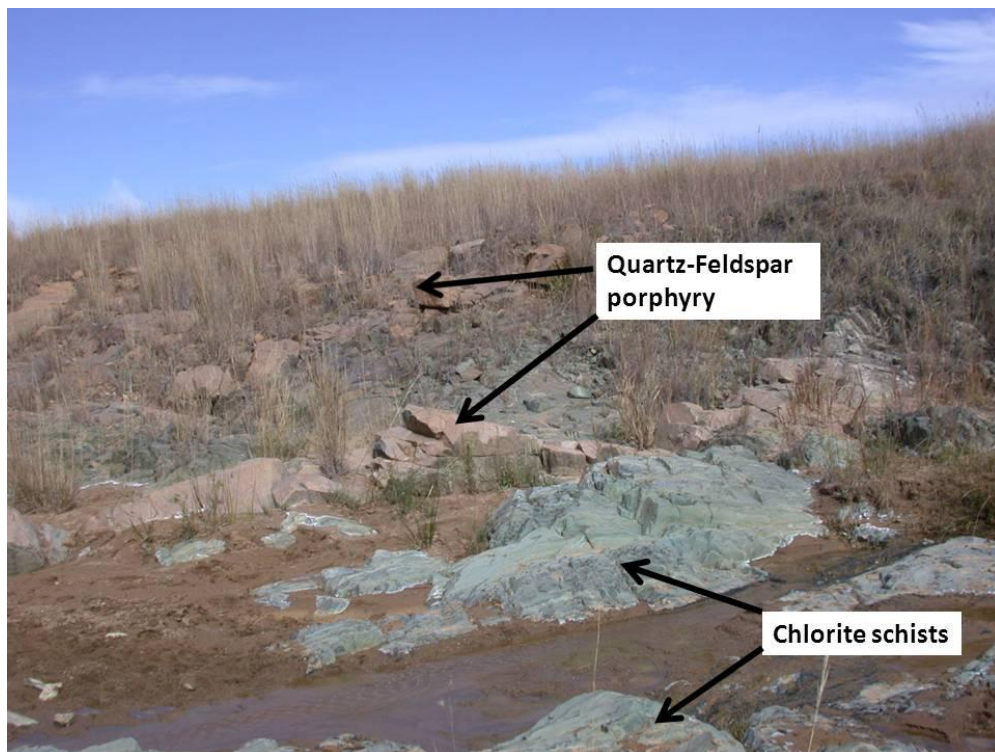


Figure 2.6 Photograph showing outcrops of chlorite schists from the Toggekry Formation in the Scheelite Stream (E 030°51'57, 9"; S 28°10'00, 5")



Figure 2.7 (a) Pillow basaltic andesite exposure in the Scheelite Stream ($E 030^{\circ}51'45, 6''$; $S 28^{\circ}09'48, 9''$). (b) Interlayered deformed pillow basaltic andesites with massive units interpreted as sills in the Scheelite Stream ($E 030^{\circ}51'45, 7''$; $S 28^{\circ}09'49, 4''$)

2.2.2.2.1 Petrography of the basaltic andesites

Samples NJ-10-SS1 to NJ-10-SS8

Samples NJ-10-SS1 to NJ-10-SS8 are a sequence/package of basaltic andesites that indicate clear progressive deformation from least deformed to highly strained/deformed pillows north of the Scheelite Stream (see map 3 and map 4B in Appendix 5).

The least deformed pillowed basaltic andesites comprise pyroxene, plagioclase, hornblende and quartz (Fig 2.8). The pyroxene displays an exsolution texture and is partially altered to chlorite and amphibole (Fig 2.9). The plagioclase grains in the rocks are fine-grained, subhedral to anhedral and have undergone sericitization. Opaque minerals and sphene occur as accessory phases in the rocks (Fig 2.10).

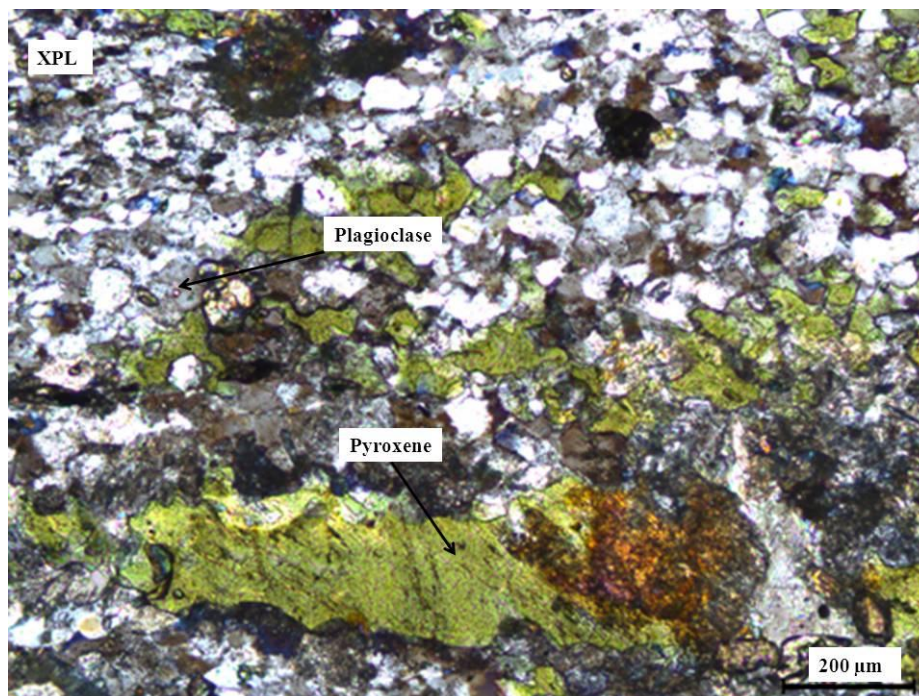


Figure 2.8 Photomicrographs of least deformed basaltic andesite (NJ-10-SS1) comprising pyroxene, plagioclase feldspar and secondary quartz (See Map 3 in Appendix 5 for locality).

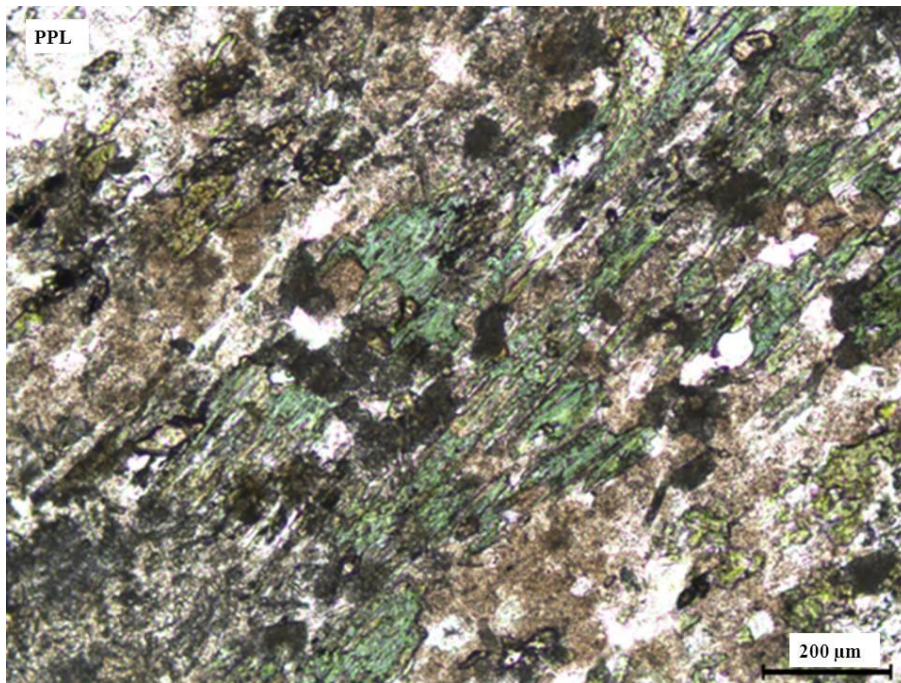
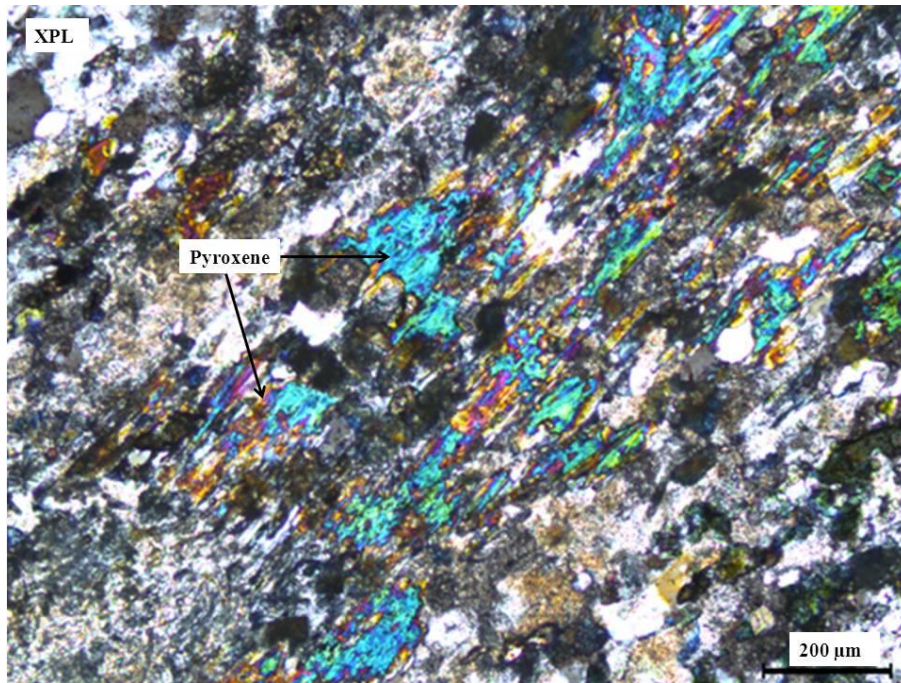


Figure 2.9 Photomicrograph of basaltic-andesite (NJ-10-SS1) showing pyroxene exsolution texture. Note the preferred orientation of the minerals(See Map 3 in Appendix 5 for locality)

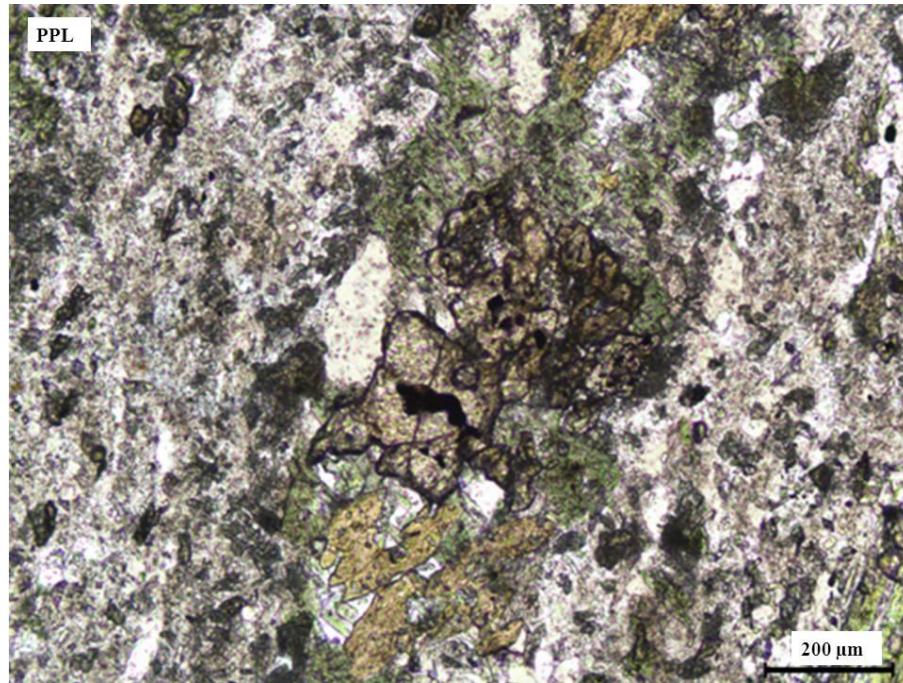
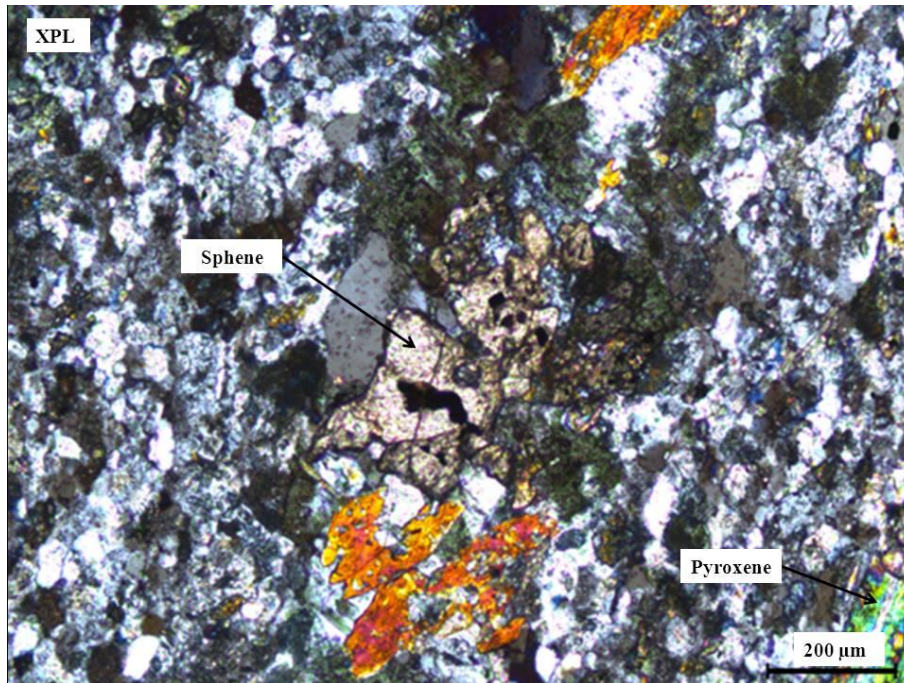


Figure 2.10 Photomicrograph of basaltic andesite (NJ-10-SS1) with fractured sphenes and pyroxene exsolution. (See Map 3 in Appendix 5 for locality)

Three types of quartz are present in the rocks; (1) Fine-grained quartz in the groundmass which may represent primary quartz, (2) Coarse-grained layers of quartz representing veins resulting

from in-filling pre-existing fractures created by strain (Fig 2.11) and (3) quartz lenses which may represent secondary quartz that has in-filled vesicles. The presence of undulose extinction in the coarse quartz indicates that after fracture formation and infill the basaltic-andesites were subjected to strain.

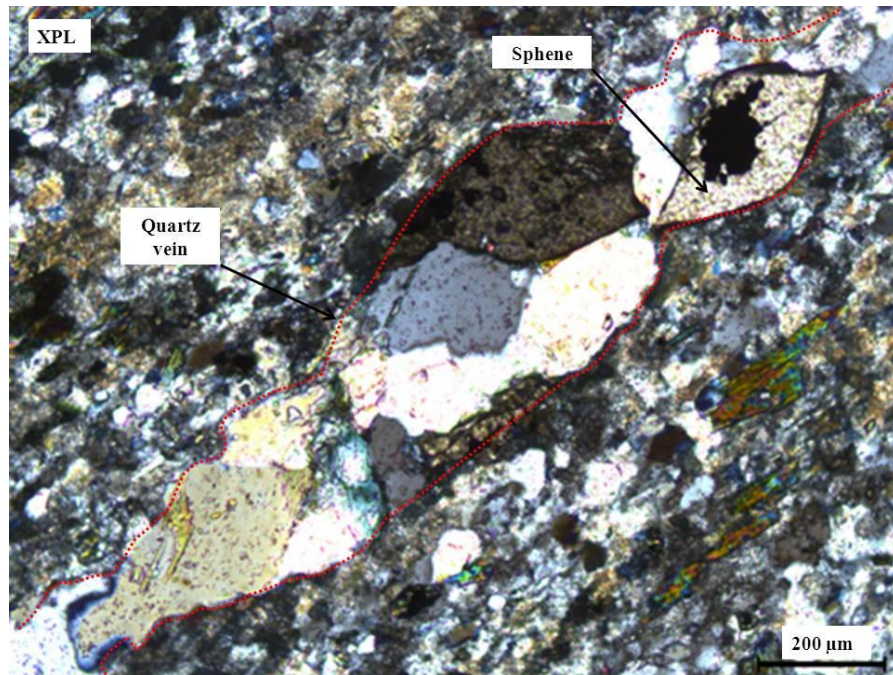


Figure 2.11 Photomicrograph of basaltic andesite (NJ-10-SS1) with quartz vein and euhedral sphene. (See Map 3 in Appendix 5 for locality)

The basaltic andesites become progressively more deformed towards the south. In thin section the increased deformation is accompanied by a decrease in modal abundance of the mafic minerals and the rocks become richer in quartz and plagioclase. The rocks exhibit a pronounced foliation and the coarse quartz in the form of quartz lenses show a preferred elongation direction angular to the groundmass fabric. Thus they indicate a flattening event which may pre or post-date the tectonic event which caused the fabric in the groundmass (Fig 2.12).

In the highly deformed rocks (Samples NJ-10-SS4 to NJ-10-SS8), where pillow structures have been obliterated, the mineralogy is quartz, plagioclase, muscovite, chlorite and sericite. Rutile is present as an accessory phase (Fig 2.13). The basaltic andesites exhibit both textural and compositional lamination (Fig 2.14). Textural/compositional lamination is represented by the alternation of fine-grained quartz-biotite-muscovite zones with coarse-grained quartz zones.

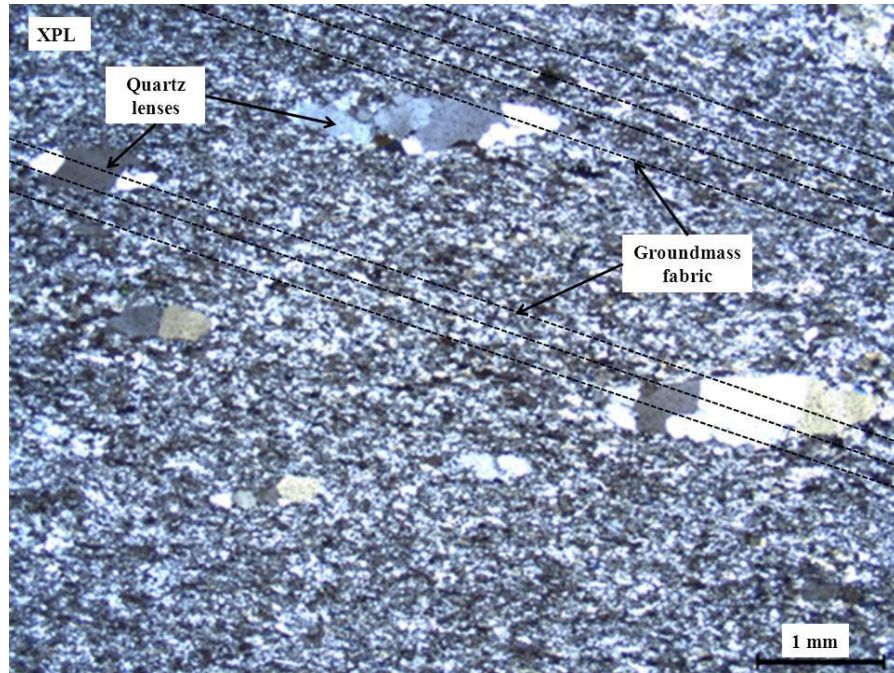


Figure 2.12 Photomicrograph of basaltic andesite (NJ-10-SS5) showing quartz lenses indicating flattening and orientation of their long axis angular to groundmass fabric. (See Map 3 in Appendix 5 for locality)

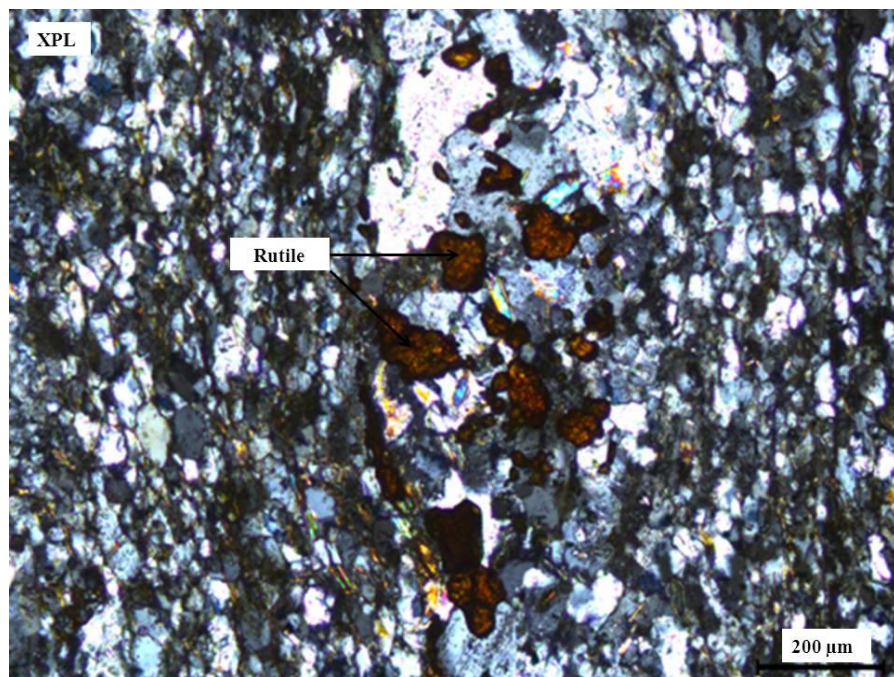


Figure 2.13 Photomicrograph of basaltic-andesite (NJ-10-SS8) showing subhedral rutile grains. (See Map 3 in Appendix 5 for locality)

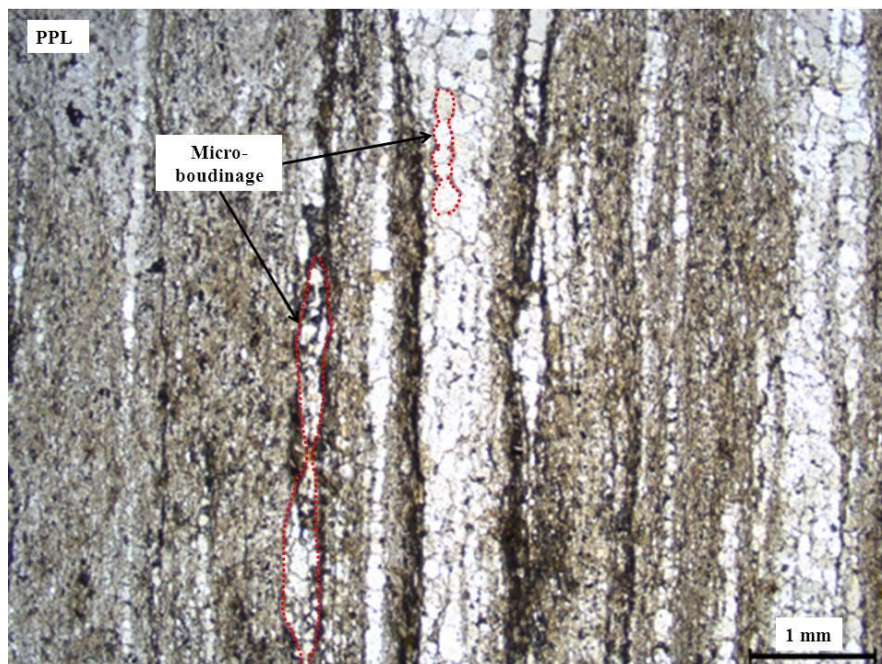
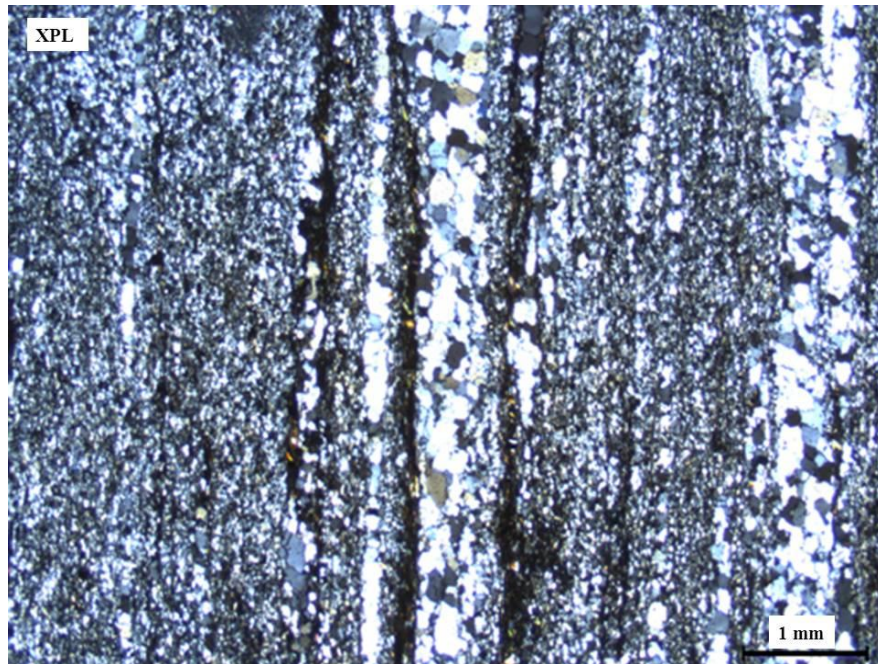


Figure 2.14 Photomicrograph of basaltic andesites (NJ-10-SS8) showing a strong fabric and textural lamination defined by quartz, plagioclase and sub-parallel fine mica flakes. Note the boudins in PPL image. (See Map 3 in Appendix 5 for locality)

The massive sills intrusive into the basaltic andesites consist of plagioclase and hornblende (Fig 2.15). The plagioclase in the rock has been partially altered to sericite. The plagioclase occurs as a fine-grained groundmass and phenocrysts about 600 microns in length giving the rock a

phenocrystic texture. Chlorite, epidote and opaque minerals occur as minor phases. Quartz occurs as a secondary mineral. The quartz grains exhibit undulose extinction indicating the rock has been strained.

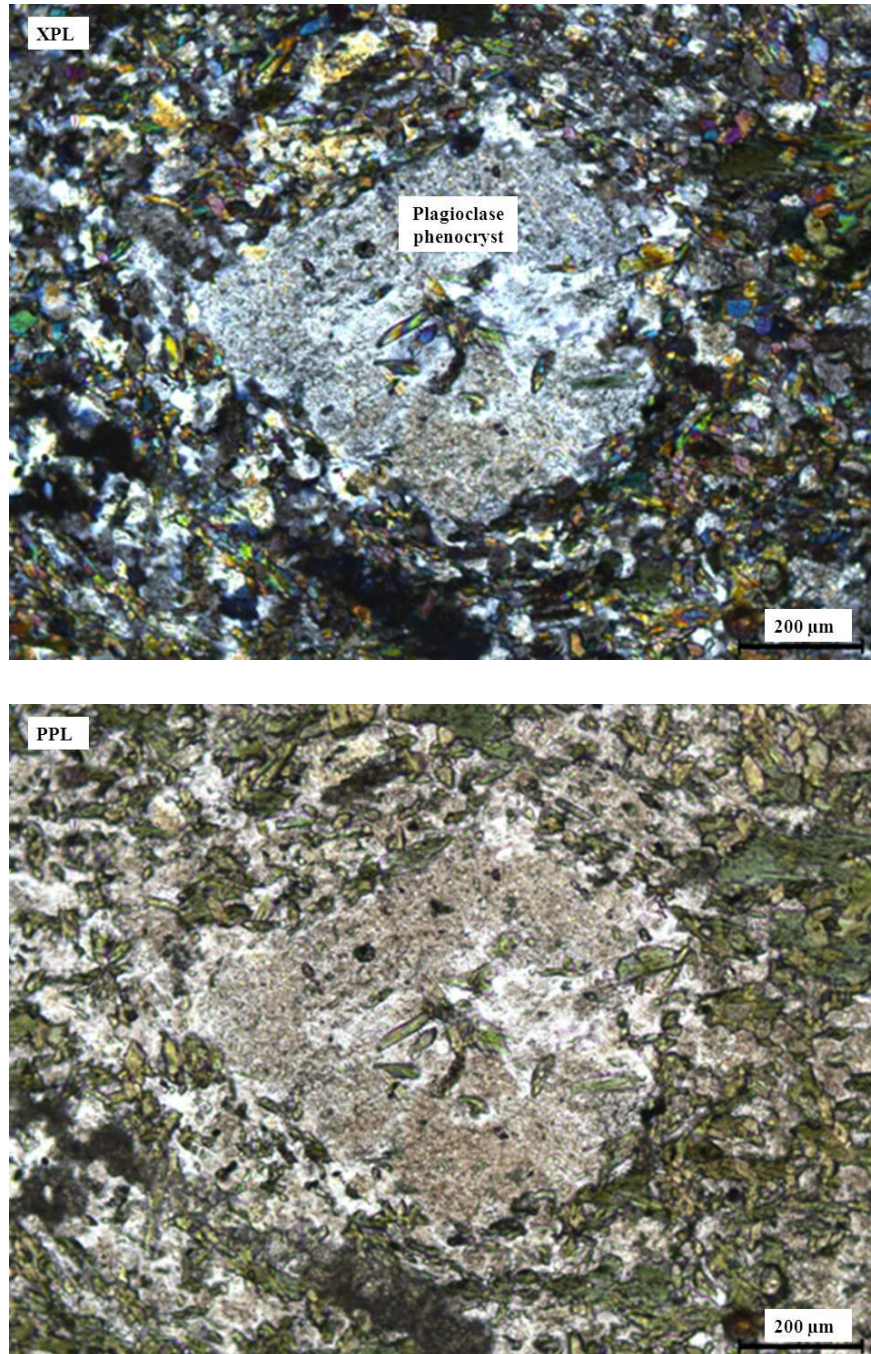


Figure 2.15 Photomicrograph of andesitic sill (NJ-10-SS2) showing phenocrystic texture. (See Map 3 in Appendix 5 for locality)

Sample SC 3

This rock contains quartz, plagioclase and muscovite. Relict pyroxene is also present in the section. Partially sericitized plagioclase occurs as large phenocrysts in a fine-grained groundmass giving the rock a porphyritic texture. Chlorite is present as an alteration phase with rutile occurring as an accessory phase. Quartz ranges from fine to coarse-grained and displays undulose extinction. The coarse-grained quartz represents later quartz introduced in the rocks in the form of veining. The rock shows a well-defined foliation defined by the preferred orientation of platy minerals.

Sample NG 14

Sample NG 14 contains quartz, plagioclase, hornblende, pyroxene, chlorite and sericite. Pyroxene in various stages of alteration is also observed in thin section. The pyroxene crystals exhibit a corona texture with pyroxene mantled by chlorite (Fig 2.16). The pyroxene in the sample has altered to chlorite in the outer zone and in the inner zone pyroxene is still preserved.

Coarse grained zones are present in the rock, representing deformed veins of quartz and K-feldspar, in the form of microcline, suggesting that the fluids that infiltrated the rock were not only silica rich but also high in alkalis (Fig 2.17). The foliated nature of the rock and the undulose extinction displayed by the quartz indicates the rock was subjected to strain after crystallization of the minerals.

Sample NG 18

The rock contains plagioclase, pyroxene, amphibole, quartz and chlorite. Opaque minerals form a minor but significant portion of the rock. Fine-grained laths of pyroxene which exhibit an acicular texture have been partially altered to tremolite (Fig 2.18).

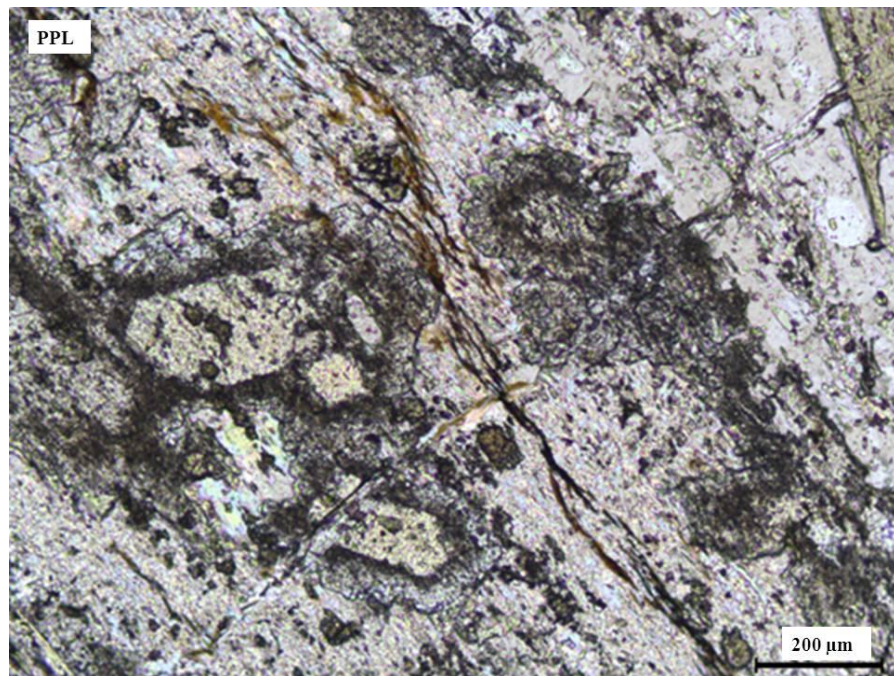
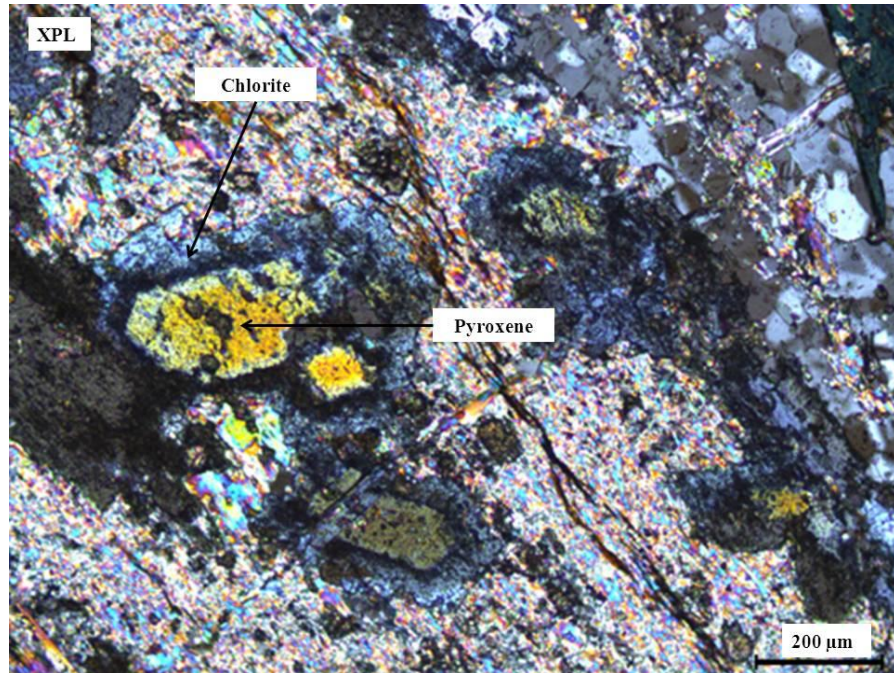


Figure 2.16 Photomicrograph of basaltic andesite (NG 14) showing corona texture in pyroxene. Pyroxene is mantled by chlorite. (See Map 3 in Appendix 5 for locality)

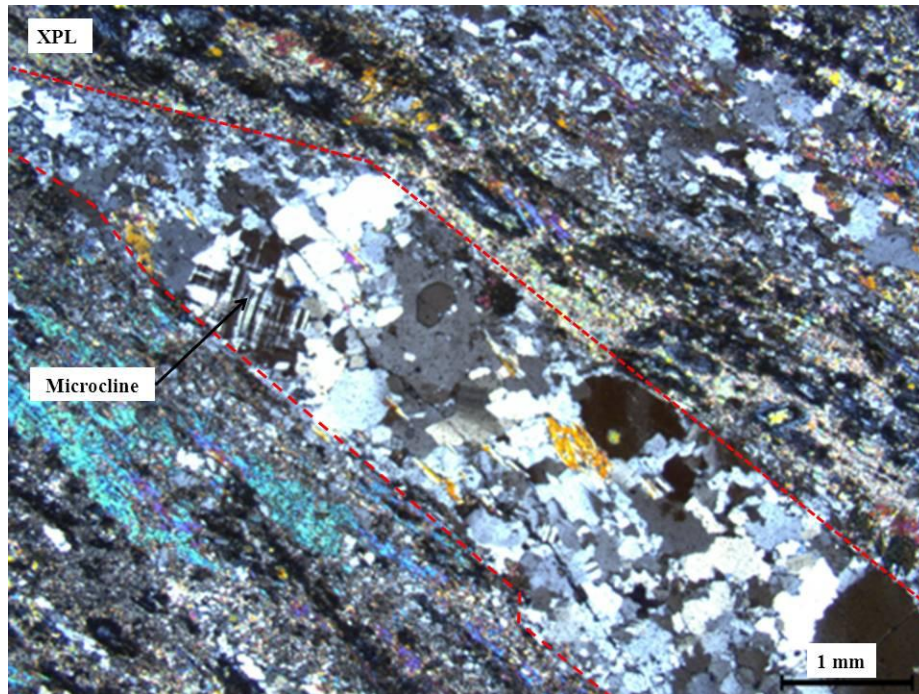


Figure 2.17 Photomicrograph of basaltic andesite (NG 14) showing quartz-microcline vein in a fine-grained groundmass, where microcline has cross-hatched twins. (See Map 3 in Appendix 5 for locality)

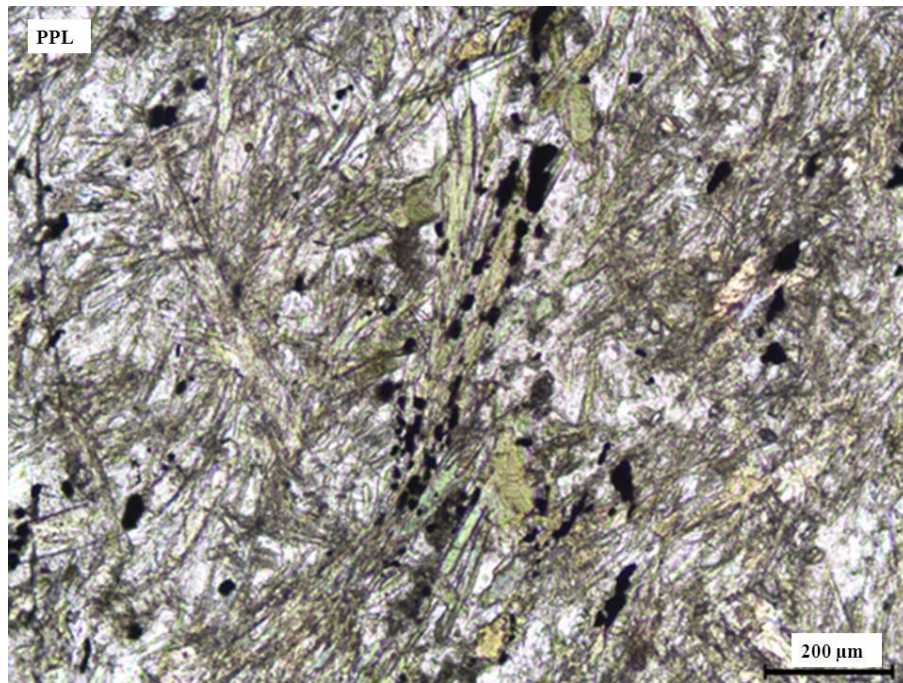
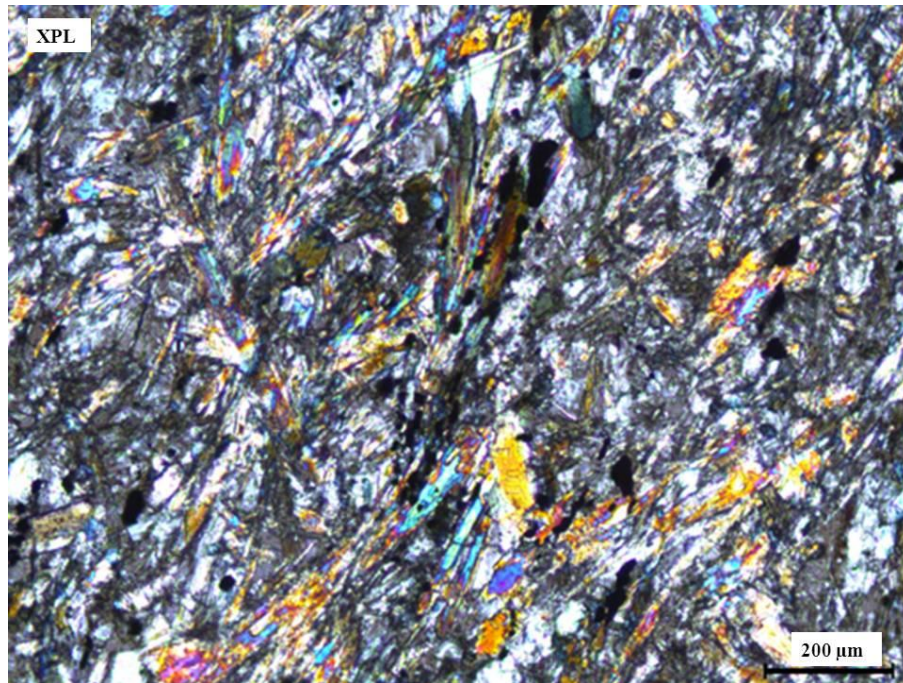


Figure 2.18 Photomicrograph of basaltic andesite (NG 18) showing acicular texture in pyroxene/tremolite. (See Map 3 in Appendix 5 for locality)

2.2.2.3 Rhyolites

A felsic unit termed the Mount Vernon rhyolite crops out on Mount Vernon Farm. Wilson and Versveld (1994a) found the sequence to be 200m thick and extend along strike for 1, 5 km. The unit has a light grey fresh colour and breaks with a conchoidal fracture as is typical of quartz rich rocks. The rock is fine-grained in appearance. A notable feature of the rhyolites is the presence of columnar jointing which may represent one of the oldest columnar jointing in the geological record. An outcrop map of the rhyolite is in Appendix 5 (Map 2). The presence of columnar jointing and orientation of the joints suggest that the outcrops may represent rhyolite flows dipping at about 25° with thicknesses ranging from 1m to 12.5m.

In thin section the rock is fine-grained and contains quartz, muscovite, K-feldspar and plagioclase with microcline as the common feldspar (Fig 2.19). Chlorite occurs as a minor phase with zircon and ore minerals occurring as accessory phases (Fig 2.20) . The quartz grains in the rock exhibit undulose extinction indicating strain after crystallization. In contrast to the rocks of basaltic andesitic composition there is no evidence of preferred orientation of minerals in the photomicrographs but in the field a pronounced foliation can be observed in the rhyolites and the foliation has similar dip and strike as the rocks of basaltic andesitic composition.

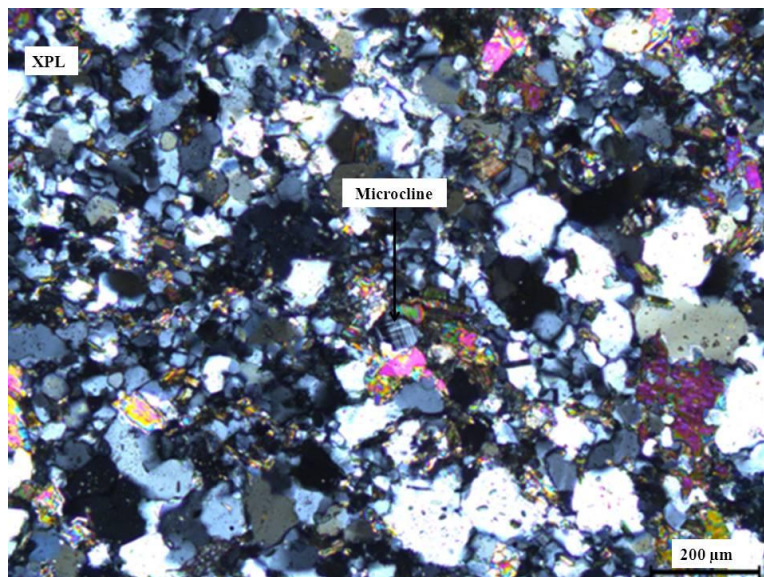


Figure 2.19 Photomicrograph of the Mount Vernon rhyolite (NJ-10-L10A) with microcline exhibiting cross-hatched twinning. (See Map 2 and Map 3 in Appendix 5 for locality)

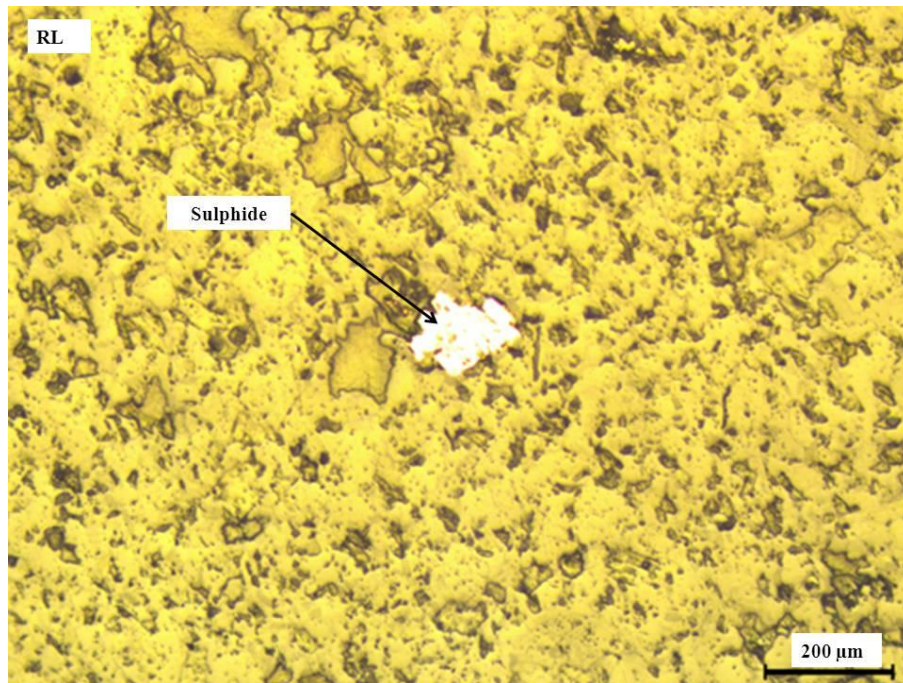
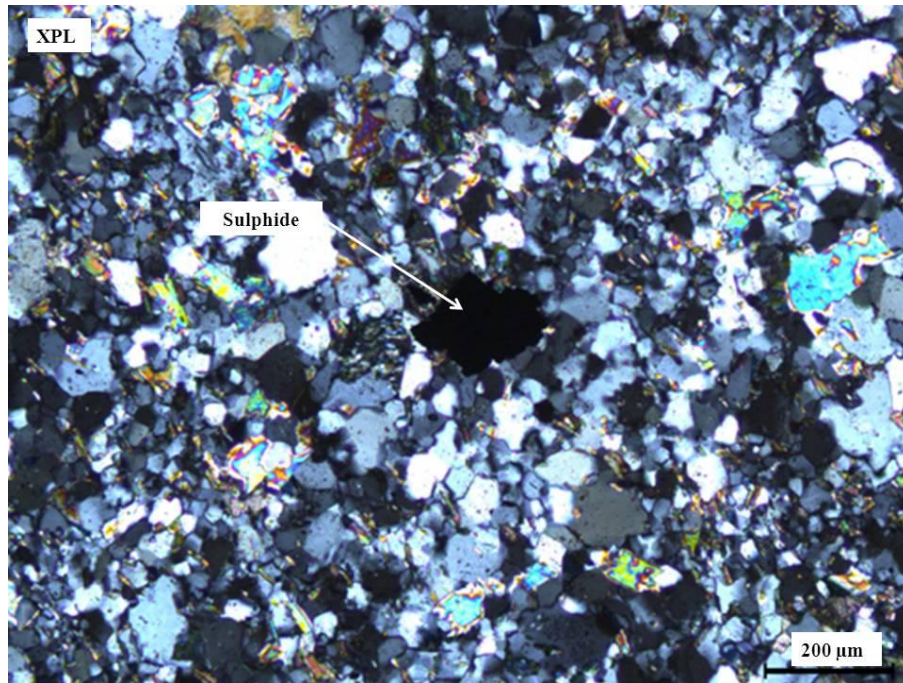


Figure 2.20 Photomicrograph of Mt Vernon rhyolite (NJ-10-L10A) showing ore minerals in (a) cross nicols and (b) reflected light (RL). . (See Map 2 and Map 3 in Appendix 5 for locality)

2.2.2. 4 Andesites

Rocks of andesites composition constitute a major component of the Toggekry Formation and have been deformed to schists. Where deformation is not pervasive, the andesites exhibit pillow structures indicative of sub-aqueous extrusion, such as along the Scheelite Stream. In the following section, the deformed schists of andesitic composition will be termed andesites according to their geochemical composition.

Sample SC 2

Sample SC 2 contains plagioclase, quartz, biotite and muscovite. The plagioclase is partially sericitised and occurs as phenocrysts in a fine-grained matrix of plagioclase, quartz and muscovite. The plagioclase phenocrysts are about 1mm in length and contain Carlsbad twinning (Fig 2.21).

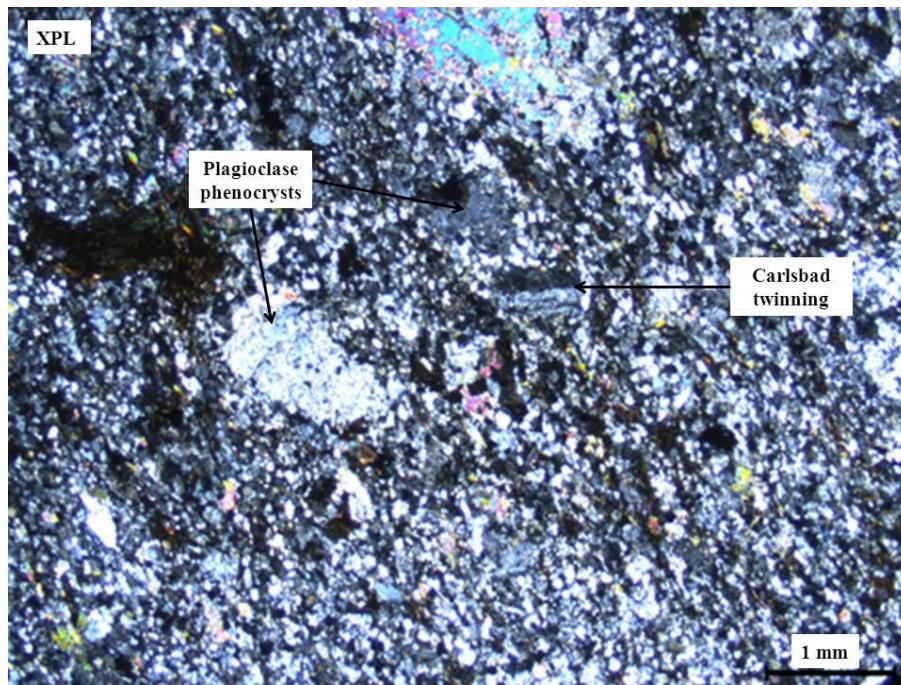


Figure 2.21 Photomicrograph of Toggekry andesite (SC 2) showing phenocrystic texture with plagioclase phenocrysts displaying Carlsbad twinning. (See Map 3 in Appendix 5 for locality)

Sample NG 3A

NG 3A comprises fine to medium-grained quartz, plagioclase and muscovite. Zircon occurs as an accessory phase in the rock. Feldspar occurs as phenocrysts in a fine to medium-grained groundmass of quartz and feldspar. The plagioclase phenocrysts are subhedral in form and display Carlsbad twinning (Fig 2.22).

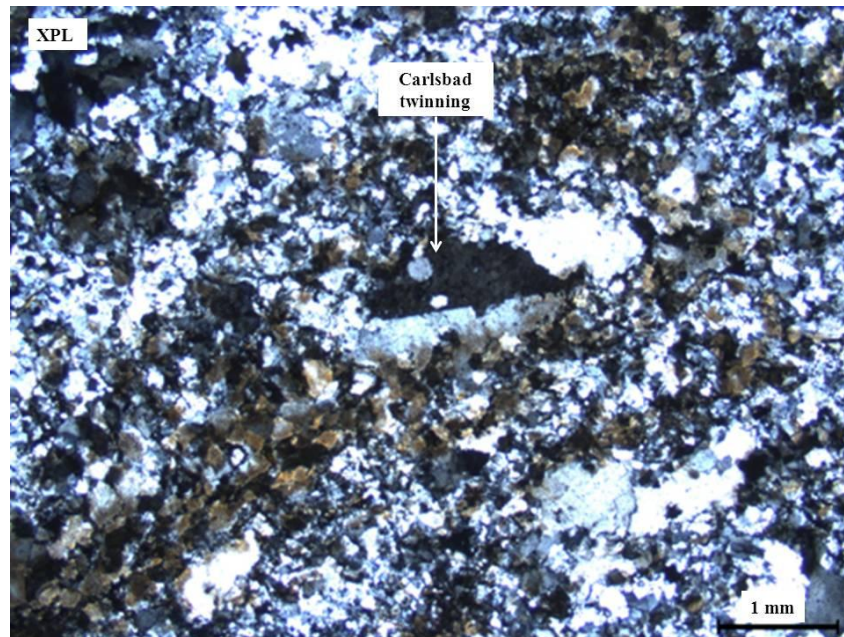


Figure 2.22 Photomicrograph of andesite (NG 3A) with Carlsbad twins in plagioclase. . (See Map 3 in Appendix 5 for locality)

Sample NG 15

NG 15 A2 is the centre of the pillow. In the centre of the pillow the rock consists of quartz, plagioclase and muscovite. Calcite and chlorite occur as minor phases. The quartz ranges from fine to coarse-grained. The coarse-grained quartz occurs as lenses in a matrix of fine quartz, plagioclase and muscovite (Fig 2.23).

NG 15 A1 is a thin section of the pillow edge, close to the pillow rim. Here the rock contains quartz, plagioclase, muscovite and biotite (Fig 2.24). The rock has a pronounced foliation (Fig 2.24) defined by the preferred orientation of micas. Lenses of quartz are present in section with

their long axis parallel to groundmass fabric and preferred orientation of the fine micas. The compositional and textural lamination in the pillow rim may represent primary alteration.

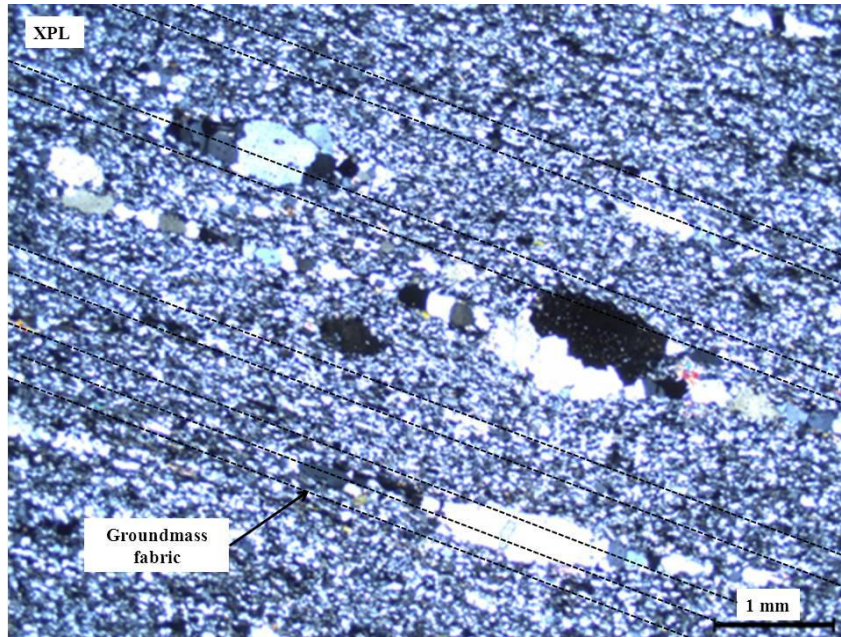


Figure 2.23 Photomicrograph of the Toggekry andesite (NG 15 A2) showing coarse quartz lenses with their long axis parallel to the groundmass fabric. . (See Map 3 and Map 4B in Appendix 5 for locality)

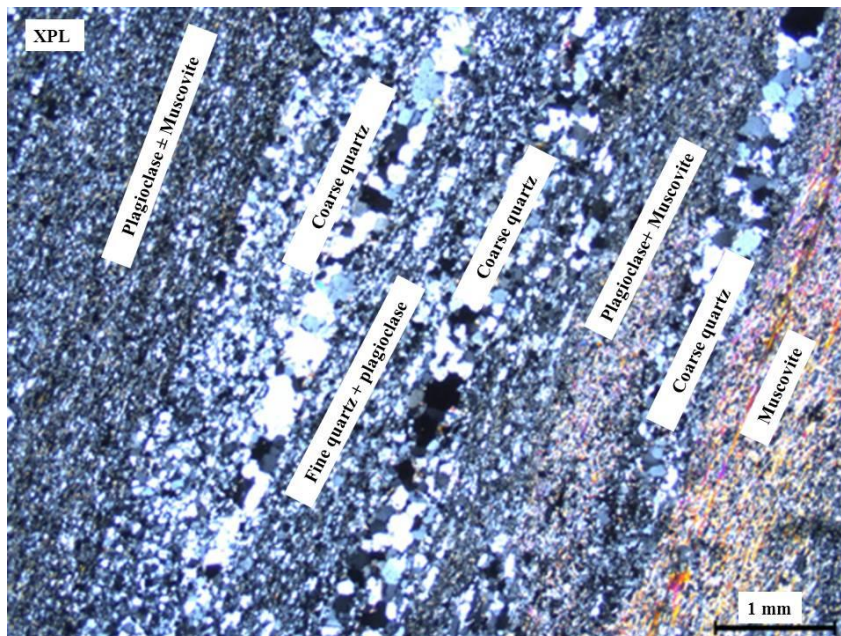


Figure 2.24 Photomicrograph of the Toggekry andesite (NG 15 A1) with textural and compositional lamination. . (See Map 3 and Map 4B in Appendix 5 for locality)

Sample NG 16

Sample NG 16 contains quartz, feldspar and muscovite. Plagioclase with albite twinning occurs as phenocrysts in a fine-grained matrix of plagioclase, quartz and muscovite (Fig 2.25). Plagioclase is the main feldspar type present in the rock and contains albite and Carlsbad twinning (Fig 2.26). The coarse quartz lenses in thin section display undulose extinction suggesting the rock must have been subjected to strain after crystallization.

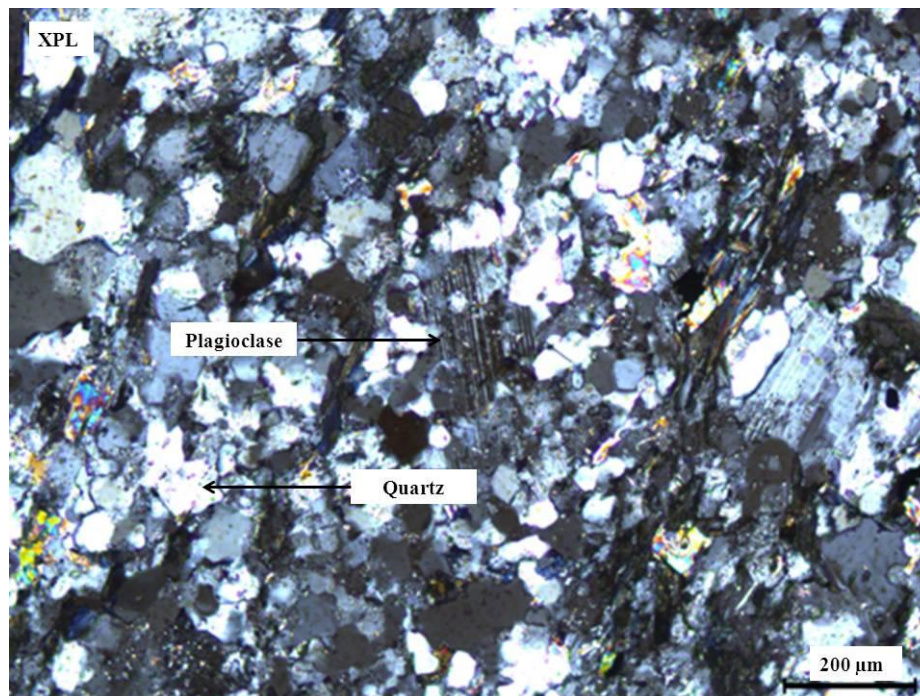


Figure 2.25 Photomicrograph of an andesite (NG 16) showing groundmass in the Toggekry andesite. Note the albite twinning in plagioclase. (See Map 3 in Appendix 5 for locality)

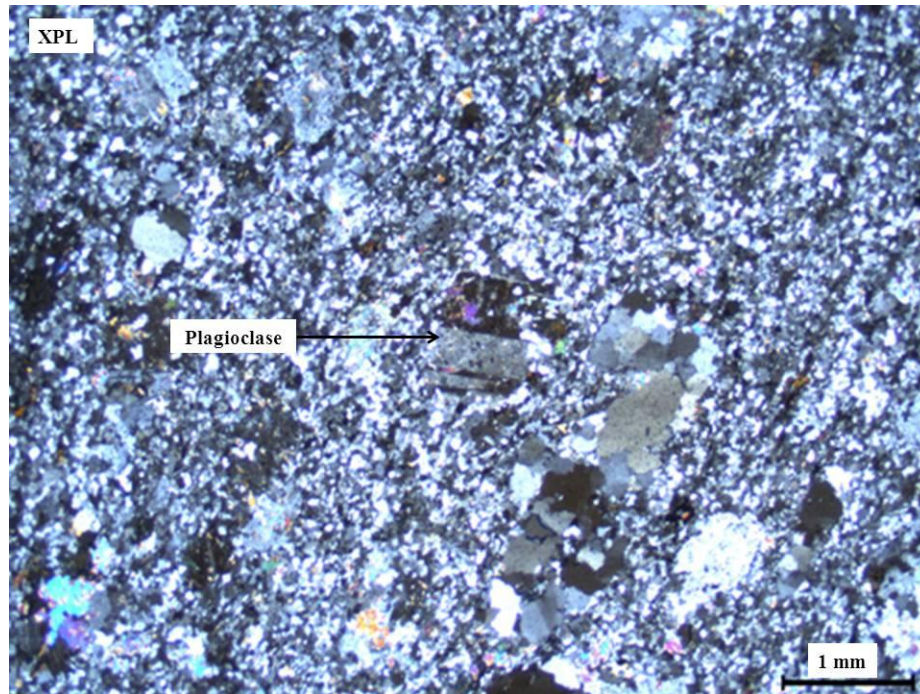


Figure 2.26 Photomicrograph of andesite (NG 16) showing plagioclase phenocrysts in a fine-grained matrix. (See Map 3 in Appendix 5 for locality)

2.2.2.5 Quartzites

Various quartzite units outcrop in the Toggekry Formation. One such unit is termed the central zone quartzite (Fig 2.27a). The unit, which is 900m in strike-length, occurs 150m north of the Black Hills serpentinite body. The unit ranges from 1.5m to 5m in width and is highly deformed (see Map 1 in Appendix 5). This unit lies within the quartz-sericite schists and is vertically dipping. This quartzite has been associated with sulphide minerals (Fig 2.27b). Extensive drilling by Anglo American Corporation in the 1980's supervised by Adrian Versfeld revealed the presence of narrow, low-grade copper-zinc sulphide bodies that showed little strike continuity.

2.2.2.6 Graphitic schist

A notable number of graphitic schists are present in the quartz-sericite schists (Wilson and Versfeld, 1994a). Outcrops of this unit are scarce and most have been mapped by electromagnetic survey and drilling. The units are parallel to the regional strike and vary in thickness from 1 metre to about 6 metres (Versfeld, 1988).



Figure 2.27(a) Quartzite from the Central zone (see map 1 in Appendix 5). (b) Hand specimens of the central zone quartzite with sulphide mineralization (E 030°53'08, 1"; S 28°09'34, 2").

2.2.3 The Witkop Formation

The Witkop Formation covers an area of about 300 km² and has a thickness of 7500 m, although this is due to tectonic duplication (Wilson and Versfeld, 1994b). Way-up direction on the northern limb of the fold (Fig. 2.1) is to the south while on the south-eastern limb it is to the west, indicating that the fold is a syncline.

This formation comprises about 33% medium sized (1m wide) variolitic pillows (which are komatiitic basalts), spinifex textured and massive flow units (Wilson and Versfeld (1994a, b). Pillow basalts constitute about 25% of the formation, with massive brecciated and spinifex textured komatiites making up 17% of the sequence and basaltic andesites constituting 10%. Diorites, chert, rhyolite, felsic tuffs, quartzites, calc-silicates and silicified stromatolites and evaporites comprise 15% of the formation.

The presence of stromatolites and evaporate deposits indicates a shallow water environment. Wilson and Versfeld (1994b) interpreted the coned structures present in the spinifex as evidence of high heat loss from top of lava flows as expected in shallow water environments.

2.3 Intrusions into the Nondweni Group

2.3.1 Quartz-feldspar porphyries

Quartz-feldspar porphyries are a minor component of the Toggekry Formation and are exposed along the Scheelite Stream (Fig 2.28). A number of these felsic units show chilled margins and cross cutting relationships with the overlying and underlying units indicating that they are intrusive in nature. These intrusive units are on average 1m in width. The units are steeply dipping and strike sub-parallel to the fabric in the underlying and overlying schists. These light greyish felsic rocks are fine-grained and have feldspar phenocrysts about 1mm in diameter. The porphyries show a weak foliation parallel to that of the underlying and overlying units.

The quartz-feldspar porphyries contain quartz, plagioclase and muscovite (Fig 2.29 and 2.30). Chlorite, biotite and opaque minerals occur as minor phases. Quartz and plagioclase occur as phenocrysts in a fine-grained groundmass of quartz, plagioclase and muscovite (Fig 2.29 and 2.30). The quartz phenocrysts display undulose extinction indicating rock was strained after

crystallization. The plagioclase phenocrysts are subhedral to euhedral and display multiple twins and have been partially to completely altered to muscovite and sericite.



Figure 2.28 Contact between the quartz-feldspar porphyry and chlorite schists (E 030°51'57, 9"; S 28°10'00, 5")

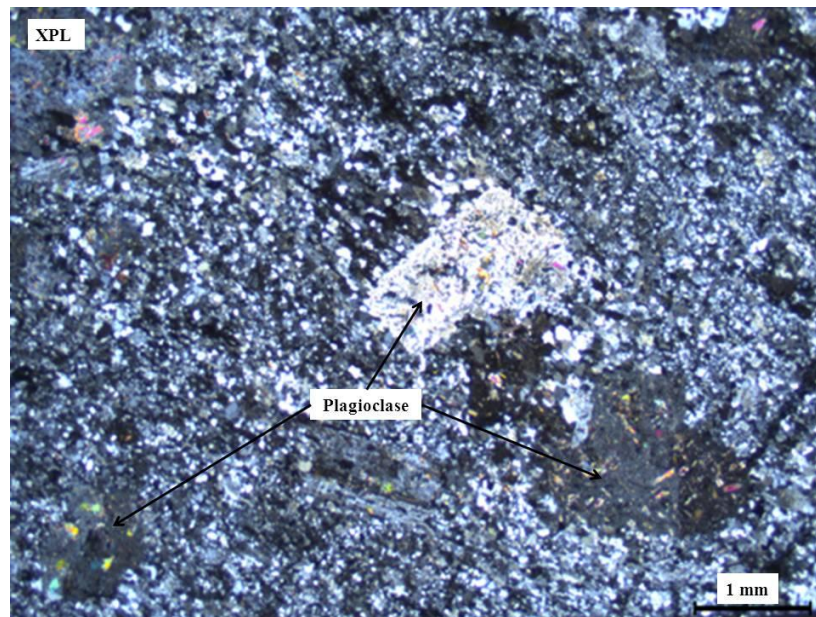


Figure 2.29 Photomicrograph of quartz-feldspar porphyry (NG 13) showing plagioclase phenocrysts in a fine-grained matrix of quartz and feldspar. Photo also shows partial alteration of plagioclase to sericite. (See Map 3 in Appendix 5 for locality)

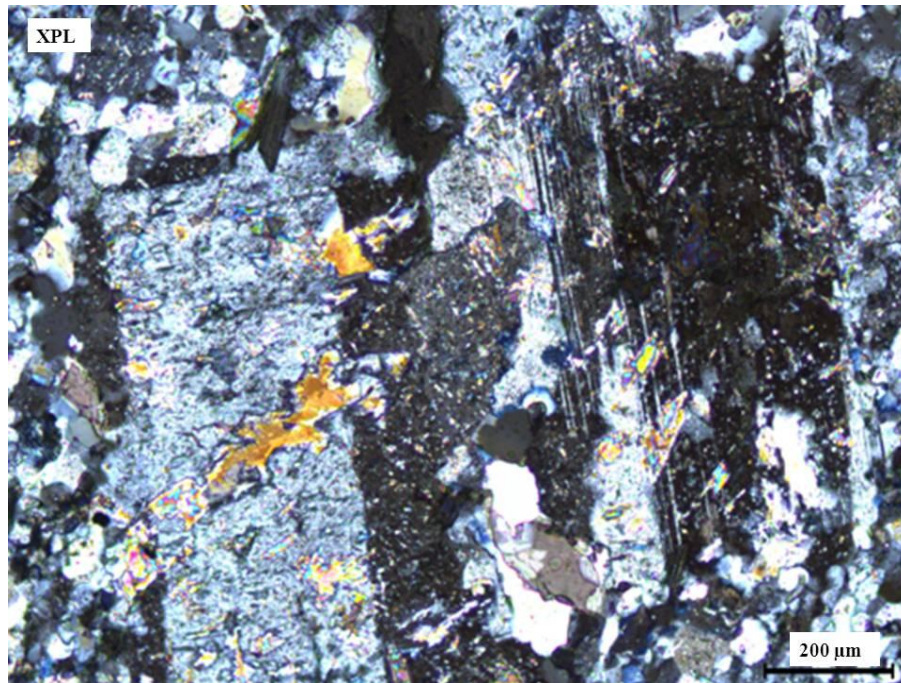


Figure 2.30 Photomicrograph of quartz-feldspar porphyry (NG 13) showing euhedral plagioclase phenocrysts displaying multiple twins. (See Map 3 in Appendix 5 for locality)

2.3.2 Serpentinite

Ultramafic bodies intrude the sericite schists of the Toggekry Formation (Fig 2.31) and have been altered to serpentinite. The size of the bodies ranges from a square metre to hundreds of square metres. A large serpentinite body called the Black Hills serpentinite (Fig 2.31a) intrudes into the sericite schists of the Toggekry Formation and may have a control on the concentration of the mineralization. The serpentinite body is un-layered, structure-less.

Petrographically the rock comprises acicular laths of lizardite, magnetite and relict olivine (Fig 2.32). Lizardite crystals are colourless under plane polarized light and exhibit a bluish colour under crossed nicols. Magnetite also forms a major constituent of the Toggekry serpentinites (~15% magnetite). The magnetite grains are anhedral. Alternation of compositionally different laminae is a prominent feature of the rock (Fig 2.33). The ultramafic protolith of the rock is uncertain but the presence of relict olivine and cleavage like features in the lizardite suggest that the rock may have been a peridotite consisting of olivine and pyroxene.



Figure 2.31 (a) Photograph of the Black hill serpentinite body intruding the Toggekry Formation (E 030°52'55, 2"; S 28°09'42, 4"). (b) Outcrop of the ultramafic intrusion (now altered to serpentinite) in the Toggekry Formation (E 030°52'37, 1"; S 28°09'58, 7").

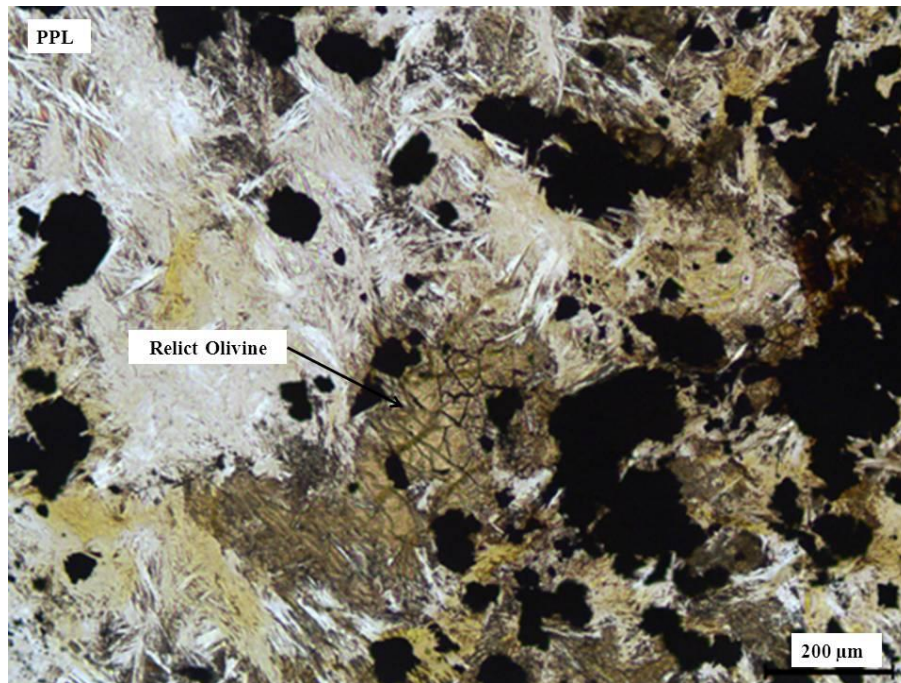
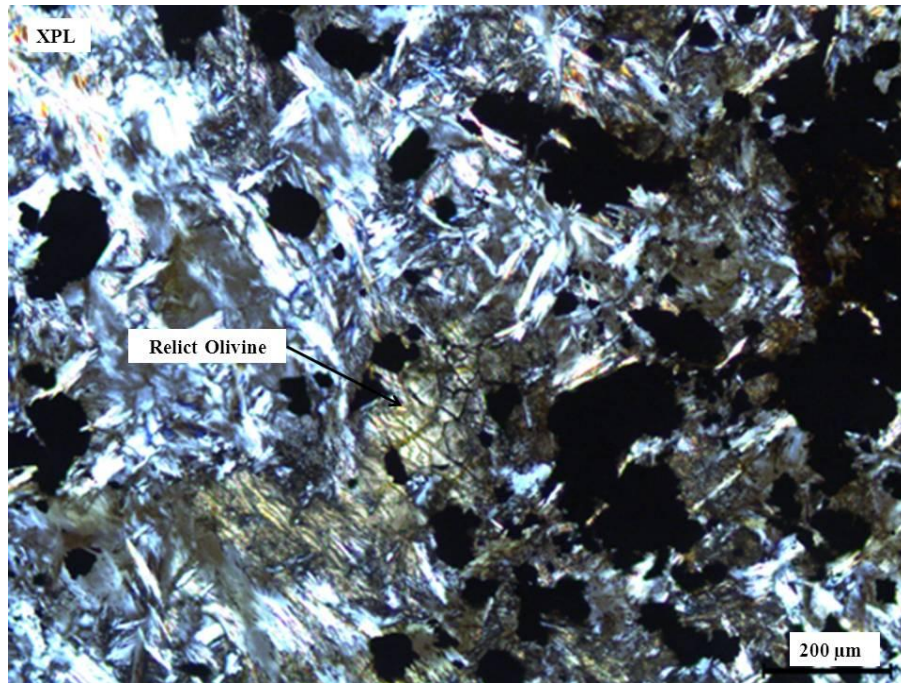


Figure 2.32 Photomicrograph of serpentinite (SPN 1) from Black Hill showing relict olivine. (See Map 3 in Appendix 5 for locality)

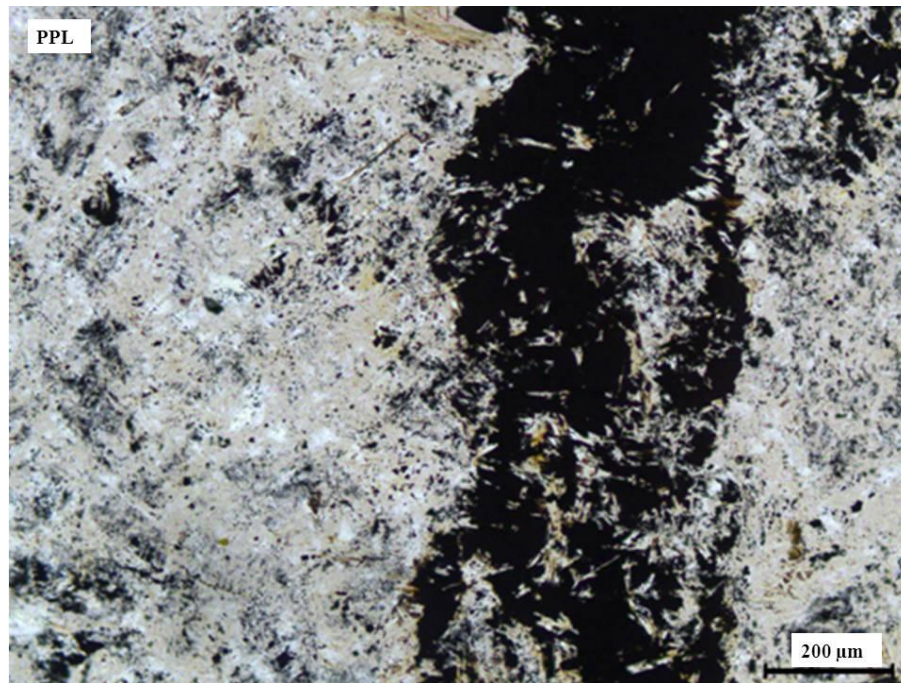
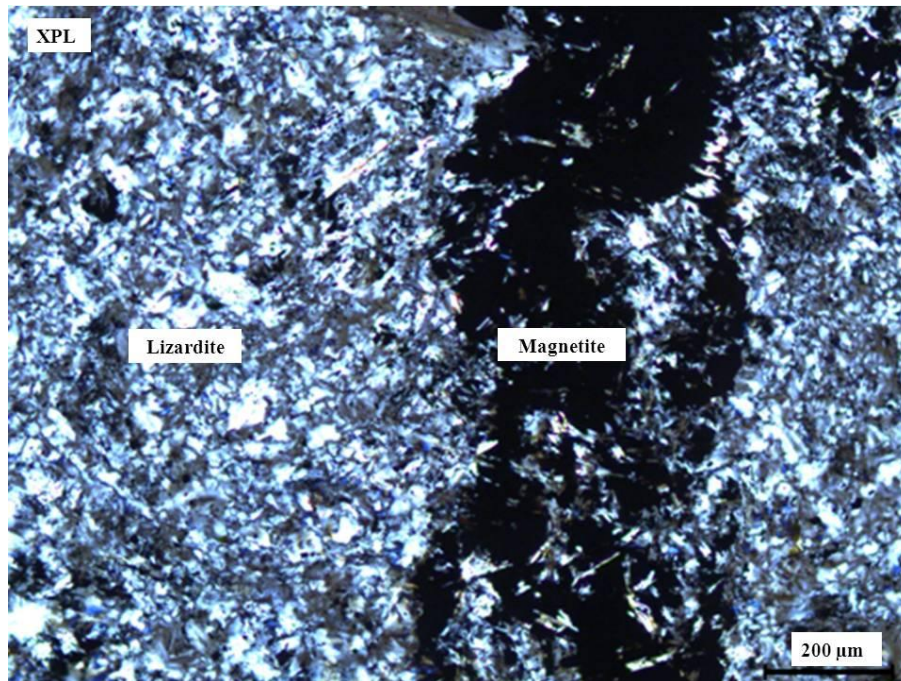


Figure 2.33 Photomicrograph of serpentinite (SPN 1) from Black Hill showing Alternation of compositionally different laminae. (See Map 3 in Appendix 5 for locality).

2.3.3 Mvunyana Granodiorite

The Toggekry Formation is intruded by a granitic body that is exposed mainly in the east with small outcrops present in the sericite schists. Matthews et al. (1989) identified two main granitoids in the area; a fine to medium-grained homogenous granite termed the Mvunyana granodiorite (Fig 2.34) and grey heterogenous gneiss that was not named. Matthews et al. (1989) obtained an age of 3290 ± 33 Ma for the Mvunyana granodiorite (Rb-Sr whole rock dating).



Figure 2.34 The Mvunyana granodiorite with pegmatites SW of St James Mine (E 030°52'33, 4"; S 28°10'02, 2").

The Mvunyana granitoids cross-cuts the lithological layering and the prominent east-west foliation in the Nondweni Group (Matthews et al., 1989). Enclaves of quartz-mica schists, metabasic schists, cherty quartzites, banded chert, fine-grained amphibolites, banded contact migmatites and serpentinite occur in the granodiorite along the contact between the granitoids and the Nondweni greenstones (Matthews et al. 1989). These enclaves range from centimetre scale to about 0.5 km in length. These were interpreted to indicate that the early phase of the granitoid event produced migmatitic gneisses, followed by the intrusion of the granitoids that then incorporated the migmatitic gneisses and rocks of the Nondweni Group.

2.3.4 Undeformed mafic dykes, sills and stocks

Various mafic dykes and sills intrude into the Nondweni Group and granitoids. These mafic dykes and sills range from metadolerite, vesicular-dolerite to dolerite and gabbroic stocks and sills. Versfeld (1988) mapped them out and obtained relative ages of the intrusions. He interpreted them to range from late Archaean to Jurassic in age. A meta-dolerite dyke from the Babanango area 30 km SE of Nondweni, which is considered part of the same Mesoproterozoic dark swarm as Nondweni dykes was dated by Burger and Walraven (1980) and an age of 1550 Ma was obtained.

The Toggekry Formation is also intruded by various gabbros/diorite bodies that are intruded by metadolerite dykes (Versfeld, 1988). Versfeld (1988) correlated them with the gabbroic suite that intrudes the Usushwana Complex in the Piet Retief-Amsterdam area about 100 km north of Nondweni.

2.4 Metamorphism of the Nondweni Group

Metamorphism of the Nondweni Group may be the result of three processes: sea-floor hydrothermal processes, regional metamorphism and contact metamorphism (Hofmann and Wilson, 2007; Saha et al., 2012).

2.4.1 Sea-floor hydrothermal processes: veins and silicification of the Toggekry Formation

Versfeld (1988) recognized carbonitization, silicification and talcification as the major alteration phenomena in the Nondweni greenstone belt. Hofmann and Wilson (2007) recognized silica alteration zones in the Witkop and Magongolzi Formations. The silica alteration zones are below chert horizons and silicification intensity increases towards the contact with the chert. This led to the conclusion that silicification in the Nondweni greenstone belt is directly related to the chert horizons.

Hofmann and Wilson (2007) proposed that silicification in the Nondweni greenstone belt is the result of low-temperature (<150°C) hydrothermal processes. According to the authors, alteration took place beneath Archaean seafloor by heated seawater that moved in shallow sub-seafloor convection cells driven by regional high heat flow. Rapid cooling of the fluid during mixing with colder seawater caused a decrease in silica solubility and silicification of volcanic rocks and

overlying seafloor sediments. This resulted in the silica alteration zones and bedded cherts horizons observed in the Nondweni greenstone belt. Carbonitization in the Nondweni greenstone belt is associated with alteration of ultramafic lithologies (Hofmann and Wilson, 2007).

Hofmann and Wilson (2007) identified two types of chert in the Nondweni Greenstone Belt, namely: Black-and- white banded chert and chert veins. The bedded chert horizons (Fig 2.35) are the result of sediments being deposited on the ocean floor and subsequently silicified by hydrothermal fluids (Hofmann and Wilson, 2007). According to Hofmann and Wilson (2007) these chert horizons do not represent pure chemical sedimentary rocks but rather consist of clastic, tuffaceous and biogenic material that have been surrounded by and partially replaced chemically precipitated chert.



Figure 2.35 Banded chert of the Toggekry Formation (E 030°52'29, 6"; S 28°09'57, 0").

Chert veins occur as stratiform veins of pure, translucent chert, and cross-cutting veins of carbonaceous chert. The chert veins present in the Toggekry Formation are of carbonaceous nature. This chert may be similar to the chert associated with the felsic rocks of the Theespruit Formation in the Barberton greenstone belt (Hofmann and Harris, 2008). The geometry of the

veins, evidence of hydraulic fracturing and wall rock replacement suggests that they may be associated with chert dykes and the veins were the result of hydrothermal fluids flowing upward through the footwall (Rouchon and Orberger, 2008; Hofmann and Wilson, 2007; Tice and Lowe, 2006; Van Den Boorn et al., 2010).

2.4.2 Regional metamorphism

The Nondweni greenstone belt has been subjected to greenschist facies regional metamorphism (Versfeld, 1988). This was deduced from the presence of lower greenschist facies mineral assemblages of tremolite-actinolite-plagioclase-chlorite-epidote observed in the basalts. As these minerals form the dominant planar fabric, this metamorphism most probably took place during the deformation that formed this fabric. The preservation of primary igneous minerals in the basalts and komatiitic andesites is ascribed to these rocks not being affected by the early hydrothermal event, leaving them less susceptible to the regional metamorphism (Versfeld, 1988).

2.4.3. Contact metamorphism

A zone of amphibolite facies 100 to 200m wide around the Mvunyana granodiorite is interpreted to be a thermal contact metamorphic aureole (Versfeld, 1988). Amphibolite facies mineral assemblages (garnet-hornblende-plagioclase) were observed in this study in pillow basalts of the Witkop Formation. The pillow rims are coarse-grained and comprise garnet-hornblende-chlorite-plagioclase and ilmenite. Garnets in these rims have average diameters of 6.4 mm. The pillow cores are devoid of garnets and are fine-grained with quartz, plagioclase, hornblende, epidote and minor calcite. For a detailed description of the mineralogy and texture of the garnet-bearing basalts of the Witkop Formation, see Appendix 6.

P-T conditions of metamorphism were calculated for the garnet-hornblende-plagioclase-quartz assemblages of the pillow rims using internally consistent thermodynamic data-set of Holland and Powell (1998) and THERMOCALC (Table 3, Appendix 6). This assemblage records peak metamorphic conditions of ~6 - 6.5 kb and 600 – 650 °C (Saha et al., 2012).

2.5 Structural Geology

2.5.1 Previous structural studies

Earlier studies on the structural geology of the Nondweni Group (Watkeys, 1981; Versfeld, 1988) recognised three major phases of deformation.

The first phase of deformation (D_1) is recumbent isoclinal folding of the primary bedding or layering (S_0) which imposed a strong penetrative axial planar cleavage (S_1) on the Toggekry Formation. These folds are gently plunging with E to W fold axes. Translation of the bedding (S_0) into the S_1 cleavage occurred as a result of this deformation. Mafic rocks of the Magongolozi and Witkop Formations do not exhibit the penetrative fabric associated with D_1 . Instead, narrow zones of high strain parallel to strike of the lithologies are present and represent early thrusting with a top-to-south sense of movement (Wilson and Versfeld, 1994a). This resulted in structural duplication of stratigraphy due to stacking of internally undeformed tectonic units (Watkeys, 1981; Wilson and Versfeld, 1994a).

The second phase of deformation (D_2) folded the greenstone belt into a south-westward plunging syncline (Fig 2.1). Plotting the bedding (S_0) and sub-parallel S_1 fabric from Wilson and Versfeld (1994a) reveals a fold plunging at 58° towards 247° (Fig 2.36). Minor folds in the limbs of this major fold formed in this second phase of deformation together with the S_2 axial planar cleavage. As a result of D_2 folding, D_1 folds are refolded and now have variable plunges (Watkeys, 1981). The Mvunyana granodiorite sharply transgresses the major synformal fold closure showing that the granitoid intrusion is post- D_2 . Figure 2.1 and the rest of the stereographic projection plots in this section were plotted using Georient ver 9.5.0.

The final phase of deformation (D_3) resulted in upright folds with axes steeply plunging to SSE deforming the earlier structures (Watkeys, 1981). This last phase of deformation also resulted in the stretching of the massive serpentinite bodies into boudins (Appendix 5, Map 1) (Watkeys, 1981). The emplacement of the granitoids east of the Nondweni greenstone belt was associated with the D_3 events (Wilson and Versfeld, 1994a).

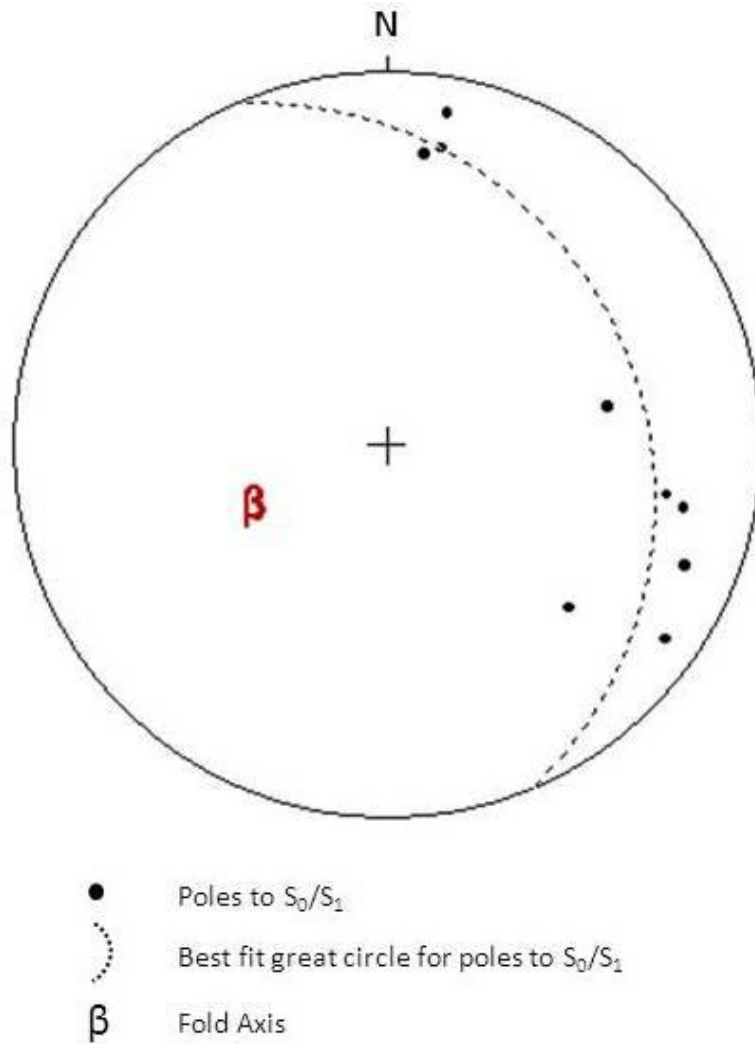


Figure 2.36 Orientation of D_2 fold structure (Structural data taken from Wilson and Versfeld, 1994a).

2.5.2 Structure of the Toggekry Formation

The study area has been divided into two domains for structural analysis, namely, the Eastern and Western domain, separated by the road to Vryheid (Fig 2.37).

Stereographic projections of the individual Toggekry Formation lithologies indicate that S_0/S_1 is steeply dipping to the SSW (Figure 2.38 a-d) however the quartz-sericite schists and amphibolites have variable S_0/S_1 orientations with a majority steeply dipping SSW to WNW (Fig 2.38 e, f).

Figure 2.38 (g and h) shows all the S_0/S_1 data for the Eastern and Western domains respectively. In the Western domain S_0/S_1 is consistently steeply dipping to the S to SW at an average dip of 80° and strike of 106° . The Eastern domain S_0/S_1 exhibits variable orientations indicating folding plunging steeply to the SW and reflecting later deformation of the quartz-sericite schists in this domain.

The lineations in the Toggekry Formation have similar plunges (Fig 2.39 a-f) in the Western (Fig 2.39 g) and Eastern domains (Fig 2.4 h) with the average plunge of 70° . The lineations all plot on or close to the average S_0/S_1 plane (Fig. 2.38 g). They also plot on or close to the fold axis defined by the folded S_0/S_1 in the quartz-sericite schists (Fig 2.38 e). It is off note that the lineations are steeply plunging in the S_0/S_1 plane.

The lineations measured in rocks exposed in Scheelite Stream are parallel to the long axis stretched pillow basaltic andesites (Fig 2.40), and thus they represent stretching lineations. However in the Eastern domain there is uncertainty as to whether this is also the case as here they may represent either intersection lineations (between layering and cleavage) or stretching lineations.

GEOLOGICAL MAP OF THE TOGGEKRY FORMATION (NONDWENI GREENSTONE BELT)

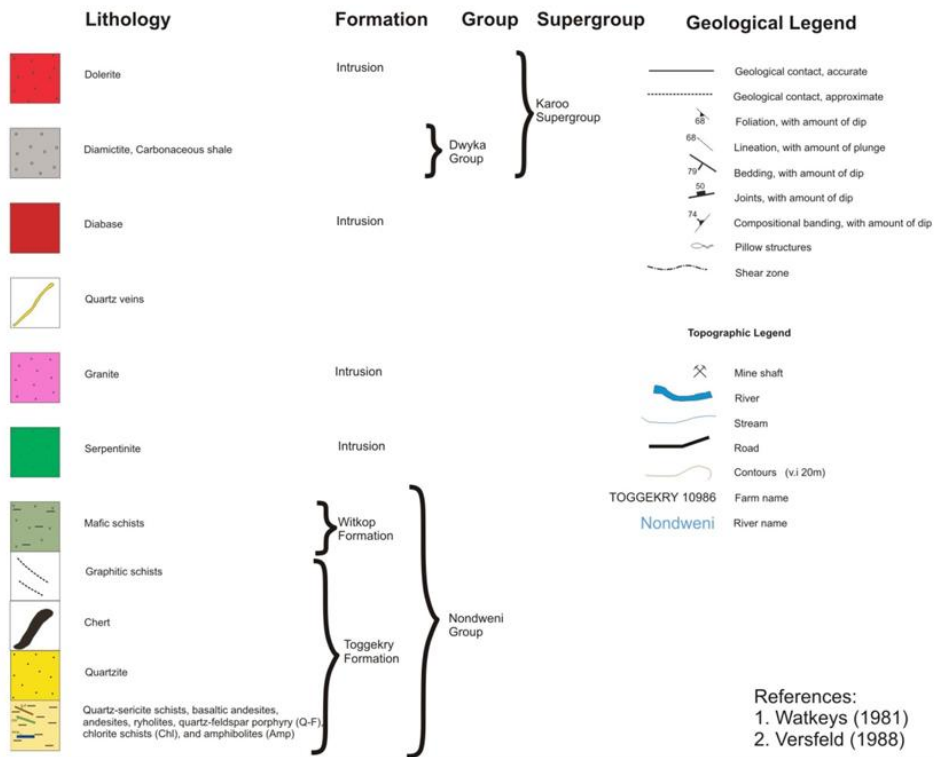
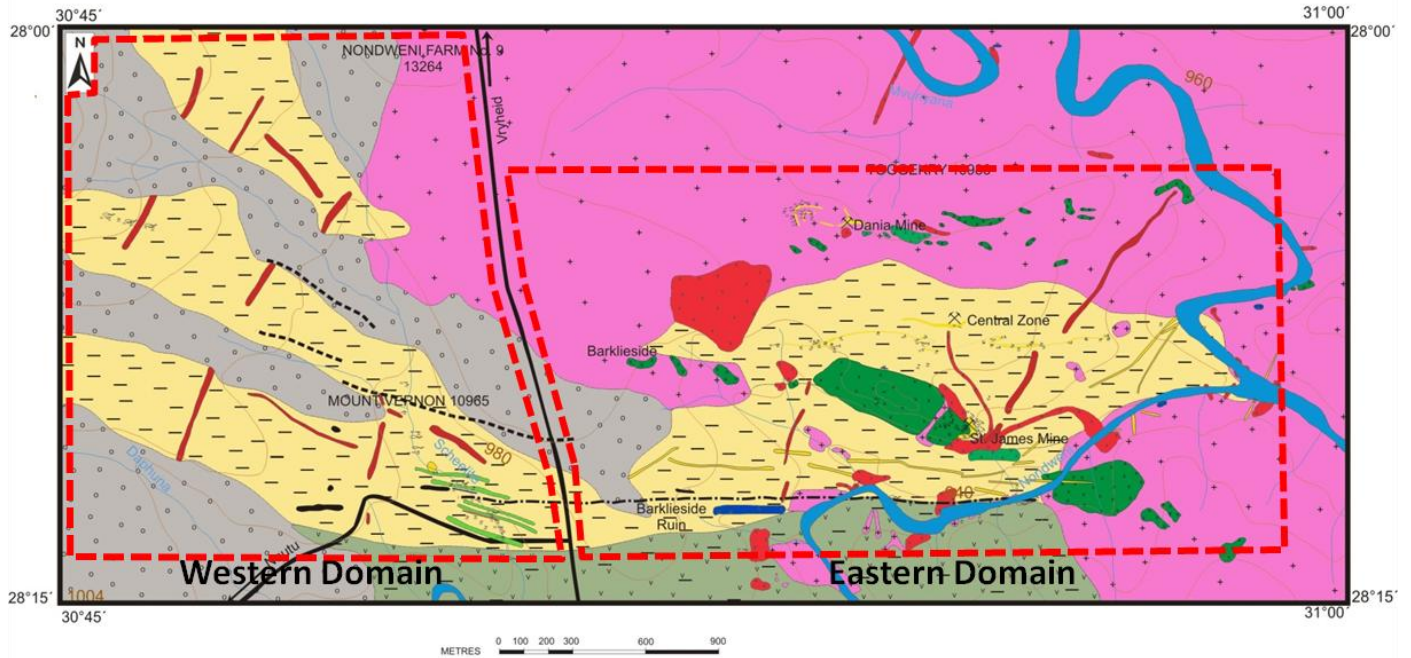


Figure 2.37 Geology map of the Toggekry Formation.

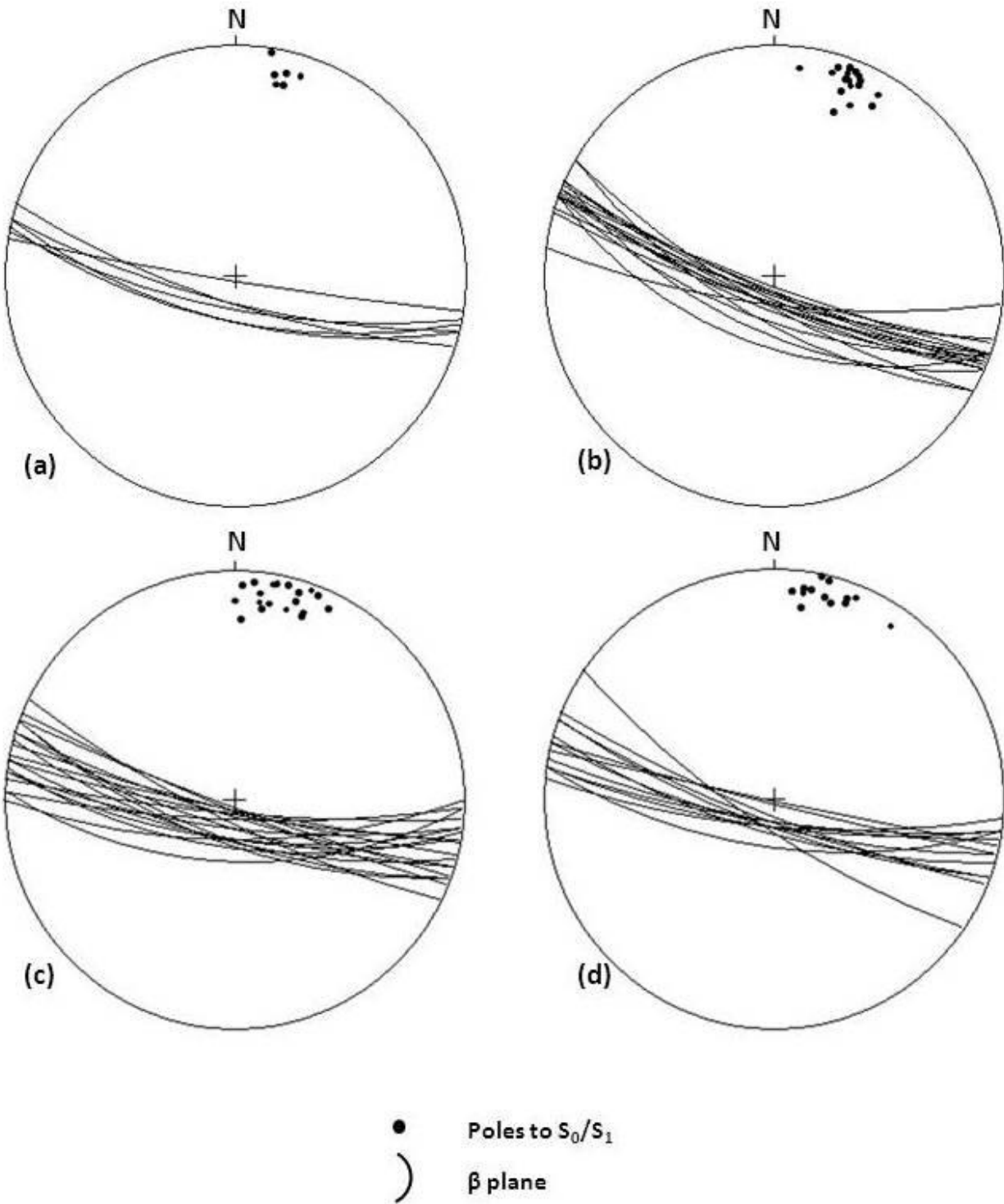


Figure 2.38 S_0/S_1 poles for the Toggekry Formation. (a) Mt. Vernon rhyolite. (b) Basaltic andesites. (c) Undifferentiated felsic schists. (d) Chlorite schists.

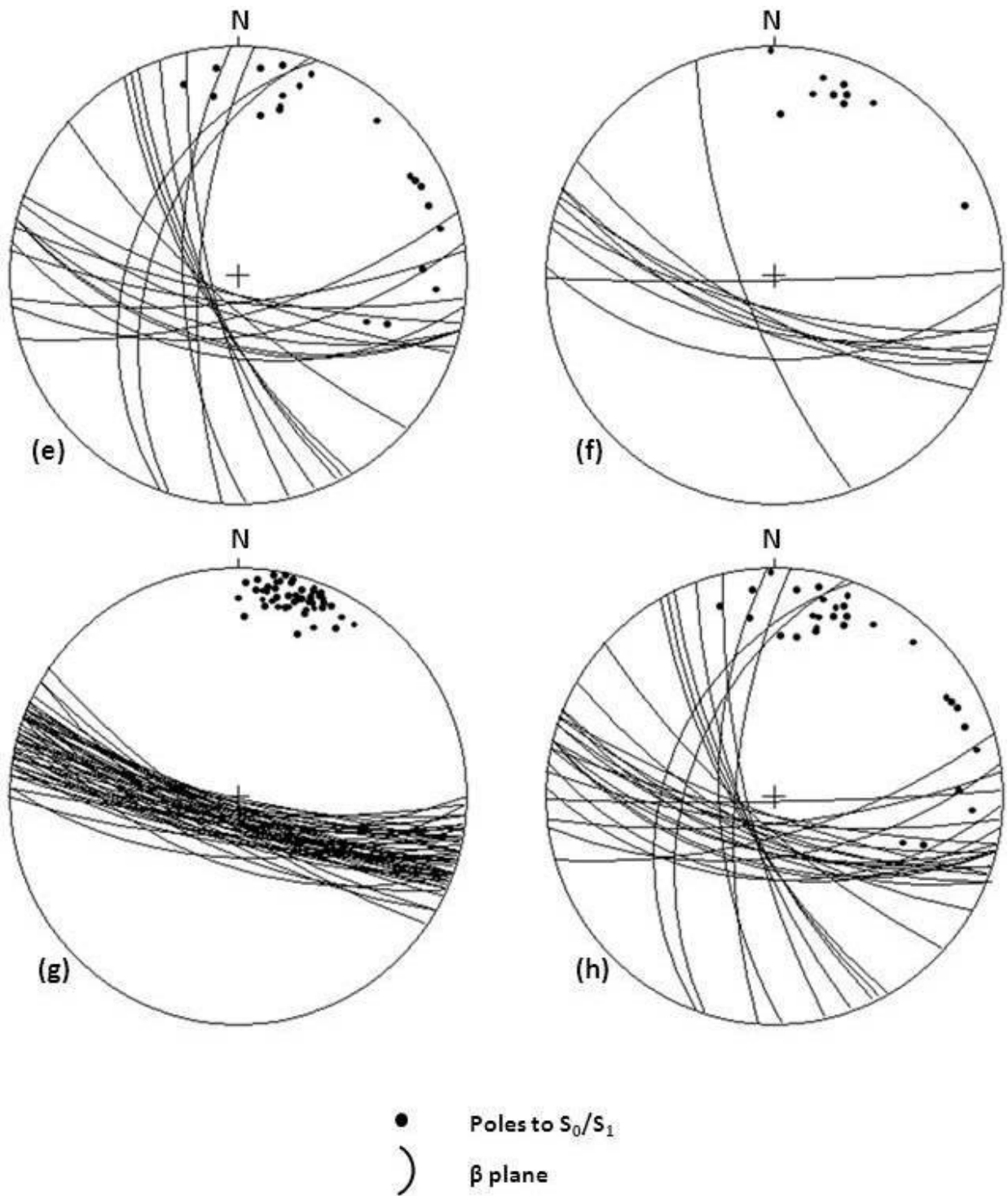


Figure 2.38 S_0/S_1 poles for the Toggekry Formation (e) Quartz-sericite schists. (f) Amphibolites. (g) All S_0/S_1 in the Western domain. (h) All S_0/S_1 in the Eastern domain.

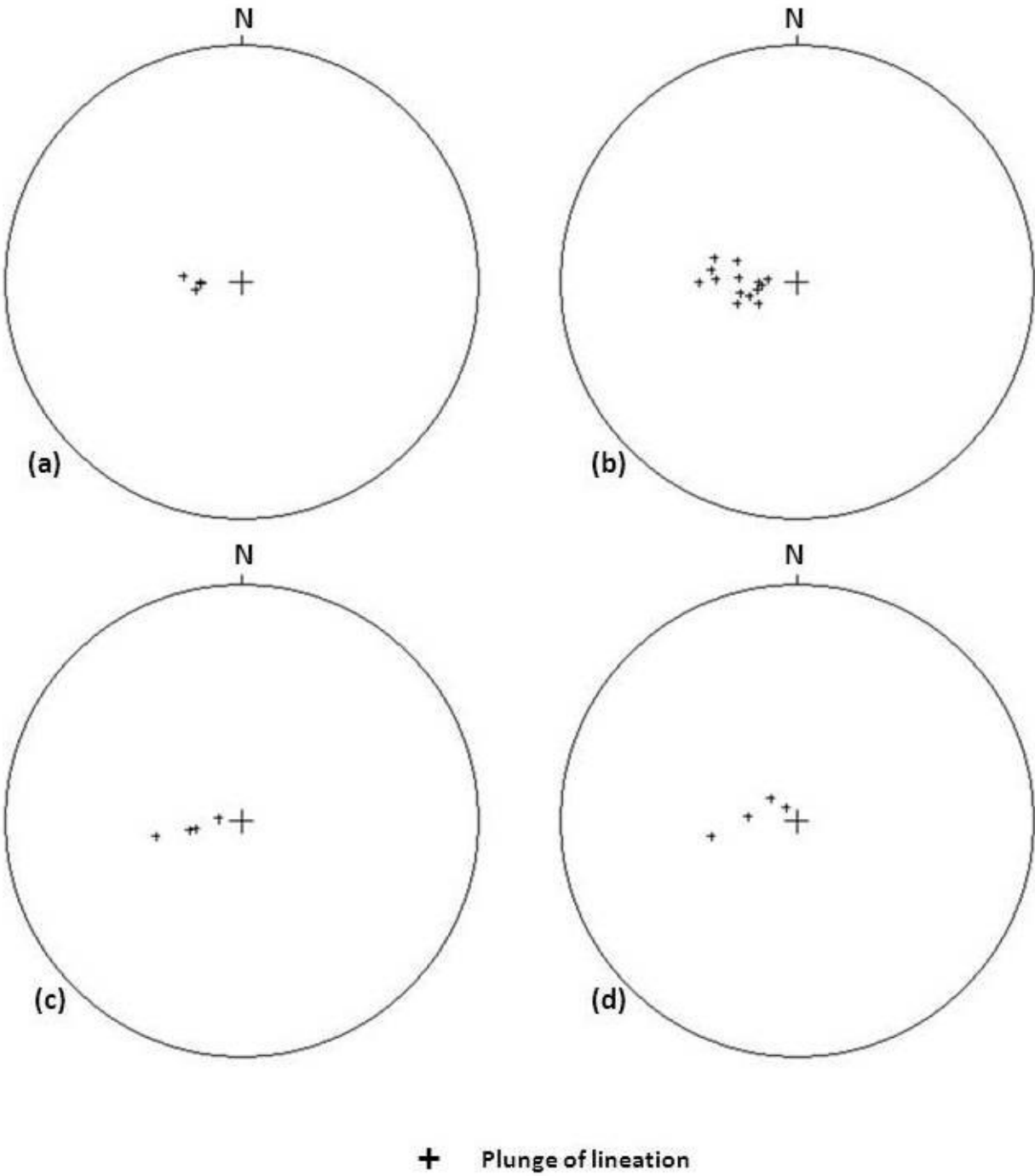


Figure 2.39 Lineations of the Toggekry Formation. (a) Mt. Vernon rhyolite. (b) Basaltic andesites. (c) Undifferentiated felsic schists. (d) Chlorite schists.

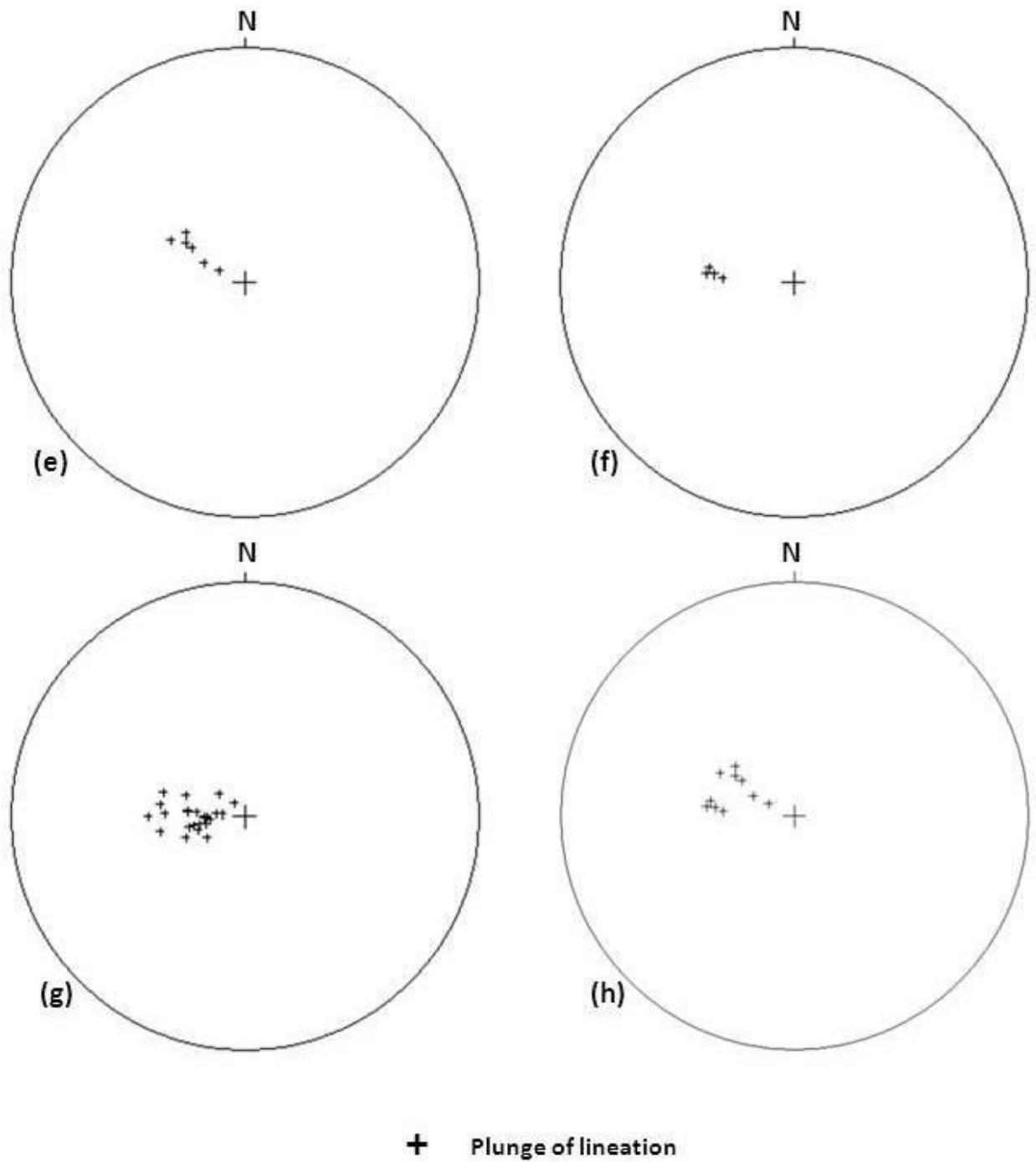


Figure 2.39 Lineations of the Toggekry Formation. (e) Quartz-sericite schists. (f) Amphibolites. (g) Western domain. (h) Eastern domain.

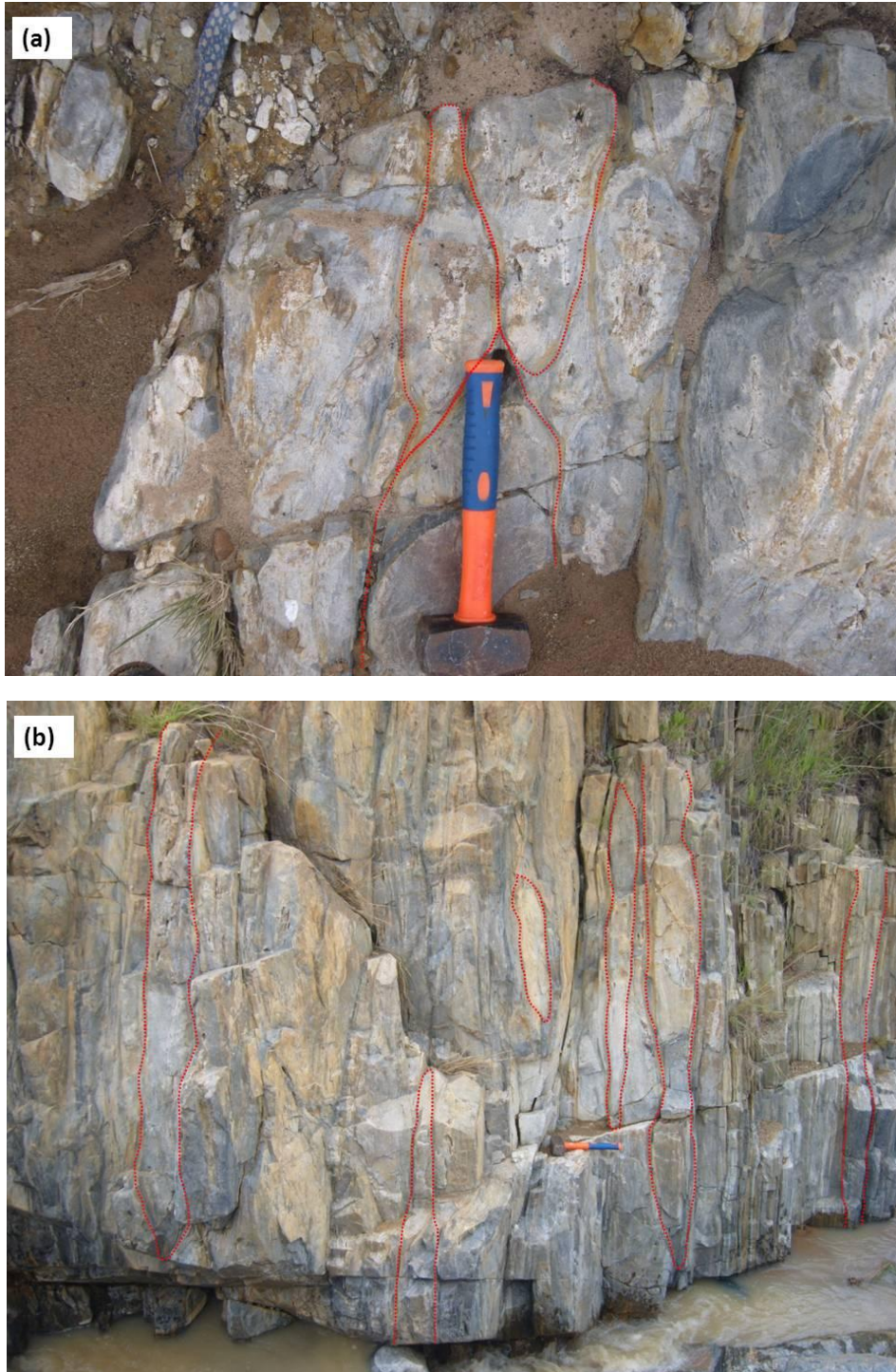
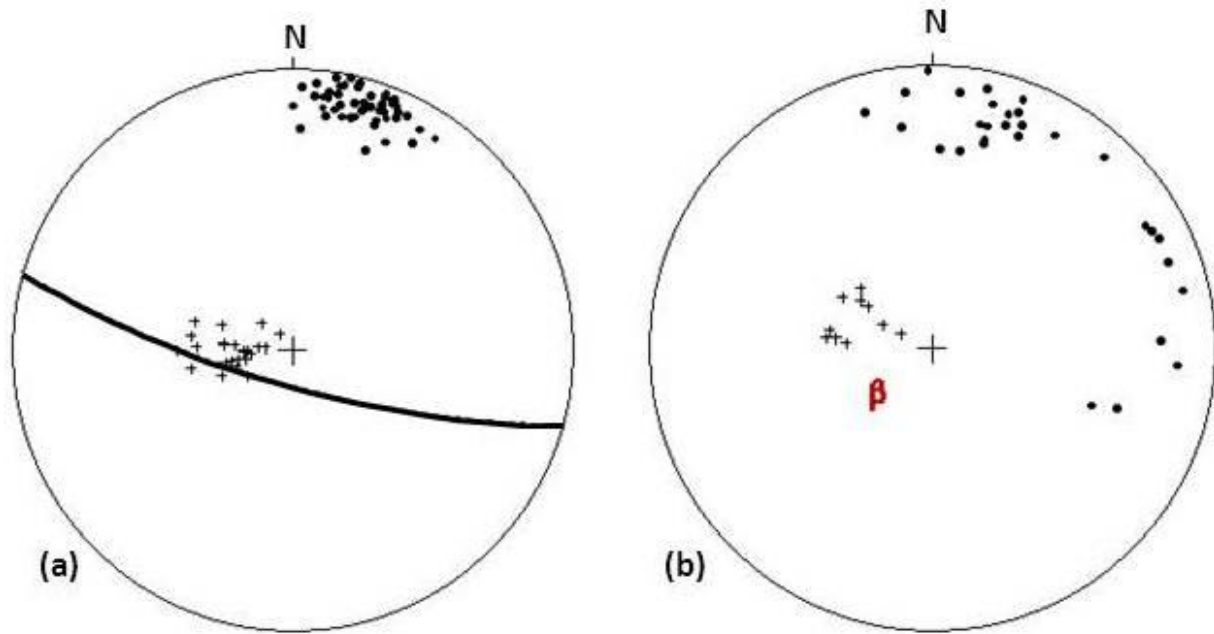


Figure 2.40 Stretched pillows in basaltic andesites of the Toggekry Formation. (a) Plan view of least deformed pillows in the Scheelite Stream (E 030°51'45, 6"; S 28°09'48, 9"). (b) Section view of flattened pillows in the Scheelite Stream (E 030°51'45, 7"; S 28°09'49, 4").

Poles to the S_0/S_1 fabric of the Western domain cluster and yield an average S_0/S_1 dip of 80° S and strike of 106° (Fig 2.41 a). The “L” fabric has an average plunge of 71° and plunge direction of 269° . The S_0/S_1 poles for the Eastern domain spread along a great circle indicating a F_2 fold axis plunging at 70° towards 233° (Fig 2.41 b). This fold axis plots close to the lineations in both this domain and the Western domain. It is also close to the D_2 regional synformal axis (Fig 2.36). There is no spread of data in the Western domain indicating no evidence of folding of the foliation as can be seen in the Eastern domain.

The reason for the folding in the Eastern domain is probably the competency contrast provided by the presence of the quartzite layers and serpentinite bodies. Figure 2.42 shows a simplified 3D sketch of the structures around the St. James mine. The cleavage trace which strikes at $\sim 200^\circ$ is adjacent to the granitoid intrusion and thus may have been transposed during the intrusion of the Mvunyana granodiorite. The cleavage which strikes between 150° and 185° is in the lithologies directly adjacent to the Black Hill serpentinite body. This cleavage was refracted around the serpentinite body which was also boudinaged during deformation. The fold axis defined by the refracted cleavage may reflect the fold mullion or axis of the boudins.



- Poles to S_0/S_1
- ⊕ Plunge of lineation
-) Average S_0/S_1 β plane
- β F_2 Fold Axis

Figure 2.41 S_0/S_1 and lineations of the Toggekry Formation. (a) Western domain. (b) Eastern domain.

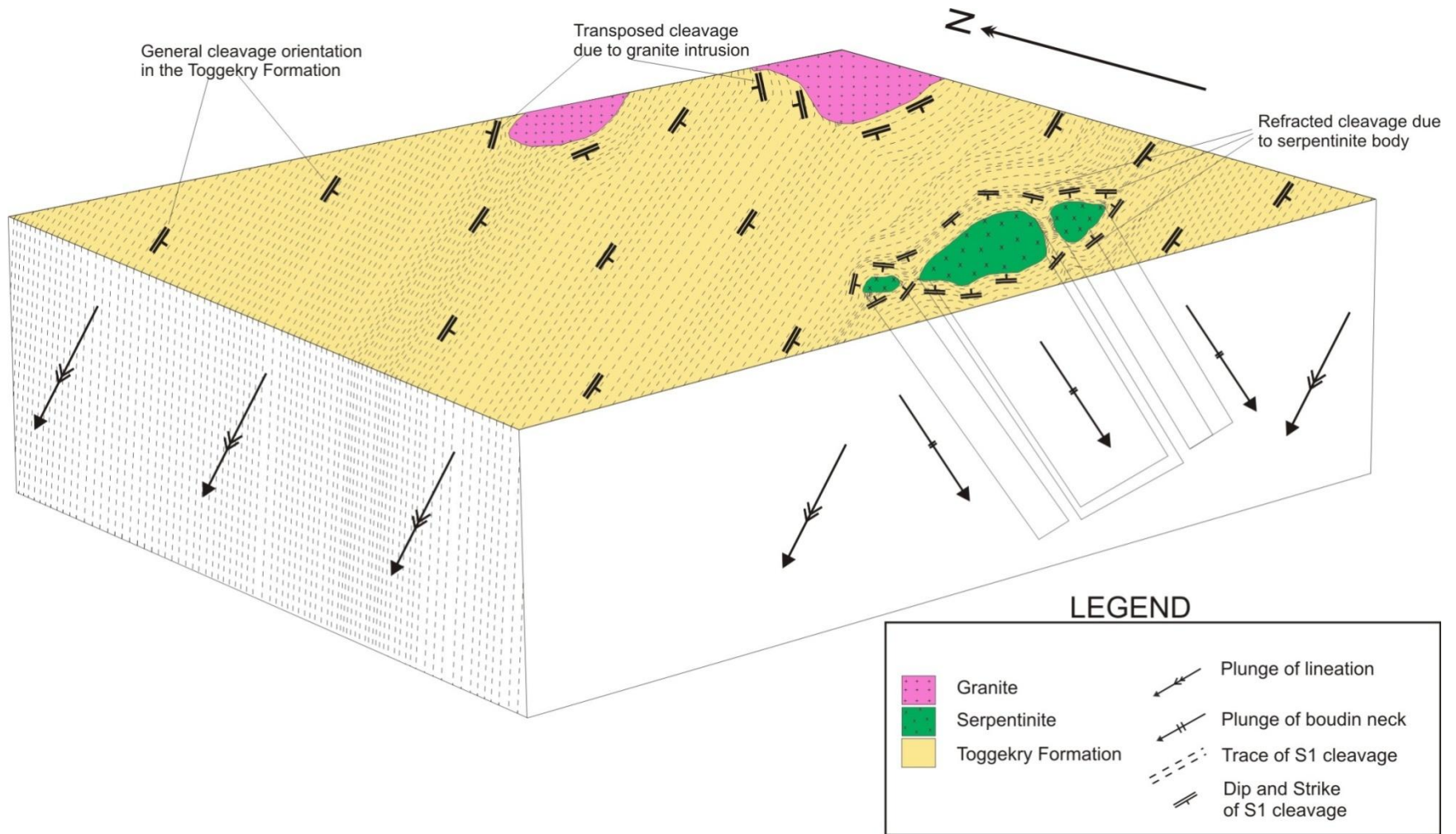


Figure 2.42 3D Sketch of structures in the eastern domain

2.5.3 Interpretation of the tectonic history of the Toggekry Formation

On first inspection of the data it appears that the lineations are parallel or sub-parallel to F_2 fold plunge in the Eastern Domain (Fig 2.41 b) and regional syncline (Fig 2.36). Furthermore, the elongation direction of stretched pillows exposed in the Scheelite Stream section is parallel to the regional lineation and the pillows have an overall prolate shape (Fig 2.40). Therefore one possible interpretation is that, during folding of an originally oblique layer under prolate strain conditions, stretching occurred parallel to the D_2 fold axis and an axial planar cleavage developed. In this case the lineations present in the Toggekry Formation would represent both stretching and intersection (L_2) lineations. Both F_2 and L_2 would be parallel to X axes of D_2 strain ellipsoid in the XY plane (Fig 2.43).

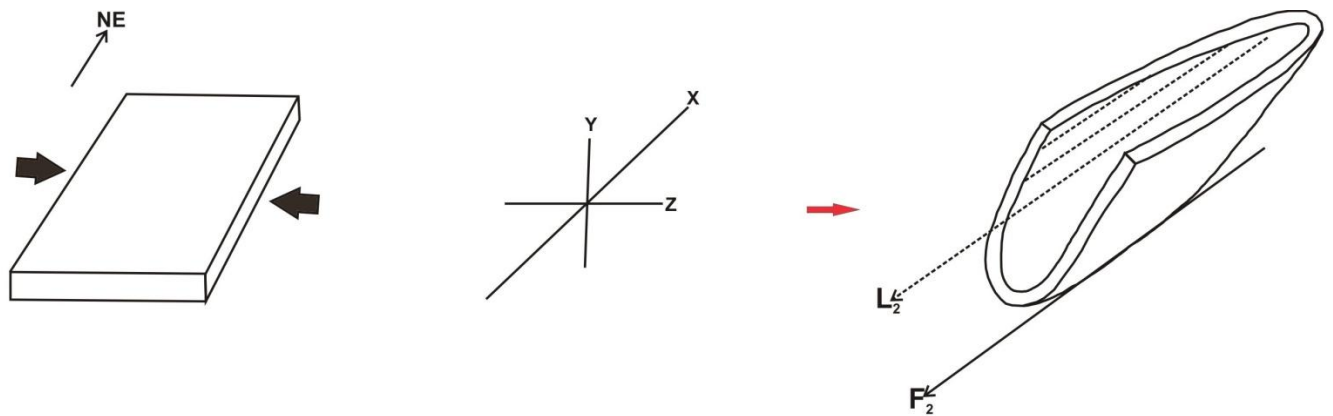


Figure 2.43 Simplified sketch showing stretching lineations (L_2) parallel to F_2 and the axes of D_2 strain ellipsoid.

However more detailed analysis shows that the the lineations are not always parallel or sub-parallel to F_2 , they plunge W to WNW while F_2 plunges SW. This raises two other possibilities:

- (1) Prior to F_2 the layering may have been oblique to the principal axes of the F_2 strain ellipsoid as a result of tilting or earlier deformation event (D_1). Here the orientation of the original layering defined the plunge of F_2 . The deformed pillows reveal that in F_2 prolate strain occurred, with the X-axes of the strain ellipsoid defined by the orientation of the lineations which are stretching lineations. In this interpretation, the F_2 fold axis formed at an angle to the L_2 stretching direction. F_2 is parallel to layering in the XY plane of D_2 strain ellipsoid while L_2 is parallel to X axes of D_2 strain ellipsoid (Fig 2.44).

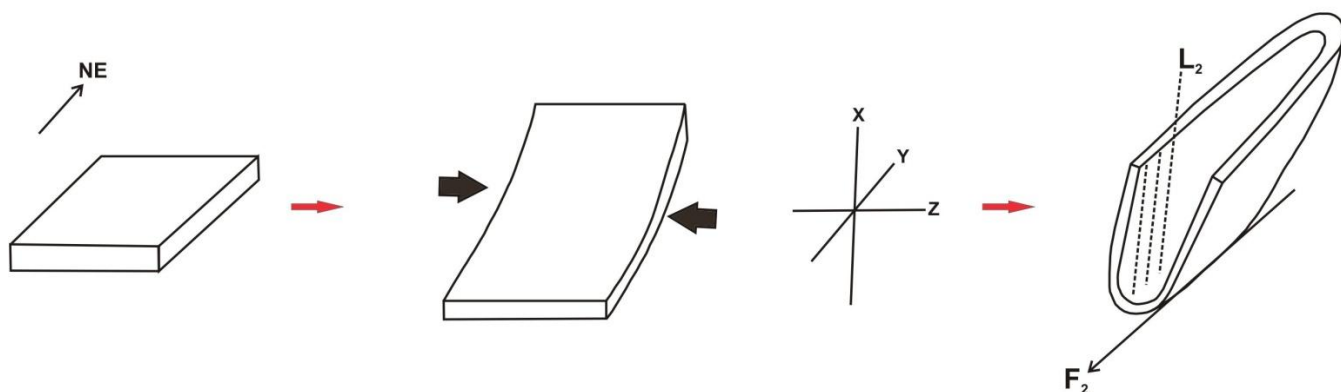


Figure 2.44 Simplified sketch showing stretching lineations (L_2) parallel to X axes of D_2 strain ellipsoid.

(2) The second possibility is that the lineations predate D_2 but had an original L_1 orientation close to the subsequent F_2 fold axis. Therefore the L_1 lineations were deformed by D_2 around F_2 , which was parallel to XY plane of the D_2 strain ellipsoid (Fig 2.45).

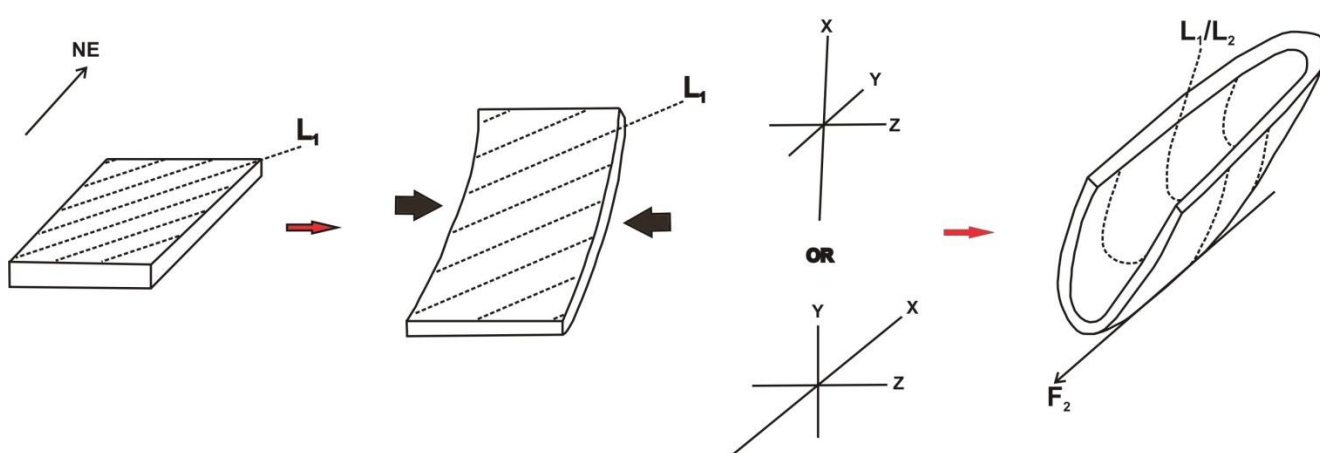


Figure 2.45 Simplified sketch showing lineations (L_1) pre and post D_2 deformation.

In this interpretation L_1 was deformed by D_2 buckling. The end-member mechanisms of buckle folds are flexural folding and tangential longitudinal strain (TLS) (Ramsay, 1967). In the former case lineations deform around a fold axis along a small circle and the latter display more complex loci (Fig 2.46). According to Ramsay (1967) folding under TLS results in the increase in the angle between the deformed lineations and the fold axis in the outer arc by an amount which depends on the amount of extension. In the inner arc the angle between the deformed lineations and the fold axis decreases. On a stereonet, folding under TLS will thus exhibit a shape similar to the one shown in Figure 2.46a, where the fold axis is horizontal.

When the fold axis (F_2) for the Nondweni greenstone belt is restored to the horizontal and the lineations restored by a similar amount a shape similar to one described by Ramsay (1967)

for TLS can be seen (Fig 2.47). Due to limited amount of structural data the shape is not obvious but can be seen and a clear spread of data is visible. The only difference between the shape exhibited by the Toggekry lineations and that of an ideal TLS fold is that the neutral surface looks concave with respect to fold axis instead of being convex. The reason for this may be due to limited structural data.

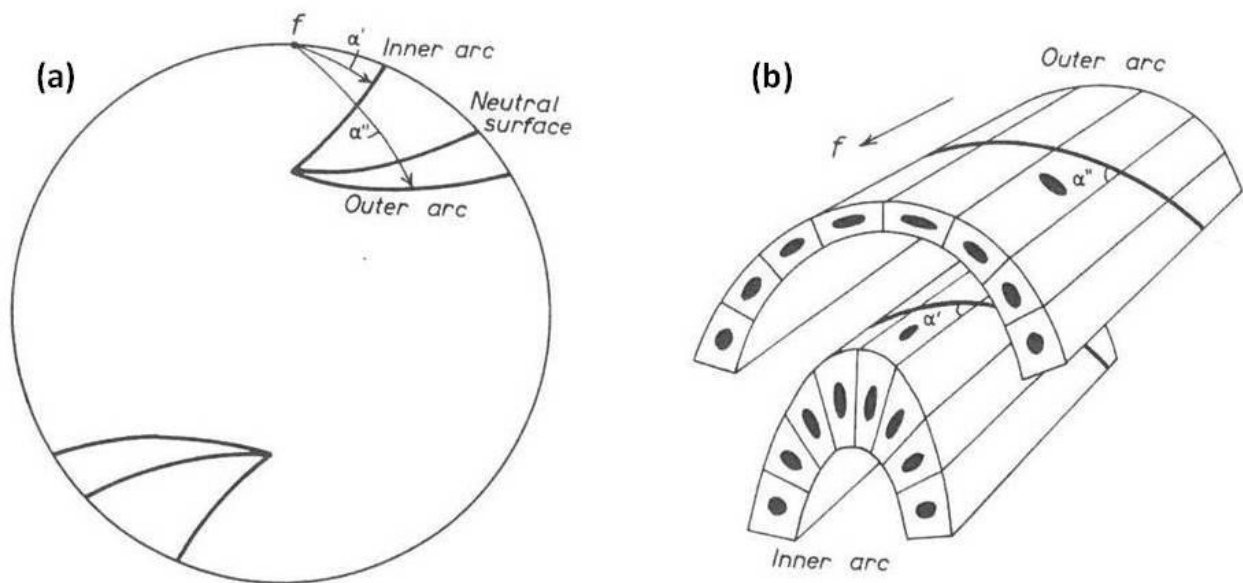


Figure 2.46 Linear structures deformed by Tangential longitudinal strain from Ramsay (1967).

CHAPTER 3: GEOCHRONOLOGY

3.1 Introduction

Earliest geochronological studies by Matthews et al. (1989) of the Nondweni greenstone belt gave a minimum age of 3290 ± 33 Ma, based on whole rock Rb-Sr dating on an intrusive granodiorite (Mvunyana granodiorite), which is located east of the Nondweni greenstone belt. More recent SHRIMP zircon studies by Xie et al. (2012) have yielded $^{207}\text{Pb}/^{206}\text{Pb}$ ages of 3525 Ma to 3539 Ma and a mean age of 3532 ± 4 Ma for the Toggekry Formation.

In this chapter, additional U-Pb ages are presented, and these data, together with previous geochronological studies on the formation as well as tectono-metamorphic events in the area are used to improve our understanding of the tectonic evolution of the Nondweni greenstone belt. For this reason five rock samples were analysed using laser ablation multi-collector inductively coupled plasma-mass spectrometry (LA-MC-ICP-MS). Two andesitic samples (NG 3A and NG 15), a quartz-feldspar porphyry (NG 13) and a rhyolite (NJ 10 L 5A) were analysed using zircon crystals. A quartz-sericite schist (NG 3B) was analysed using monazite.

Detailed analytical techniques and data analyses are found in Appendix 1. The U-Pb isotopic data for the samples analysed is given in Table 4.1 (for zircons) and Table 4.2 (for monazites) in appendix 4.

3.2 Rhyolite (NJ-10-L5A)

Only one zircon was found in the Mount Vernon rhyolite. This may have been a result of the zircons being fine grained resulting in most of them being washed away during the sample treatment process. The zircon crystal is $100\mu\text{m}$ in width and shows fine oscillatory zoning in cathodoluminescence (CL) imaging, indicating a magmatic origin (Fig 3.1 a).

The single zircon gave a concordia age of 3547 ± 54 Ma with a MSWD (of concordance) of 4.1 and 0.042 probability of concordance (Fig 3.1 b).

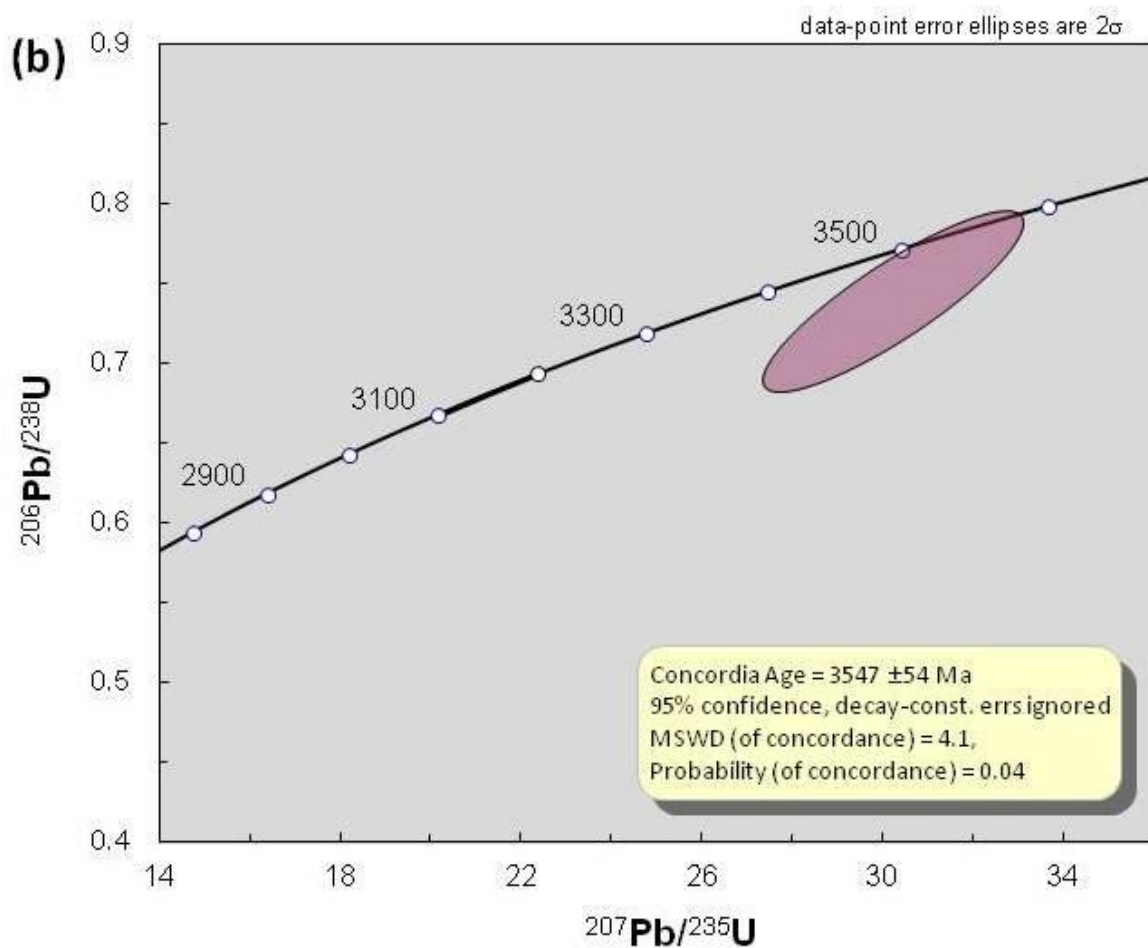
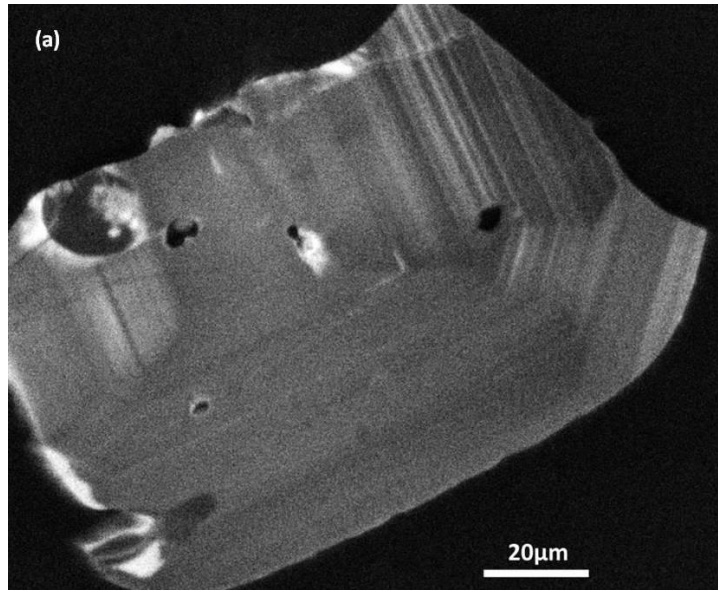


Figure 3.1 (a) Cathodoluminescence image of the zircon from Mount Vernon rhyolite with magmatic zoning (b) U-Pb concordia plot for the NJ-10-L5A zircon. In this plot, as in the following diagrams, data point error ellipses are 2σ and decay constant errors have been ignored.

3.3 Andesite (NG 3A)

Thirty-three zircons were analysed from sample NG 3A. The zircons exhibit strong magmatic zoning (Fig 3.2a). The bright zones in the CL images represent U-Hf- and Y-depleted zones in the zircon (Williams et al., 1996b; Poller et al., 2001).

A cumulative probability plot and histogram for the thirty-three zircon crystals analysed reveals one distinct age population (Fig 3.2b). All the grains analysed are discordant and thus reflect Pb loss but one discordant grain yielded a $^{207}\text{Pb}/^{206}\text{Pb}$ an age of 3048 ± 30 Ma, which is interpreted to reflect greatest Pb loss than the other analysed grains. Table 4.1 in Appendix 4 indicates the grain 29 has the greatest % of discordance (86% discordance) and this is the same grain that yielded a $^{207}\text{Pb}/^{206}\text{Pb}$ age of 3048 ± 30 Ma indicating high Pb loss and thus the age is not meaningful. The Wetherill U-Pb concordia curve reveals radiogenic Pb-loss but gives an upper intercept age of 3545 ± 12 Ma and lower intercept age of 197 ± 25 Ma with a MSWD of 0.85 at 95% confidence (Fig 3.2c).

3.4 Andesite (NG 15)

Sample NG 15 yielded five zircons. Some zircons are strongly zoned, indicating a magmatic origin (Fig 3.3a). Some of the zircons have undergone metamictization which has resulted in the internal development of fractures within the zircons and destruction of the original magmatic zoning (Fig 3.3b).

A cumulative probability plot and histogram for the five zircon crystals analysed reveals one distinct age population (Fig 3.4c). The Wetherill U-Pb concordia curve also reveals radiogenic Pb-loss but gives an upper intercept age of 3574 ± 61 Ma and lower intercept of 439 ± 410 Ma with a MSWD of 0.048 at 95% confidence (Fig 3.3c). One concordant point gives a concordia age of 3540 ± 61 Ma with a MSWD (of concordance) of 2.5 and 0.11 probability of concordance (Fig 3.3d).

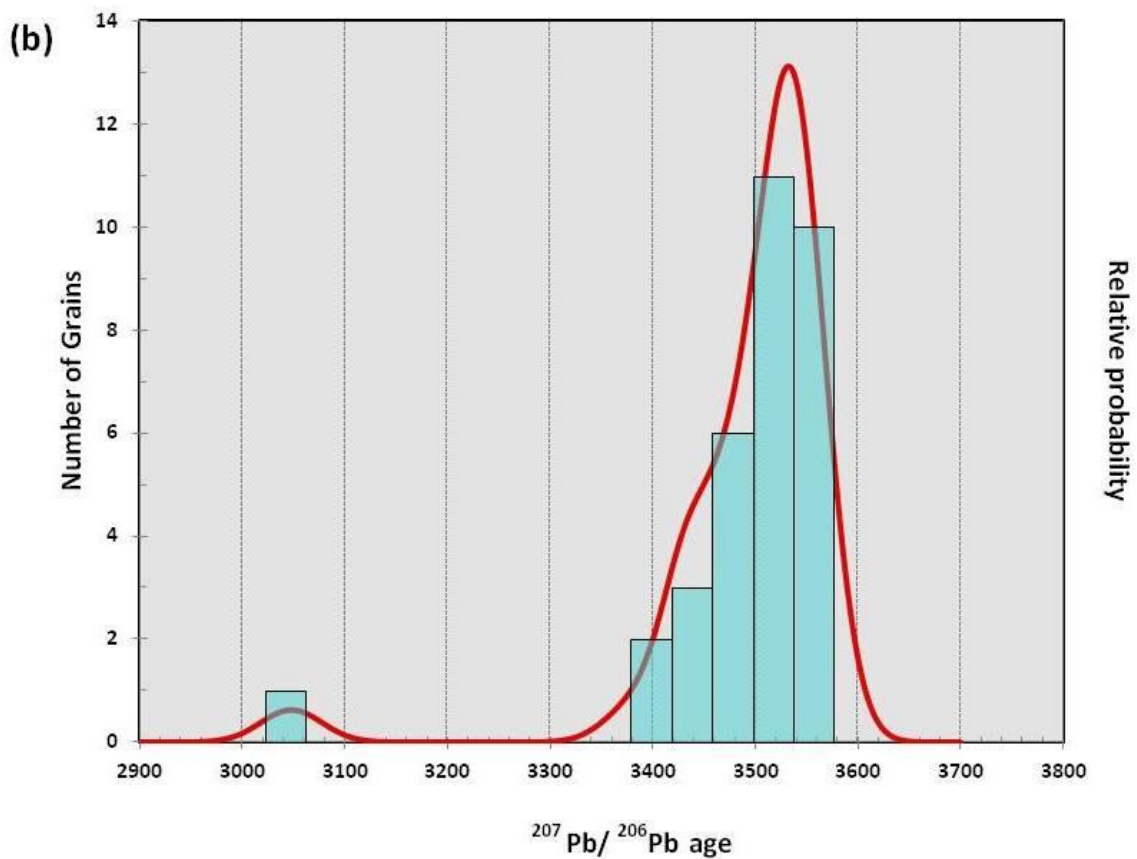
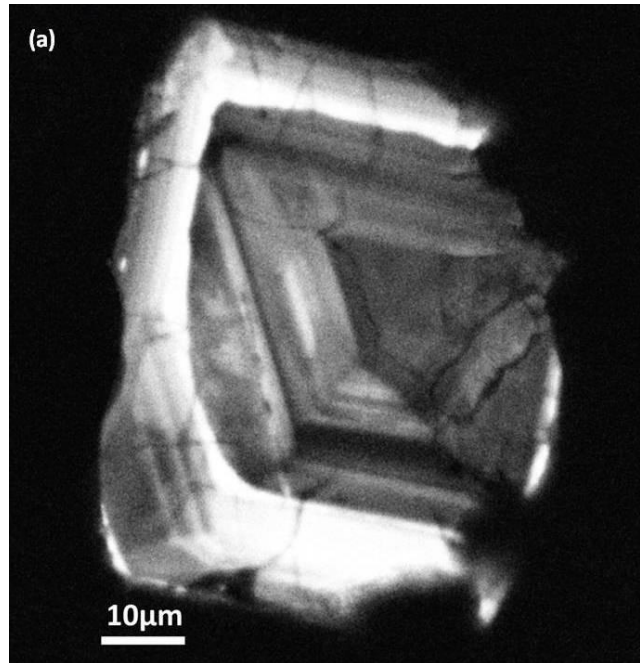


Figure 3.2 (a) Cathodoluminescence image of a selected zircon from sample NG 3A exhibiting strong magmatic zoning and trace element depletion. (b) Cumulative probability plot and histogram of the 33 analysed zircon crystals for sample NG 3A.

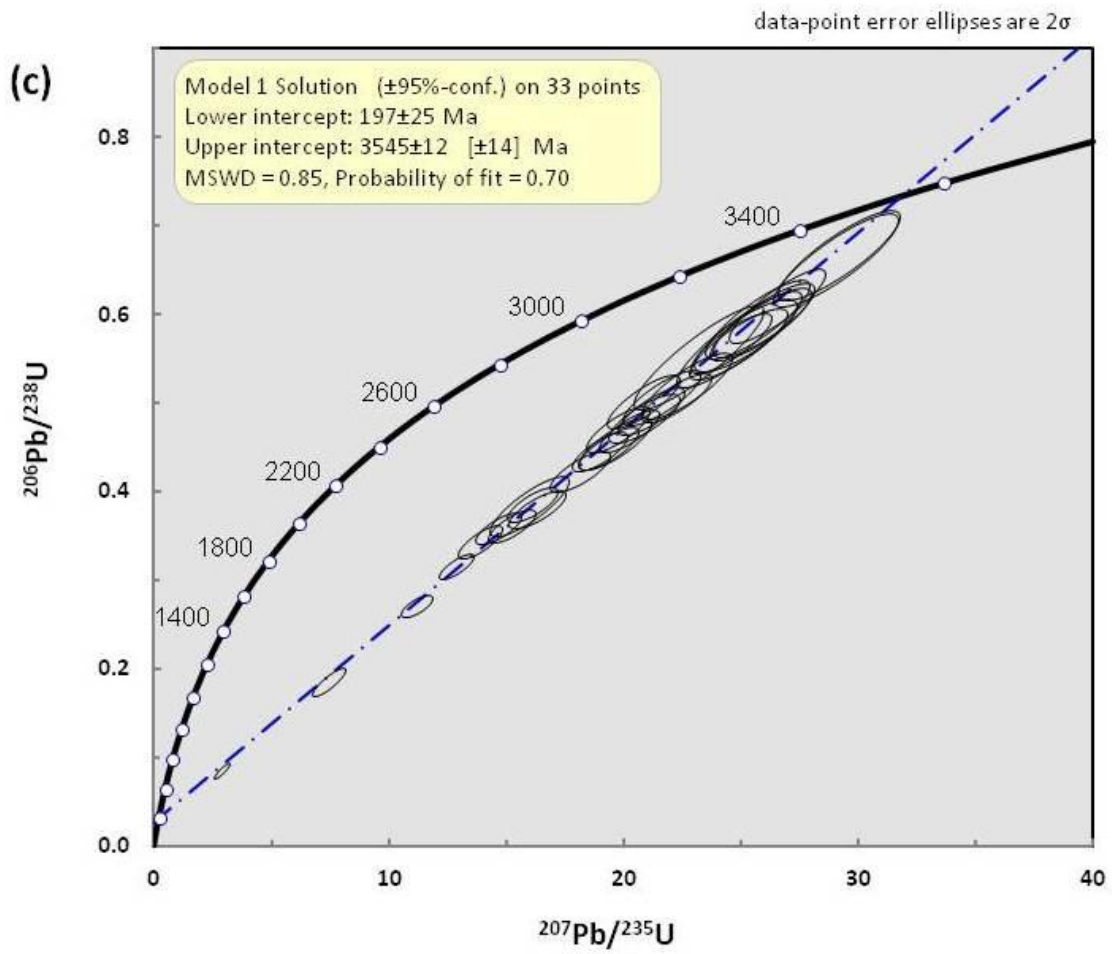


Figure 3.2 (c) U-Pb concordia plot for the NG 3A zircon isotopic data.

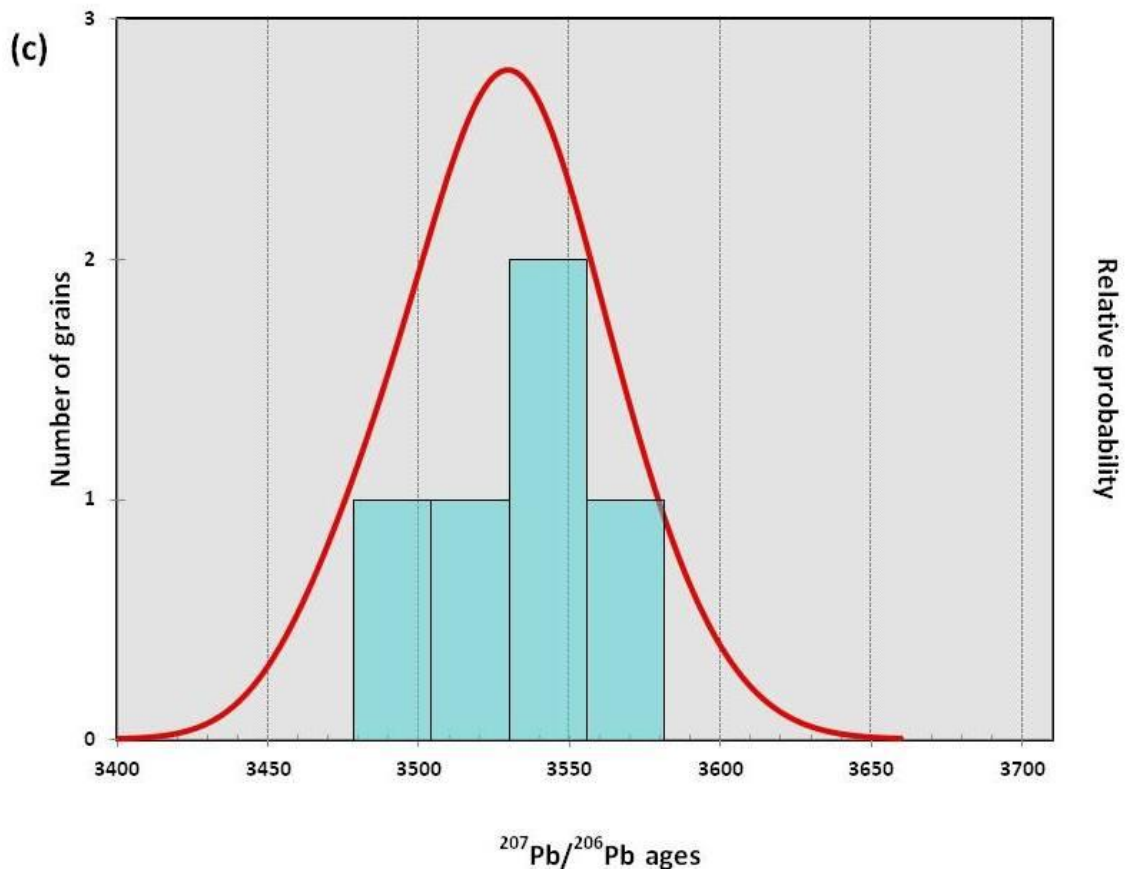
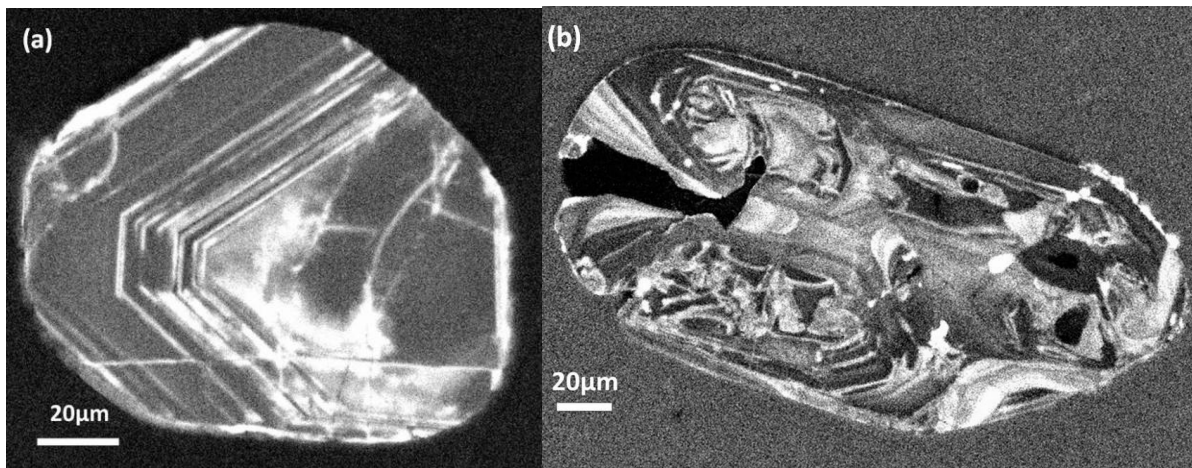


Figure 3.3 (a) + (b) Cathodoluminescence image of a selected zircon crystal from sample NG 15. (a) The zircon crystal shows strong magmatic zoning and has metamict core. (b) Metamict zircon with a large fracture. (c) Cumulative probability plot and histogram of the five analysed zircon crystals for sample NG 15.

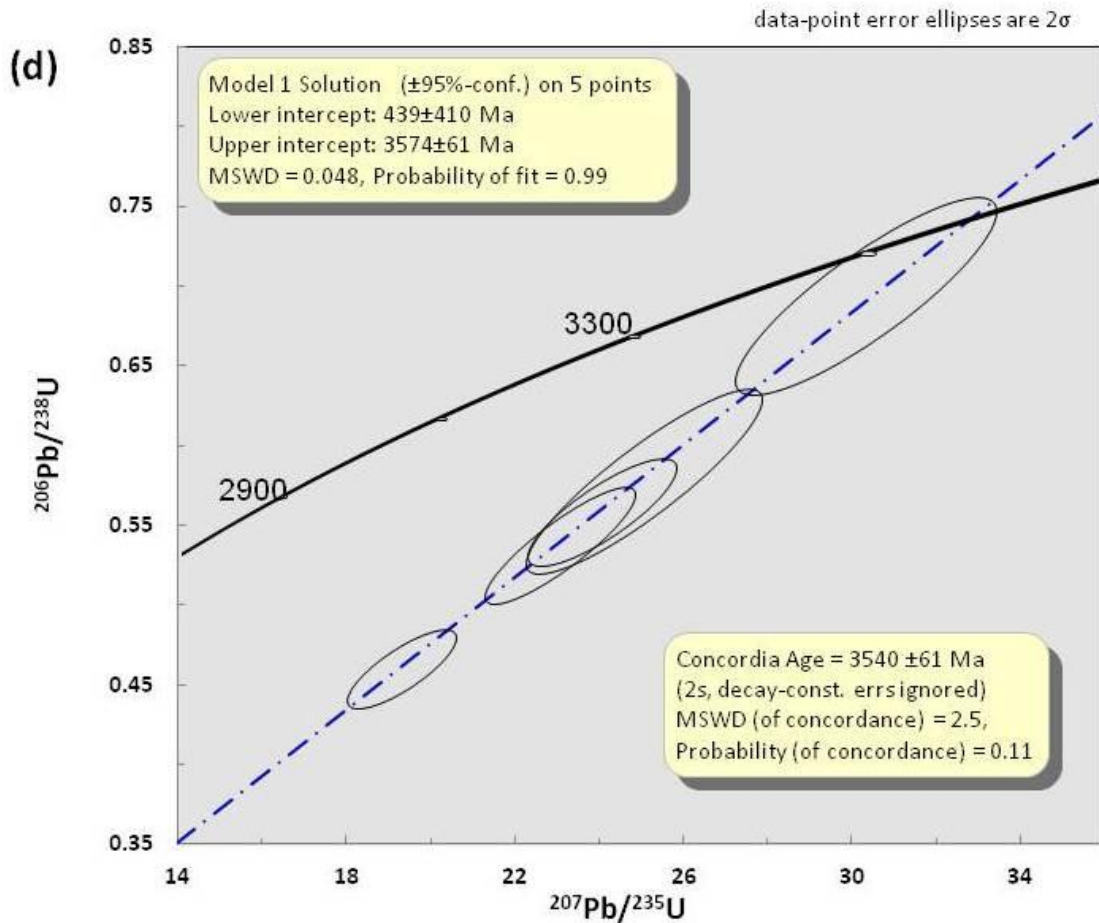


Figure 3.3 (d) U-Pb concordia plot for the NG 15 zircon isotopic data.

3.5 Quartz-feldspar porphyry (NG 13)

Sample NG 13 yielded forty-five zircons for analysis. Some of the zircons have retained their original magmatic zoning (Fig 3.4a), but most have undergone metamictization.

A cumulative probability plot and histogram for the forty-five zircon crystals analysed reveals three distinct age populations (three grains between 2200 Ma– 2400 Ma, nine grains between 2700 Ma – 3000 Ma and thirty grains between 3200 Ma – 3600 Ma) (Fig 3.4b). The three grains in the 2200 Ma– 2400 Ma and the nine grains in the 2700 Ma – 3000 Ma population have the highest % of discordance (> 63% discordance for the former and > 40% for the latter) as can be seen from table 4.1 in Appendix 4. Thus these ages are statically not meaningful. The grains that show a discordance of < 10 % and more statically meaningful give an age of ± 3520 Ma. The Wetherill U-Pb concordia curve reveals radiogenic Pb-loss

but gives an upper intercept age of 3537 ± 28 Ma and lower intercept of 841 ± 86 Ma with a MSWD of 48. Two concordant points give a concordia age of 3529 ± 12 Ma with a MSWD (of concordance) of 1.9 and 0.16 probability of concordance (Fig 3.4c).

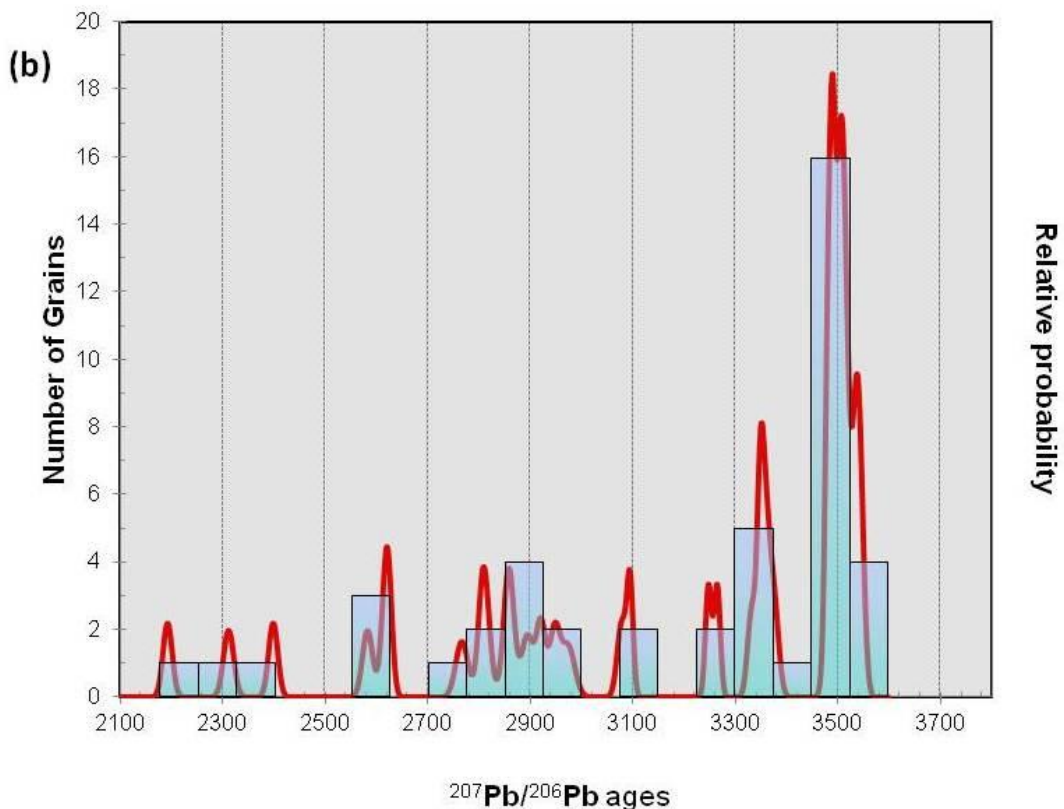
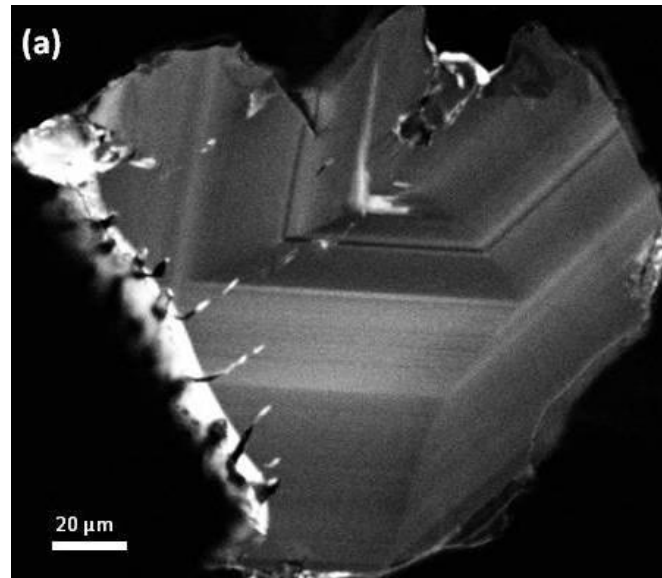


Figure 3.4 (a) Cathodoluminescence image of a selected zircon crystal from sample NG 13. The zircon crystal shows strong magmatic zoning. (b) Cumulative probability plot and histogram of the forty-five analysed zircon crystals for sample NG 13.

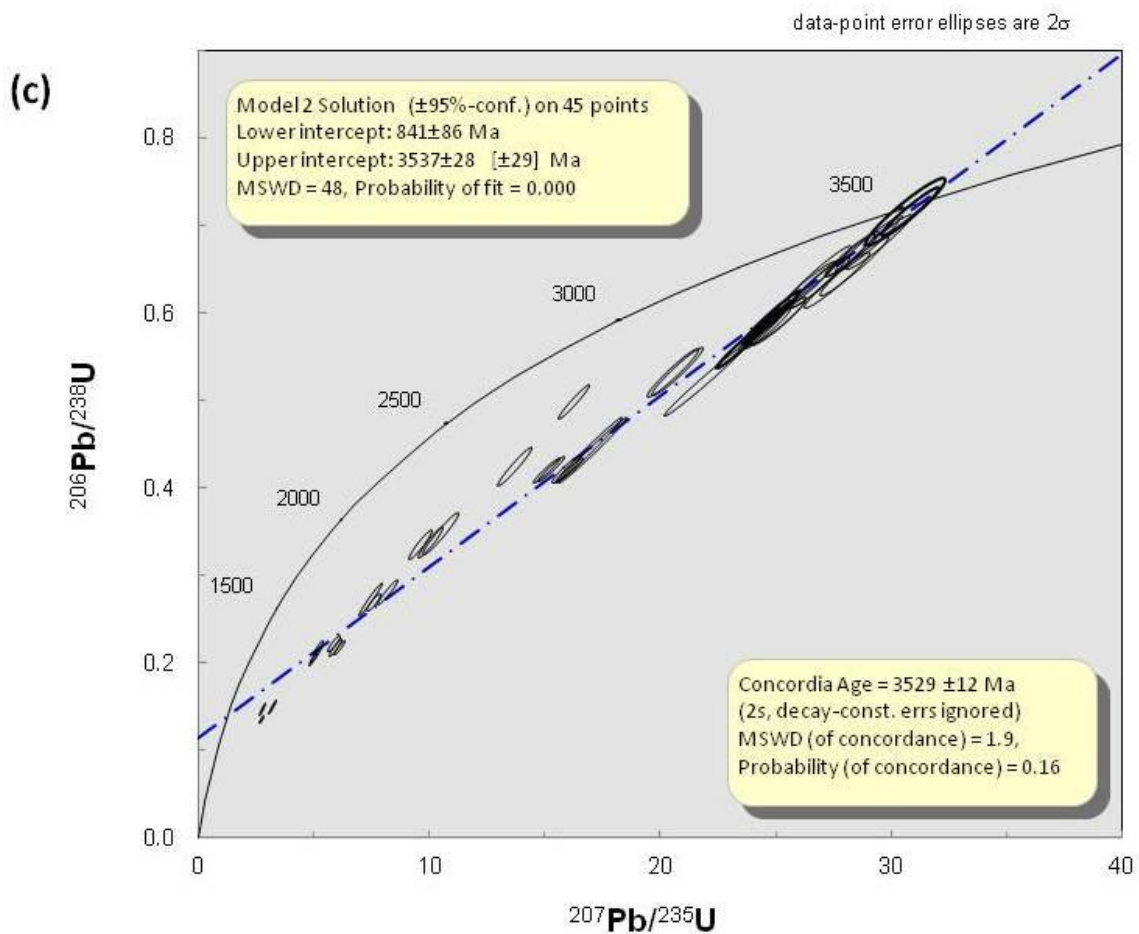


Figure 3.4 (c) U-Pb concordia plot for the NG 13 zircon isotopic data.

3.6 Quartz-sericite schist (NG 3B)

For sample NG 3B monazite was analysed since no zircon crystals were found. Eighteen monazite crystals were analysed. The monazite crystals are about $40 \mu\text{m}$ in width and $140 \mu\text{m}$ in length. Xenotime inclusions are observed in the monazite crystals (Fig 3.5a).

A cumulative probability plot and histogram for the eighteen monazite crystals analysed reveals one distinct age population (Fig 3.5b). The concordant points yielded a concordia age of 3230 ± 5 Ma age on the Wetherill U-Pb Concordia curve with a MSWD (of concordance) of 0.27 and 0.60 probability of concordance (Fig 3.5c). The U-Pb data also yielded an upper intercept age of 3233.3 ± 4.4 Ma and lower intercept age of 156 ± 220 with a MSWD of 1.3 at 95% confidence (Fig 3.5c).

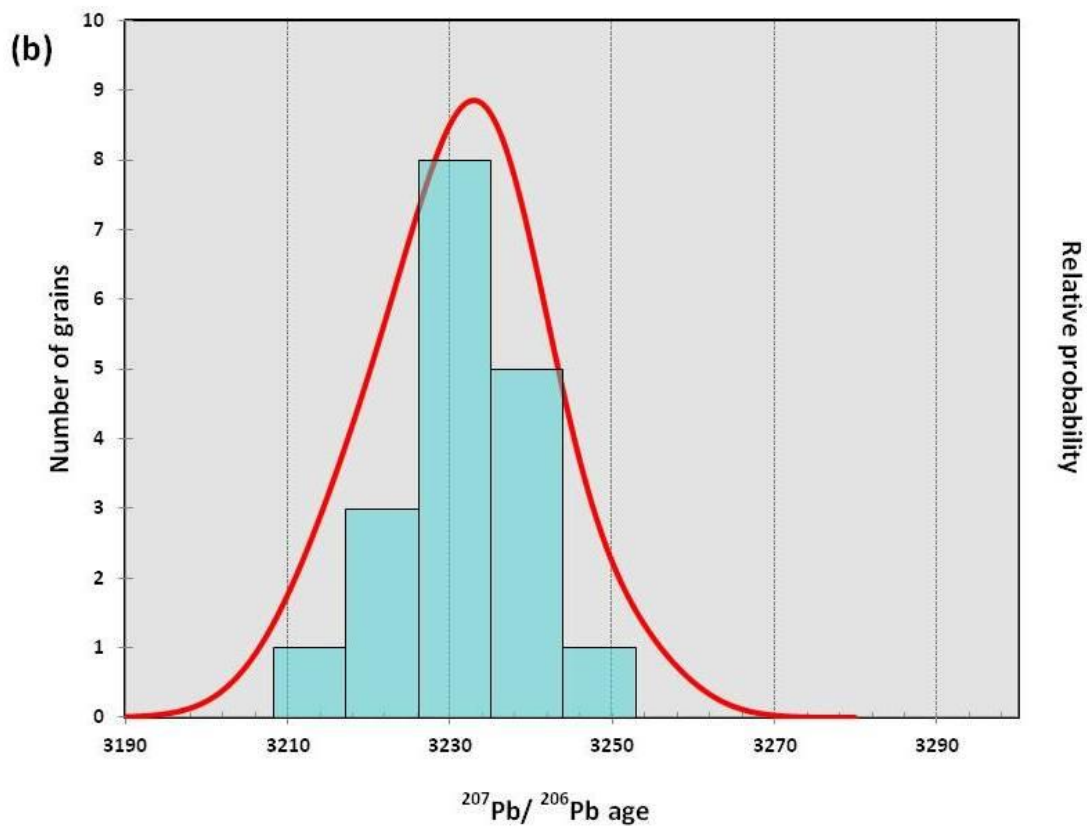
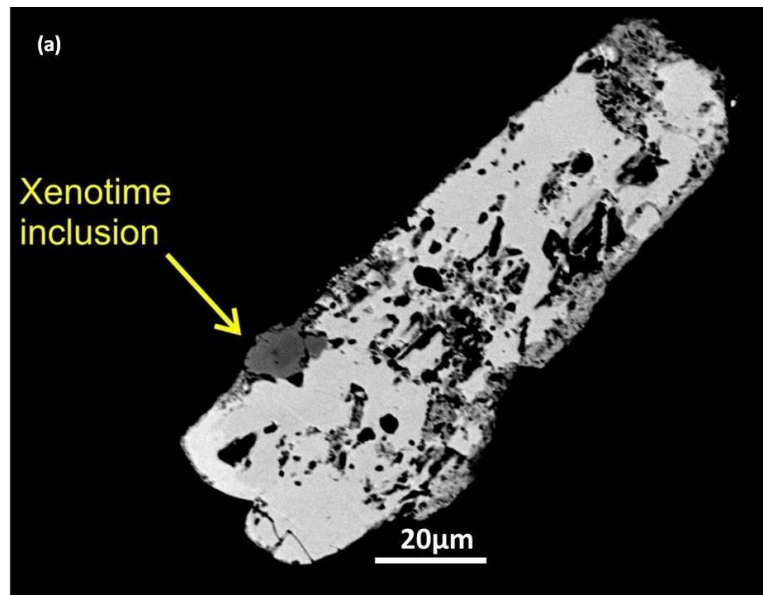


Figure 3.5 (a) Back-scattered electron image of monazite from sample NG 3B. The monazite crystal has a xenotime inclusion. (b) Cumulative probability plot and histogram of the eighteen analysed monazite crystals for sample NG 3B.

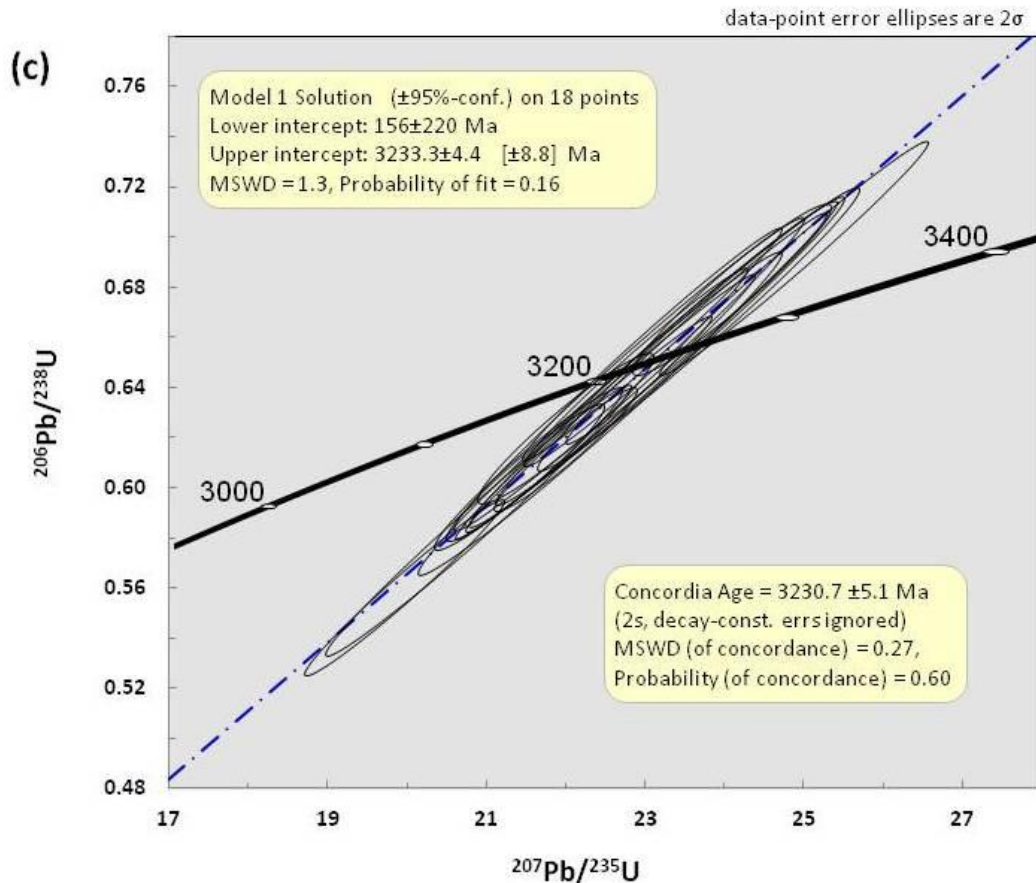


Figure 3.5 (c) U-Pb concordia plot for the NG 3B monazite isotopic data.

3.7 Discussion

Five samples from the Toggekry Formation were analysed for zircons and only four yielded zircons for dating and one yielded monazites (NG 3B). The absence of zircons in the sample may suggest the protolith of the rock may have been a mafic volcanic rock or the zircons were too fine grained and thus lost during the sample treatment process.

One zircon was analysed for the Mount Vernon rhyolite (NJ-10-L5A) and it yielded a concordia age of 3547 ± 54 Ma with a high MSWD (4.1) reflecting a minor amount of Pb-loss. The two andesitic samples, NG 3A and NG 15, yielded an upper intercept age of 3545 ± 12 Ma and a 3540 ± 61 Ma concordia age. Sample NG 13 which is a quartz-feldspar porphyry gave a concordia age of 3529 ± 12 Ma (based on two zircons) with most zircons showing variable ages.

The quartz-sericite schist (NG 3B) analyzed for monazite gave a concordia age of 3230 ± 5 Ma. The Toggekry Formation has been intruded by the Mvunyana granodiorite which was dated by Matthews et al. (1989) and has an age of 3290 ± 33 Ma. Sample NG 3B was collected from an area which is in close proximity to this granodiorite and thus the monazite age from sample NG 3B represents the metamorphic age of the rock rather than the igneous age.

CHAPTER 4: GEOCHEMISTRY

4.1 Introduction

The main objective of this study of the Nondweni greenstone belt is to elucidate the origin of the quartz-sericite schists of the Toggekry Formation which are hosts to massive sulphide deposits. Rocks of the Toggekry Formation plot in four distinct fields according to revised Winchester and Floyd (1977) and Pearce (1996) geochemical classification diagrams (Fig 4.1). The fields are rhyolites, andesites, basaltic andesites and basalts and they will be referred to as such for the rest of the chapter. The quartz-sericite schists of the Toggekry Formation will be compared with these four rock compositions to determine the protolith of the quartz-sericite schists and then infer the tectonic setting in which the protolith was formed.

Apart from our own analyses, data from Xie et al. (2012) who analyzed felsic schists from the Toggekry Formation will be shown. Samples Using LA-MC-ICP-MS Lu-Hf analyses of zircons, this chapter will attempt to deduce the petrogenesis of the Toggekry Formation magmas. The Toggekry Formation lithologies will also be compared to the basalts of the overlying Witkop Formation. Major and trace element data of the samples are given in Table 3.1 in Appendix 3 and Hf isotope data is given in Table 4.3 in Appendix 4. Analytical techniques are described in appendix 1. Due to problems with zircon dissolution for ICPMS analyses, samples NG 20, NJ-10-L4A, NJ-10-L5A and NJ-10-SS1 and NJ-10-SS8 were also analyzed with the XRF and the Zr and Hf data presented in Table 3.1 (Appendix 3) is the XRF data.

Note: see legend at the back of the references

4.2 Geochemical classification diagrams

Various geochemical classification diagrams are available to classify igneous rocks. Some examples are: (a) The LeBas et al. (1986) TAS diagram which plots total alkalis ($\text{Na}_2\text{O} + \text{K}_2\text{O}$) against SiO_2 , (b) The Cox-Bell-Pankhurst (1979) diagram which also plots alkalis against SiO_2 , (c) The Pearce (1996) diagram which plots trace element ratios (Nb/Y vs Zr/Ti) against each other to determine the rock type. The problem with using some of these diagrams is that the samples analyzed for this study have undergone alteration. Due to alteration certain elements may be enriched or depleted in rocks and this may cause them to

plot in different fields. To address this problem the best geochemical plots are those that rely on immobile elements such as the high-field strength elements Nb, Ta, Zr and Hf.

Figure 4.1 is the Pearce (1996) geochemical classification diagram. The diagram shows that the analyzed samples plot in three distinct fields namely the basaltic, andesite-basaltic andesite to trachy-andesites and rhyolite-dacite to alkali rhyolite fields. In the diagram, four groups of rocks can be distinguished. They are rhyolites, andesites, basaltic andesites and basalts. The quartz-sericite schists plot in the rhyolite field. The felsic schists from Xie et al. (2012) can be separated into rhyolites and andesites. In the LeBas et al. (1986) TAS geochemical classification diagram (Fig 4.2) the basaltic andesites plot in a wide range of fields ranging from the andesitic to rhyolitic field and andesites plot in the rhyolitic field. This may be a result of silicification described by Hofmann and Wilson (2007) of the Nondweni greenstone belt lavas.

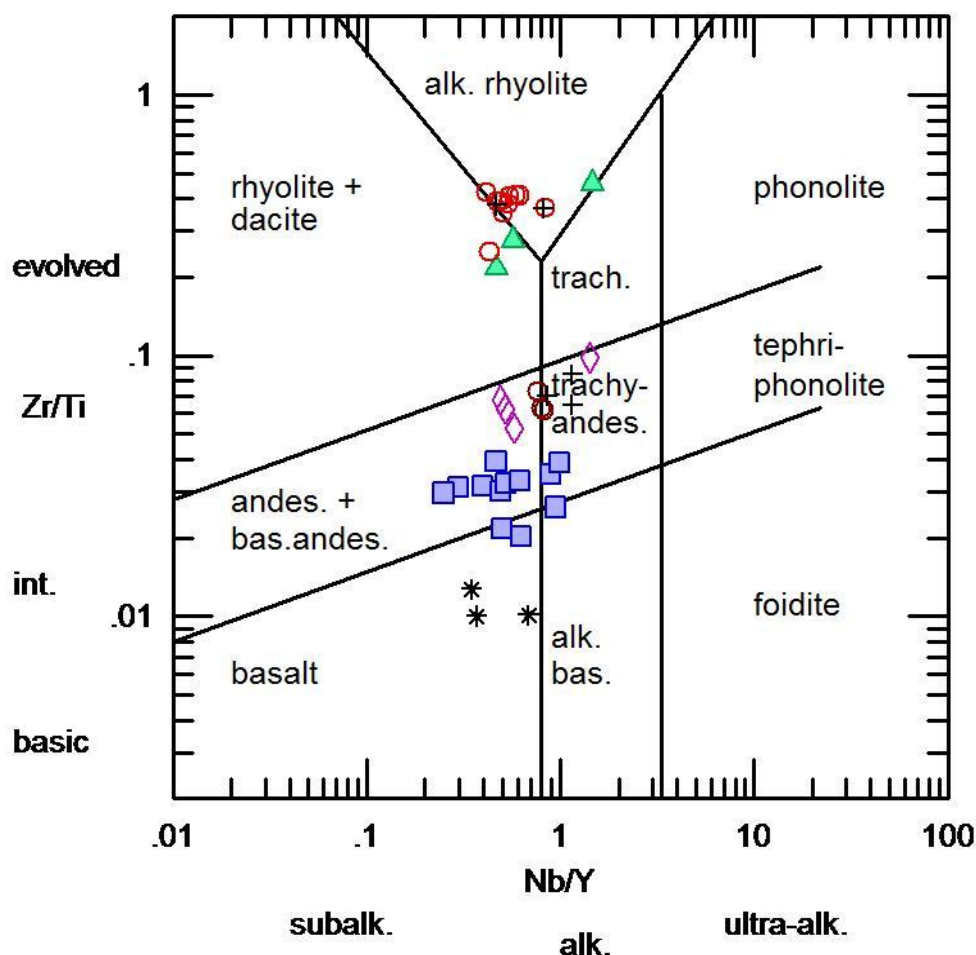


Figure 4.1 Rock classification diagram after Pearce (1996).

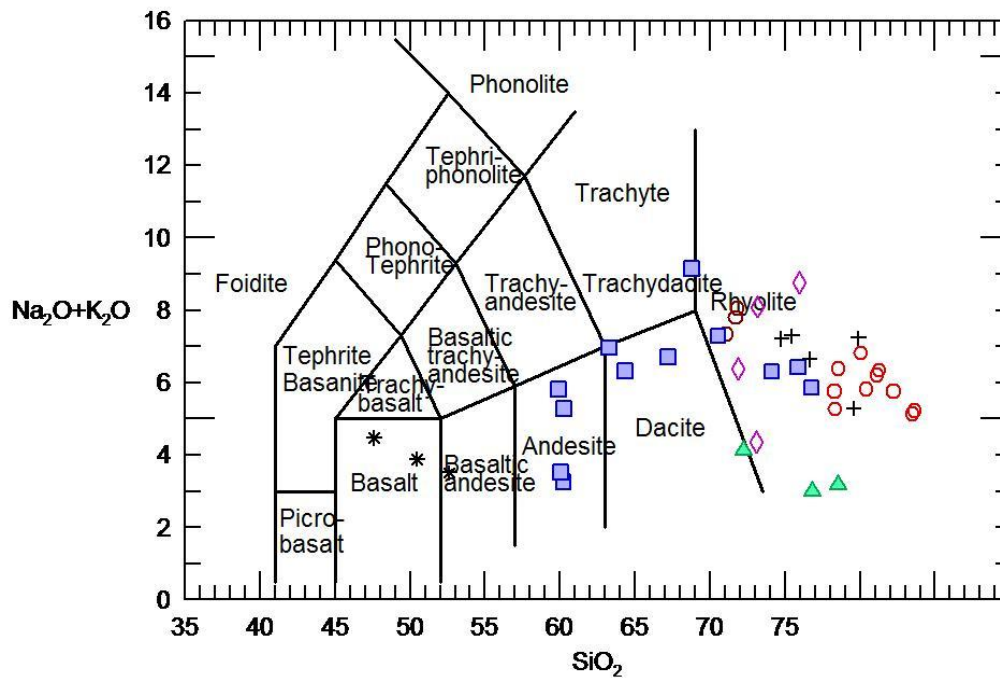


Figure 4.2 LeBas et al. (1986) rock classification diagram.

4.3 Major and trace element geochemistry

In the major element variation diagrams MgO and SiO₂ were used as differentiation indices. MgO contents decrease with differentiation as it is incorporated in the early-forming high temperature phases such as olivine and pyroxene. With progressive differentiation SiO₂ increases as it is concentrated in the melt.

The CaO vs MgO and SiO₂ plot (Fig 4.3) shows that the intermediate to mafic rocks are more CaO-rich than the felsic rocks and quartz-sericite schists. The quartz-sericite schists have relatively high concentrations of MgO and low CaO contents. This is unusual because with increasing differentiation CaO and MgO decrease due to phases like olivine, pyroxene and Ca-plagioclase fractionating. Thus the high MgO combined with low CaO is a sign of element mobility meaning that MgO must have been introduced in the rocks at a later stage or CaO removed from the rocks. The Toggekry Formation is intruded by large ultramafic bodies (now serpentinites) and thus the high concentrations of MgO may have been sourced from the nearby ultramafic bodies. Sample NG 18 has the highest concentrations of MgO which is reflected by the presence of pyroxene and amphibole.

In the CaO vs SiO₂ plot there is a decrease in CaO with increasing fractionation. The more evolved rocks have low CaO and high SiO₂ and the primitive rocks are high in CaO and low

in SiO_2 . Sample NG 14 has a high concentration of CaO compared to the other samples. This is reflected by the presence of clinopyroxene which is still preserved in the rock (Fig 2.17).

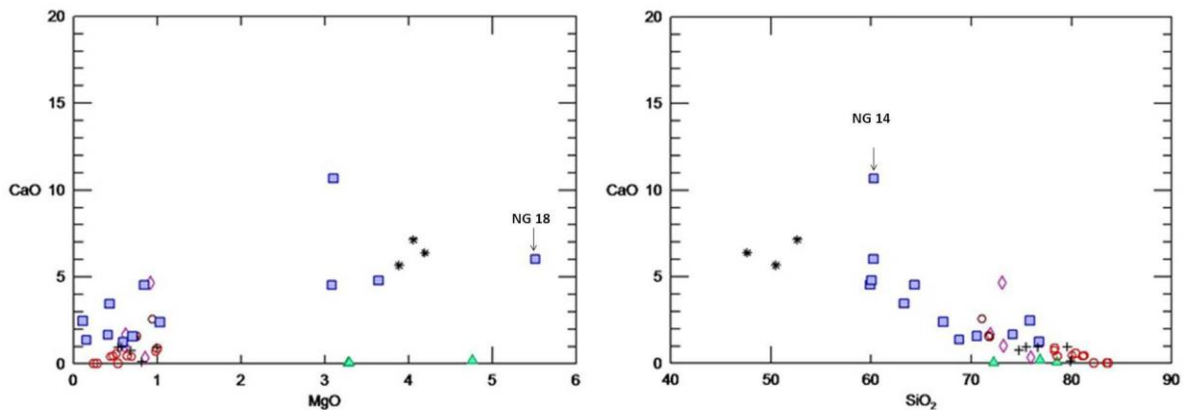


Figure 4.3 Cao plotted against MgO and SiO_2 .

The most primitive rocks are basalts and they are enriched in Fe_2O_3 . The basaltic andesites and quartz-sericite schists have moderate to low concentrations of Fe_2O_3 (Fig 4.4). The high concentrations of Fe in the basalts of the Witkop Formation indicate the fractionation of ferromagnesian minerals like olivine and pyroxene. The fractionation of these phases depletes the melt in MgO and FeO, thereby decreasing the MgO and FeO content of the residual melt. The three basaltic andesites (NJ-10-SS2, NJ-10-SS6 and NG 18) with the highest amount of Fe_2O_3 are also enriched in MgO relative to the other samples. The high amounts of Fe_2O_3 result in the presence of pyroxene (NG 18) and amphiboles (hornblende in SS2 and actinolite in SS6) in these samples (Fig 4.4). The Fe_2O_3 and MgO relationship depicted by the plot is what would be expected from fractional crystallization trends.

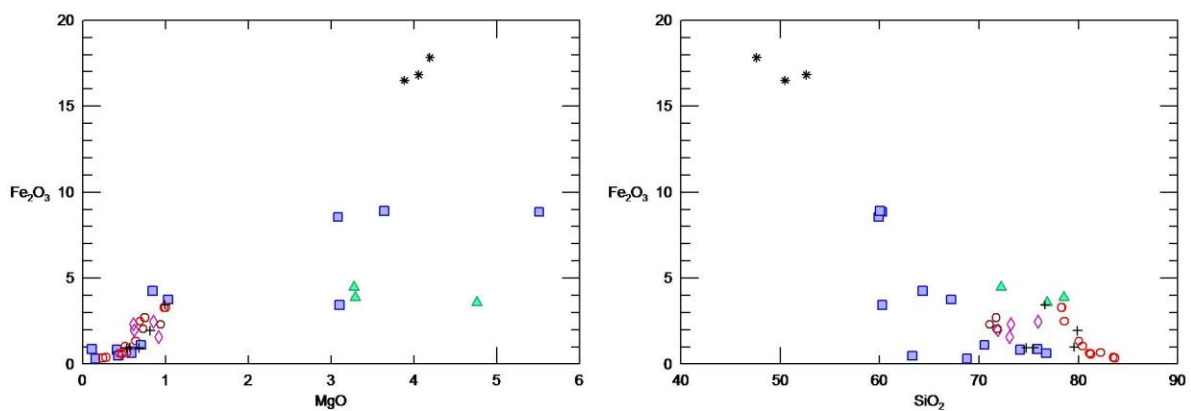


Figure 4.4 Fe_2O_3 plotted against MgO and SiO_2 .

K_2O is highly variable in the samples (Fig 4.5). The plot indicates that with increasing fractionation, K_2O is enriched in the samples. The quartz-sericite schists and rhyolites have higher K_2O contents compared to the basaltic andesites and basalts. This means that as Fe, Ca and Mg decrease K is enriched in the melt and can be incorporated into phases that fractionate later (biotite, K-feldspar and muscovite). The quartz-sericite schists have higher contents of K_2O reflecting their modal abundance of white mica. Basaltic andesites NG 14 and NJ-10-SS7 with high K_2O have veins comprising quartz and microcline (Fig 2.16) meaning alkali-rich fluids must have infiltrated the rocks resulting in the K_2O enrichment of the samples. Two of the felsic schists from Xie et al. (2012) (08 NOND 13 and NOND 6/9) have the highest concentrations of K_2O . These samples plot as rhyolites in the Pearce (1996) classification diagram. The samples that are andesitic according to the Pearce (1996) classification diagram have low K_2O concentrations.

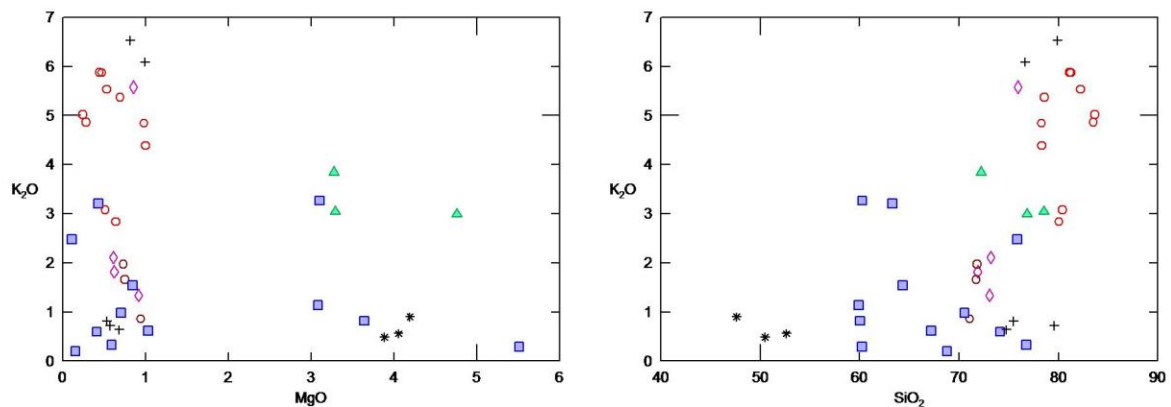


Figure 4.5 K_2O plotted against MgO and SiO_2 .

The variation in the MnO in the samples is 0.4 weight % (Fig 4.6). Basalts have relatively high concentrations of MnO. With an increase in silica the MnO content decreases. Mn^{2+} usually substitutes for Fe^{2+} . Thus rocks which have Fe-rich minerals are enriched in Mn.

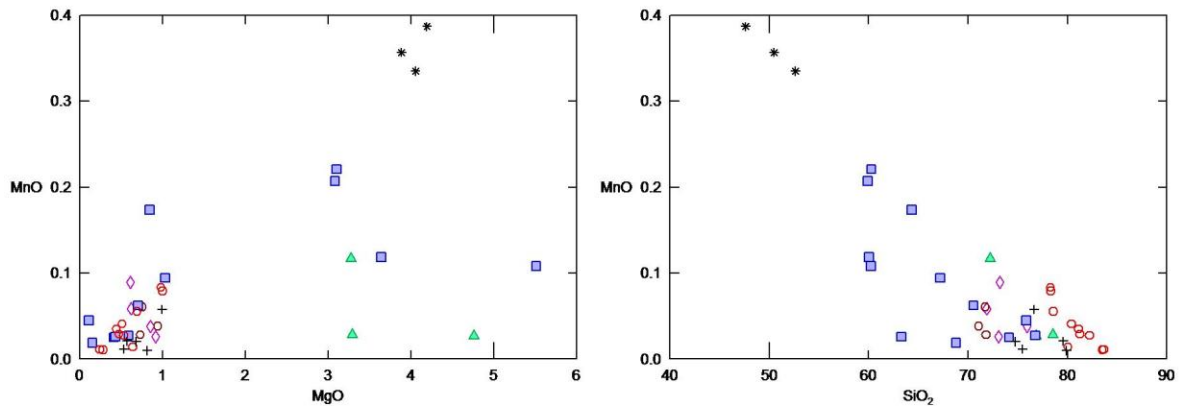


Figure 4.6 MnO plotted against MgO and SiO₂.

Na₂O shows an increase with progressive fractionation (Fig 4.7). The quartz-sericite schists have little to no Na₂O. The rhyolites are depleted in Na₂O which is unusual as rhyolites normally have higher Na₂O than the mafic and intermediate rocks. This indicates that element mobility must have occurred, resulting in the depletion of Na₂O in the rhyolites and possibly the quartz-sericite schists. Samples 08 NOND 13 and NOND 6/9 which have high concentrations of Na₂O also have high concentrations of K₂O.

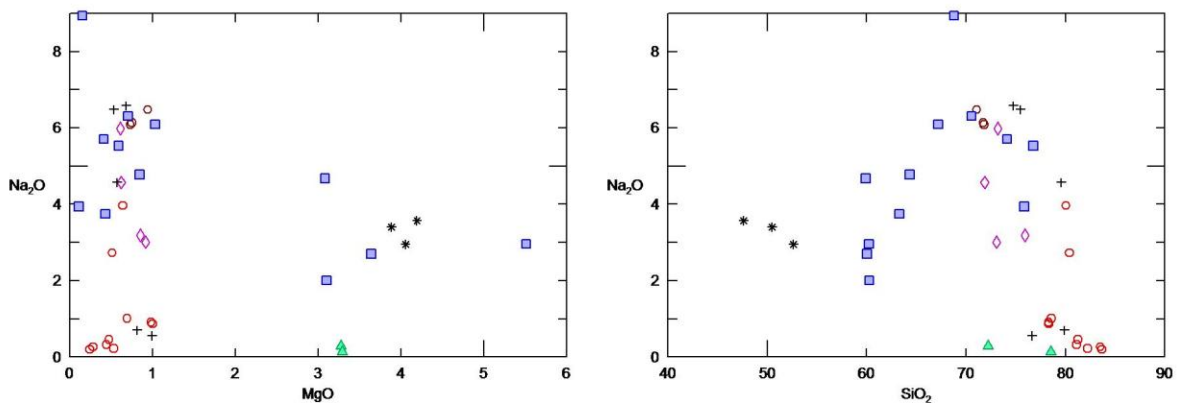


Figure 4.7 Na₂O plotted against MgO and SiO₂.

Basalts, basaltic andesites and andesites have similar concentrations of Al₂O₃ (12-19%). Rhyolites have very low concentrations of Al₂O₃ (Fig 4.8). Sample NJ-10-SS8 has abnormally high concentrations of Al₂O₃. The sample also has high concentrations of K₂O and MnO suggesting an introduction of these elements into the rocks after crystallization by fluids rich in the respective elements. The high concentrations in Al₂O₃ likely indicate the enrichment of Al in the igneous protolith rather than later introduction because Al is not very fluid-mobile. The plot also shows a decrease in Al₂O₃ with an increase in SiO₂.

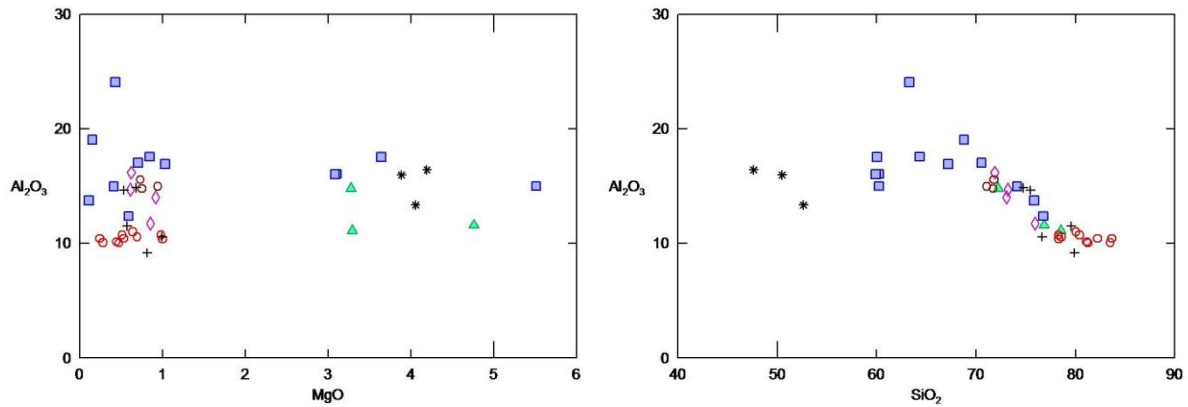


Figure 4.8 Al_2O_3 plotted against MgO and SiO_2 .

Basalts and basaltic andesites have higher P_2O_5 than the andesites, felsic schists and rhyolites (Fig 4.9) With the exception of NJ-10-SS8 the basalts have the highest P_2O_5 contents. The high concentrations of P_2O_5 in NJ-10-SS8 indicate the fractionation of apatite. The P_2O_5 vs SiO_2 plot clearly shows that there is a decrease in P_2O_5 with increasing SiO_2 indicative of apatite fractionation.

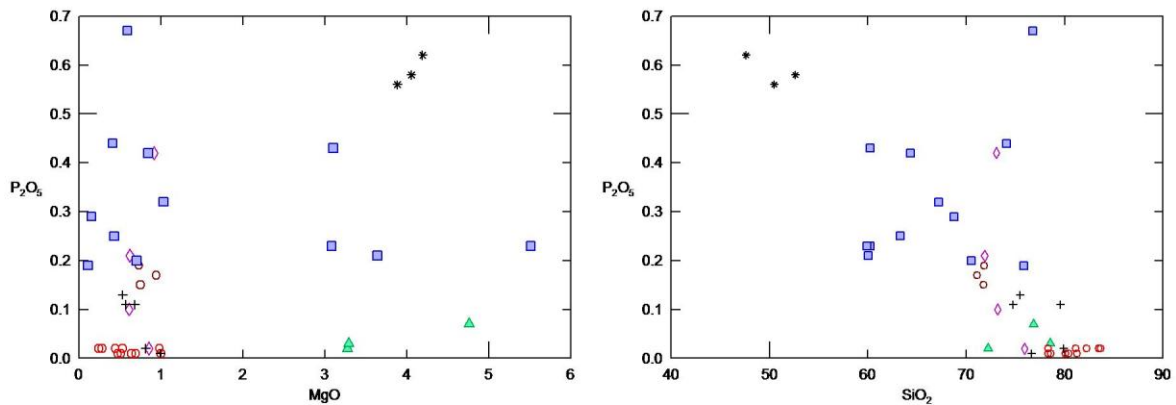


Figure 4.9 P_2O_5 plotted against MgO and SiO_2 .

Basalts have the highest Ti concentrations and the rhyolites, felsic schists and quartz-sericite schists have the lowest (Fig 4.10). The TiO_2 vs SiO_2 plots shows that SiO_2 increases (fractionation occurs) as TiO_2 decreases. Ti partitions in ilmenite, titanite or titaniferous magnetite in igneous rocks and the thin section petrography shows that the basaltic andesites have more opaque minerals than the rhyolites which have minor amounts in terms of modal %. Another reason for the low concentrations of Ti in the felsic rocks is that Ti can also replace Al and thus may be present in pyroxenes, amphiboles and biotite and the felsic rocks are devoid of some of these minerals. The high Ti contents of the basalts combined with their

high Fe_2O_3 content indicate that fractionation of Fe-Ti-oxides only started later in the liquid line of descent.

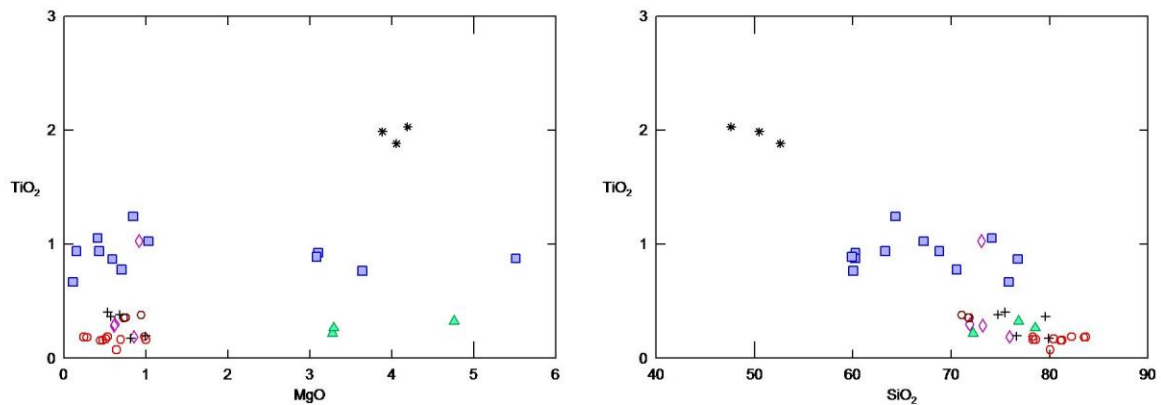


Figure 4.10 TiO_2 plotted against MgO and SiO_2 .

Rhyolites and quartz-sericite schists have low Ni contents and the andesites have moderate Ni contents while the basalts and basaltic andesites have high Ni contents (Fig 4.11). In the Ni vs SiO_2 plot there is a decrease in Ni with an increase in SiO_2 . Ni concentrations are higher in the mafic rocks because Ni is highly compatible and will be concentrated in the early forming Mg minerals, so the magma will become depleted in Ni when these phases start fractionating.

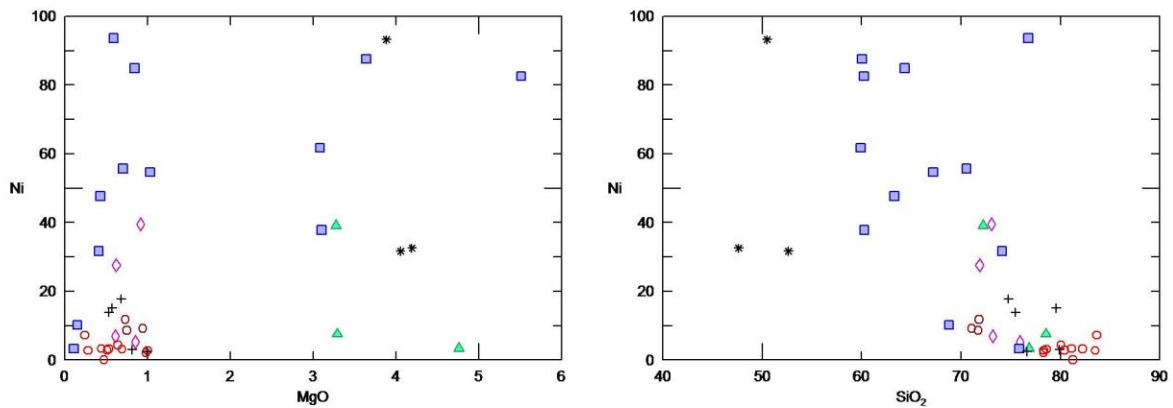


Figure 4.11 Ni plotted against MgO and SiO_2 .

Cr shows only slight variations in the different rock types (Fig 4.12). The basalts and basaltic andesites have slightly higher concentrations of Cr than the quartz-sericite schists and rhyolites. Only one sample (NJ-10-SS8) has higher Cr contents of about 400 ppm. Magmas with high Cr-contents can start crystallizing chromite, thereby depleting the residual melt in Cr. Early-crystallizing ferromagnesian silicates such as diopside can also contain appreciable amounts of Cr. Thus the mafic rocks will be richer in Cr than the felsic rocks.

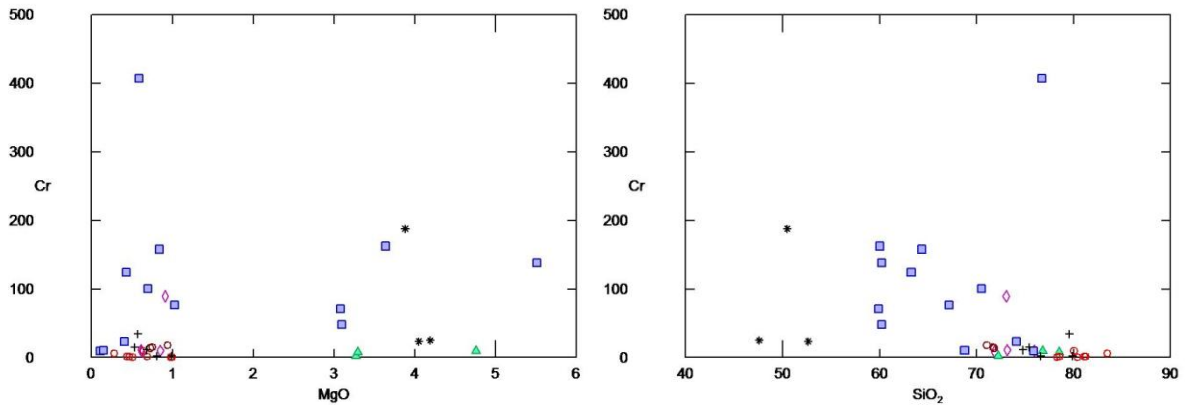


Figure 4.12 Cr plotted against MgO and SiO₂.

Basalts and basaltic andesites have high concentrations of Co while the intermediate rocks and quartz-sericite schists have moderate to low concentrations of Co (Fig 4.13). The rhyolites and felsic schists have extremely low concentrations of Co. The plots show a decrease in Co with progressive fractionation. The reason for the higher concentrations of Co in the primitive rocks relative to the evolved rocks is that Co is removed from the magma by the early formed magnesian minerals because of its similarity in geochemical behavior to Mg.

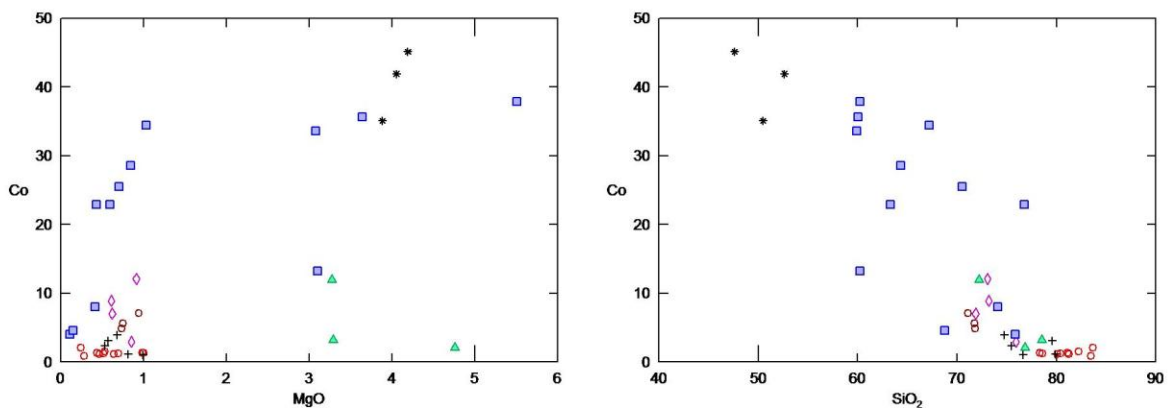


Figure 4.13 Co plotted against MgO and SiO₂.

Basalts and basaltic andesites have higher concentrations of Sc than the felsic schists, andesites, rhyolites and quartz-sericite schists (Fig 4.14). The Sc vs SiO₂ plot shows a decrease in Sc with progressive fractionation. Sc mainly partitions in clino-pyroxene.

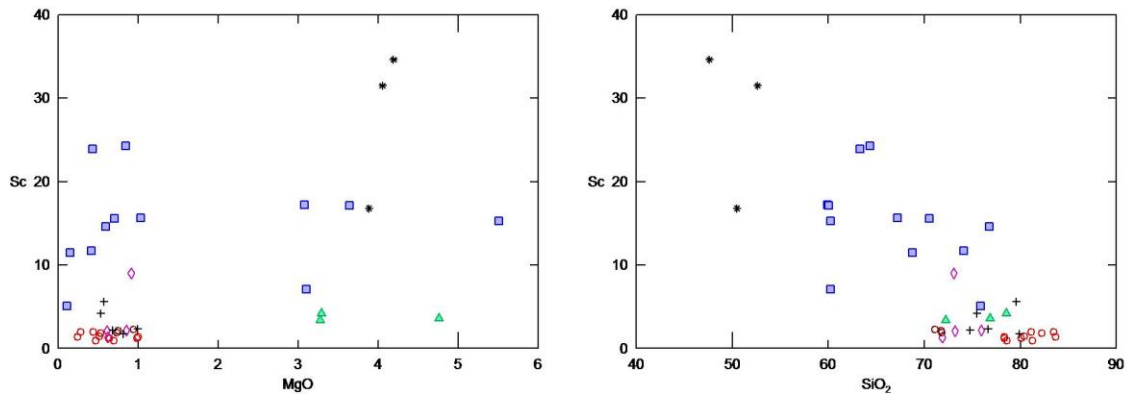


Figure 4.14 Sc plotted against MgO and SiO₂.

Basalts and basaltic andesites have higher concentrations of V than the felsic schists, andesites, rhyolites and quartz-sericite schists (Fig 4.15). The quartz-sericite schists and rhyolites have little to no V. The plot shows a decrease in V with progressive fractionation. V shows strong fractionation into Fe-Ti oxides and thus will be enriched in early formed magnetite, and thereby depleted in more felsic magmas. In this respect, the lower V contents of basalt sample NG 2B is surprising, considering its similarity in Fe and Ti contents to the other two basalts.

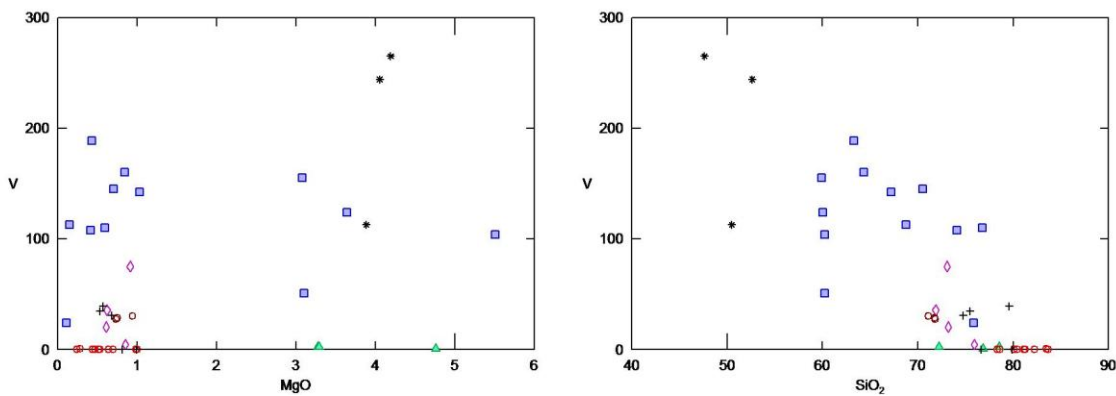


Figure 4.15 V plotted against MgO and SiO₂.

The trends shown by these variation diagrams from the Nondweni lavas are largely characteristic of igneous processes like crystal fractionation/differentiation for unaltered rocks apart from those observed for the alkalis. One has to be cautious when analyzing these variation diagrams because Nondweni greenstone belt has undergone silicification (Versfeld, 1988; Hofmann and Wilson, 2007), three phases of deformation (Watkeys, 1981; Wilson and Versfeld, 1994b) and greenschist facies metamorphism (Versfeld, 1988; Saha et al., 2012).

These processes are more likely to affect the concentrations of MgO and SiO₂ than, for instance TiO₂. We can therefore use the TiO₂ contents of the samples as an index of fractionation.

Nondweni greenstone belt rocks show well-defined clusters in variation diagrams against TiO₂ (Fig 4.16). The basalts, basaltic andesites, quartz-feldspar porphyries and andesites plot as clusters in the four variation diagrams while the rhyolites and quartz-sericite schists show the greatest scatter in the Y vs TiO₂ and La vs TiO₂ plots. Felsic rocks of the Toggekry Formation show two well-defined clusters, those with high Y, Nb, La and Zr (rhyolites and sericite schists) and those with low Y, Nb, La and Zr (andesites and Q-F- porphyries). Of these elements, Nb and Zr are the most immobile during alteration and the rock types of similar compositions plot as clusters. In general the more evolved rocks are higher in Y, Nb, La and Zr than the primitive rocks. This is because Y, Nb, La and Zr are incompatible elements and will thus be concentrated in the melt rather than the solids meaning the evolved igneous rocks will be enriched in these elements. The presence of felsic rocks with both high and low Zr and Nb contents suggests that two different magmatic series are present.

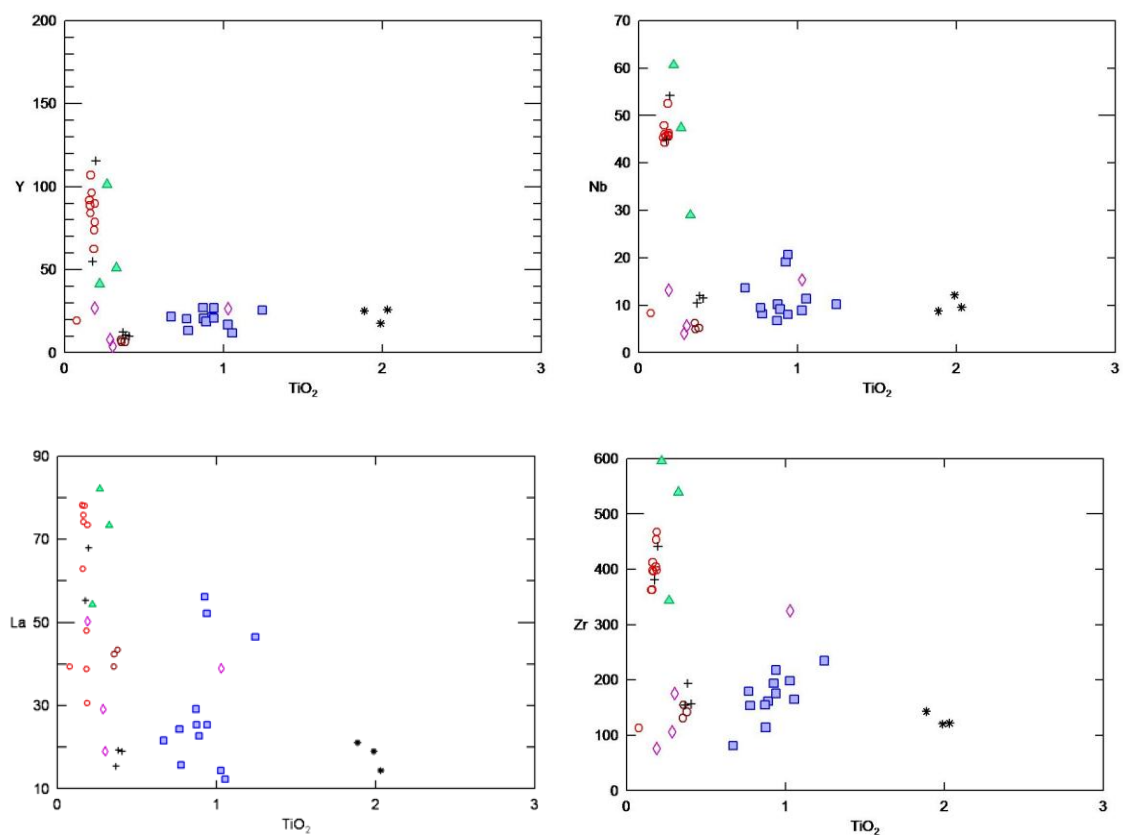


Figure 4.16 Immobile elements plotted against TiO₂.

Figure 4.17 shows variation diagrams of mobile elements vs TiO_2 . These diagrams show more scatter than those for the immobile elements. The Ba contents in the quartz-sericite schists are intermediate between the mafic and the felsic rocks. This is due to the fact that Ba has geochemical behavior that is similar to potassium and thus will be enriched in K-rich minerals like K-feldspar and mica but also amphibole and will not be incorporated into olivine and pyroxene. Rb is low in the mafic and intermediate lavas and moderate to high in the felsic lavas. The quartz-sericite schists have similar amount of Rb as the felsic rocks. Rb behaves similar to K and will thus be enriched in samples containing K-rich minerals. Sr is lowest in the rhyolites and quartz-sericite schists. As a general rule Sr will substitute for Ca, thus it will be admitted largely in Ca-rich minerals like plagioclase and amphibole. This does not apply for pyroxenes because pyroxene structure does not accommodate Sr. In the Pb vs TiO_2 plot Pb shows well-defined clusters for the basalts, basaltic andesites, quartz-sericite schists and rhyolites and shows variation in the andesites and quartz-feldspar porphyries.

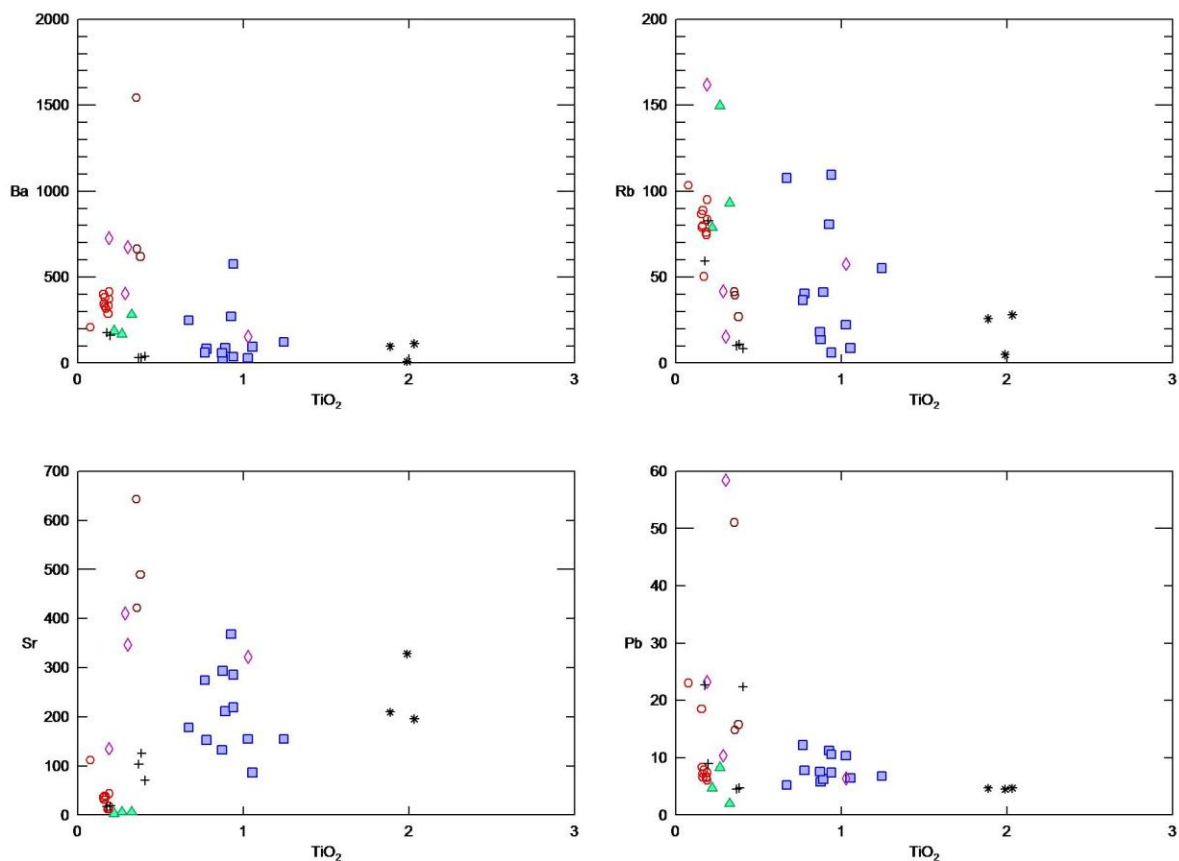


Figure 4.17 Mobile elements plotted against TiO_2 .

Rhyolites and quartz-sericite schists are enriched in Zr, Ta, Nb, Hf and Y (Fig 4.18). Basaltic andesites, andesites and quartz-feldspar porphyries have similar concentrations of Zr, Ta, Hf, Nb and Y with the exception of Hf and Zr where basaltic andesites have slightly higher concentrations. The basalts of the Witkop Formation have on average the lowest Zr and Hf. The four plots of the immobile elements show good correlations, mainly indicating enrichment during differentiation, although some felsic samples have noticeably lower contents of the HFSE and REE than the others.

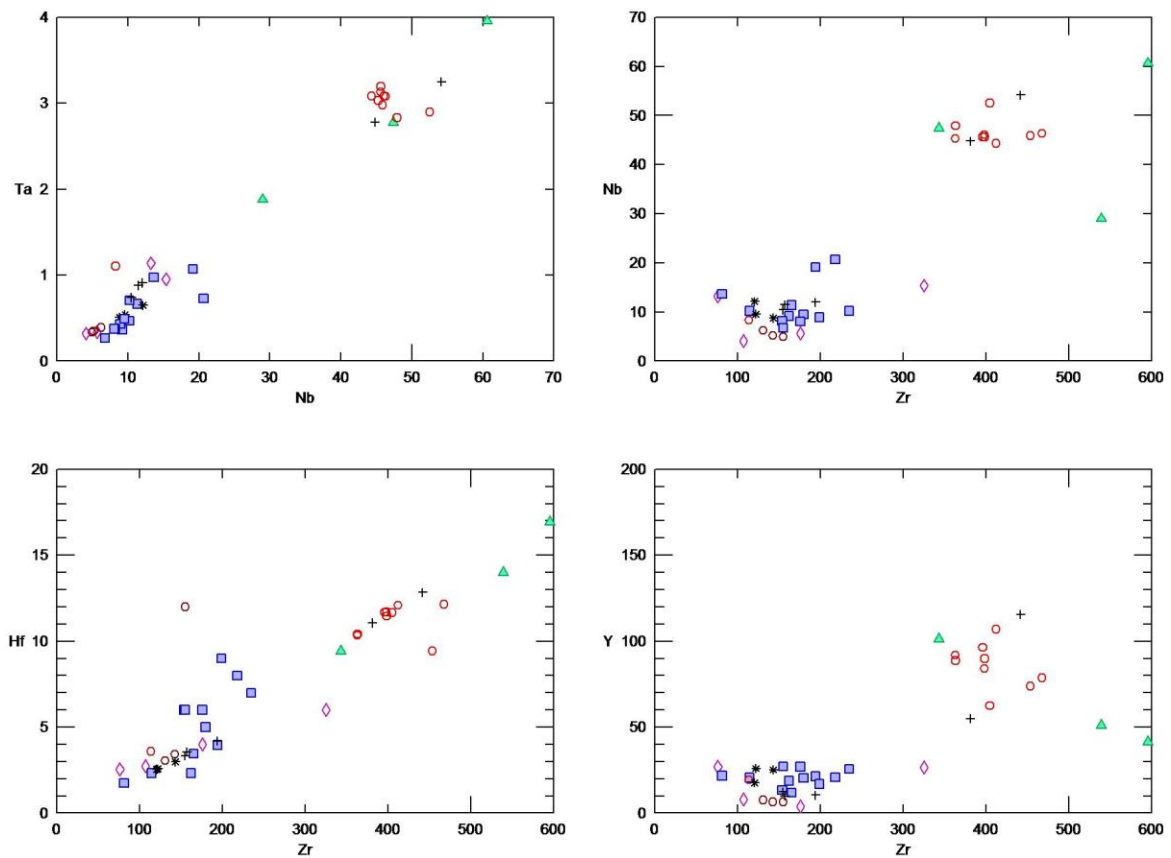


Figure 4.18 Harker variation diagrams for immobile elements.

4.4 Magma series

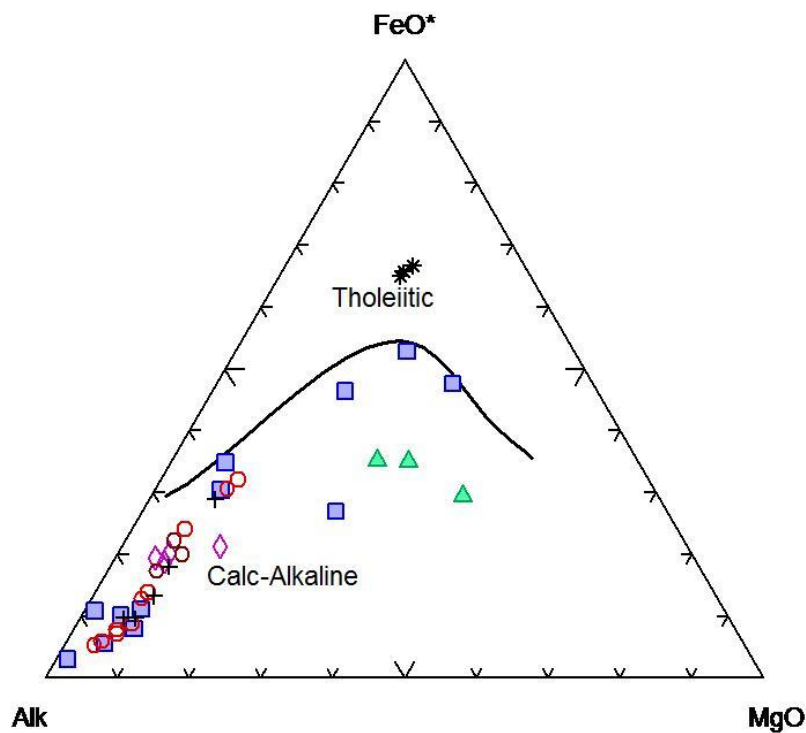


Figure 4.19 AFM diagram of the Nondweni greenstone belt rocks after Irvine and Baragar (1971)

Basalts from the Witkop Formation are tholeiitic. There is uncertainty as to whether rocks of the Toggekry Formation are part of the calc-alkaline trend or the tholeiitic trend in the MgO-FeO^{*}-Total Alkali triangular diagram (Irvine and Baragar, 1971) (Fig 4.19 above). The quartz-sericite schists have been enriched in MgO as seen in Figure 4.3 which is why they show such high MgO concentrations in the AFM diagram. Presuming that the rocks of the Toggekry Formation are part of the calc-alkaline trend, this trend can be produced by fractional crystallization or magma mixing. This can be achieved between mixing rhyolitic and basaltic magma to produce intermediate andesites and dacites. Considering the evidence for alkali mobility and MgO enrichment in some samples, the diagram should be treated with caution.

4.5 Normalized trace element diagrams

In the primitive mantle normalized trace element diagrams (Fig 4.20), basalts of the Witkop Formation exhibit negative Ba, Hf, Sr anomalies and positive Pb anomalies (Fig 4.20 A). Insert in Figure 4.20 A is the general pattern for ocean island basalt (OIB), normal mid-ocean ridge basalt (N-MORB) and island arc basalt (IAB). The basalts also exhibit a small negative

Ta-Nb anomaly. Sample NG 2B shows extreme depletion in Ba while sample NG 7 shows depletion in Ti relative to the neighbouring elements. Basaltic andesites of the Toggekry exhibit negative Ba, Nb-Ta, Sr and Ti anomalies (Fig 4.20 B). The basaltic andesites also exhibit positive Zr-Hf and Pb anomalies. Sample NJ-10-SS5 shows K depletion while sample NJ-10-SS7 shows enrichment in K.

Toggekry andesites show negative Nb-Ta, P and Ti anomalies (Fig 4.20 C). The andesites also exhibit a positive Pb anomaly and enrichment in K. The quartz-feldspar porphyries show negative Nb-Ta, P and Ti anomalies (Fig 4.20 D). Insert in Figure 4.20 D shows the pattern for average continental crust. Positive Zr-Hf and Pb anomalies are also exhibited by the quartz-feldspar porphyries. Sample NG 12 shows enrichment in Hf. The Toggekry rhyolites have negative Ba, Ce, Sr, P, Sm and Ti anomalies (Fig 4.20 E). A small Nb-Ta anomaly is also shown by the rhyolites. The rhyolites also show enrichment in K. The quartz-sericite schists of the Toggekry Formation have negative Ba, Sr, P, Sm and Ti anomalies (Fig 4.20 F). The quartz-sericite schists also exhibit a small Nb-Ta anomaly. Felsic schists of the Toggekry from Xie et al. (2012) have negative Ba, Sr, P, Sm and Ti anomalies (Fig 4.20 G). The felsic schists also exhibit a small negative Nb-Ta and positive Pb anomaly. Samples 08 NOND 13 and NOND 6/9 show enrichment in K.

The negative Ba anomaly in the basaltic andesites may be due to fractionation of amphibole. The negative Ba anomaly in the rhyolites, quartz-sericite schists and felsic schists from Xie et al. (2012) reflects the fractionation of K-feldspar. The negative Ce anomaly in the rhyolites may be the result of alteration or a source feature.

The negative P anomaly in the andesites, quartz-feldspar porphyries, rhyolites, quartz-sericite schists and felsic schists is due to the fractionation of apatite. The negative Sr anomaly in the basalts, basaltic andesites, rhyolites, quartz-sericite schists and felsic schists reflects the fractionation of plagioclase. Fractionation of sphene or Fe-Ti-oxides in all the rocks is indicated by the negative Ti anomaly.

The positive Pb is characteristic of continental crust and indicates crustal contamination. The positive Pb anomaly is also characteristic of arc settings. All the lavas have a negative Nb-Ta anomaly. The negative Nb-Ta anomaly is characteristic of a subduction zone signature, where this anomaly is regarded as the non-enrichment of these elements by fluids. The Nb-Ta anomaly is also characteristic of continental crust and may indicate crustal involvement in the

magma process (Rollinson, 1993). Riganti (1996) suggested that sialic crust already existed before the eruption of the Nondweni Group lavas. This was based on the discovery of xenocrystic zircons older than the Nondweni greenstone belt and indications of felsic contamination in some of the mafic rocks.

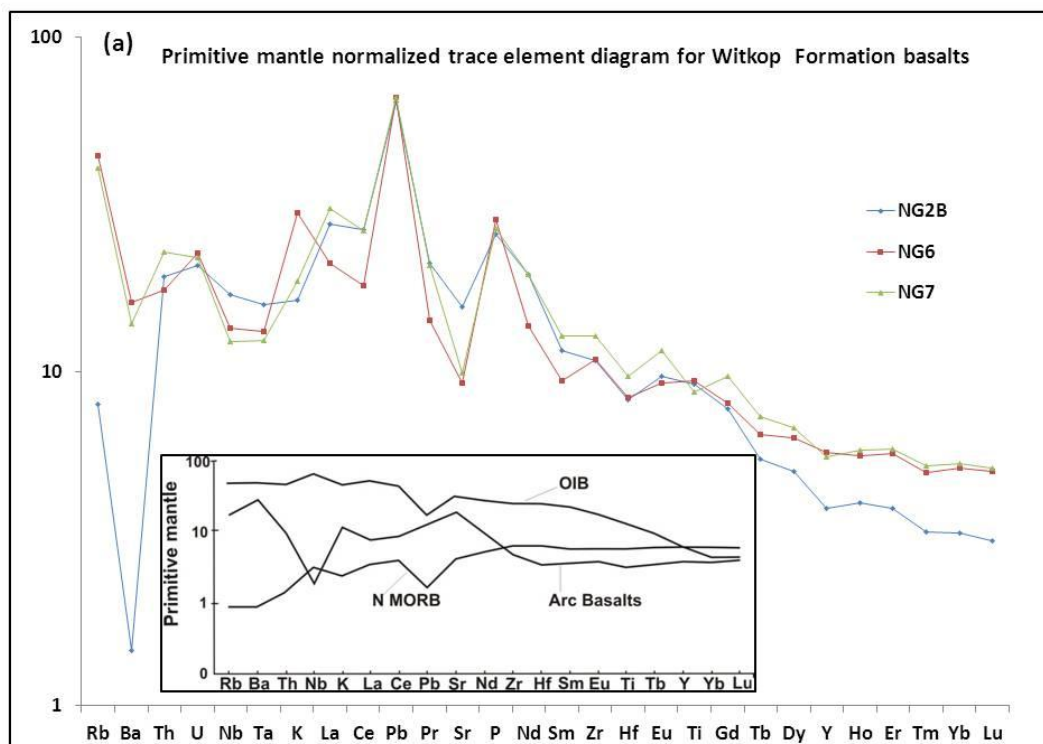


Figure 4.20 Primitive mantle normalized trace element diagrams. Normalizing values from Sun and McDonough (1989). (a) Primitive mantle normalized trace element diagrams for Witkop Formation basalts. Insert shows patterns for ocean island basalts (OIB), normal mid-ocean ridge basalts (N-MORB) and arc basalts.

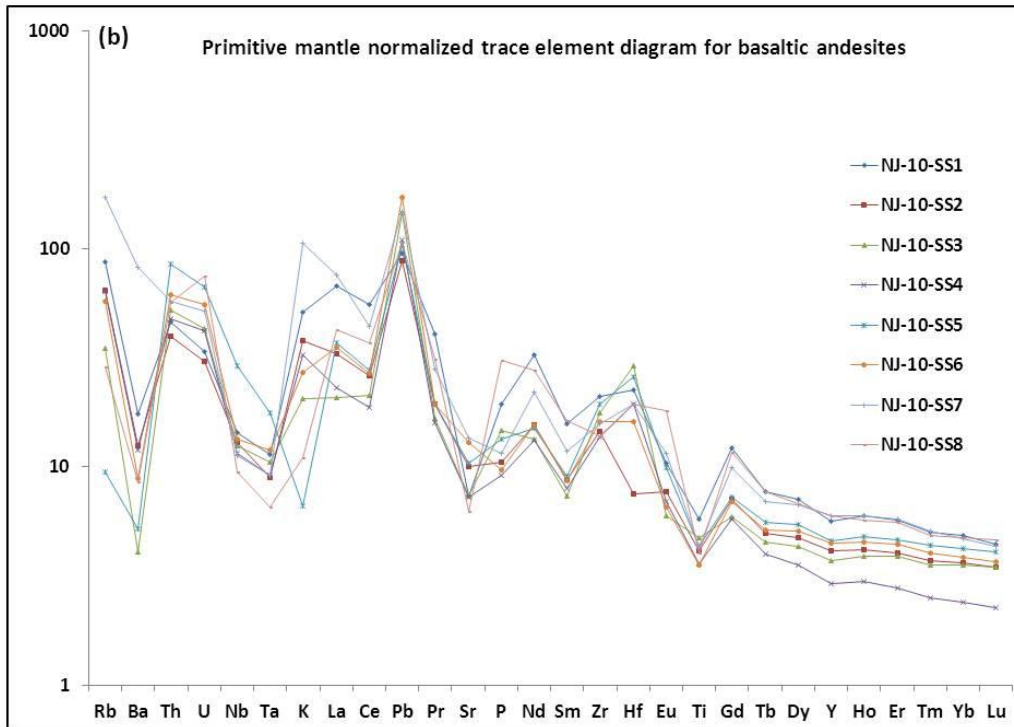


Figure 4.20 (b) Primitive mantle normalized trace element diagram for Toggekry Formation basaltic andesites.

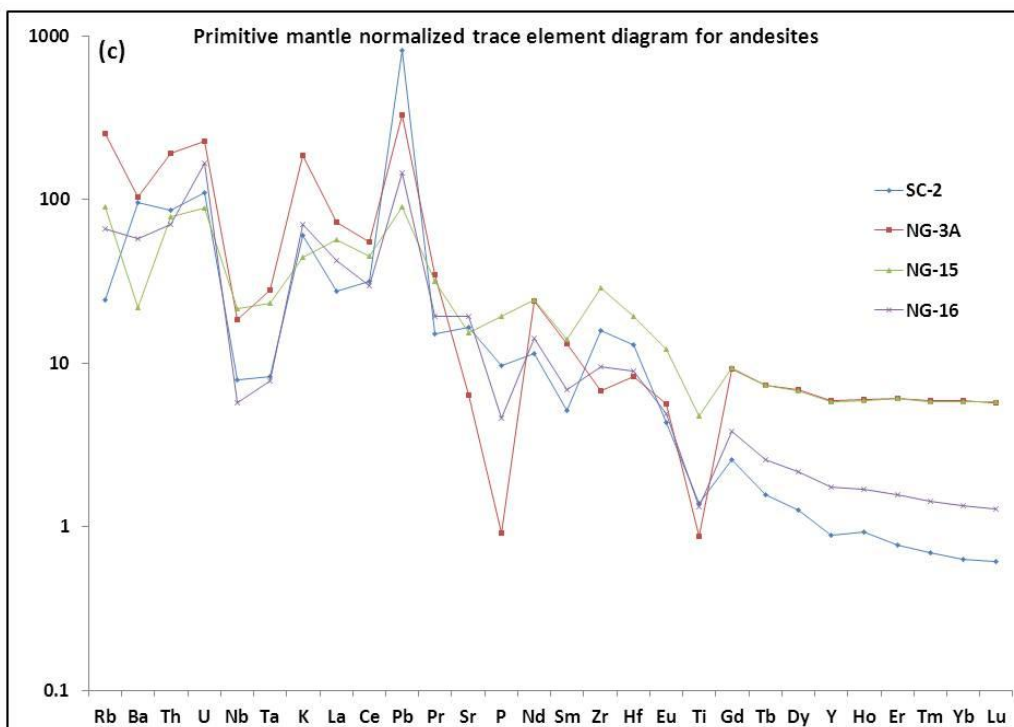


Figure 4.20 (c) Primitive mantle normalized trace element diagrams for Toggekry Formation andesites.

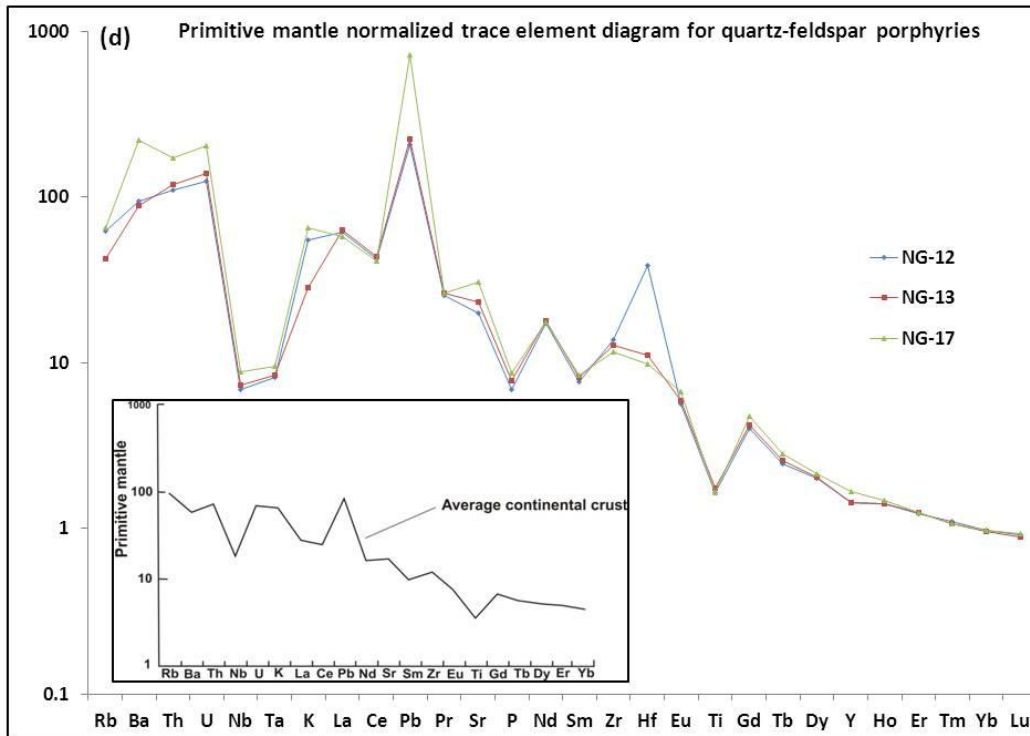


Figure 4.20 (d) Primitive mantle normalized trace element diagram for Toggekry Formation quartz-feldspar porphyries. Insert shows pattern for average continental crust.

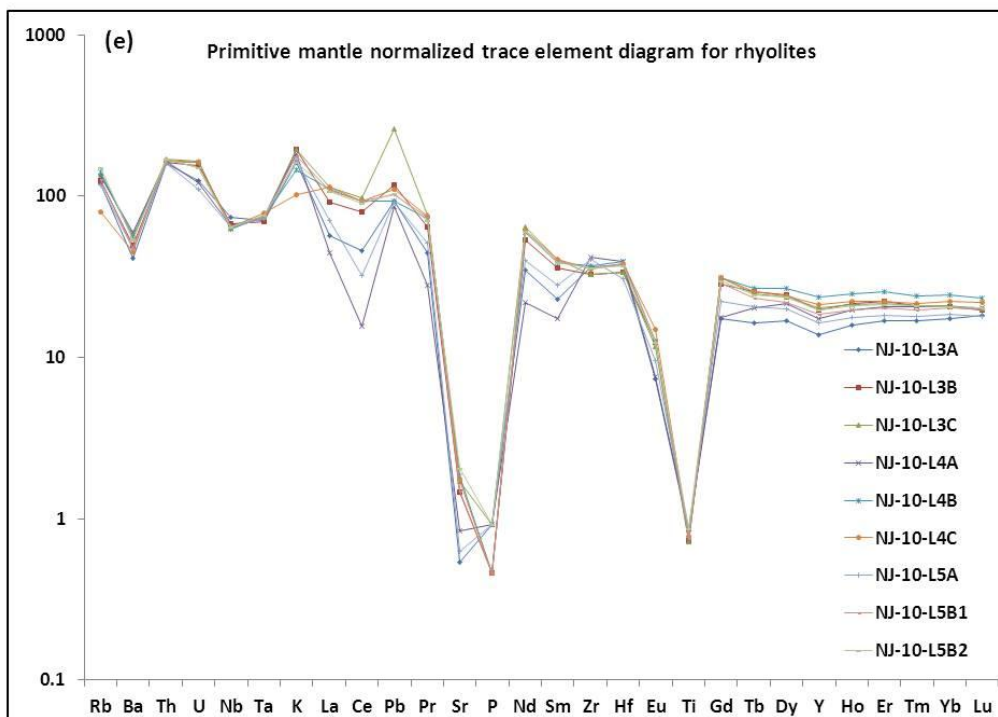


Figure 4.20 (e) Primitive mantle normalized trace element diagram for Toggekry Formation rhyolites.

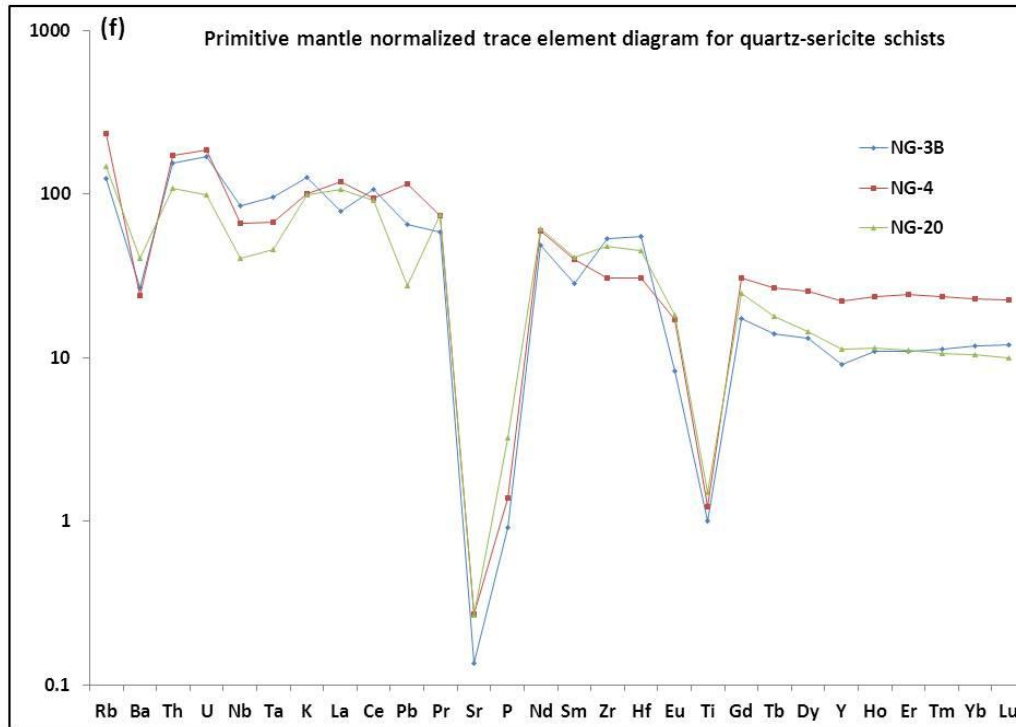


Figure 4.20 (f) Primitive mantle normalized trace element diagram for Toggekry Formation quartz-sericite schists.

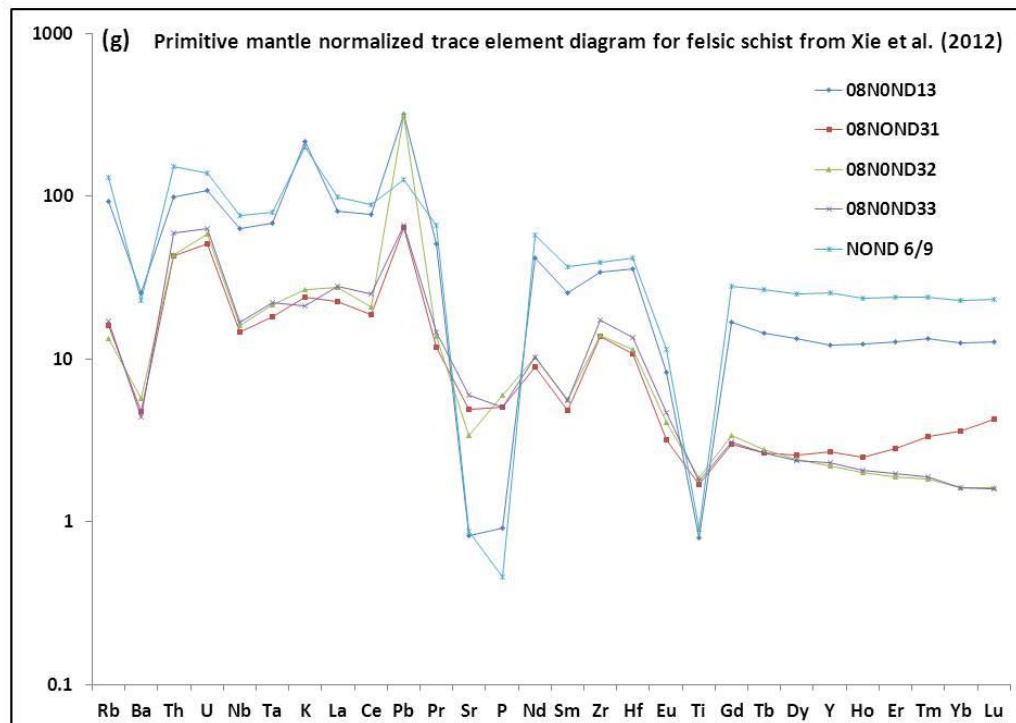


Figure 4.20 (g) Primitive mantle normalized trace element diagram for Toggekry Formation felsic schists from Xie et al. (2012).

Chondrite-normalized REE diagrams are shown in Figure 4.21. Considering the evidence for alteration, and the fact that Ce, as a tetravalent ion, can be fractionated from the other REE under oxidizing conditions implies that the positive and negative Ce-anomalies in some of the diagrams are most likely related to alteration.

The REE diagram show that the Witkop Formation basalts are less enriched in REE than the Toggekry Formation lavas (Fig 4.21 A - note change of scale relative to the other diagrams). In the Toggekry Formation basaltic andesites samples NJ-10-SS5 and NJ-10-SS8 have positive Eu anomalies indicating the accumulation of plagioclase (Fig 4.21 B). Samples NJ-10-SS1 and NJ-10-SS6 have negative Eu anomalies

Sample NG 3A in the Toggekry andesites has a negative Eu anomaly (Fig 4.21 C). The positive Ce anomaly in sample SC-2 may be the result of alteration. The Mount Vernon rhyolites have a negative Eu anomaly and flat HREE patterns (Fig 4.21 E) which contrasts with the more depleted HREE patterns of the quartz-feldspar porphyries (Fig 4.21 D). Samples NJ-10-L3A, NJ-10-L4A and NJ-10-L5A have negative Ce anomalies which may be due to alteration.

The quartz-sericite schists have a negative Eu anomaly, but sample NG 3B also exhibits a positive Ce anomaly (Fig 4.21 F). The sericite schists, with the exception of NG 20 show flat HREE patterns. Sample NG 4 has higher HREE than the other two sericite schists. Felsic schists from Xie et al. (2012) can be separated into two groups (Fig 4.21 G). One group has a negative Eu anomaly and flat HREE patterns. Those samples are more enriched in REE relative to the other samples. The other group shows slight depletion in REE's and a gentle HREE's pattern. Sample 08 NOND 31 shows a concave HREE pattern indicative of amphibole fractionation (Bottazzi et al., 1999; Xie et al. 2012)

The negative Eu anomaly in the samples indicates the fractionation of plagioclase feldspar. The Toggekry lavas show enrichment in LREE's relative to HREE. The enrichment in LREE relative to HREE is characteristic of crustal contamination, subduction zone magmas, enriched mantle, small degrees of partial melting or crystal fractionation which is unlikely to have played a role for the basalts.

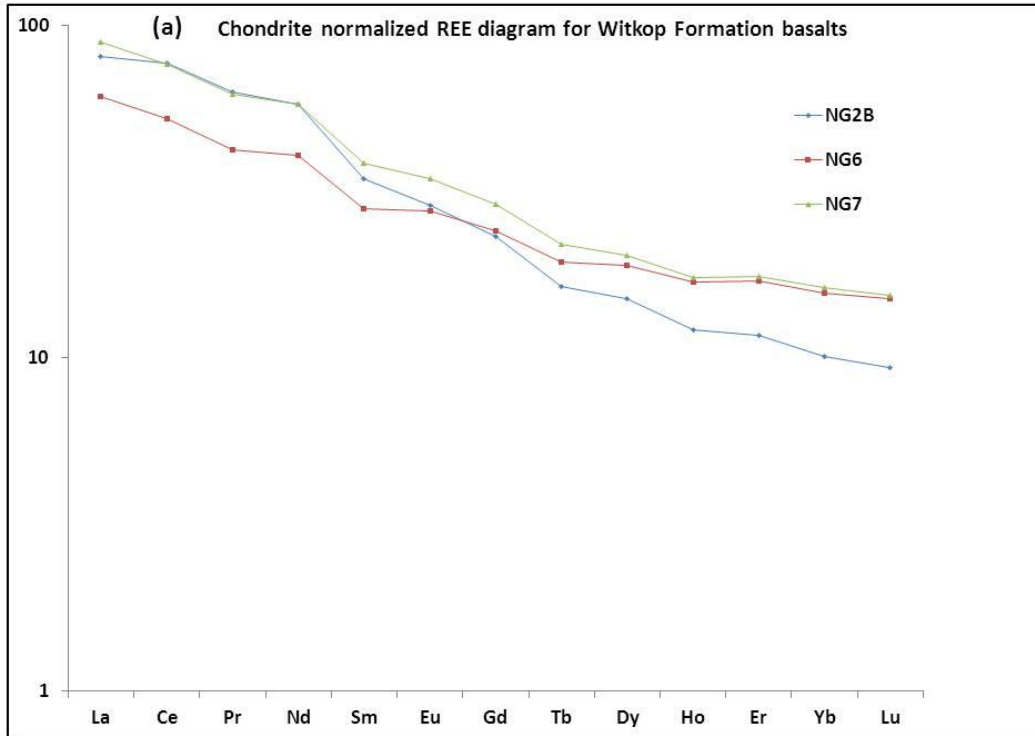


Figure 4.21 Chondrite-normalized REE diagrams for Witkop basalts. Normalizing values from Sun and McDonough (1995). (a) CI-normalized REE diagram for Witkop basalts.

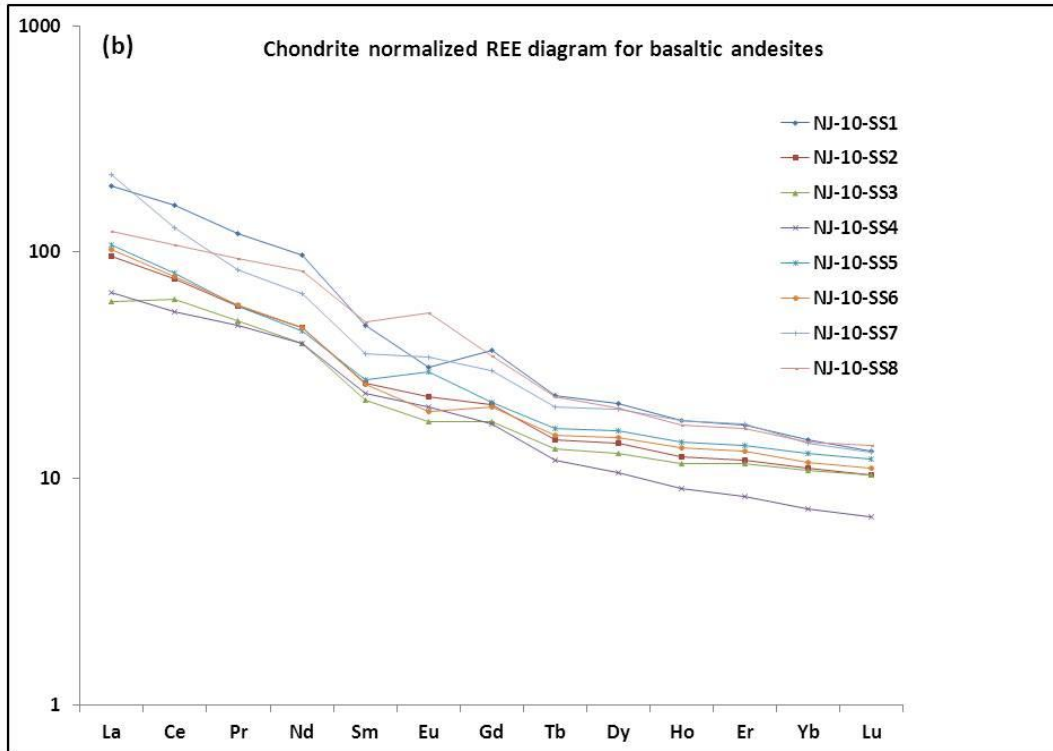


Figure 4.21(b) Chondrite-normalized REE diagram for Toggekry Formation basaltic andesites.

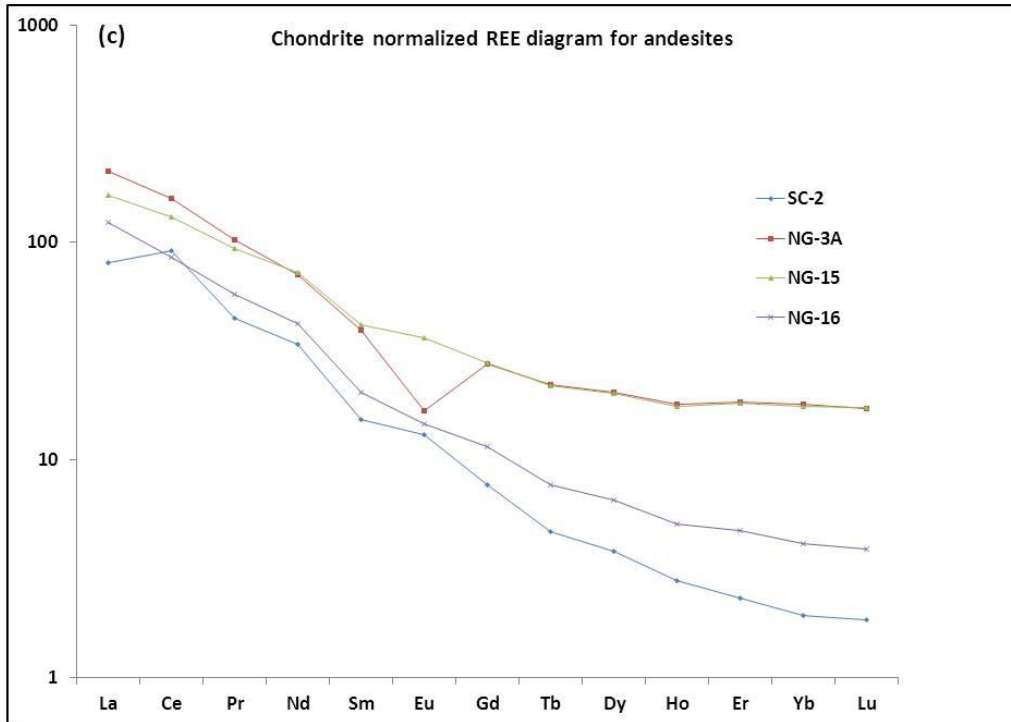


Figure 4.21(c) Chondrite-normalized REE diagram for Toggekry Formation andesites.

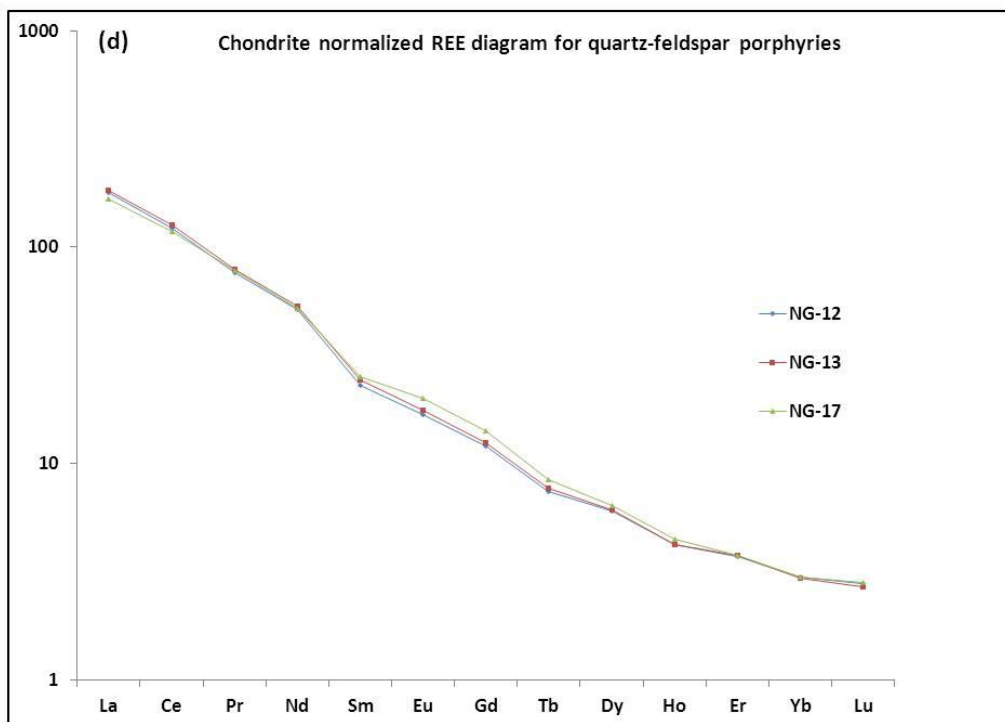


Figure 4.21(d) Chondrite-normalized REE diagram for Toggekry Formation quartz-feldspar porphyries.

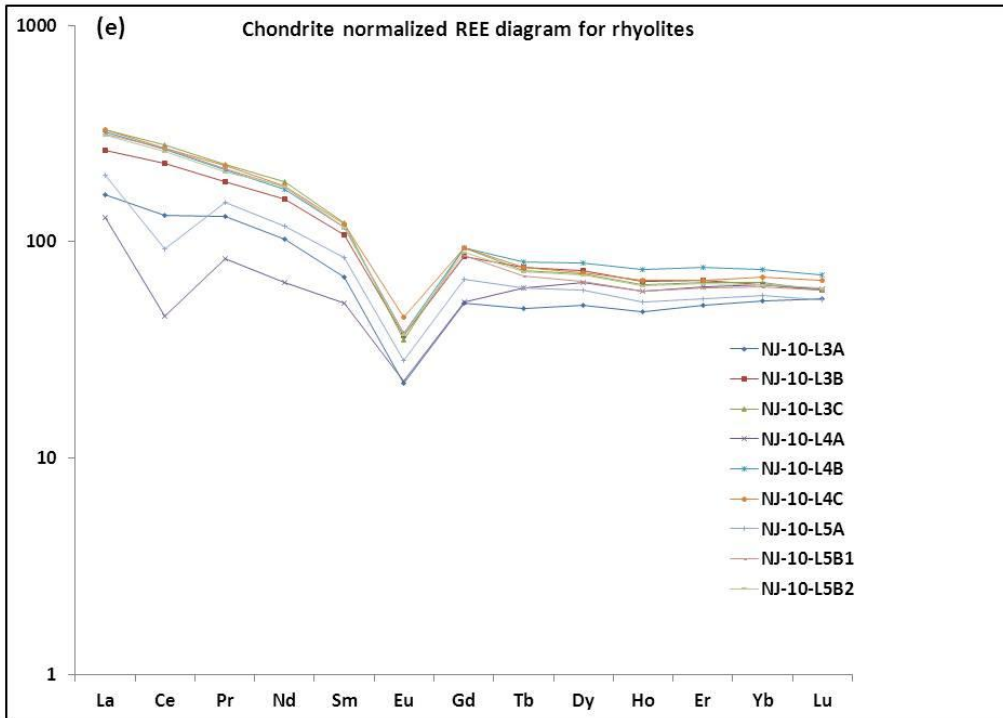


Figure 4.21(e) Chondrite-normalized REE diagram for Toggekry Formation rhyolites.

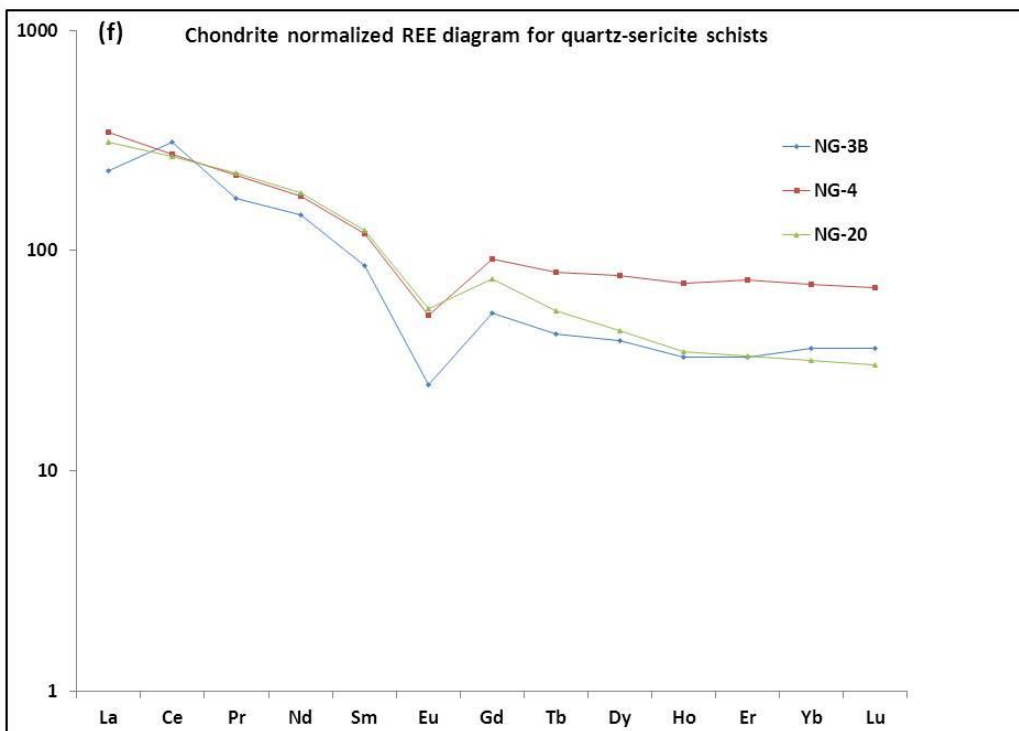


Figure 4.21(f) Chondrite-normalized REE diagram for Toggekry Formation quartz-sericite schists.

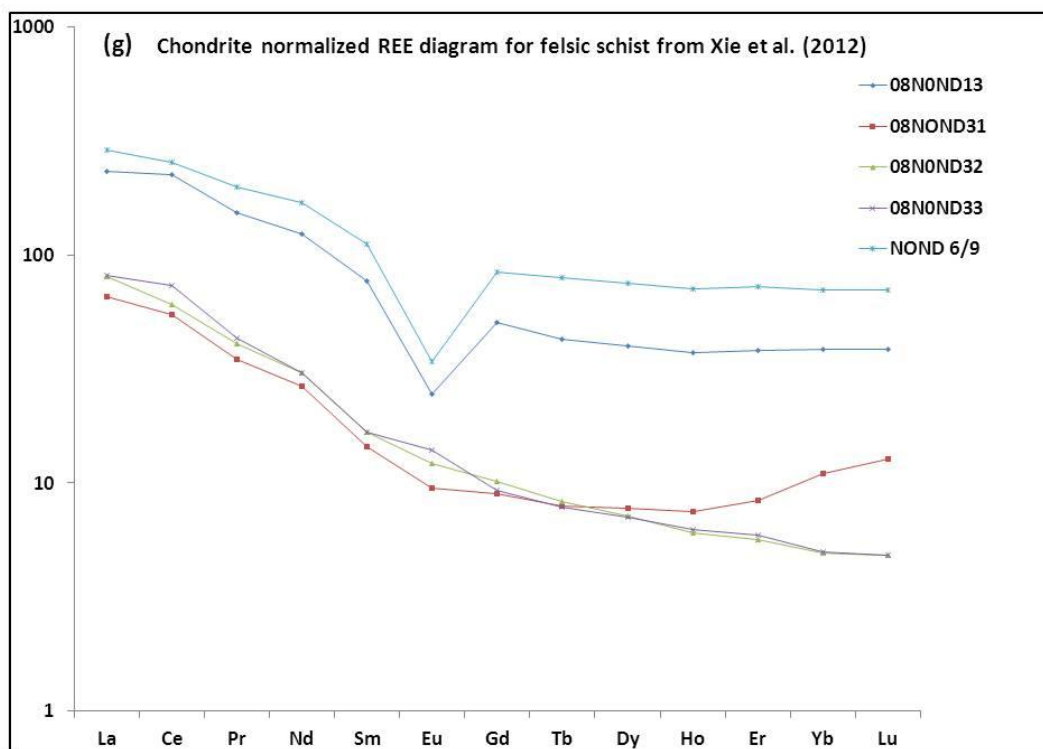


Figure 4.21(g) Chondrite-normalized REE diagram for Toggekry Formation Felsic schists from Xie et al. (2012).

4.6 Element mobility (isocon diagrams)

Since geochemical, petrology and field evidence points towards an important role for alteration in the petrogenesis of the quartz-sericite schists, isocon diagrams (Fig 4.22) have been constructed to constrain element mobility during alteration. Primitive mantle normalized trace element and chondrite normalized REE diagrams indicate that the rhyolites of the Toggekry Formation are geochemically similar to the quartz-sericite schists from the Toggekry thus the rhyolites can be assumed to be the protolith of the quartz-sericite schists. For the quartz-sericite schists the two samples taken are the ones with lowest (NG 3B) and highest (NG 4) HREE concentrations of the all sericite samples. The rhyolite samples used for the isocon diagram are those that have not been affected by alteration (i.e. the ones that do not display a Ce anomaly).

The isocon line/envelope is constructed using the elements which are considered immobile. In this case Al, Ti, Zr and Hf are assumed to be the immobile elements. Elements that fall within the isocon envelope are considered to not have been lost or gained during alteration. Since the isocon line does not coincide with the 1:1 line, it can be concluded that the quartz-sericite schist NG3B have undergone loss in volume during alteration from its assumed protolith NJ-10-L4B.

Losses in K_2O , Na_2O , SiO_2 , CaO , REE's, Pb, Ba, Th, U, Rb and Sr and gains in Co, Ni, V, Sc, Zn and MgO are observed for the schist-protolith pair (Fig 4.42 A). Major gains are notably Co, Ni and V with high losses observed for K_2O , Na_2O , CaO , La, Nd, Pr, Sm, Y, Ba and Sr.

Figure 4.42 (B) using NG4 as the schist and NJ-10L3B as the protolith, shows that most elements have not been affected by the alteration process. The diagram also shows decoupling of LREE and HREE. There are major losses in K_2O , CaO , Na_2O , Sr and Ba. There are gains in Fe_2O_3 , MgO, Ni, Co, Rb, V, Sc, Cu and Zn with major gains notably being Fe_2O_3 , MgO, V, Sc, Cu and Zn.

Both of the isocon diagrams show decoupling of LREE and HREE. This may suggest that the protolith of the sericite-schists could be a rock with lower HREE similar to the felsic schists from Xie et al. (2012).

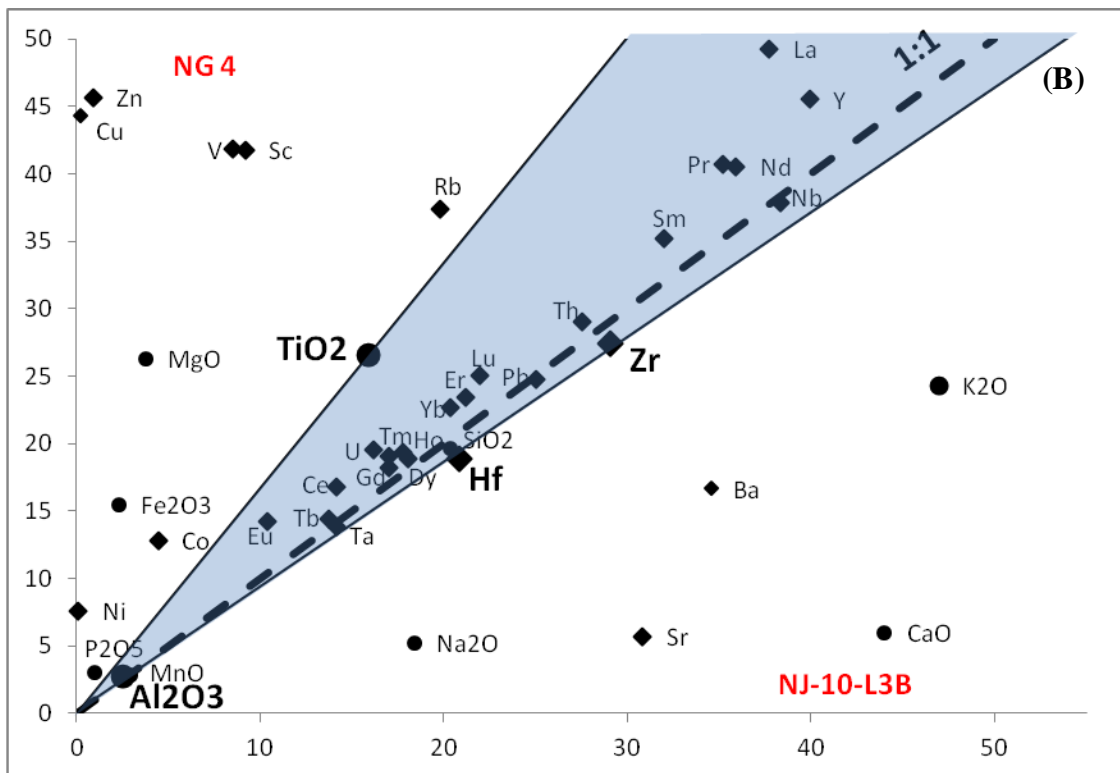
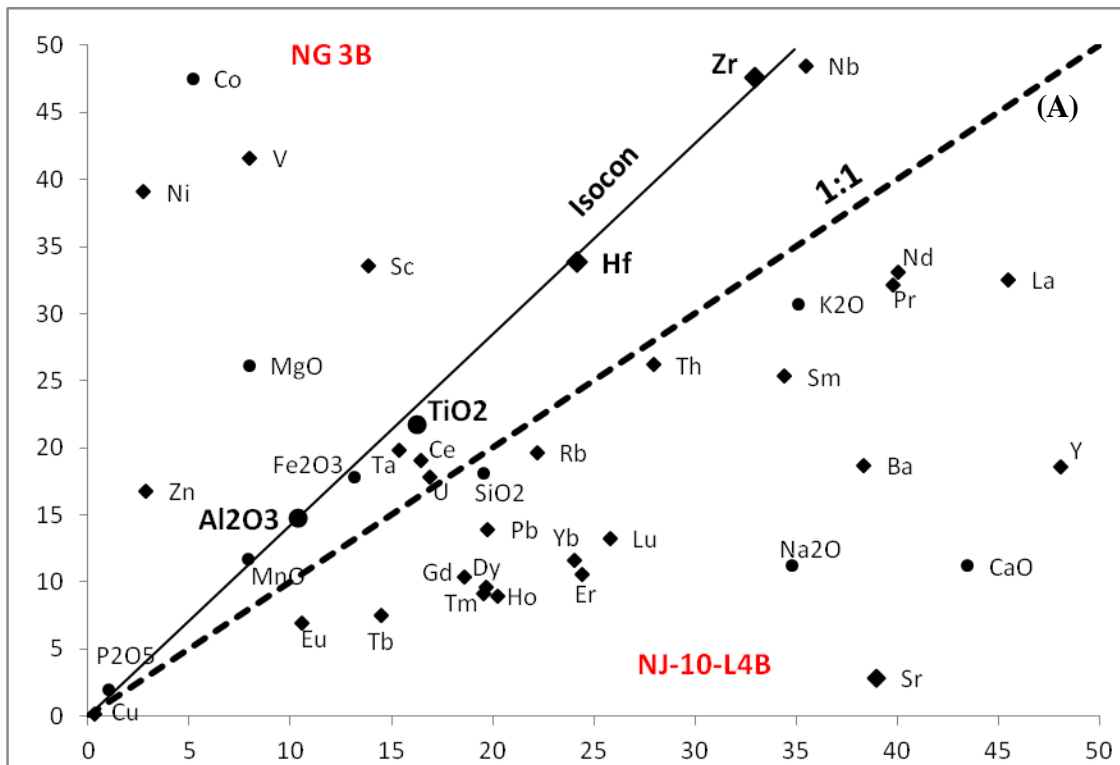


Figure 4.22 Isocon diagram for altered quartz-sericite schists versus least altered rhyolites. The major oxides (circles) and trace elements (diamonds) were scaled by multiplying with a constant for ease of representation. The blue envelopes indicate the range of elements that are typically assumed to be immobile (Ti, Al, Zr) during alteration; the isocon is likely to lie within this envelope. A: quartz-sericite schist NG 3B versus unaltered Mount Vernon rhyolite NJ-10-L4B; B: quartz-sericite schist NG 4 versus Mount Vernon rhyolite NJ-10-L3B.

4.7 Tectonic discrimination diagrams

There are a large number of tectonic discrimination diagrams that use immobile trace elements, minor and major elements. These diagrams are applicable for rocks of basaltic to andesitic composition (Rollinson, 1993). The Wood (1980) tectonic discrimination diagram is also applicable for mafic to intermediate rocks. Thus the basaltic andesites of the Toggekry Formation can be plotted in this diagram. According to Wood's (1980) tectonic discrimination diagram based on ratios of the fairly immobile elements (Fig 4.43) basaltic andesites of the Toggekry Formation are classified as arc basalts while the Witkop Formation basalts show variation ranging from arc-like signatures to E-MORB signatures. Figure 4.20 (a) primitive mantle normalized trace element diagrams for Witkop Formation basalts also shows an insert of patterns for typical MORB (mid-ocean ridge basalts), IAB (island-arc basalts) and OIB (ocean island basalts). The only pattern that resembles the one shown by the basalts of the Witkop Formation and Toggekry Formation basaltic andesites is that of the IAB. The patterns show similar negative Nb and Ti anomalies which are arc signatures.

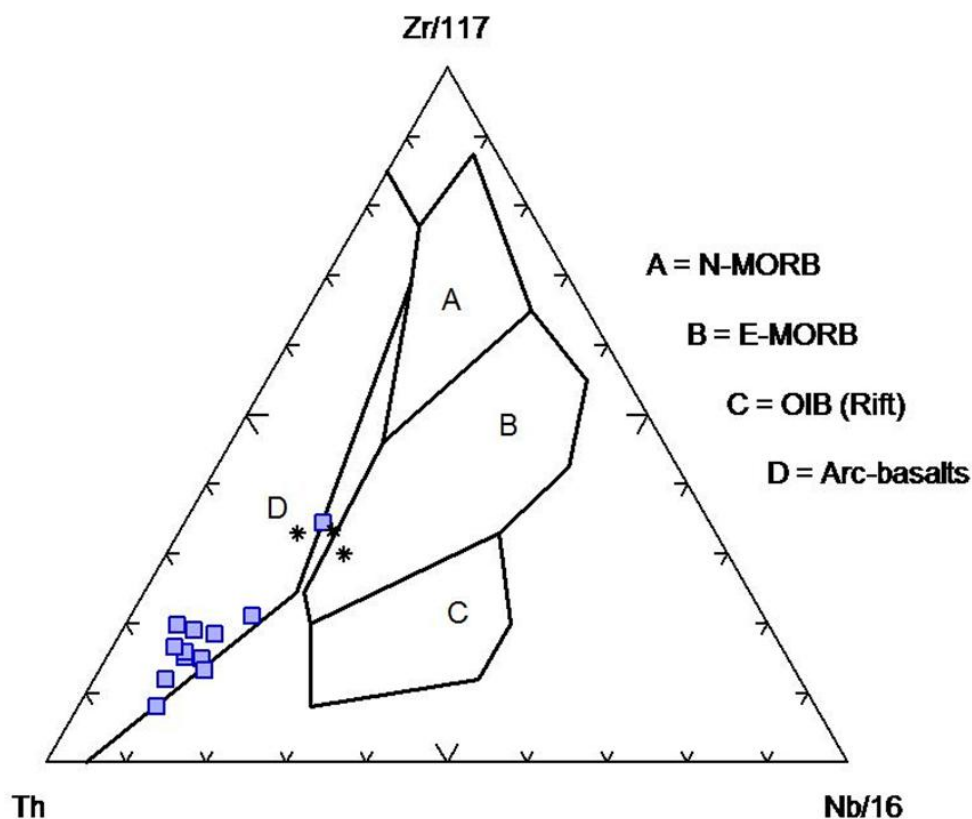


Figure 4.43 Tectonic discrimination diagram after Wood (1980)

4.8 Petrogenesis of the magma

The Lu-Hf isotope system can be used as a geochemical tracer to track the history of chemical differentiation of the silicate earth (i.e crust and mantle) (Kinny and Maas, 2003). This is because Lu fractionates from Hf during magma generation. The chondritic initial Lu/Hf ratio for the Earth is progressively modified over time by partial melting in the upper mantle during the generation of basaltic magmas and thus depleting the residual mantle in Hf relative to Lu, and enriching the basaltic crust which has been generated (Kinny and Maas, 2003). This means that over time the Hf isotopic composition of depleted mantle and the enriched crust will diverge from that of the CHUR. The Lu-Hf isotope systems will be used here to trace the evolution of the Nondweni greenstone belt lavas.

Lu-Hf analyses were carried out on zircons and as mentioned before most of the zircons from the Toggekry lavas have undergone metamictization and thus Pb-loss. This poses a question of whether Pb-loss will affect the Lu-Hf system. Hoskins and Black (2000) demonstrated that zircons may lose U,Th and radiogenic Pb during metamorphism yet retain primary abundance of both Lu and Hf. They showed that although U-Pb isotopes may be susceptible to resetting; the Lu-Hf isotopes are not. Thus metamictisation will not affect the Lu-Hf system.

The Hf isotopic data for zircons from the four analyzed samples is listed in Appendix 4, Table 4.3. Sample NJ-10-L5A has a positive ϵ_{Hf} value and plots above the chondritic uniform reservoir line (Fig 4.44). Sample NG 15 data plots on the chondritic uniform reservoir line. NG 15 shows little variation in ϵ_{Hf} values compared to the other samples. When looking at the primitive mantle normalized trace element diagram for the Toggekry Formation andesites (Fig 4.20 c) it can be seen that sample NG 15 has positive Pb and negative Nb-Ta anomalies. These anomalies are characteristic of crustal contamination.

Samples NG 3A and NG 13 have varying data ranging from negative ϵ_{Hf} to positive ϵ_{Hf} . Sample NG 13 shows the largest variation, with ϵ_{Hf} values ranging from -2.2 to +5.8 ϵ_{Hf} values, with the average being $+2.6 \pm 0.8$. This variation may reflect varying amounts of crustal contamination.

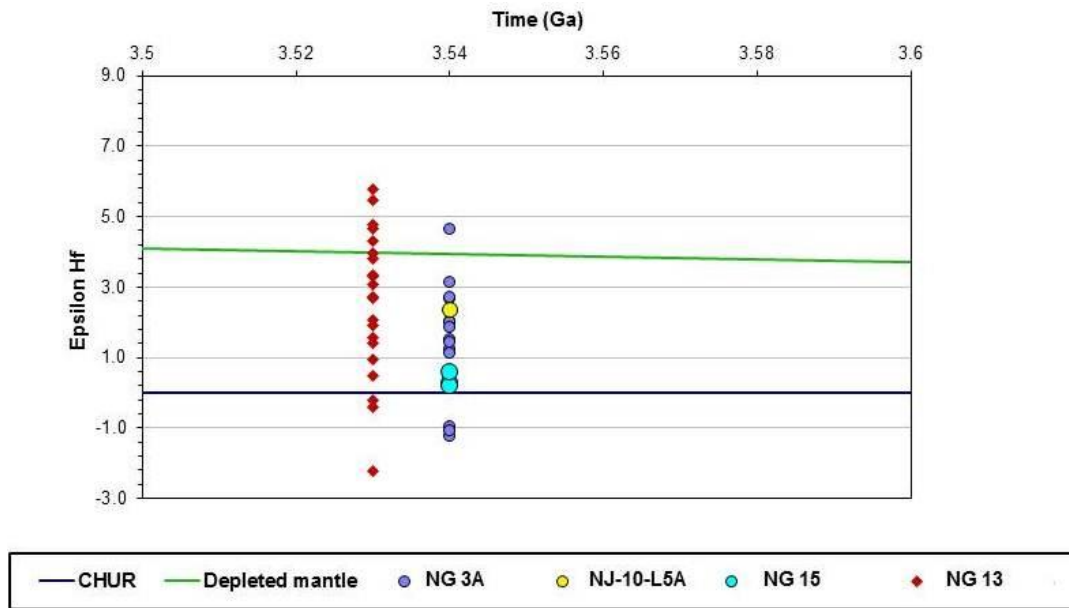


Figure 4.44 ϵ_{Hf} data for the analyzed zircons from the Toggekry Formation, where CHUR is the chondritic uniform reservoir.

Figure 4.45 shows the ϵ_{Hf} data for zircons from the Onverwacht Group, Barberton greenstone belt from Kröner et al. (2013). The authors carried out 32 analyses from 3 samples of the Theespruit Formation and 45 analyses from 4 samples of the Hooggenoeg Formation by LA-ICP-MS. The Hf isotopic data for the zircons analysed can be found in table 3 in Kröner et al. (2013). See Kröner et al. (2013) for analytical methods and procedures. In Figure 4.45 positive ϵ_{Hf} values indicates that the material which melted to form the magma from which the zircons crystallized was derived from a mantle which had experienced an earlier depletion event (period of melt removal). The zircons with the negative ϵ_{Hf} value indicates that pre-existing continental crust was involved in magma genesis. Thus samples which show ϵ_{Hf} values ranging from negative to positive indicate that both a depleted mantle and continental crust played a role in the formation of the rocks.

Barberton greenstone belt comprises three major stratigraphic units: the lower Onverwacht Group, the middle Fig Tree Group and upper Moodies Group (Lowe and Byerly, 1999; Viljoen and Viljoen, 1969a). The Onverwacht Group is subdivided into the lower Sandspruit Formation, Theespruit Formation, Hooggenoeg Formation, Kromberg Formation and upper Mendon Formation (Lowe and Byerly, 1999, Viljoen and Viljoen, 1969a, b). The Theespruit Formation has an age of 3530 ± 0.2 Ma and the Hooggenoeg Formation has an age ranging from 3445 ± 3 to 3416 ± 5 Ma (De Ronde and De Wit, 1994).

Zircons from the Theespruit Formation samples show a wide range in Hf isotopic compositions. Kröner et al. (2013) observed ϵ_{Hf} values ranging from -3.7 to +3.09. Most of the analyses show negative ϵ_{Hf} values indicating the involvement of older crust in the generation of the rocks of the Theespruit Formation.

The zircons from the Hooggenoeg Formation also have a wide range of Hf isotopic compositions, ranging from ϵ_{Hf} values of -1.9 to +1.54. Most of the Hf isotopic compositions have negative ϵ_{Hf} values, also indicating derivation of the Hooggenoeg Formation from an older crust. Both the Theespruit and Hooggenoeg Formation Hf isotopic compositions also show some positive ϵ_{Hf} values indicating the involvement of the depleted mantle as well in the generation of the rocks.

Thus it can be concluded that rocks of the Toggekry Formation were derived from a depleted mantle source with contamination by older continental crust or from a depleted mantle at an earlier age, followed by remelting. On the other hand rocks of the Theespruit and Hooggenoeg Formations, with predominantly negative hafnium isotopic compositions, formed as a result of melting of older crust probably of felsic composition (Kröner et al. 2013).

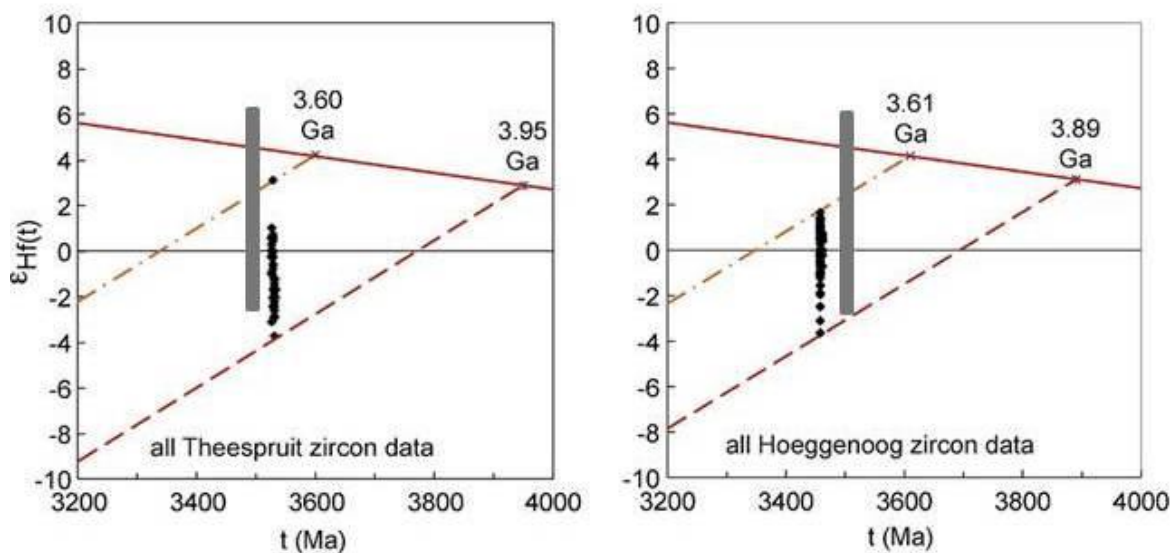


Figure 4.45 ϵ_{Hf} diagram for the felsic volcanic rocks of the Onverwacht Group, Barberton greenstone belt from Kröner et al. (2013). The grey area indicates range of data for the Toggekry Formation obtained from this study.

CHAPTER 5. COMPARISON OF THE TOGGEKRY FORMATION WITH THE THEESPRUIT FORMATION, BARBERTON GREENSTONE BELT (BGB).

5.1 Introduction

The lithologies and age of the Toggekry Formation are similar to the Theespruit Formation of the Barberton greenstone belt. Therefore a more detailed comparison is given here in order to ascertain whether the formations are part of the same succession or developed in different but coeval basins.

The Barberton greenstone belt (BGB) is one of the best-studied greenstone belts in the World. It covers an area of 160 x 50 km and is located on the southeastern margin of the Kaapvaal craton (Kohler and Anhaeusser, 2002). It is an ENE trending, strongly folded volcano-sedimentary succession 3600 to 3100 Ma years in age and surrounded by various granitoid rocks of the Kaapvaal craton (De Wit et al., 1992; Kröner et al., 1996; Kohler and Anhaeusser, 2002; Brandl et al., 2006).

The greenstone belt succession is termed the Barberton Supergroup and comprises three major stratigraphic units: the lower Onverwacht Group, the middle Fig Tree Group and upper Moodies Group (Viljoen and Viljoen, 1969a; Lowe and Byerly, 1999). The Onverwacht Group is 8–12 km thick succession, consisting largely of komatiites, komatiitic basalts and tholeiitic basalts with minor dacitic to rhyolitic calc-alkaline rocks and quartz–muscovite schists (Viljoen and Viljoen, 1969a; Byerly, 1999). It is subdivided into the lower Sandspruit Formation, Theespruit Formation, Hooggenoeg Formation, Kromberg Formation and upper Mendon Formation (Viljoen and Viljoen, 1969a, b; Lowe and Byerly, 1999).

De Wit et al. (2011) reviewed the Barberton stratigraphy and suggested that the Onverwacht Group is a suite better subdivided into seven complexes. In ascending tectonostratigraphic order, these are: the Sandspruit Complex, Theespruit Complex, Komati Complex, Hooggenoeg Complex, Noisy Complex, Kromberg Complex and Mendon Complex.

5.2 Summary of the Toggekry Formation

The Toggekry Formation comprises: quartz-sericite schists, mafic schists, rhyolites, pillowed basalts-basaltic andesites, pillowed andesites, and komatiitic basalts. In addition the formation contains massive serpentinite bodies, metaquartzites, graphitic schist and quartz

feldspar porphyries. Dating of the rocks of the Toggekry Formation yielded ages from 3547 Ma to 3529 Ma (Chapter 3). Studies by Xie et al. (2012) also yielded similar ages of ~3.53 Ga.

The rocks of the Toggekry Formation are generally more deformed than the underlying and overlying rocks of the Magongolozi and Witkop Formations respectively. Hofmann and Wilson (2007) attributed the higher degree of deformation and metamorphism of the Toggekry Formation to the close proximity of the sequence to syntectonic intrusive Mvunyana granodiorite and to the hinge of the synclinal fold closure south of the Toggekry Formation (Wilson and Versfeld, 1994a). The Nondweni greenstone belt has been deformed and metamorphosed under amphibolite facies conditions. Metamorphic assemblages (garnet-hornblende-plagioclase-quartz) of the Witkop Formation basalts directly overlying the Toggekry Formation give peak metamorphic conditions of ~6.5 kbar and 600 to 650 °C (Saha et al., 2012). The monazite U/Pb data indicates that peak metamorphism occurred at 3230 ± 5 Ma in the Toggekry Formation.

Tectonic discrimination diagrams indicate that the mafic rocks of the Toggekry and Witkop Formations formed as arc basalts. Wilson and Versfeld (1994b) suggested a back-arc basin tectonic setting for the Nondweni greenstone belt. This is based on the tholeiitic and calc-alkaline signatures of the mafic and felsic rocks.

5.3 Theespruit Complex Geology

5.3.1 Geochronology

The age of 3530 ± 0.2 Ma for the Theespruit Complex, Onverwacht Suite, has been established from the U/Pb zircon dating of 13 Theespruit felsic volcanic rocks by Van Kranendonk et al. (2009). This shows that it is coeval with the Toggekry Formation.

5.3.2 Lithologies

The Theespruit Complex comprises pillowed metabasalts, basaltic komatiites, quartz-muscovite schists with metachert, felsic schists, interlayered mafic-ultramafic schists, massive ultramafic rocks, talc-serpentinite schists and intrusive quartz-feldspar porphyry (Diener, 2004; Van Kranendonk et al., 2009). The quartz-muscovite schists were interpreted as originally felsic volcanics and pyroclastic units by De Wit et al. (1983, 1987) and Diener

(2004). Thus the Theespruit Complex and the Toggekry Formation have very similar lithologies. In addition chert veins present in the Toggekry Formation are of carbonaceous types similar to the chert associated with the felsic rocks of the Theespruit Formation (Hofmann and Harris, 2008).

5.3.3 Structure and metamorphism

The Theespruit Complex was intruded at 3460–3440 Ma and 3210–3240 Ma by tonalite to trondhjemite plutons and shows a higher grade of metamorphism than the structurally overlying complexes (De Wit et al., 2011; Furnes et al., 2013). The Theespruit Complex is metamorphosed to amphibolite-facies with peak metamorphic assemblages garnet-epidote-hornblende-plagioclase-quartz in the amphibolites giving peak metamorphic conditions of 7.4 ± 1.0 kbar and 560 ± 20 °C (Diener, 2004). This peak metamorphism occurred at ~ 3230 Ma (Dziggel et al., 2002; Diener, 2004; Diener et al., 2005), which is identical to the peak metamorphism in the Toggekry Formation.

5.3.4 Geochemistry

Felsic rocks of the Theespruit Complex are depleted in trace elements relative to the Toggekry quartz-sericite schists and felsic schists (Fig 5.1). They also exhibit negative Ba, Sr, Nb-Ta and Ti anomalies and positive Pb and Zr-Hf anomalies also shown by the Toggekry felsic schists and quartz-sericite schists. The primitive mantle normalised REEs diagram for the different rocks also indicates that the Theespruit Complex felsic schists are depleted in REEs relative to the Toggekry Formation lava (Fig 5.2). Therefore, although the age, lithologies and peak metamorphism are all similar for the Theespruit Complex and Toggekry Formation, the geochemistry indicates that there are significant differences between the felsic rocks. This implies that, although they are coeval, the two formations are not part of a single succession. Nevertheless the similarity of the flat HREE patterns and steep LREE patterns of both formations suggest generation by geochemically similar magmas.

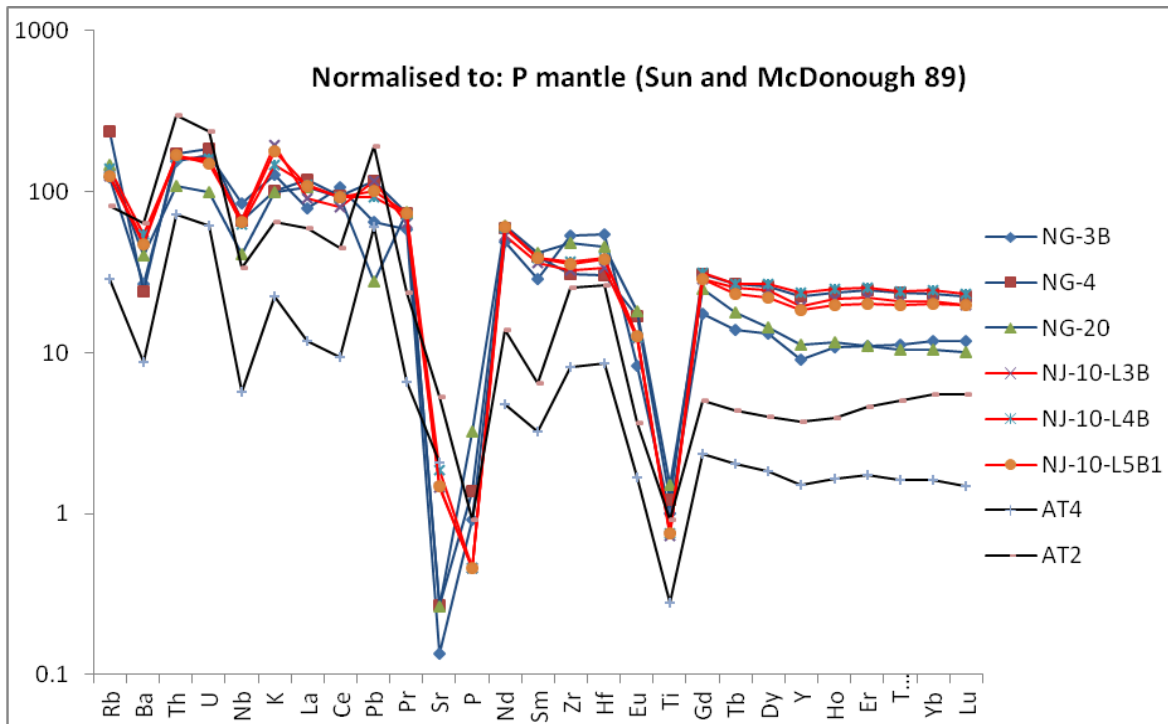


Figure 5.1 Primitive mantle normalized trace element diagram for the Toggekry Formation quartz-sericite schists (NG 3B, NG 4, NG 20-blue line), Toggekry Formation rhyolites (NJ-10-L3B, NJ-10-L4B, NJ-10-L5B1-red line) and Theespruit Complex felsic schists (AT 4, AT 2-black line). Theespruit Complex data are from Hofmann and Harris (2008).

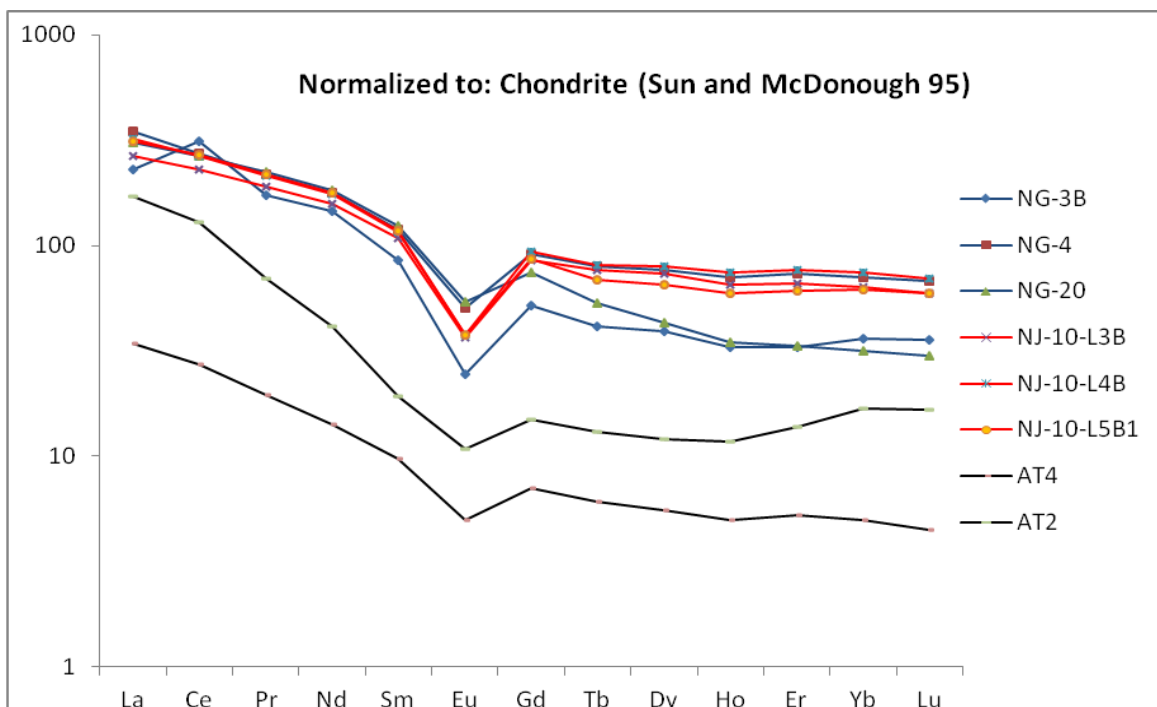


Figure 5.2 Chondrite normalized REEs diagram for the Toggekry Formation quartz-sericite schists (NG 3B, NG 4, NG 20-blue line), Toggekry Formation rhyolites (NJ-10-L3B, NJ-10-L4B, NJ-10-L5B1-red line) and Theespruit Complex felsic schists (AT 4, AT 2-black line). Theespruit Complex data are from Hofmann and Harris (2008).

5.4 Summary of the evolution of the Nondweni and Barberton greenstone belts

Any comparison between the Barberton greenstone belt and Nondweni greenstone belt (Table 5.1) is hampered by the good exposure and amount of research on the former compared to the scant exposure and little research on the latter. However Table 5.1 reveals certain similarities and differences. The Nondweni Group has similar lithologies and age as the lower part of the Onverwacht Group, both were formed in arc settings. The Nondweni greenstone belt does not have any intrusive equivalent to the Steyndorp, Theespruit and Stolzburg plutons, but both have ca. 3.3 to 3.2 Ma intrusions. These correspond to peak metamorphism during D_2 and M_2 . In the BGB peak metamorphism M_2 is contact metamorphism, like in Nondweni Group, but is the result of the intrusion of the Kaap Valley Pluton. Earlier D_1 and M_1 show similarities in both belts. Silicification and Au mineralization also affected both greenstone belts at about the same time. The difference in the mineralization is that Cu-Zn sulphide mineralization present in the Toggerykry Formation is absent in the Theespruit Complex.

The one problem in the summary table is the age and stratigraphic location of the Mangongolozi Formation. According to Wilson and Versfeld (1994a,b), the Mangongolozi Formation is the oldest formation in the Nondweni Group but recent ages by Xie et al. (2012) indicate that the formation is the same age to slightly younger than the Witkop Formation. One possible explanation for this is that the ages obtained by Xie et al. (2012) may reflect reset age due to an as yet not recognised granitoid intrusion of that age as perhaps an equivalent of the Stolzburg Pluton. Various granitoid bodies are in contact with the Mangongolozi Formation which have not been dated but thought to be part of the Mvunyanan granodiorite but may possibly be much older. Dating of these granitoid bodies may help with a better understanding about the age of the Mangongolozi Formation. The other possibility is that the Mangongolozi Formation is younger than the Toggerykry Formation and is part of the Witkop Formation and was thrust N-S during an earlier deformation event.

One obvious issue is that if the Nondweni greenstone belt is equivalent to the Barberton greenstone belt, why does it not contain economic Au mineralization. One possible reason is the poor exposure of Nondweni greenstone belt with parts obscured by Karoo Supergroup cover. Alternatively it could reflect fundamental differences between the two belts.

Barberton greenstone belt		Nondweni greenstone belt	
Intrusions	Structure and Metamorphism	Intrusions	Structure and Metamorphism
Nelspruit Batholith (3106 ± 3 Ma)		Mpuluzi Batholith (3107 ± 4 Ma)	
	Au mineralization (3126 - 3084)		Au mineralization (3150-3100)
	MOODIES GROUP (3226 ± 1 Ma)		
Kaapvalley Pluton (3227 ± 1 Ma)	<ul style="list-style-type: none"> • D₃ (<3226 Ma): SE to NW directed thrusting and shortening, resulting in the NE-SW trending structure of BGB. (D₃ maybe a continuum of D₂) 	Mvunyanu Granodiorite (3290 ± 33 Ma)	<ul style="list-style-type: none"> • D₂ : NW to SE compression resulting in NE-SW trending regional syncline plunging to the SW.
	FIG TREE GROUP (3227 ± 3 Ma)		M2 : Amphibolite facies metamorphism. Peak metamorphism (6.5 kbar, 600 - 650° C) at 3230 ± 6 Ma
			Mobilization of sulphides and concentration into F₂ folds during D₂
	Silicification		Silicification
	Mendon Formation (3298 ± 3 Ma)		
	Kromberg Formation (3416 ± 3 to 3334 ± 6 Ma)		
			• D₁ : NE to SW thrusting and shortening resulting in small scale isoclinal folds. Followed by tilting to SW.
			M1 : Regional metamorphism. Greenschist facies metamorphism
	ONVERWACHT GROUP		
		??Magogolozi Formation (3431 - 3371 Ma) ??	
Stoltzburg Pluton (3445 ± 3 Ma)			
Theespruit Pluton (3443 ± 3 Ma)		Witkop Formation (3418 ± 5 Ma)	
	Hoogenoeg Formation (3445 ± 3 to 3416 ± 3 Ma)		
	Komati Formation (3472 ± 5 Ma)		
Steyndorp Pluton (3510 Ma)		Intrusion of Ultramafic rocks	
	Tectonic boundary	Q-F porphyry sills (3529 ± 12 Ma)	
			Cu-Zn sulphide mineralization
	Theespruit Formation (3547 ± 2 to 3530 ± 0.2 Ma)		Toggekry Formation (3547 ± 5 to 3532 ± 4 Ma)
	Sandspruit Formation		??Magogolozi Formation (3431 - 3371 Ma) ??

Table 5.1 Geological evolution of the Barberton and Nondweni greenstone belt. References: De Ronde and De Wit, 1994; Riganti, 1996; Dann, 2000; Poujol et al., 2003; Van Kranendonk et al., 2009; Xie et al., 2012 and Furnes et al., 2013.

Various models have been proposed for the origin of greenstone belts. Tectonic environments ranging from plate related continental drifts, accretionary complexes, intracontinental flood basalts, intra-oceanic arcs, ocean spreading ridges, oceanic plateaus, oceanic islands, back-arc basins, diachronous blocks formed during multiple periods of extension and magmatic and tectonic accretion and convective overturn (Condie and Hunter, 1976; De Wit et al., 1987; De Wit et al., 1992; Lowe, 1994; Dann, 2000; Chavagnac, 2004; Dann and Grove, 2007; Van Kranendonk, 2011; Furnes et al., 2013). The various tectonic environments for the formations of the Barberton greenstone belt are listed in Furnes et al. (2013) and some of these models are discussed below.

De Wit et al. (1992) proposed that the Barberton greenstone belt formed as a result of horizontal tectonics in which diapirism played no role. They proposed that the earliest continental nuclei may have originated through regional intraoceanic obduction resulting in stacking, tectonic loading and subsidence of the hydrated oceanic thrust stacks. Stacking of these oceanic slabs is thought to have resulted in trondjemite-tonalite melts under variable pressures and temperatures at depths exceeding 20 km. According to the authors the main “requirements” for obduction-dominated tectonism and granitoid formation would have been a buoyant and hydrated oceanic crust. High MgO and H₂O in the rocks would have been required for such processes.

Archaean oceanic crust has higher MgO contents than modern oceanic crust and hydration of mantle material takes place at mid-ocean ridges (MOR) during oceanic lithosphere formation. De Wit et al. (1992) postulated that before 4.0 Ga the MOR stood above sea level resulting in rapid “dry” recycling of oceanic lithosphere and therefore little continental crust formed. That is why the earliest preserved mafic-ultramafic rocks on Earth were derived from a mantle source that had already had a long history of relative chemical depletion and extraction of even earlier but recycled crust.

Recent publications have cast doubt on the thrust- accretion model. Van Kranendonk et al. (2009) produced a summary based on previous work by various authors as to why there is doubt about this model. One of the reasons was that Byerly et al. (1996) showed that greenstones above the Komati Shear Zone (KSZ) are continuous, progressively upward-younging successions which formed over more than 200 Ma. Therefore the succession is not a tectono-stratigraphic assemblage as implied in the thrust accretion model. Secondly Kisters

and Anhaeusser (1995) showed that the granitoid rocks flanking the greenstones exhibit evidence consistent with emplacement of granitoids as diapirs in contrast to diapirism playing no role as proposed by De Wit et al. (1992).

Lowe, 1994 proposed that early continental formation took place by magmatic accretion and tectonic amalgamation of small proto-continental blocks. According to Lowe (1994) the BGB comprises a series of four discrete tectono-stratigraphic blocks that were progressively accreted to one another between 3550 and 3220 Ma to form ancient continental fragments now referred to as the Kaapvaal Craton. Each block consists of an early sequence of extension-related mafic-ultramafic volcanism representing oceanic plateaux or back-arc spreading centres. This was followed by a period of subsidence and chemical sedimentation and then thickening and stabilisation of the newly formed block as a result of subduction-like calc-alkaline magmatism (Lowe, 1994). Figure 5.1 shows a schematic model for the evolution of the Kaapvaal craton by Poujol et al. (2003) based on Lowe (1994).

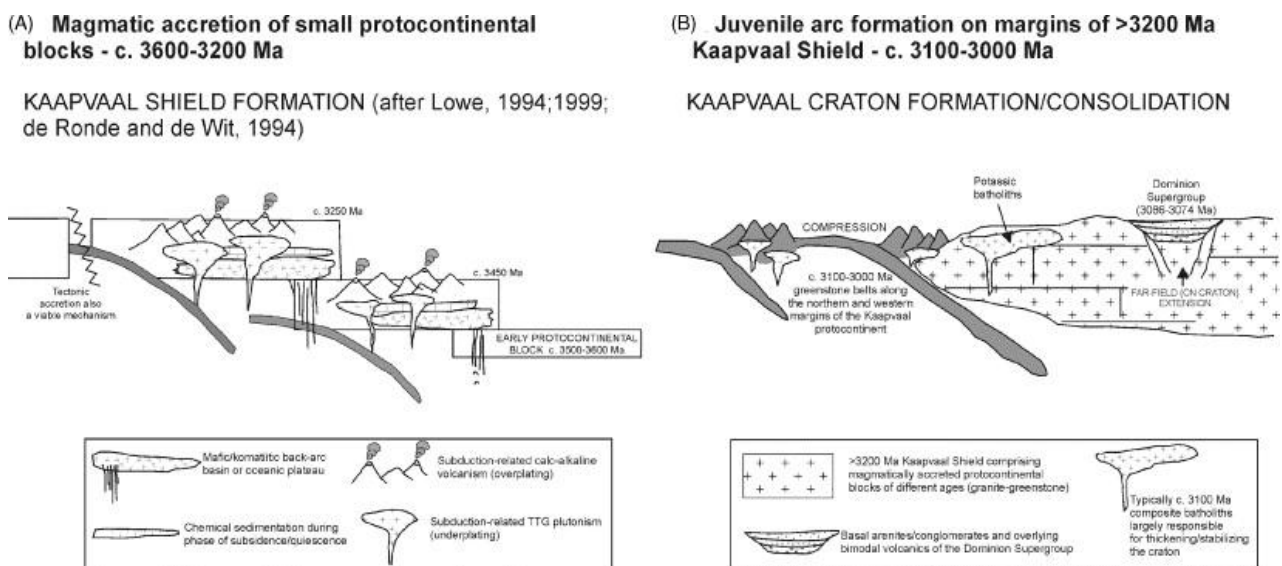


Figure 5.1 Schematic models for the evolution of the Kaapvaal craton from Poujol et al. (2003)

Moyen et al. (2007) provided a geodynamic model for the evolution of the BGB (Fig 5.2) which commenced with accretion of the Steynsdorp nucleus at 3.52 Ga after the lower Onverwacht had formed in the eastern domain. At 3.45 Ga the Stoltzburg arc formed as a result of SE directed subduction. In the western domain subduction was NW directed and

resulted arc-continent collision (3.23 – 3.21 Ga) resulting in the current structure of the BGB. This was the final phase in the evolution of the Barberton greenstone belt.

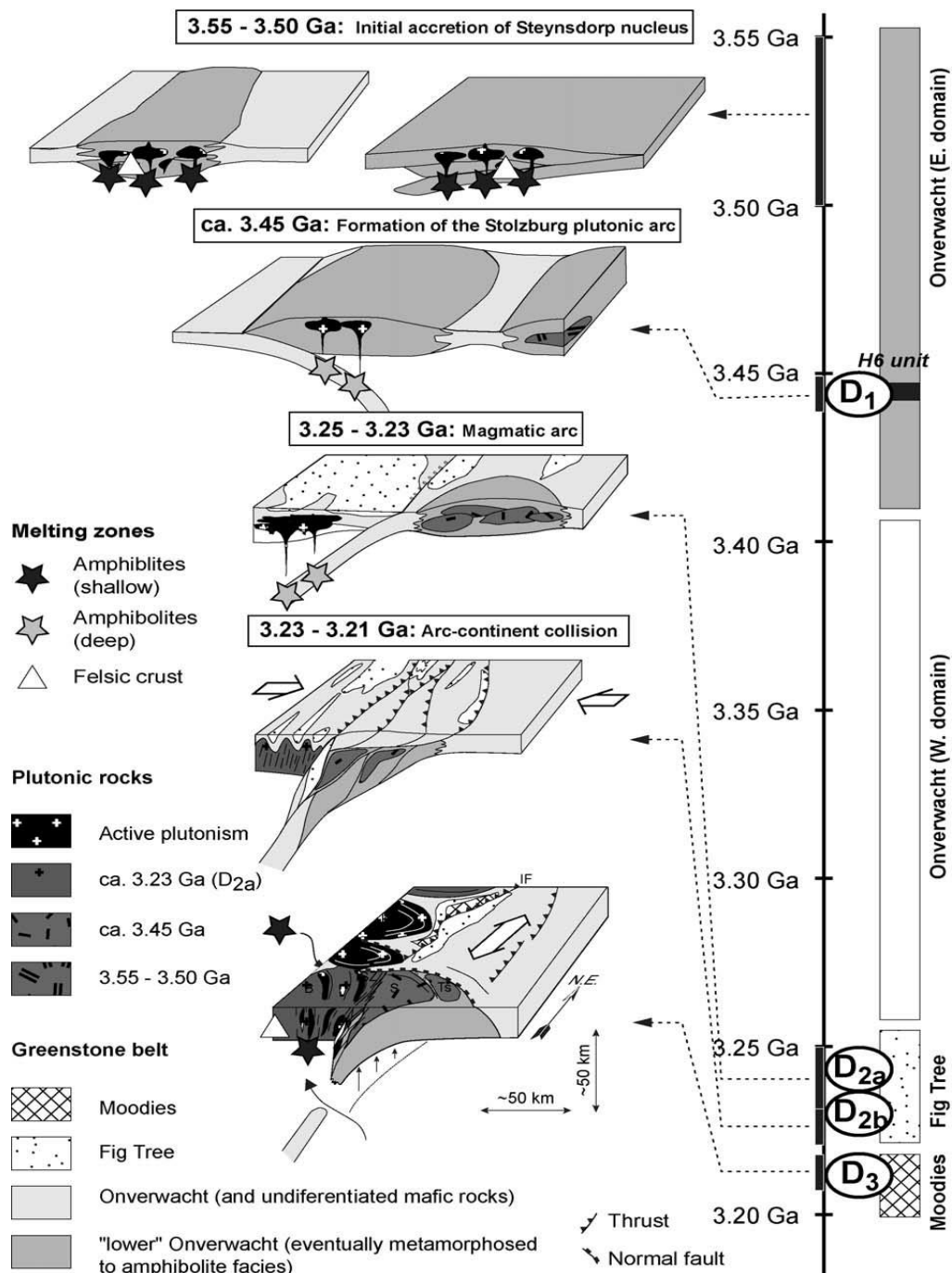


Figure 5.2 Geodynamic model of the evolution of the BGB from Moyén et al. (2007). Note: The top three figures are inspired from Lowe (1999)

None of the models, however, give an indication of the direction of subduction at 3.54 Ga. In this study it has been deduced that the coeval Toggekry Formation and Theespruit Complex

formed in separate back-arc basins. These could be related to separate subduction zones, giving rise to four possible models with regards to the direction of subduction (Fig 5.3).

In model 1 the BGB and NGB were formed in the coeval back-arc basins that formed as the result of northward directed subduction. The Ancient Gneiss Complex (AGC) lay on the southern side of the BGB subduction zone and was transported northwards. Its arrival at the trench would have cause subduction to cease. In model 2, subduction is directed southwards in both cases. Again, the AGC is between the two and this time is transported southwards to the NGB trench where it causes subduction to cease. In model 3 the two subduction zones dip in opposite directions. This would imply that the AGC was a micro-continent rifted during the lithospheric stretching that formed the intervening MOR. Model 4 has the two subduction zones dipping towards each other. In their present positions, this presents a space problem. However, it could be a possibility if they were originally well separated and then only brought closer during the ca. 3.2 Ga accretionary event.

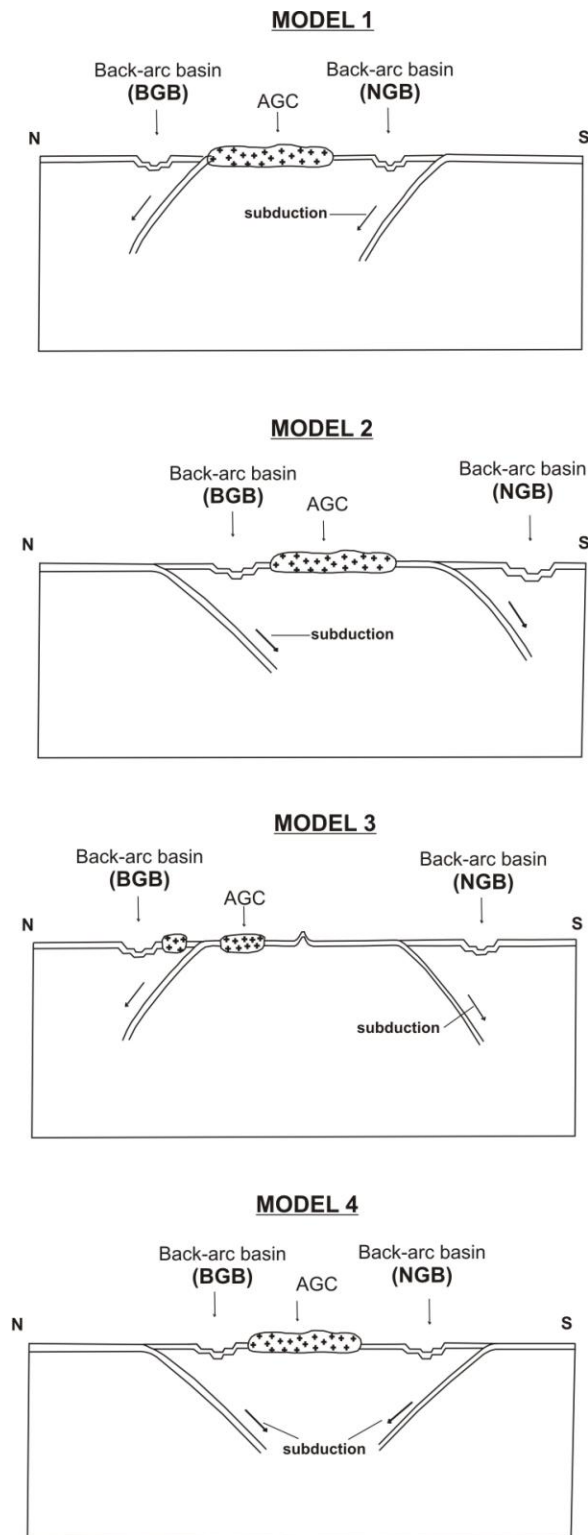


Figure 5.3 Models for the tectonic setting of the coeval Theespruit Complex, Barberton greenstone belt (BGB), and the Toggekry Formation, Nondweni greenstone belt (NGB). AGC (Ancient Gneiss Complex).

CHAPTER 6: CONCLUSIONS

The Nondweni greenstone belt contains sulphide mineralization hosted within quartz sericite schists of the Toggekry Formation. As rocks in this formation are 3.53 Ga in age (Xie et al. (2012), this is the oldest known occurrence of this type of mineralization. Therefore it is of interest to better understand its setting.

The schists have a calc-alkaline affinity while geochemical classification diagrams of immobile elements indicate a rhyolitic origin. Major element data and isocon diagrams indicate that the schists are MgO enriched with respect to typical rhyolite compositions. This elevated value may have been derived from adjacent ultramafic bodies (now serpentinites) that intruded prior to deformation of the greenstone belt (Versfeld and Wilson, 1992a). Isocon diagrams show decoupling of LREE and HREE. This may suggest that the protolith of the sericite schists could be a rock with lower HREE similar to the felsic schists from Xie et al. (2012).

The quartz-sericite schists show extensive alteration that is not present in the rhyolites and other units of the Toggekry Formation. In part this may have occurred during D₂ deformation and metamorphism, but the major reason is that the schists lie within the contact metamorphic aureole of the ca. 3230 Ma Mvunyana granodiorite.

It has been proposed that the overall tectonic setting for the Nondweni greenstone belt was a back-arc basin (Wilson and Versfeld, 1994b). This conclusion was based on the tholeiitic and calc-alkaline signatures of the mafic and felsic rocks. The same conclusion is reached from this present study in which AFM diagram indicate that the Nondweni rocks have tholeiitic and calc-alkaline signatures, while tectonic discrimination diagrams and primitive mantle normalized trace element diagrams suggest that the mafic rocks of the Toggekry and Witkop Formations are arc basalts.

The Toggekry lavas show enrichment in LREE relative to HREE on the primitive mantle normalized trace elements diagram. The enrichment in LREE relative to HREE is characteristic of crustal contamination and/or subduction zone magmas, enriched mantle source or small degrees of melting. The positive Pb anomalies and negative Nb-Ta are characteristic of subduction zone processes and indicate crustal involvement in the magma

process. The predominantly positive Epsilon Hf data suggest that the Toggekry Formation rocks were derived either from a depleted mantle source with contamination by older continental crust or from a depleted mantle at an earlier age followed by re-melting.

Taking all the evidence, it is concluded that the Toggekry Formation lavas were derived from depleted mantle with the magma undergoing a small amount of crustal contamination before being extruded in a back-arc basin in an aqueous environment. Riganti (1996) suggested that sialic crust already existed before the eruption of the Nondweni Group lavas based on the discovery of xenocrystic zircons older than the Nondweni Group. The results of the present study further strengthen this interpretation of an as yet unidentified pre-greenstone granitic crust being present in the area.

Similarities in sequences, age and composition of the Toggekry Formation and the Theespruit Complex indicate that both formed in back-arc basin environments at about ~ 3.54 Ga. However, multi-element variation diagrams reveal significant differences between the sequences. Significantly, the epsilon Hf diagram indicates that, whereas the Toggekry Formation lavas were derived from a depleted mantle with small degrees of crustal contamination according to this study, the Theespruit Complex lavas were derived from the melting of older felsic crust (Kroner et al, 2013). Given their geographical positions on the Kaapvaal craton this implies that, although the Toggekry Formation and Theespruit Complex are coeval, they probably formed in separate back-arc basins associated with different subduction zones. The peak metamorphic event, at 3230 Ma, with accompanying deformation and granite intrusion in both the Nondweni and the Barberton greenstone belts, reflects a later accretionary event during the development of the Kaapvaal craton.

A number of tectonic models were proposed for the evolution of the Kaapvaal craton ~3.54 Ga. The most probable models for the tectonic evolution of the craton ~3.54 Ga seems to be models 1 and 2 where both subduction zones dip in the same direction are considered. This is due to the fact that this situation is most common today, most notably around the northern and western rim of the Pacific Ocean. Model 2, with a southward dipping subduction zone beneath the AGC, seems more compatible with the Theespruit Complex being derived from pre-existing crust (Fig 6.1). This would be similar to the mature island arcs today, such as the Japanese arc, where the volcanic arc is developed on pre-existing continental crust while the back-arc basin resulted from rifting of that crust. In contrast, the Toggekry Formation would

be equivalent to the modern intra-oceanic subduction zone (Fig 6.1). In this model the arrival of the AGC at the NGB trench would cause subduction to cease there, whereas at the BGB subduction processes continue, giving rise to the younger stratigraphy preserved in that greenstone belt.

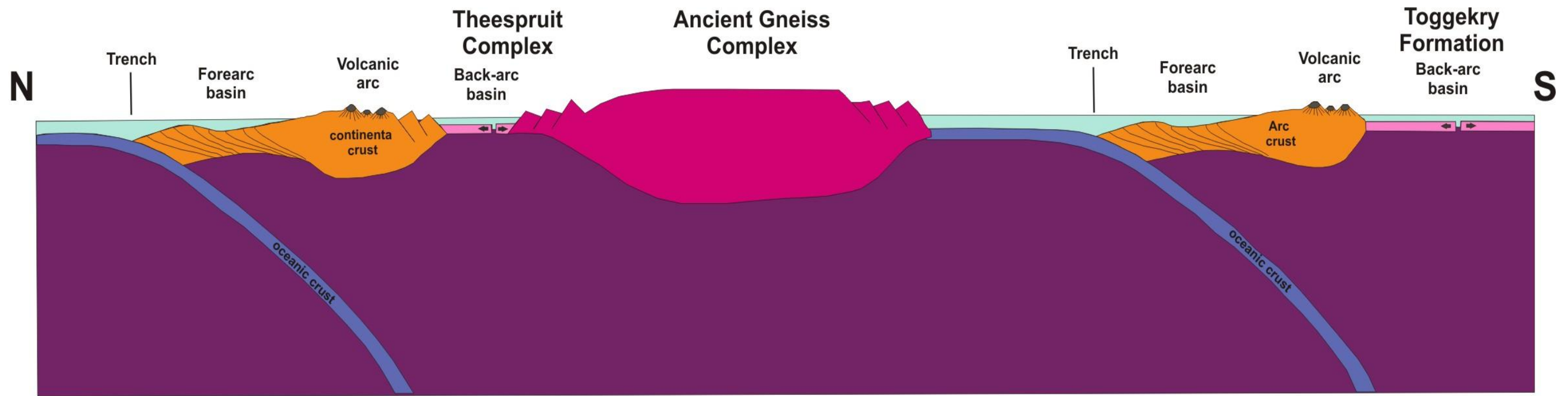


Figure 6.1 Tectonic setting at ~ 3.53 Ga of the Toggekry Formation and the Theespruit Complex.

ACKNOWLEDGEMENTS

The author would like to acknowledge Prof. Micheal Watkeys and Dr Marlina Elburg of the University of KwaZulu Natal for their assistance as supervisor and co-supervisor respectively. This dissertation would not have been possible without their supervision. Tom Anderson, from Oslo University, is greatly acknowledged for his contribution and assistance on the isotope analyses done for the samples. The author would also like to thank Prof Axel Hofmann and Dr Lopamudra Saha for their assistance and input.

The author would also like to thank Nokwanda Mkhize, Nonkululeko Dlala, Errol Wiles, Palesa Leuta-Madondo, Warwick Hastie and all other postgraduates from the School of Geological Sciences for their assistance and encouragement.

Sbongakonke Nqayi and Bongumusa Ngongo must be thanked for their support, advice, words of encouragement and friendship. Their presence in my life is too valuable and precious.

Other people who deserve credit are as follows:

- Mr. Mukesh Seyambu for preparing and cutting all thin section blocks used in this study
- Mr. Pat Sultan and the late Roy Seyambu for XRF and ICP-MS analyses
- Ms. Lulu Sephula for helping with sample preparations
- Mrs. Debbie Mackrory for continuous support and assistance
- Dr Andrew Green for his constant encouragement and advice.

Finally, I would like to thank my family, **Tholakele Jele**, Golden Jele, Bheki Mkhize, Nonhlanhla Mkhize, Ayanda Jele, Zanele Jele, Lucky Mantso, Gcinaphi Mantso, Siyabonga Jele and Mbali Jele. Thank you for all your help, support and love. This work is a product of your belief and faith in me. The amount of love and support you have given me mom is incredible. You are a blessing in my life. Last but not least I would like to thank my girlfriend Dr. Nomfundo “Fufutjie” Maphumulo for always being there for me during the for me and putting up with me during the tough and testing times. I could not have done this without you.

REFERENCES

- Bottazzi, P., Tiepolo, M., Vanucci, R., Zanetti, A., Brumm, R., Foley, S.F., and Oberti, R., 1999. Distinct site preferences for heavy and light REE in amphibole and the prediction of $A_{\text{Amph/L}}D_{\text{REE}}$. *Contributions to Mineralogy and Petrology*, **137**, 36-45.
- Brandl, G., Cloete, M., Anhaeusser, C.R., 2006. Archaean greenstone belts, In: Johnson, M.R., Anhaeusser, C.R., Thomas, R.J. (Eds.), *Geology of South Africa*. Geological Society of South Africa / Council for Geoscience. Pretoria, 461-500.
- Brandl, G. and M. J. De Wit (1997). The Kaapvaal Craton, South Africa, In De Wit, M.J and Ashwal, L.D. (Eds), *Greenstone Belts*. Oxford, Clarendon Press: 581-607.
- Burger, A.J., Walraven, F., Allsopp, H.L., 1980. Summary of age determinations carried out during the period April 1978 to March 1979. *Annals. Geological Survey of South Africa*, **14**, 109-118
- Byerly, G.R., 1999. Komatiites of the Mendon Formation: late-stage ultramafic volcanism in the Barberton Greenstone Belt. In: Lowe, D.R., Byerly, G.R. (Eds.), *Geologic Evolution of the Barberton Greenstone Belt, South Africa: Boulder, Colorado, Geological Society of America Special Paper*, **329**, 189–211.
- Byerly, G.R., Kröner, A., Lowe, D.R., Todt, W., Walsh, M.M., 1996. Prolonged magmatism and time constraints for sediment deposition in the early Archaean Barberton greenstone belt: evidence from the Upper Onverwacht and Fig Tree Groups. *Precambrian Research*, **78**, 125–138.
- Chavagnac, V. 2004. A geochemical and Nd isotopic study of Barberton komatiites (South Africa): implication for the Archean mantle. *Lithos*, **75**, 253–281.
- Compston, W. and A. Kröner (1988). Multiple zircon growth within early Archaean tonalitic gneiss from the Ancient Gneiss Complex, Swaziland. *Earth and Planetary Science Letters*, **87**, 13-28.
- Condie, K. C. (1981). *Archean Greenstone Belts*, Elsevier, Amsterdam: 425 pp

Condie, K. C., and Hunter, D. R., 1976. Trace element geochemistry of Archaean granitic rocks from the Barberton region, South Africa. *Earth and Planetary Science Letters*, **29**, 389-400.

Cox, K.G., Bell, J.D., Pankhurst, R.J., 1979. *The Interpretation of Igneous Rocks*. George Allen & Unwin Ltd, London: 450 pp.

Dann, J. C. 2000. The 3.5 Ga Komati Formation, Barberton Greenstone Belt, South Africa, part I: New maps and magmatic architecture. *South African Journal of Geology*, **103**, 47–68.

Dann, J.C. and Grove, T.L., 2007. Volcanology of the Barberton greenstone Belt, South Africa: inflation and evolution of flow fields. In: Van kranendonk, M.J., Smithies, R.H., Bennett, V.C. (Eds.), *Earth's Oldest Rocks. : Developments in Precambrian Geology*. Elsevier, Amsterdam, **15**, 527–570.

De Ronde, C. E. J. and M. J. De Wit (1994). Tectonic history of the Barberton Greenstone Belt, South Africa: 490 million years of Archaean crustal evolution. *Tectonics*, **13**, 983–1005.

De Wit, M.J., Fripp, R.E.P. and Stanistreet, I.G. (1983) Tectonic and stratigraphic implications of new field observations along the southern part of the Barberton Greenstone Belt, *Special Publication, Geological Society of South Africa*, **9**, 21 – 29

De Wit, M.J., Armstrong, R.A., Hart, R.J. and Wilson, A.H. (1987) Felsic igneous rocks within the 3.3 to 3.5 Ga Barberton Greenstone Belt: high-level equivalents of the surrounding tonalite trondhjemite terrain, emplaced during thrusting, *Tectonics*, **6**, 529 –549

De Wit, M. J. and Ashwal, L.D. (Eds), 1997. *Greenstone Belts*, Clarendon Press, Oxford, 809 pp

De Wit, M.J., Furnes, H., Robins, B., 2011. Geology and tectonostratigraphy of the Onverwacht Suite, Barberton Greenstone Belt, South Africa. *Precambrian Research*, **186**, 1-27.

De Wit, M. J. and R. A. Hart (1993). Earth's earliest continental lithosphere, hydrothermal flux, and crustal recycling. *Lithos*, **30**, 309-336.

De Wit, M.J., Roering, C., Hart, R.A., Armstrong, R.A., de Ronde, C.E.J., Green, R.W.E., Tredoux, M., Peberdy, E., Hart, R.A., 1992. Formation of an Archean continent. *Nature*, **357**, 553-562.

Denier, J. F. A. (2004). *The Tectono-Metamorphic Evolution of the Theespruit Formation in the Tjakastad Schist Belt and Surrounding Areas of the Barberton Greenstone Belt, South Africa*. University of Stellenbosch. MSc dissertation (unpubl.): 210 pp.

Diener, J.F.A., Stevens, G., Kisters, A.F.M., Poujol, M., 2005. Metamorphism and exhumation of the basal parts of the Barberton greenstone belt, South Africa: constraining the rates of Mesoproterozoic tectonism. *Precambrian Research*, **143**, 87-112.

Duncan A. R. & Marsh, J. S., 2006. The Karoo Igneous Province. In: Johnson, M.R., Anhaeusser, C.R., Thomas, R.J. (Eds.), *Geology of South Africa*. Geological Society of South Africa / Council for Geoscience. Pretoria, 501-520.

Du Toit, A. L. (1931). *The Geology of the Country Surrounding Nkandla, Natal*. An explanation of Sheet 109 (Nkandla), Department of Mines and Industry. Union of South Africa, Government Printer Pretoria, : 111 pp.

Dziggel, A., Stevens, G., Poujol, M., Anhaeusser, C.R. and Armstrong, R.A. (2002) Metamorphism of the granite-greenstone terrane south of the Barberton greenstone belt, South Africa: an insight into the tectono-thermal evolution of the 'lower' portions of the Onverwacht Group. *Precambrian Research*, **114**, 221 – 247

Furnes, H., De Wit, M.J., Robins, B. (2013). A review of new interpretations of the tectonostratigraphy, geochemistry and evolution of the Onverwacht Suite, Barberton Greenstone Belt, South Africa. *Gondwana Research*, **23**, 403-428

Gold, D. J. C. (2006). The Pongola Supergroup. In: Johnson, M.R., Anhaeusser, C.R., Thomas, R.J. (Eds.), *Geology of South Africa*. Geological Society of South Africa / Council for Geoscience. Pretoria: 135-148.

- Gutzmer, J., Nhleko, N., Beukes, N.J., Pickard, A., Barley, M.E., 1999. Geochemistry and ion microprobe (SHRIMP) age of a quartz porphyry sill in the Mozaan Group of the Pongola Supergroup: Implications for the Pongola and Witwatersrand Supergroup. *South African Journal of Geology*, **102**, 139-146.
- Hatch, F. H. (1910). Report on the mines and minerals resources of Natal (other than coal), R. Clay and Sons Ltd., London: 142 pp.
- Hegner, E., Kröner, A., Hunt, P., 1994. A precise U-Pb zircon age for the Archaean Pongola Supergroup volcanics in Swaziland. *Journal of African Earth Sciences*, **18**, 339-341.
- Hofmann, A. and C. Harris (2008). Silica alteration zones in the Barberton greenstone belt: A window into subseafloor processes 3.5–3.3 Ga ago. *Chemical Geology*, **257**, 221-239.
- Hofmann, A. and A. H. Wilson (2007). Silicified Basalts, Bedded Cherts and Other Sea Floor Alteration Phenomena of the 3.4 Ga Nondweni Greenstone Belt, South Africa. In: Van Kranendonk, M. J., Smithies, R. H. & Bennett, V. C. (Eds), *Earth's Oldest Rocks. Developments in Precambrian Geology*. Elsevier. Amsterdam. The Netherlands: 571-606.
- Holland, T.J.B. and Powell, R., 1998. An internally consistent thermodynamic data set for phases of petrological interest. *Journal of Metamorphic Geology*, **16**, 309-343.
- Hoskin, P.W.O., and Black, L.P., 2000. Metamorphic zircon formation by solid state recrystallization of protolith igneous zircon: *Journal of Metamorphic Geology*, **18**, 423-439.
- Irvine, T. N. and W. R. A. Baragar (1971). A guide to the chemical classification of the common volcanic rocks. *Canadian Journal of Earth Sciences*, **8**, 523-548.
- Johnson, M.R., Van Vuuren, C.J., Visser, J.N.J., Cole, D.I., Wickens, H.d.V., Christie, A.D.M., Roberts, D.L., Brandl, G., 2006. Sedimentary Rocks of the Karoo Supergroup., In: Johnson, M.R., Anhaeusser, C.R., Thomas, R.J. (Eds.), *Geology of South Africa*. Geological Society of South Africa / Council for Geoscience., Pretoria: 461-500.
- Kinny, P.D., and Maas, R., 2003. Lu-Hf and Sm-Nd isotope systems in zircon, in Hanchar, J.M., and Hoskin, P.W.O., (Eds), *Zircon: Mineralogical Society of America Reviews in Mineralogy and Geochemistry*, **53**, 327–341.

Kisters, A.F.M. and Anhaeusser, C.R., 1995. Emplacement features of Archaean TTG plutons along the southern margin of the Barberton greenstone belt, South Africa. *Precambrian Research*, **75**, 1–15.

Kohler, E. A. and C. R. Anhaeusser (2002). Geology and geodynamic setting of Archaean silicic metavolcanics of the Bien Venue Formation, Fig Tree Group, northeast Barberton greenstone belt, South Africa. *Precambrian Research*, **116**: 199-235.

Kröner, A., Compston, W., Williams, I.S., 1989. Growth of early Archaean crust in the Ancient Gneiss Complex of Swaziland as revealed by single zircon dating. *Tectonophysics*, **161**, 271-298.

Kröner, A., Hegner, E., Wendt, J.I., Byerly, G.R., 1996. The oldest part of the Barberton granitoid-greenstone terrain, South Africa: evidence for crust formation between 3.5 and 3.7 Ga. *Precambrian Research*, **78**, 105-124.

Kröner, A. and A. Tegtmeier (1994). Gneiss-greenstone relationships in the Ancient Gneiss Complex of southwestern Swaziland, southern Africa, and implications for early crustal evolution. *Precambrian Research*, **67**, 109-139.

Kröner, A., Hoffmann, J.E., Xie, H., Wu, F., Münker, C., Hegner, E., Wong, J., Wan, J., Liu, D., 2013. Generation of early Archaean felsic greenstone volcanic rocks through crustal melting in the Kaapvaal, craton, southern Africa. *Earth and Planetary Science Letters*, **381**, 188-197

Le Bas, M.J., LeMaitre, R.W., Streckeisen, A.L., Zanettin, B., 1986. A chemical classification of volcanic rocks based on the total alkali-silica diagram. *Journal of Petrology*, **27**, 745-750.

Linstrom, W. (1987). The Geology of the Dundee Area. Explanation of Sheet 2830. *Geological Survey of South Africa*. Government Printer, Pretoria: 52pp.

Lowe, P.E. (1994). Accretionary history of the Archaean Barberton Greenstone Belt (3.55-3.22 Ga), Southern Africa. *Geology*, **22**: 1099-1102.

Lowe, D. R. and G. R. Byerly (1999). Stratigraphy of the west-central part of the Barberton Greenstone Belt, South Africa. In Lowe, D. R. and G. R. Byerly (Eds). *Geologic Evolution of the Barberton Greenstone Belt, South Africa*. Special Paper, *Geological Society of America*, **329**, 1-36.

Mathe, H. L. M. (1997). *Tectonostratigraphy, structure and metamorphism of the Archaean Ilangwe granite-greenstone belt south of Melmoth, KwaZulu Natal*. University of Natal, Durban. PhD dissertation (unpubl.): 365 pp.

Matthews, P. E. (1959). The metamorphism and tectonics of the pre-Cape formations in the post-Ntingwe thrust-belt, S.W. Zululand, Natal. *Transactions of the Geological Society of South Africa*, **62**: 257-322.

Matthews, P.E., Charlesworth, E.G., Englington, B.M., Harmer, R.E., 1989. A minimum 3.29 age for the Nondweni greenstone complex in the south-eastern Kaapvaal Craton. *South African Journal of Geology*, **92**, 272-278.

Pearce, J. A. (1996). A user's guide to basalt discrimination diagrams. *Trace Element Geochemistry of Volcanic Rocks: Applications for Massive Sulphide Exploration*. D. A. Wyman (Ed), Geological Association of Canada, Short Course Notes, **12**, 79-113.

Pearce, J. A. and J. R. Cann (1973). Tectonic setting of basic volcanic rocks determined using trace element analyses. *Earth and Planetary Science Letters*, **19**, 290-300.

Poller, U., Huth, J., Hoppe, P., 2001. REE, U, Th, and Hf distribution in zircon from Western Carpathian Variscan granitoids: a combined cathodoluminescence and ion microprobe study. *American Journal of Science*, **301**, 858-876.

Poujol, M., Robb, L.J., Anhaeusser, C.R., Gericke, B., 2003. A review of the geochronological constraints on the evolution of the Kaapvaal Craton, South Africa. *Precambrian Research*, **127**, 181-213.

Ramsay, J.G., (1967). *Folding and Fracturing of Rocks*. McGraw-Hill Book Company, New York, 560pp

Riganti, A. (1996). The Northern Segment of the Early Archaean Nondweni Greenstone Belt, South Africa. Field Relationships and Petrogenetic Constraints, University of Natal, Pietermaritzburg. Ph.D thesis (unpubl.): 383 pp.

Riganti, A. and A. H. Wilson (1995). Geochemistry of the mafic/ultramafic volcanic associations of the Nondweni greenstone belt, South Africa, and constraints on their petrogenesis. *Lithos*, **34**, 235-252.

Robb, L.J., Brandl, G., Anhaeusser, C.R., Poujol, M., 2006. Archaean Granitoid Intrusions. In: Johnson, M.R., Anhaeusser, C.R., Thomas, R.J. (Eds.), *Geology of South Africa*. Geological Society of South Africa / Council for Geoscience., Pretoria: 57-94.

Rollinson, H. R. (1993). *Using Geochemical Data: Evaluation, Presentation, Interpretation*. Harlow, Prentice Hall, 352 pp

Rollinson, H. R. (2009). *Early Earth Systems: A Geochemical Approach*. Wiley-Blackwell. Oxford, 296 pp

Rouchon, V. and B. Orberger (2008). Origin and mechanisms of K–Si-metasomatism of ca. 3.4–3.3 Ga volcanoclastic deposits and implications for Archean seawater evolution: Examples from cherts of Kittys Gap (Pilbara craton, Australia) and Msauli (Barberton Greenstone Belt, South Africa). *Precambrian Research*, **165**, 169-189.

Saha, L., Hofmann, A., Xie, H., Hegner, E., Wilson, A., Wan, Y., Lui, D. and Kröner, A., 2010. Zircon ages and metamorphic evolution of the Archaean Assegai-De Kraalen granitoid-greenstone terrain, Southeastern Kaapvaal Craton. *American Journal of Science*, **310**, 1384-1420

Saha, L., Hofmann, A., Jele, N., Harris, C., 2012. Palaeoarchaeoan sea-floor alteration and metamorphism of pillow basalts from the Nondweni Greenstone Belt, SE Kaapvaal Craton. *South African Journal of Geology*, **115**, 259-282.

Sugitani, K., Yamamoto, K., Wada, H., Binu-Lal, S.S., Yoneshige, M., 2002. Geochemistry of Archean carbonaceous cherts deposited at immature island-arc setting in the Pilbara Block, Western Australia. *Sedimentary Geology*, **151**, 45-66.

- Sun, S. S. and W. F. Mc Donough (1989). Chemical and isotopic systematics of oceanic basalts, implications for mantle composition and processes. *Magmatism in Ocean Basins*. A. D. Saunders and M. J. Norry (Eds). Special Publication, *Geological Society of London*, **42**, 313-435.
- Sun, S. S. and W. F. Mc Donough (1995). The composition of the Earth. *Chemical Geology*, **120**, 223-254
- Tice, M. M. and D. R. Lowe (2006). The origin of carbonaceous matter in pre-3.0 Ga greenstone terrains: a review and new evidence from the 3.42 Ga Buck Reef chert. *Earth-Science Reviews*, **76**, 259-300.
- Truter, F.C. (1950). A review of volcanism in the geological history of South Africa. *Proceedings of the Geological Society South Africa*, **52**, xxix-lxxxix.
- Van Den Boorn, S.H.J.M., van Bergen, M.J., Vroon, P.Z., de Vries, S.T., Nijman, W. 2010. Silicon isotope and trace element constraints on the origin of ~3.5 Ga cherts: implications for Early Archaean marine environments. *Geochimica et Cosmochimica Acta*, **74**, 1077-1103.
- Van Den Kerkhof, A.M., Kronz, A., Simon, K., Riganti, A., Scherer, T., 2004. Origin and evolution of Archean quartzites from the Nondweni greenstone belt (South Africa): inferences from a multidisciplinary study. *South African Journal of Geology*, **107**, 559-576.
- Van Kranendonk, M.J., 2011. Cool greenstone drips and the role of partial convective overturn in Barberton Greenstone Belt evolution. *Journal of African Earth Sciences*, **60**, 346–352.
- Van Kranendonk, M.J., Kröner, A., Hegner, E., Connelly, J., 2009. Age, lithology and structural evolution of the c. 3.53 Ga Theespruit Formation in the Tjakastad area, southwestern Barberton Greenstone Belt, South Africa, with implications for Archaean tectonics. *Chemical Geology*, **261**, 115-139.
- Versfeld, J. A. (1988). *The Geology of the Nondweni Greenstone Belt, Natal*, University of Natal, Pietermaritzburg. PhD dissertation (unpubl.): 299 pp.
- Versfeld, J. A. and A. H. Wilson (1992). Nondweni Group. *Catalogue of South African Stratigraphy Units*. South African Commission for Stratigraphy. **4**: 19-20.

- Viljoen, M.J., Viljoen, R.P., 1969a. The geology and geochemistry of the lower ultramafic unit of the Onverwacht Group and a proposed new class of igneous rocks. *Geological Society of South Africa, Special Publication*, **2**, 55–86.
- Watkeys, M. K. (1981). Report on a visit to the Nondweni Greenstone Belt. Unpublished Report for Anglo-American Prospecting Services. 19 pp
- Williams, I.S., Shah, J.S., Stowe, S., 1996. Elemental and isotopic microanalysis of zircons and backscattered electron contrast. *Proceedings of the 6th European Conference on Applications of Surface and Interface Analysis*, 1007-1010.
- Wilson, A. H. and Versfeld, J.A. (1994a). The early Archaean Nondweni Greenstone Belt, southern Kaapvaal Craton, South Africa, Part I. Stratigraphy, sedimentology, mineralization and depositional environment. *Precambrian Research*, **67**, 243-276.
- Wilson, A. H. and Versfeld, J.A. (1994b). The early Archaean Nondweni Greenstone belt, southern Kaapvaal Craton, South Africa, Part II. Characteristics of the volcanic rocks and constraints on magma genesis. *Precambrian Research*, **67**, 277-320.
- Wilson, A. H. and Carlson, R.W., (1989). A Sm-Nd and Pb isotope study of Archaean greenstone belts in the southern Kaapvaal Craton, South Africa. *Earth and Planetary Science Letters*, **96**, 89-105.
- Winchester, J. A. and Floyd, P.A., (1977). Geochemical discrimination of different magma series and their differentiation products using immobile elements. *Chemical Geology*, **20**, 325-343.
- Wood, D.A., Joron, J.L., Treuil, M., 1979. A re-appraisal of the use of trace elements to classify and discriminate between magma series erupted in different tectonic settings. *Earth and Planetary Science Letters*, **45**, 326-336.
- Xie, H., Hofmann, A., Hegner, E., Wilson, A., Wan, Y., Liu, D., 2012. Zircon SHRIMP dating confirms a Palaeoarchean supracrustal terrain in the southeastern Kaapvaal Craton, southern Africa. *Gondwana Research*, **21**, 818-828.

GEOCHEMISTRY LEGEND

-  Quartz-sericite schists
-  Basaltic andesites
-  Andesites
-  Rhyolite
-  Witkop basalts
-  Q-F porphyry
-  Felsic schists from Xie et al. (2012)

APPENDIX 1: ANALYTICAL METHODS

ANALYTICAL METHODS

1. Field work and sampling

Field work was carried out by the Author over a period of 4 months and involved producing a geological map of the Toggekry and Mount Vernon farms (appendix 5) and sample collection for laboratory analysis. A total of 57 Samples were collected during the course of the mapping for laboratory analysis (Appendix 2).

2. Sample preparation

The 57 collected samples were cut clean using the diamond coated rock saw and then stored in clean plastic bags. The samples were cut to small blocks so that they could feed into the jaw crusher some were kept for polished section preparations. These blocks were ultrasonically washed for 10 minutes and then rinsed using distilled water. After samples had been washed they were completely dried in the oven for a period of 2 hours at a temperature of 110⁰C. From the oven samples were allowed to cool and then crushed to smaller fractions using a hardened steel jaw crusher. In between the sample crushing the jaw crusher had to be cleaned using a steel brush and acetone and vacuum cleaner. To get representative reduced sample sizes for milling, the crushed samples first had to be coned and quartered.

The crushed samples were then sieved in a 500 µm and then 425 µm sieves to ensure that only the material which is 425µm or less was left. The fine material underwent further separation. The sieved particles wash put in glass beakers and water was added to it "Floatation". The lights less dense minerals and clay sized particles floating in the water were washed out. The process was repeated until certainty that the clay sized material was removed from the samples. The samples were oven dried and allowed to cool then placed in airtight labelled sample bags. These samples were sent to the University of Oslo in Norway. At the University of Oslo zircon and monazite grains were selected for U-Pb and Hf isotope analysis.

For XRF, ICP-MS and XRD analysis, the final stage of the preparation involved milling the crushed fractions to a fine powder for about 3 minutes using a carbon steel swing mill. Great care was taken in preventing contamination, thus cleaning the mill between samples was done using a steel brush, vacuum and acetone. After 3 samples the mill was cleaned with quartz to avoid contamination of samples by residue left in the mill. The milled fine powders were stored in sealed plastic bags to minimise contamination. The sample preparation work was done by the author at the School of Geological Sciences at the University of Kwa-Zulu Natal Westville campus.

3. Petrography (Thin section and BSE)

Polished sections were prepared for representative samples

Carefully selected cut blocks were forwarded to Mr M. Seyambu for polished section preparation. A petrographic description was carried out using a transmitted light microscope to determine mineralogy, alteration and texture of the samples. Samples were carbon coated and analysed using the LEO 1450 and BSE images were acquired at the University of Kwa-Zulu Natal Westville campus Electron Microscope unit. See Appendix 6

4. X-ray Fluorescence (XRF) Spectrometry

Whole rock analysis for major and trace elements using XRF spectrometry was conducted in the School of Geological Sciences at the University of Kwa-Zulu Natal. The XRF analyses were carried out using a Phillips X'Unique spectrometer. Major and trace elements were obtained using fused glass discs and pressed powder pellets.

To make fused glass discs, silica crucibles were cleaned in a diluted solution of HCL. Approximately 0.5 g of sample was weighted into the silica crucibles and dried at 100°C. These crucibles were placed in a furnace at 1000°C for 4 hours, then removed and allowed to cool in the desiccators. The spectroflux used in Pt crucibles at 1000°C, and approximately 0.4 g of the ashed sample was added as close to the ratio weight sample/ weight flux = 2.2 as possible. The samples were fused at 1000°C and the product cast in brass die maintained at 250°C. Discs were annealed approximately 3 hours on a heated asbestos plate and then allowed to cool gradually. The flux was Johnson Matthey Spectroflux 105. Each new batch of flux was homogenized and a new set of standards made up. Fusion discs were then stored separately in sealed plastic bags.

To make pressed powder pellets approximately 0.45 g of finely milled sample was mixed with 0.3 ml of Mowiol and homogenized using a mortar and pestle. The sample was then placed into a metal die (position cylinder) and then compressed to a pellet. The pellets were hardened in an oven at 110°C for 3-4 hours. Ragged edges were trimmed off the pellets. Contact with the surface to be radiated was avoided. The pellets were then stored in airtight containers.

Instrument calibration was controlled with international standards and internal synthetic standards and blanks. International standards used were DTS-1, PCC-1, W-1, BCR-1, G-2, AGV, NIM-G, NIM-P, NIM-D, NIM-S, NIM-L, BHVO, and DRN.

5. Inductively Coupled Plasma-Mass Spectrometry(ICP-MS)

Trace elements were analyzed using the ICP-MS at the Geological Sciences at the University of Kwa-Zulu Natal. The analyses were conducted using a Perkin-Elmer Elan 6100 ICP-MS. 50 mg of sample powder was dissolved using HF and HNO₃ in an Anton-Paar Multiwave high pressure and temperature microwave digester with 40 minutes digestion times and evaporated to dryness in Teflon beakers. The digested samples were analysed in 5% HNO₃. 103Rh, 115In, 187Re and 209Bi were used as internal standards and calibration solutions were prepared from certified single and multi-element standard solutions. Only high purity bottle-distilled acids and water were used. Quality of data was monitored using the international standards BCR-1, BHVO-1 and BIR-1.

6. Isotope Analysis

The selected grains were mounted in epoxy and polished for analysis. U–Pb dating and Lu–Hf isotope analysis were performed by ICPMS using a Nu Plasma HR multicollector system with a U–Pb collector block and a New Wave/Merchantek LUV-213 laser microprobe at the Department of Geosciences, University of Oslo by **professor Tom Andersen**. U–Pb ages and Hf isotope data were determined separately on adjacent spots, using laser operating conditions that secured ‘soft’ ablation and preservation of the un-ablated part of the zircon.

Note: The analytical procedures presented below were taken directly from Andersen et al.(2012) and Elburg (in press)

Lu-Hf isotope analysis

Masses 172 to 179 were measured simultaneously in Faraday collectors, using the Nu Plasma U-Pb collector block. Laser ablation conditions are: 55-60 µm static spot (aperture imaging mode), 5 Hz pulse frequency and ca. 2 J/cm² beam fluence. Each ablation was preceded by a 30 seconds on-mass background measurement. The total Hf signal obtained was in the range

1.5-4.0 V, and rarely as high as 6 V. Under these conditions, 120-150 seconds of ablation are required to obtain an internal precision of $\leq \pm 0.000020$ (1SE).

Isotope ratios were calculated using the Nu Plasma time-resolved analysis software. The raw data were corrected for mass discrimination using an exponential law, and the mass discrimination factor for Hf (f_{Hf}) was determined assuming $^{179}\text{Hf}/^{177}\text{Hf} = 0.7325$ (Patchett and Tatsumoto, 1980). The invariant ratio $^{178}\text{Hf}/^{177}\text{Hf}$ was monitored during analytical sessions to monitor the quality of the data.

In order to obtain precise $^{176}\text{Hf}/^{177}\text{Hf}$ results, the isobaric interference from ^{176}Lu and ^{176}Yb on ^{176}Hf must be corrected. For a zircon with an average $^{176}\text{Yb}/^{177}\text{Hf} = 0.04$, the total signal on mass 176 consists of about 87% ^{176}Hf , 13% ^{176}Yb and 0.2% ^{176}Lu , while for a REE-rich zircon with $^{176}\text{Yb}/^{177}\text{Hf} = 0.25$ the numbers will be 53%, 46.3% and 0.7% respectively. ^{176}Lu is calculated from the interference-free ^{175}Lu using $^{176}\text{Lu}/^{175}\text{Lu} = 0.02655$ (Vervoort et al., 2004) and $f_{\text{Hf}} \cdot ^{176}\text{Yb}$ is calculated from ^{172}Yb and the ratio $^{176}\text{Yb}/^{172}\text{Yb} = 0.58715$ and the Yb mass discrimination factor (f_{Yb}). There are several possible Yb isotope ratios that can be used to calculate the f_{Yb} value; Yuan et al. (2008). Yuan et al., (2008) found that $^{173}\text{Yb}/^{171}\text{Yb}$ gave a better relative standard deviation for the calculated f_{Yb} than $^{173}\text{Yb}/^{172}\text{Yb}$ and $^{172}\text{Yb}/^{171}\text{Yb}$. The geometry of the Nu Plasma U-Pb collector block does not allow simultaneous measurement of mass 171 with the other masses of interest, therefore using the $^{173}\text{Yb}/^{171}\text{Yb}$ ratio for calculating f_{Yb} is not an option.

The mass discrimination factor f is defined by the expression $f = \frac{\log R_i / \log R_o}{\log(M_1 / M_2)}$, where R_i is

a true, stable isotope ratio, R_o the corresponding observed value and M_1 and M_2 the masses of the isotopes ($M_1 > M_2$). In this expression, only R_o is subject to analytical error (s_{R_o}), and the resulting error in f (s_f) is given by: $s_f = \frac{s_{R_o}}{R_o \log(M_1 / M_2)}$. Assuming that two different stable

isotope ratios of an element (R_1, R_2) can be measured with comparable internal precision, the ratio of uncertainties in mass discrimination factors calculated from the two pairs of isotopes

will be given by $\frac{s_{f_1}}{s_{f_2}} = \frac{R_1 \log(M_{1,2} / M_{2,2})}{R_2 \log(M_{1,1} / M_{2,1})}$, where isotopes with masses $M_{1,i}$ and $M_{2,i}$ are used

to calculate f_1 , and $M_{2,1}$ and $M_{2,2}$ to calculate f_2 . An optimal value for f can therefore be determined from pairs of isotopes for which values of both R and M_1/M_2 are as high as possible.

Calculating f_{Yb} from the $^{174}\text{Yb}/^{172}\text{Yb}$ ratio gives an advantage in theoretical error of 75% compared to using the $^{173}\text{Yb}/^{172}\text{Yb}$ ratio, but is complicated by the isobaric overlap between

^{174}Yb and ^{174}Hf . For an average zircon the 174 mass will be 7% Hf and 93% Yb, and for the REE-rich case 1.4% Hf and 98.6% Yb. Stripping ^{174}Hf from ^{174}Yb is a much smaller correction than the ^{176}Hf isobaric correction. ^{174}Hf is calculated from the ratio $^{174}\text{Hf}/^{177}\text{Hf} = 0.008658$ (Thirlwall and Anczkiewicz, 2004) and used for peak stripping ^{174}Yb before calculating f_{Yb} from $^{174}\text{Yb}/^{172}\text{Yb} = 1.46182$.

The Yb isotope ratios used ($^{174}\text{Yb}/^{172}\text{Yb} = 1.46182$ and $^{176}\text{Yb}/^{172}\text{Yb} = 0.58715$) are in-house values. These values give the best fit for repeated runs of LV-11, which is a 10 mm euhedral crystal from the nepheline syenite pegmatite at Låven island in the Oslo Rift (290 Ma, source: Mineralogical collection of the Natural History Museum collection, University of Oslo). This crystal has a range of $^{176}\text{Yb}/^{177}\text{Hf}$ from 0.075 to 0.45 and solution analysis give a present-day $^{176}\text{Hf}/^{177}\text{Hf} = 0.282837 \pm 28$ (Heinonen et al., 2010). A summary of the data obtained on standard zircons by the method outlines here is given in Table 1.

U-Pb isotope analysis

For zircon U-Pb dating, Masses 204, 206 and 207 were measured in secondary electron multipliers, and 238 in the extra high mass Faraday collector of the Nu Plasma U-Pb collector block. The geometry of the collector block does not allow simultaneous measurement of ^{208}Pb and ^{232}Th . ^{235}U was calculated from the signal at mass 238 using natural $^{238}\text{U}/^{235}\text{U} = 137.88$. Laser conditions were beam diameter 40 μm in aperture imaging mode, pulse frequency 10 Hz and beam energy density c. 0.06 J cm^{-2} . Each U-Pb analysis comprised 30 s of on-mass background measurement, followed by 60 s of ablation.

Mass number 204 was used as a monitor for common ^{204}Pb . In an ICPMS analysis, ^{204}Hg originating from the argon supply contaminates mass 204, giving a background counting-rate of c. 1000 c.p.s. The contribution of ^{204}Hg from the plasma was eliminated by on-mass background measurement prior to each analysis. At the low laser energy used, there was no increase in signal at mass 204 during ablation of reference zircons such as 91500 or GJ-1, which contain negligible common lead. This suggests that there is no excess ionization of ^{204}Hg from the gas supply during ablation, so that the on-mass background measurement is representative for the conditions during analysis. Where necessary, the observed signals at masses 206 and 207 were corrected for common ^{206}Pb and ^{207}Pb after integration of the signal, using observed ^{204}Pb and average common-lead composition given by the Stacey & Kramers (1975) global lead evolution curve at the uncorrected $^{206}\text{Pb}/^{238}\text{U}$ age.

Raw data from the mass spectrometer were reduced to U and ^{206}Pb concentrations and U-Pb isotope ratios by a sample standard bracketing routine similar to that of Jackson et al. (2004). Output files from the Nu Plasma Time Resolved Analysis software were imported into an in-

house Microsoft Excel interactive spreadsheet program for background subtraction and correction for mass bias, laser-induced U–Pb fractionation and instrumental drift. Background-corrected signals for mass numbers 204, 206, 207 and 238 and the $^{207}\text{Pb}/^{206}\text{Pb}$, $^{206}\text{Pb}/^{238}\text{U}$ and $^{207}\text{Pb}/^{235}\text{U}$ isotope ratios were plotted as traces of observed voltage and voltage ratios against ablation time. This allows homogeneous parts of the run to be interactively selected for integration. The procedure for correction of laser-induced fractionation follows that of Jackson et al. (2004). A series of analyses consists of blocks of c. 10 unknowns, bracketed by 2–4 analyses of a concordant zircon of known age and U–Pb composition. To compensate for drift in instrument sensitivity and Faraday v. electron multiplier gain during an analytical session, a linear correlation of signal v. time was assumed for each group of reference zircon ablations. Isotopically homogeneous segments of the time-resolved traces were calibrated against the corresponding time-interval for each mass in the reference zircon, recalculated to the time of analysis of the unknown. The first signal received at the detector serves as zero-point for time for each ablation. The errors reported for isotopic ratios were calculated using standard error propagation formulae (Taylor 1997), and incorporate contributions from counting statistics on backgrounds and signals for standards and unknowns, as well as the uncertainties of the published compositions of reference zircons.

The zircons used for calibration included international zircon standards GJ-01 ($^{207}\text{Pb}/^{206}\text{Pb}$ age = 609 ± 1 Ma) Belousova et al. (2006), 91500 ($^{207}\text{Pb}/^{206}\text{Pb}$ age = 1065 ± 1 Ma) Wiedenbeck et al. (1995) and Temora-2 (417 ± 1 Ma), Black et al. (2003); and a multi-grain zircon separate from sample A382, Voinsalmi hypersthene granite, Finland, that has an average age of 1877 ± 2 Ma by isotope dilution (ID)-TIMS U–Pb. Eighty-seven LAM-ICPMS ablations on 91500 calibrated against Temora-2 gave an average age of 1059 ± 4 Ma. The long-term (>2 years) precision is <1% for $^{206}\text{Pb}/^{238}\text{U}$ and $^{207}\text{Pb}/^{206}\text{Pb}$ (2SD). IsoplotEx 4.15 (Ludwig 2008) was used to plot concordia diagrams.

For monazite U–Pb dating, masses 204, 206 and 207 were measured in secondary electron multipliers, and 238 in the extra high mass Faraday collector of the Nu Plasma U–Pb collector block. ^{235}U was calculated from the signal at mass 238 using natural $^{238}\text{U}/^{235}\text{U}=137.88$. Laser conditions were: Beam diameter: 40 μm in aperture imaging mode, pulse frequency: 10 Hz, beam energy density: ca. 0.06 J/cm². At these conditions, the depth-to-diameter ratio of the ablation pits remained low, and laser-induced elemental fractionation was minimized. Each U–Pb analysis comprised 30 seconds of on-mass background measurement, followed by 60 seconds of ablation with a stationary beam.

Mass number 204 was used as a monitor for common ^{204}Pb . In an ICPMS analysis, ^{204}Hg originating from the argon supply contaminates mass 204, giving a background counting-rate of ≤ 1000 cps. The contribution of ^{204}Hg from the plasma was eliminated by on-mass background measurement prior to each analysis. Analyses that yielded peak/background ratios at mass 204 of less than $1+3\text{RSDB}$ (where RSDB is the observed relative standard deviation of the on-peak background measurement) were considered to have common lead below the detection limit. At the low laser energy used, there was no observable increase in signal at mass 204 during ablation of reference zircons such as 91500 or GJ-1, which contain negligible common-lead. This suggests that there is insignificant excess ionization of ^{204}Hg from the gas supply during ablation, so that the on-mass background measurement is representative for the conditions during analysis. Where necessary, the observed signals at masses 206 and 207 were corrected for common ^{206}Pb and ^{207}Pb after integration of the signal, using observed ^{204}Pb and average common-lead composition given by the Stacey & Kramers (1975) global lead evolution curve at the uncorrected $^{206}\text{Pb}/^{238}\text{U}$ age.

Monazite analyses were standardised to the B0109 monazite from Hisøy, Norway, analysed by TIMS-ID to 1136 ± 2 Ma (concordia age) by (Bingen et al., 2008); according to the TIMS analyses, this monazite has negligible common lead ($^{206}\text{Pb}/^{204}\text{Pb} > 10\,000$). Monazites from Moacir, Brazil (504 ± 0.2 Ma $^{207}\text{Pb}/^{235}\text{U}$ age, Gasquet et al., 2010) and Luumäki, Finland (1628 ± 4 Ma $^{207}\text{Pb}/^{206}\text{Pb}$ age by ID-TIMS. O.T. Rämö, pers. comm.) were run as unknowns, and the zircon standard GJ-1 (600 Ma; (Jackson et al., 2004) was used as an extra monitor for the common lead baseline at mass 204. During the analytical session, common-Pb corrected data for our split of the Moacir monazite yields a weighted average $^{206}\text{Pb}/^{238}\text{U}$ age of 509 ± 3 Ma ($n=10$); the Luumäki monazite yielded a near-concordant concordia intercept age of 1630 ± 10 Ma ($n=10$).

Raw data from the mass spectrometer (converted to volts) were corrected for background, laser induced elemental fractionation, mass discrimination and drift in ion counter gains and reduced to U and ^{206}Pb concentrations and U–Pb isotope ratios by calibration to concordant reference zircons of known age, using protocols adapted from those of Jackson et al. (2004). The calculations were done off-line, using the in-house interactive spreadsheet NuAge.xlt.

Background-corrected signals for mass numbers 204, 206, 207 and 238 and the $^{207}\text{Pb}/^{206}\text{Pb}$, $^{206}\text{Pb}/^{238}\text{U}$ and $^{207}\text{Pb}/^{235}\text{U}$ isotope ratios were plotted as traces of observed voltage and voltage ratios against ablation time. Time-intervals that were homogeneous in isotopic composition were interactively selected for integration, and calibrated against the corresponding time-interval for each mass in the reference zircon(s). To compensate for drift in instrument

sensitivity and Faraday vs. electron multiplier gain during an analytical session, a linear correlation of signal vs. time was assumed for the reference zircons.

The calibration algorithm applied to the monazite data assumes that the isotopic ratio is a linear function of signal ratio and time, i.e. $y = x(a + c \cdot t)$, where y is the isotopic ratio to be determined, x is the observed voltage ratio and t the time since the start of the analytical session. The coefficients a and c are determined by linear regression of the calibration standard B0109. This approach is equivalent to that incorporated in the commercial software package GLITTER (Griffin et al., 2008).

All isochrons and concordance ages were calculated using the program Isoplot (Ludwig, 2008), version 4.15.

	$^{176}\text{Hf}/^{177}\text{Hf}$	2SD	$^{178}\text{Hf}/^{177}\text{Hf}$	2SD	$^{176}\text{Yb}/^{177}\text{Hf}$	2SD	$^{176}\text{Lu}/^{177}\text{Hf}$	2SD	n	age	$^{176}\text{Hf}/^{177}\text{Hf}$ Solution
LV11	0.282824	0.000080	1.46726	0.00008	0.26	0.26	0.003	0.003	254	~290Ma	0.282837
Temora											
2	0.282679	0.000051	1.46727	0.00009	0.045	0.030	0.0011	0.0007	322	418Ma	0.282686
Mud											
Tank	0.282510	0.000043	1.46727	0.00008	0.002	0.002	0.00003	0.00004	351	732Ma	0.282507

Table 1: Summary of zircon standards measured by laser ablation on the Oslo Nu MC-ICPMS, using the correction protocol described in the text, compared to solution data (Temora-2 and Mud Tank: Woodhead and Hergt, 2005; LV11: Heinonen et al., 2010)

References

- Andersen, T., Andersson, U.B., Graham, S., Aberg, G. , Simonsen, S.L., 2009. Granitic magmatism by melting of juvenile continental crust: new constraints on the source of Palaeoproterozoic granitoids in Fennoscandia from Hf isotopes in zircon. *Journal of the Geological Society* 166, 233-247.
- Belousova, E.A., Griffin, W.L. & O'Reilly, S.Y. 2006. Zircon crystal morphology, trace element signatures and Hf isotope composition as a tool for petrogenetic modelling: Examples from eastern Australian granitoids. *Journal of Petrology*, 47, 329–353.
- Bingen, B., Davis, W.J., Hamilton, M.A., Engvik, A.K., Stein, H.J., Skar, O. , Nordgulen, O., 2008. Geochronology of high-grade metamorphism in the Sveconorwegian belt, S. Norway: U-Pb, Th-Pb and Re-Os data. *Norwegian Journal of Geology* 88, 13-42.
- Black, L.P., Kano, S.L., Allen, C.M., Aleinikoff, J.N., Davis, D.W., Korsch, R.J. & Foudoulis, C. 2003. TEMORA 1: a new zircon standard for Phanerozoic U–Pb geochronology. *Chemical Geology*, 200, 155–170.
- Gasquet, D., Bertrand, J.-M., Paquette, J.-L., Lehmann, J., Ratzov, G., De Ascençao Guedes, R., Tiepolo, M., Boullier, A.M., Scaillet, S. , Nomade, S., 2010. Miocene to Messinian deformation and hydrothermal activity in a pre-Alpine basement massif of the French western Alps: new U-Th-Pb and argon ages from the Lauzière massif. *Bulletin de la Société géologique de France* 181, 227-241.
- Griffin, W.L., Powell, W.J., Pearson, N.J. , O'Reilly, S.Y., 2008. Glitter: Data reduction software for laser ablation ICP-MS. In: Sylvester, P. (Ed.), *Laser Ablation ICP–MS in the Earth Sciences: Current Practices and Outstanding Issues*, pp. 308-311.
- Heinonen, A.P., Andersen, T. , Rämö, O.T., 2010. Source constraints from the Hf isotope composition of zircon in the rapakivi granites and associated mafic rocks of southern Finland. *Journal of Petrology* 51, 1687-1709.
- Jackson, S.E., Pearson, N.J., Griffin, W.L. , Belousova, E.A., 2004. The application of laser ablation-inductively coupled plasma-mass spectrometry to in situ U-Pb zircon geochronology. *Chemical Geology* 211, 47-69.
- Ludwig, K., 2008. User's Manual for Isoplot 3.6, a geochronological toolkit for Microsoft Excel. Special Publication No. 4, Berkeley Geochronology Center.

Patchett, P.J. , Tatsumoto, M., 1980. Lu-Hf total-rock isochron for the eucrite meteorites. *Nature* 288, 571-574.

Rosa, D.R.N., Finch, A.A., Andersen, T. , Inverno, C.M.C., 2009. U–Pb geochronology and Hf isotope ratios of magmatic zircons from the Iberian Pyrite Belt. *Mineralogy and Petrology* 95, 47-69.

Seydoux-Guillaume, A.M., Paquette, J.L., Wiedenbeck, M., Montel, J.M. , Heinrich, W., 2002. Experimental resetting of the U-Th-Pb systems in monazite. *Chemical Geology* 191, 165-181.

Stacey, J.S. & Kramers, J.D. 1975. Approximation of terrestrial lead isotope evolution by a two-stage mode. *Earth and Planetary Science Letters*, 26, 207–221.

Taylor, J.R. 1997. An Introduction to Error Analysis, 2nd edn. University Science Books, Sausalito, CA. Vaasjoki, M., Huhma, H.,

Thirlwall, M.F. , Anczkiewicz, R., 2004. Multidynamic isotope ratio analysis using MC-ICP-MS and the causes of secular drift in Hf, Nd and Pb isotope ratios. *International Journal of Mass Spectrometry* 235, 59-81.

Vervoort, J.D., Patchett, P.J., Soderlund, U. , Baker, M., 2004. Isotopic composition of Yb and the determination of Lu concentrations and Lu/Hf ratios by isotope dilution using MC-ICPMS. *Geochemistry Geophysics Geosystems* 5.

Wiedenbeck, M., Alle, P., Corfu, F., et al. 1995. Three natural zircon standards for U–Th–Pb, Lu–Hf, trace element and REE analyses. *Geostandards Newsletter*, 19, 1–23.

Woodhead, J.D., Hergt, J.M., 2005. A preliminary appraisal of seven natural zircon reference materials for in situ Hf isotope determination. *Geostandards and Geoanalytical Research* 29, 183-195.

Yuan, H.L., Gao, S., Dai, M.N., Zong, C.L., Gunther, D., Fontaine, G.H., Liu, X.M. , Diwu, C., 2008. Simultaneous determinations of U-Pb age, Hf isotopes and trace element compositions of zircon by excimer laser-ablation quadrupole and multiple-collector ICP-MS. *Chemical Geology* 247, 100-118.

**APPENDIX 2: SAMPLE LOCALITIES AND TYPE OF ANALYSIS
DONE**

Table 2.1 Location of sampling areas and type of analysis done on each sample.

Sample Name	Formation	Farm	Latitude(S)	Longitude(E)	PTS	XRF	ICPMS	$\delta^{18}\text{O}$	Age
NG1	Toggekry	Toggekry 10986	28.163778	30.88622222	X				
NG2-A	Witkop	Toggekry 10986	28.166083	30.88258333	XX	X	X	X	
NG2-B	Witkop	Toggekry 10986	28.166083	30.88258333	X	X	X	X	
NG3-A	Toggekry	Toggekry 10986	28.163889	30.88658333	X	X	X		Zr
NG3-B	Toggekry	Toggekry 10986	28.16325	30.88638889	X	X	X		Monazite
NG4	Toggekry	Toggekry 10986	28.155778	30.88058333	X	X	X		
NG5	Intrusion	Toggekry 10986	28.155778	30.88058333	X				
NG6-C	Witkop	Toggekry 10986	28.166007	30.88795247	X	X	X	X	
NG6-R	Witkop	Toggekry 10986	28.166007	30.88795247	X	X	X	X	
NG7	Witkop	Toggekry 10986	28.166156	30.88773186	X	X	X	X	
NG8	Witkop	Toggekry 10986	28.166156	30.88773186	X	X	X	X	
NG9	Witkop	Toggekry 10986	28.166156	30.88773186	X	X	X	X	
NG10	Witkop	Toggekry 10986	28.166156	30.88773186	X	X	X	X	
NG11	Witkop	Toggekry 10986	28.166156	30.88773186	X	X	X	X	
NG12	Toggekry	Mount Vernon 10965	28.166967	30.86631677	X	X	X		
NG13	Toggekry	Mount Vernon 10965	28.166809	30.86609356	X	X	X		Zr
NG14	Toggekry	Mount Vernon 10965	28.166809	30.86609356	X	X	X		
NG15	Toggekry	Mount Vernon 10965	28.166619	30.86591746	XX	X	X		Zr
NG16	Toggekry	Mount Vernon 10965	28.165431	30.86474315	X	X	X		
NG17	Toggekry	Mount Vernon 10965	28.164999	30.8636494	X	X	X		
NG18	Toggekry	Mount Vernon 10965	28.163928	30.86271138	X	X	X		
NG19	Toggekry	Mount Vernon 10965	28.163478	30.86279553	XX	X	X		
NG20	Toggekry	Kromellenboog 266	28.159472	30.89541667	X	X	X		
NG21	"Toggekry"	Toggekry 10986	28.16597	30.88848473	X	X	X		
NG22	Witkop	Toggekry 10986	28.166077	30.88798885	X				
NG23	Toggekry	Toggekry 10986	28.159493	30.88557704	X				

Table 2. 1 (continued) Location of sampling areas and type of analysis done on each sample

Sample Name	Formation	Farm	Latitude(S)	Longitude(E)	PTS	XRF	ICPMS	$\delta^{18}\text{O}$	Age
NJ-10-L3A	Toggekry	Lot 8 Nondweni 10840	28.155278	30.85	X	X	X		
NJ-10-L3B	Toggekry	Lot 8 Nondweni 10840	28.155278	31.85	X	X	X		
NJ-10-L3C	Toggekry	Lot 8 Nondweni 10840	28.155278	32.85	X	X	X		
NJ-10-L4A	Toggekry	Lot 8 Nondweni 10840	28.155306	30.850333	X	X	X		
NJ-10-L4B	Toggekry	Lot 8 Nondweni 10840	28.155306	30.850333	X	X	X		
NJ-10-L4C	Toggekry	Lot 8 Nondweni 10840	28.155306	30.850333	X	X	X		
NJ-10-L5A	Toggekry	Lot 8 Nondweni 10840	28.155308	30.850389		X	X		Zr
NJ-10-L5B1	Toggekry	Lot 8 Nondweni 10840	28.155308	30.850389	X	X	X		
NJ-10-L5B2	Toggekry	Lot 8 Nondweni 10840	28.155308	30.850389	X	X	X		
NJ-10-L5C	Toggekry	Lot 8 Nondweni 10840	28.155308	30.850389	X	X			
NJ-10-L6A	Toggekry	Lot 8 Nondweni 10840	28.155278	30.850583	X	X			
NJ-10-L6B	Toggekry	Lot 8 Nondweni 10840	28.155278	30.850583	X	X			
NJ-10-L6C	Toggekry	Lot 8 Nondweni 10840	28.155278	30.850583	X	X			
NJ-10-L7A	Toggekry	Lot 8 Nondweni 10840	28.1555	30.850889	X	X			
NJ-10-L8A	Toggekry	Lot 8 Nondweni 10840	28.155444	30.851028	X	X			
NJ-10-L8B	Toggekry	Lot 8 Nondweni 10840	28.155444	30.851028	X	X			
NJ-10-L8C	Toggekry	Lot 8 Nondweni 10840	28.155444	30.851028	X	X			
NJ-10-L9B	Toggekry	Lot 8 Nondweni 10840	28.155583	30.851472	X	X			
NJ-10-L9B	Toggekry	Lot 8 Nondweni 10840	28.155583	30.851472	X	X			
NJ-10-L10A	Toggekry	Lot 8 Nondweni 10840	28.155583	30.851611	X	X			
NJ-10-L10B	Toggekry	Lot 8 Nondweni 10840	28.155583	30.851611	X	X			
NJ-10-L10C	Toggekry	Lot 8 Nondweni 10840	28.155583	30.851611	X	X			
NJ-10-L10D	Toggekry	Lot 8 Nondweni 10840	28.155583	30.851611	X	X			
NJ-10-SS1	Toggekry	Mount Vernon 10965	28.163583	30.862667	X	X	X		
NJ-10-SS2	Toggekry	Mount Vernon 10965	28.163667	30.862694	X	X	X		
NJ-10-SS3	Toggekry	Mount Vernon 10965	28.163694	30.862611	X	X	X		
NJ-10-SS4	Toggekry	Mount Vernon 10965	28.163667	30.862639	X	X	X		
NJ-10-SS5	Toggekry	Mount Vernon 10965	28.163722	30.862694	X	X	X		
NJ-10-SS6	Toggekry	Mount Vernon 10965	28.16375	30.862639	X	X	X		
NJ-10-SS7	Toggekry	Mount Vernon 10965	28.163833	30.863028	X	X	X		
NJ-10-SS8	Toggekry	Mount Vernon 10965	28.164083	30.862806	X	X	X		
NJ-10-SS9	Toggekry	Mount Vernon 10965	28.164167	30.862861	X				

APPENDIX 3: MAJOR AND TRACE ELEMENT DATA

Table 3.1 Major (wt%) and trace (ppm) elements geochemistry for the Toggekry and Witkop Formations.

Sample Name	SC-2	SC-3	NG3-A	NG-3B	NG4	NG12	NG13	NG14	NG15	NG16
lithology	Andesite	Basaltic Andesite	Andesite	Quartz sericite Schist	Quartz sericite Schist	Quartz-Feldspar porphyry	Quartz-Feldspar porphyry	Basaltic Andesite	Andesite	Andesite
Formation	Toggekry	Toggekry	Toggekry	Toggekry	Toggekry	Toggekry	Toggekry	Toggekry	Toggekry	Toggekry
SiO ₂	71.86	74.13	75.94	72.23	78.52	71.73	71.09	60.25	73.06	73.18
Al ₂ O ₃	16.18	14.99	11.75	14.78	11.11	14.79	14.97	16.07	14.03	14.7
Fe ₂ O ₃	1.97	0.84	2.47	4.46	3.86	2.7	2.3	3.44	1.58	2.33
MnO	0.0586	0.0252	0.0379	0.1166	0.0281	0.0605	0.0384	0.2208	0.026	0.0892
MgO	0.62	0.41	0.85	3.27	3.29	0.75	0.94	3.1	0.91	0.61
CaO	1.69	1.66	0.36	0.03	0.06	1.57	2.57	10.67	4.66	1.02
Na ₂ O	4.57	5.71	3.19	0.28	0.13	6.13	6.48	2.01	3.01	5.98
K ₂ O	1.82	0.6	5.58	3.84	3.04	1.66	0.86	3.27	1.34	2.11
TiO ₂	0.2996	1.053	0.1882	0.217	0.2652	0.3566	0.3782	0.9249	1.0276	0.2858
P ₂ O ₅	0.21	0.44	0.02	0.02	0.03	0.15	0.17	0.43	0.42	0.1
Cr ₂ O ₃	0.0185	0.0098	0.005	0.0139	0.003	0.0035	0	0.0093	0.02	0.0089
NiO	0.0058	0.0039	0	0.0067	0.0001	0	0	0.0042	0.0019	0.0005
TOTAL	99.3	99.87	100.38	99.27	100.33	99.91	99.79	100.4	100.09	100.42
L.O.I.	1.8	0.92	1.12	5.15	2.62	1.31	1.32	2.3	1.26	1.01
Sc	1.301	11.697	2.161	3.358	4.176	2.100	2.221	7.127	9.018	2.078
V	35.662	107.751	4.708	2.079	2.090	28.576	30.538	51.203	75.074	20.429
Cr	8.819	22.936	10.228	2.171	7.5745	14.82	17.54	47.7255	89.292	11.2845
Co	7.036	8.060	2.926	11.888	3.198	5.618	7.064	13.242	12.087	8.891
Ni	27.577	31.725	5.212	39.068	7.558	8.630	9.210	37.832	39.567	6.886
Cu	56.668	26.046	30.408	3.138	886.524	27.383	32.294	16.831	29.834	17.601
Zn	71.485	28.865	350.613	335.310	913.142	45.451	39.532	111.061	57.136	57.922
Rb	15.474	8.676	161.905	78.642	149.466	39.398	26.816	80.666	57.578	41.872
Sr	346.688	86.702	135.005	2.855	5.685	421.562	489.184	368.495	322.096	410.387
Y	4.000	11.894	26.889	41.242	101.137	6.468	6.480	21.405	26.455	7.910
Zr	175.879	165.037	75.997	595.238	343.155	155.1	142.348	193.855	324.9	106.753
Nb	5.655	11.342	13.231	60.600	47.349	4.930	5.183	19.155	15.348	4.085
Mo	0.403	0.414	1.535	0.461	1.112	0.664	0.615	0.373	0.425	0.781
Ba	674.607	93.587	726.970	187.036	166.593	663.576	619.494	271.399	152.730	405.073
La	19.038	12.285	50.260	54.273	82.086	42.340	43.344	56.126	39.003	29.157
Ce	55.986	31.709	97.360	190.683	167.895	75.002	77.739	118.114	79.847	52.448
Pr	4.166	4.002	9.560	16.054	20.360	7.019	7.295	12.574	8.676	5.336
Nd	15.444	16.231	32.585	66.236	81.065	23.581	24.233	45.469	33.028	19.239
Sm	2.276	3.136	5.802	12.664	17.594	3.387	3.605	7.500	6.165	3.039
Eu	0.733	1.245	0.944	1.386	2.847	0.947	0.993	2.071	2.049	0.822
Gd	1.524	2.766	5.457	10.343	18.233	2.392	2.485	6.079	5.582	2.281
Tb	0.169	0.411	0.796	1.502	2.875	0.266	0.278	0.770	0.794	0.277
Dy	0.929	2.612	5.047	9.632	18.893	1.482	1.504	4.553	4.994	1.604
Ho	0.151	0.504	0.978	1.788	3.872	0.230	0.231	0.797	0.962	0.278
Er	0.372	1.460	2.934	5.255	11.732	0.592	0.599	2.178	2.912	0.757
Tm	0.051	0.216	0.438	0.830	1.733	0.081	0.079	0.297	0.429	0.105
Yb	0.310	1.443	2.899	5.816	11.344	0.477	0.474	1.863	2.844	0.664
Lu	0.045	0.217	0.424	0.881	1.668	0.068	0.066	0.266	0.427	0.095
Hf	4.002	3.460	2.545	16.922	9.416	12.000	3.417	3.954	6.000	2.742
Ta	0.339	0.663	1.138	3.955	2.775	0.335	0.347	1.070	0.951	0.319
W	1.619	1.326	0.281	1.651	0.440	1.766	0.904	1.018	0.479	0.845
Pb	58.441	6.449	23.242	4.646	8.251	14.800	15.788	11.232	6.369	10.375
Th	7.294	1.966	16.321	13.086	14.537	9.312	10.099	5.029	6.712	6.008
U	2.303	0.619	4.787	3.557	3.902	2.636	2.896	1.645	1.864	3.511

Table 3.1 (continued) Major (wt%) and trace (ppm) elements geochemistry for the Toggekry and Witkop Formations.

Sample Name	NG17	NG18	NG19	NG20	NG2B	NG6	NG7	NJ-10-SS1	NJ-10-SS2	NJ-10-SS3
lithology	Quartz-Feldspar porphyry	Basaltic Andesite	Rhyolite	Quartz sericite Schist	Basalt	Basalt	Basalt	Basaltic Andesite	Basaltic Andesite	Basaltic Andesite
Formation	Toggekry	Toggekry	Toggekry	Toggekry	Witkop	Witkop	Witkop	Toggekry	Toggekry	Toggekry
SiO ₂	71.83	60.24	80.07	76.84	50.47	47.59	52.63	64.34	59.92	67.21
Al ₂ O ₃	15.55	15.01	11	11.58	15.99	16.42	13.35	17.58	16.04	16.94
Fe ₂ O ₃	2.04	8.85	1.33	3.58	16.51	17.83	16.82	4.26	8.56	3.75
MnO	0.0283	0.1083	0.0139	0.0268	0.357	0.3869	0.3353	0.1736	0.2072	0.0945
MgO	0.73	5.51	0.64	4.76	3.88	4.19	4.05	0.84	3.08	1.03
CaO	1.53	6.02	0.44	0.18	5.67	6.39	7.14	4.54	4.53	2.4
Na ₂ O	6.08	2.96	3.97	0	3.4	3.57	2.95	4.78	4.68	6.09
K ₂ O	1.97	0.29	2.84	2.99	0.49	0.9	0.56	1.54	1.14	0.62
TiO ₂	0.3535	0.8752	0.0757	0.3253	1.9861	2.0299	1.8842	1.2433	0.8901	1.0275
P ₂ O ₅	0.19	0.23	0.01	0.07	0.56	0.62	0.58	0.42	0.23	0.32
Cr ₂ O ₃	0.0061	0.0214	0	0.0092	0	0.0315	0.0104	0.0636	0.501	0.0494
NiO	0	0.0091	0	0.0001	0.0038	0.0083	0.006	0.016	0.0117	0.018
TOTAL	100.29	100.12	100.4	100.35	99.32	99.98	100.32	99.8	99.34	99.55
L.O.I.	1.31	1.32	0.84	3.22	0.05	2.01	3.44	0.9	0.81	0.92
Sc	1.871	15.296	1.254	3.570	16.791	34.630	31.494	24.256	17.186	15.650
V	27.809	104.218	0.420	0.751	113.051	265.192	244.348	160.239	155.543	142.275
Cr	13.6095	138.0875	9.481	9.405	187.978	24.978	23.696	157.852	70.789	76.728
Co	4.887	37.898	1.152	2.090	35.119	45.153	41.920	28.545	33.607	34.450
Ni	11.788	82.543	4.323	3.323	93.173	32.550	31.634	84.926	61.688	54.673
Cu	27.042	42.007	3.132	2.341	61.294	87.639	54.934	51.843	34.207	185.189
Zn	57.434	69.971	26.376	19.581	74.159	180.523	148.637	132.361	206.571	218.469
Rb	41.462	13.692	103.464	93.089	5.065	27.984	25.824	55.281	41.181	22.313
Sr	643.195	293.645	111.873	5.614	328.133	195.534	209.585	154.936	211.421	154.523
Y	7.589	20.610	19.213	50.980	17.717	25.962	25.203	25.657	18.650	16.922
Zr	130.650	114.210	113.462	539	120.366	121.949	143.045	234.6	161.9	198.6
Nb	6.232	10.235	8.300	28.947	12.117	9.592	8.780	10.232	9.177	8.902
Mo	0.331	1.093	2.531	0.390	0.488	0.592	0.285	0.303	BDL	BDL
Ba	1542.906	26.227	207.925	280.972	10.213	112.283	96.889	122.797	86.996	28.626
La	39.392	25.441	39.330	73.382	19.007	14.418	21.092	46.471	22.667	14.315
Ce	72.631	49.839	74.752	163.314	47.215	31.955	46.787	98.507	46.671	37.785
Pr	7.226	5.670	7.317	20.824	5.825	3.921	5.742	11.192	5.358	4.588
Nd	23.869	20.943	21.991	83.258	26.477	18.533	26.475	44.122	21.152	18.113
Sm	3.730	4.056	3.710	18.347	5.108	4.154	5.677	7.008	3.900	3.264
Eu	1.120	1.091	0.349	3.059	1.620	1.555	1.936	1.743	1.294	1.005
Gd	2.811	3.970	3.247	14.814	4.621	4.773	5.764	7.280	4.214	3.531
Tb	0.304	0.593	0.518	1.921	0.592	0.699	0.791	0.834	0.534	0.488
Dy	1.560	3.777	3.456	10.607	3.695	4.650	5.002	5.243	3.496	3.180
Ho	0.243	0.755	0.703	1.890	0.664	0.919	0.950	0.979	0.682	0.635
Er	0.601	2.148	2.109	5.315	1.872	2.725	2.808	2.749	1.932	1.859
Tm	0.079	0.309	0.329	0.778	0.246	0.370	0.385	0.373	0.274	0.263
Yb	0.482	1.989	2.245	5.108	1.625	2.525	2.611	2.389	1.782	1.749
Lu	0.069	0.281	0.330	0.742	0.230	0.371	0.379	0.326	0.255	0.256
Hf	3.039	2.315	3.590	14.000	2.541	2.571	2.987	7.000	2.313	9.000
Ta	0.391	0.706	1.103	1.878	0.647	0.538	0.509	0.468	0.368	0.429
W	1.424	0.322	0.592	0.455	0.311	0.216	0.140	1.453	1.767	1.273
Pb	51.045	5.771	23.031	1.961	4.528	4.690	4.676	6.805	6.284	10.362
Th	14.565	4.875	18.609	9.249	1.637	1.486	1.931	3.902	3.377	4.458
U	4.267	1.333	4.425	2.082	0.434	0.475	0.458	0.708	0.643	0.902

Table 3.1 (continued) Major (wt%) and trace (ppm) elements geochemistry for the Toggekry and Witkop Formations.

Sample Name	NJ-10-SS4	NJ-10-SS5	NJ-10-SS6	NJ-10-SS7	NJ-10-SS8	NJ-10-L3A	NJ-10-L3B	NJ-10-L3C	NJ-10-L4A	NJ-10-L4B
lithology	Basaltic Andesite	Rhyolite	Rhyolite	Rhyolite	Rhyolite	Rhyolite				
Formation	Toggekry	Toggekry	Toggekry	Toggekry	Toggekry	Toggekry	Toggekry	Toggekry	Toggekry	Toggekry
SiO2	70.55	68.79	60.04	63.28	76.76	83.5	81.27	81.13	82.25	78.33
Al2O3	17.04	19.04	17.53	24.08	12.38	10.08	10.04	10.14	10.43	10.36
Fe2O3	1.11	0.32	8.9	0.48	0.62	0.38	0.58	0.62	0.67	3.29
MnO	0.0623	0.0187	0.1186	0.0258	0.0273	0.0106	0.0291	0.035	0.0276	0.0791
MgO	0.7	0.15	3.64	0.43	0.59	0.28	0.47	0.44	0.53	1
CaO	1.58	1.38	4.79	3.45	1.26	0.01	0.44	0.41	0.01	0.87
Na2O	6.31	8.94	2.7	3.75	5.53	0.27	0.46	0.32	0.22	0.87
K2O	0.98	0.2	0.82	3.21	0.33	4.86	5.87	5.88	5.53	4.39
TiO2	0.7774	0.9394	0.767	0.9389	0.8696	0.183	0.1586	0.1556	0.1881	0.1627
P2O5	0.2	0.29	0.21	0.25	0.02	0.02	0.01	0.02	0.02	0.01
Cr2O3	0.474	0.0195	0.0586	0.0477	0.0868	0.0287	0.0321	0.022	0.0432	0.0423
NiO	0.0064	0.0034	0.0162	0.0094	0.0145	0.0014	0.0012	0.0041	0.0032	0.0035
TOTAL	99.37	100.09	99.61	99.95	99.14	99.63	99.35	99.18	99.92	99.4
L.O.I.	0.99	0.3	1.32	1.75	1.02	1.28	0.99	1.26	1.29	1.21
Sc	15.596	11.498	17.139	23.905	14.579	1.935	0.917	1.960	1.780	1.386
V	145.434	112.994	123.891	188.735	109.956	0.553	0.425	0.485	0.467	0.400
Cr	100.051	10.307	162.347	124.582	407.340	5.536	1.107	1.522	BDL	0.290
Co	25.518	4.617	35.696	22.952	22.923	0.901	1.112	1.331	1.565	1.296
Ni	55.674	10.187	87.559	47.665	93.591	2.736	0.091	3.304	3.215	2.737
Cu	83.088	23.900	156.741	94.137	57.144	5.639	3.501	3.826	2.292	6.158
Zn	88.347	20.113	159.964	40.557	72.159	14.840	17.831	23.003	20.883	57.270
Rb	40.405	6.039	36.673	109.463	18.170	75.982	79.039	86.630	83.372	88.725
Sr	153.050	218.867	274.604	285.956	132.556	11.260	30.808	35.685	17.720	38.994
Y	13.281	20.779	20.406	27.002	27.162	62.394	88.711	91.833	78.628	106.904
Zr	153.7	217.8	179.7	175.5	154.8	404.665	363.270	362.667	467.500	411.945
Nb	8.199	20.696	9.517	8.056	6.770	52.539	47.914	45.297	46.332	44.346
Mo	1.756	3.335	0.113	BDL	0.253	2.993	2.514	3.188	0.208	4.951
Ba	83.620	36.263	61.700	576.939	59.753	286.366	345.368	399.599	413.198	383.320
La	15.770	25.336	24.373	52.219	29.166	38.828	62.852	78.151	30.654	75.876
Ce	33.232	49.230	47.755	78.057	65.668	81.240	141.542	172.420	27.764	164.405
Pr	4.410	5.348	5.384	7.782	8.648	12.204	17.594	21.006	7.755	19.907
Nd	18.038	20.482	21.072	29.915	37.755	46.661	71.832	86.870	29.716	80.163
Sm	3.525	4.028	3.851	5.269	7.266	10.130	15.990	17.991	7.725	17.226
Eu	1.164	1.659	1.105	1.927	3.030	1.242	2.073	1.968	1.276	2.109
Gd	3.449	4.321	4.131	5.936	6.923	10.337	17.038	18.693	10.458	18.587
Tb	0.432	0.602	0.557	0.749	0.827	1.765	2.751	2.654	2.197	2.903
Dy	2.599	3.991	3.724	4.964	5.000	12.469	18.030	17.364	15.900	19.684
Ho	0.490	0.785	0.745	0.984	0.938	2.585	3.557	3.462	3.231	4.054
Er	1.332	2.228	2.113	2.770	2.657	8.088	10.583	10.300	9.870	12.224
Tm	0.185	0.324	0.298	0.375	0.360	1.249	1.546	1.536	1.530	1.780
Yb	1.175	2.085	1.888	2.309	2.326	8.554	10.188	10.370	10.181	12.014
Lu	0.167	0.300	0.272	0.321	0.342	1.344	1.464	1.468	1.488	1.721
Hf	6.000	8.000	5.000	6.000	6.000	11.656	10.414	10.327	12.133	12.094
Ta	0.377	0.727	0.489	0.376	0.267	2.895	2.832	3.031	3.078	3.082
W	1.238	0.972	0.575	2.726	0.400	1.122	1.054	1.159	1.194	0.927
Pb	7.800	7.421	12.232	10.583	7.584	6.637	8.343	18.492	6.093	6.592
Th	4.074	7.229	5.237	4.903	4.832	13.511	13.770	14.303	14.049	13.971
U	0.881	1.400	1.165	1.085	1.569	2.607	3.232	3.455	2.523	3.384

Table 3.1 (continued) Major (wt%) and trace (ppm) elements geochemistry for the Toggekry and Witkop Formations.

Sample Name	NJ-10-L4C	NJ-10-L5A	NJ-10-L5B1	NJ-10-L5B2	NJ-10-L5C	NJ-10-L6A	NJ-10-L6B	NJ-10-L6C	NJ-10-L7A	NJ-10-L8A
lithology	Rhyolite									
Formation	Toggekry									
SiO ₂	80.41	83.66	78.58	78.3	78.68	80.29	78.73	80.99	81.55	81.08
Al ₂ O ₃	10.74	10.43	10.56	10.73	10.47	10.27	10.34	9.95	10.81	10.13
Fe ₂ O ₃	1.03	0.34	2.49	3.29	2.62	2.51	3.45	1.01	0.83	0.82
MnO	0.041	0.0111	0.0551	0.0831	0.0675	0.0375	0.0789	0.0447	0.0376	0.0647
MgO	0.51	0.24	0.69	0.98	0.84	0.64	0.99	0.59	0.44	0.54
CaO	0.58	0.01	0.4	0.72	0.59	0.09	0.55	0.29	0.14	0.46
Na ₂ O	2.73	0.2	1.01	0.91	0.54	0.45	1.57	1.19	0.59	1.49
K ₂ O	3.08	5.02	5.37	4.84	5.85	4.95	3.8	4.86	5.11	4.62
TiO ₂	0.1692	0.1843	0.1621	0.1889	0.1787	0.1656	0.1637	0.1697	0.1813	0.1718
P ₂ O ₅	0.01	0.02	0.01	0.02	0.02	0.02	0.01	0.02	0.02	0.02
Cr ₂ O ₃	0.0364	0.374	0.0367	0.0411	0.394	0.0236	0.028	0.0432	0.0316	0.0303
NiO	0.0034	0.0066	0.0045	0.0043	0.0049	0.0034	0.0025	0.0071	0.0021	0.0034
TOTAL	99.35	100.17	99.37	100.11	99.9	99.44	99.72	99.17	99.74	99.43
L.O.I.	1.31	1.43	1.36	1.27	1.24	1.22	1.47	1.22	1.16	1.29
Sc	1.473	1.393	0.881	1.199						
V	0.432	0.317	0.461	0.312						
Cr	0.406	-0.307	0.861	0.067						
Co	1.227	2.041	1.268	1.339						
Ni	2.899	7.248	3.147	2.148						
Cu	3.667	2.828	6.961	14.786						
Zn	32.675	14.765	40.403	52.062						
Rb	50.426	74.539	79.875	95.011						
Sr	36.331	13.148	31.280	43.127						
Y	96.386	73.795	83.960	89.834						
Zr	395.906	453.400	397.939	398.510						
Nb	45.643	45.905	46.052	45.594						
Mo	2.170	2.269	1.669	3.152						
Ba	317.030	331.630	330.163	370.980						
La	78.046	48.038	74.124	73.430						
Ce	165.522	56.613	165.039	160.481						
Pr	20.793	14.137	20.265	19.522						
Nd	82.505	53.769	81.495	82.068						
Sm	17.870	12.416	17.336	17.173						
Eu	2.506	1.597	2.122	2.087						
Gd	18.549	13.316	17.216	17.718						
Tb	2.759	2.218	2.497	2.636						
Dy	17.639	14.659	16.063	17.278						
Ho	3.630	2.887	3.236	3.429						
Er	10.650	8.710	9.725	10.186						
Tm	1.601	1.317	1.457	1.541						
Yb	10.998	9.077	9.934	10.189						
Lu	1.621	1.331	1.467	1.499						
Hf	11.677	9.424	11.688	11.448						
Ta	3.195	2.978	3.084	3.133						
W	0.897	1.472	0.993	0.877						
Pb	7.846	6.509	7.230	7.378						
Th	14.124	13.517	14.305	14.362						
U	3.394	2.313	3.158	3.133						

Table 3.1 (continued) Major (wt%) and trace (ppm) elements geochemistry for the Toggekry and Witkop Formations.

Sample Name	NJ-10-L8B	NJ-10-L8C	NJ-10-L9B	NJ-10-L9C	NJ-10-L10A	NJ-10-L10B	NJ-10-L10C	NJ-10-L10D
lithology	Rhyolite							
Formation	Toggekry							
SiO₂	77.18	80.63	78.56	78.03	77.37	79.93	78.94	82.4
Al₂O₃	10.48	10.25	10.7	10.5	10.81	10.09	10.55	10.48
Fe₂O₃	3.76	1.21	2.55	3.43	3.05	1.71	3.07	0.99
MnO	0.1016	0.0683	0.0695	0.0849	0.0941	0.0621	0.0931	0.0308
MgO	0.93	0.68	0.79	0.94	0.86	0.67	0.84	0.52
CaO	0.57	0.55	0.54	0.75	0.69	0.46	0.22	0.01
Na₂O	1	1.75	0.67	0.91	0.5	0.37	0.27	0.13
K₂O	5.25	4	6.28	5.24	6.11	6.1	5.92	5.51
TiO₂	0.1856	0.1757	0.1847	0.1882	0.273	0.2177	0.2317	0.1905
P₂O₅	0.01	0.01	0.01	0.02	0.01	0.01	0.01	0.01
Cr₂O₃	0.035	0.0259	0.0354	0.0432	0.0373	0.0333	0.0287	0.0207
NiO	0.0035	0.0015	0.0023	0.0054	0.0063	0.0079	0.0101	0.013
TOTAL	99.5	99.35	100.41	100.15	99.81	99.67	100.16	100.32
L.O.I.	1.06	1.43	1.34	1.02	1.23	1.07	1.34	1.43

APPENDIX 4: ISOTOPE GEOCHEMISTRY

Table 4.1 U-Pb isotopic data for magmatic zircons from the Toggekry Formation, Nondweni greenstone belt, South Africa.

	U	²⁰⁶ Pb	²⁰⁶ Pbc ¹	²⁰⁶ Pb/ ²⁰⁴ Pb ²	²⁰⁷ Pb/ ²³⁵ U ³	1σ	²⁰⁶ Pb/ ²³⁸ U ³	1σ	ρ	²⁰⁷ Pb*/ ²³⁵ U ³	1σ	²⁰⁶ Pb*/ ²³⁸ U ³	1σ	²⁰⁷ Pb*/ ²⁰⁶ Pb* ³	1σ	Central	Min rim
	(ppm)	(ppm)	(%)			(abs)		(abs)			(Ma)		(Ma)		(%)	(%)	
									age			age		age		Discordance	
<i>Sample NG 3A</i>																	
NG 3A-101	337	91.3	0.00E+00	9753	12.7233	0.2941	0.3159	0.0058	0.797	2659	22	1769	29	3429	21	-55	-53.5
NG 3A-01	263	151.8	0.00E+00	17819	24.8567	1.0908	0.5727	0.0222	0.882	3303	43	2919	91	3545	31	-21.9	-17.6
NG 3A-03end	359	132.8	0.00E+00	12442	15.8447	0.6878	0.3845	0.0140	0.837	2867	41	2097	65	3464	34	-46	-42.6
NG 3A-03_front	326	105.9	0.00E+00	12699	13.7457	0.3918	0.3434	0.0077	0.787	2732	27	1903	37	3419	25	-50.9	-48.8
NG 3A-03-ALL	340	116.1	0.00E+00	12209	14.5510	0.4003	0.3588	0.0075	0.760	2786	26	1977	36	3440	26	-49.1	-46.9
NG 3A-05	278	140.7	0.00E+00	3576	22.5929	0.7882	0.5204	0.0152	0.836	3210	34	2701	64	3545	28	-29	-25.5
NG 3A-06	325	135.8	0.00E+00	5869	18.8764	0.4905	0.4464	0.0090	0.776	3036	25	2379	40	3504	24	-38.2	-35.8
NG 3A-07_CORR	418	179.2	2.00E+00	974	19.2455	0.5363	0.4492	0.0099	0.794	3054	27	2392	44	3525	25	-38.3	-35.7
NG 3A-12	325	191.1	0.00E+00	40941	26.4810	0.8503	0.6108	0.0170	0.868	3364	31	3073	68	3543	23	-16.6	-13.1
NG 3A-13	185	100.3	0.00E+00	21399	24.5135	0.7188	0.5685	0.0139	0.836	3289	29	2901	57	3535	24	-22.2	-19
NG 3A-14	289	127	0.00E+00	30642	20.1357	0.5377	0.4696	0.0100	0.8	3098	26	2482	44	3526	24	-35.5	-33
NG 3A-15	319	153	0.00E+00	52411	22.1426	0.6087	0.5074	0.0113	0.808	3190	27	2646	48	3553	24	-31	-28.2
NG 3A-16	374	173	0.00E+00	19238	21.0784	0.5717	0.4915	0.0108	0.808	3142	26	2577	47	3526	24	-32.5	-29.8
NG 3A-17_corr	309	140.9	1.50E+00	1104	19.5011	0.6387	0.4546	0.0120	0.804	3067	32	2416	53	3526	29	-37.6	-34.5
NG 3A-21_corr	292	109.5	1.10E+00	1383	16.1851	0.4940	0.3802	0.0090	0.774	2888	29	2077	42	3515	29	-47.6	-45.1
NG 3A-22	285	165.5	0.00E+00	13095	25.1223	0.8883	0.5769	0.0167	0.818	3313	35	2936	68	3550	31	-21.4	-17.4
NG 3A-25_corr	460	207.1	1.00E+00	1488	19.6510	0.5583	0.4704	0.0106	0.795	3074	27	2485	47	3486	26	-34.4	-31.6
NG 3A-26_corr	316	152.8	6.90E-01	5845	21.5207	0.6737	0.5069	0.0129	0.816	3162	30	2643	55	3510	26	-30	-26.8
NG 3A-27	465	167.6	0.00E+00	10635	15.9915	0.4381	0.3864	0.0081	0.763	2876	26	2106	38	3471	25	-45.8	-43.6
NG 3A-28	215	139.4	0.00E+00	33514	28.9913	1.0936	0.6626	0.0216	0.862	3453	37	3277	84	3557	27	-10	-5.5
NG 3A-29_front_corr	855	64.4	2.00E+00	816	2.6723	0.1290	0.0845	0.0037	0.907	1321	36	523	22	3048	30	-86	-85.2
NG 3A-29_end_corr	602	104.1	1.40E+00	1614	7.2356	0.2936	0.1852	0.0065	0.866	2141	36	1095	35	3381	29	-73.1	-71.7
NG 3A-30	188	124.5	0.00E+00	15953	29.1475	1.0652	0.6675	0.0209	0.858	3458	36	3296	81	3554	28	-9.3	-4.8
NG 3A-31_corr	723	186.1	1.90E+00	896	11.0324	0.2850	0.2715	0.0051	0.722	2526	24	1549	26	3443	27	-61.5	-60
NG 3A-32	405	187.7	0.00E+00	111415	20.7552	0.6278	0.4835	0.0116	0.791	3127	29	2543	50	3527	28	-33.6	-30.6
NG 3A-33	360	208.3	0.00E+00	88011	25.6212	0.9194	0.5960	0.0182	0.852	3332	35	3014	74	3530	28	-18.3	-14.3
NG 3A-34_front	521	231.3	0.00E+00	34008	20.7260	0.6319	0.5020	0.0126	0.822	3126	30	2622	54	3467	26	-29.5	-26.4
NG 3A-34_end	407	219.6	0.00E+00	16320	23.1116	1.1334	0.5520	0.0241	0.891	3232	48	2834	100	3489	35	-23.1	-18.5
NG 3A-35_corr	426	171.1	8.80E-01	1797	18.0339	0.5262	0.4230	0.0096	0.778	2992	28	2274	44	3517	29	-41.7	-39.1
NG 3A-36_corr	681	232	1.30E+00	1215	15.1058	0.4220	0.3610	0.0077	0.763	2822	27	1987	36	3488	29	-49.7	-47.6
NG 3A-37	246	140.2	0.00E+00	16728	25.7699	0.8836	0.5902	0.0170	0.839	3338	34	2990	69	3554	29	-19.8	-15.9
NG 3A-38	351	190.7	0.00E+00	27922	24.8200	0.8531	0.5674	0.0164	0.839	3301	34	2897	67	3557	29	-22.9	-19.3
NG 3A-42	384	220.9	0.00E+00	27019	25.8781	0.8861	0.5947	0.0171	0.839	3342	33	3009	69	3548	29	-19	-15.1

Table 4.1(continued) U-Pb isotopic data for magmatic zircons from the Toggekry Formation, Nondweni greenstone belt, South Africa.

	U	²⁰⁶ Pb	²⁰⁶ Pbc ¹	²⁰⁶ Pb/ ²⁰⁴ Pb ²	²⁰⁷ Pb/ ²³⁵ U ³	1σ	²⁰⁶ Pb/ ²³⁸ U ³	1σ	ρ	²⁰⁷ Pb*/ ²³⁵ U ³	1σ	²⁰⁶ Pb*/ ²³⁸ U ³	1σ	²⁰⁷ Pb*/ ²⁰⁶ Pb* ³	1σ	Central	Min rim
	(ppm)	(ppm)	(%)			(abs)		(abs)		(Ma)	(Ma)	(Ma)	(Ma)			(%)	(%)
										age		age		age		Discordance	
Sample NJ-10-L5A																	
LA5-01	133	89.7	0.00E+00	12726	30.2701	1.1781	0.6885	0.0233	0.870	3496	38	3377	89	3564	29	-6.7	-2.1
Sample NG 15																	
NG15-104_end	133	75.8	0.00E+00	8535	25.0413	1.1591	0.5777	0.0238	0.890	3310	45	2939	97	3543	32	-21.1	-16.7
NG15-104	154	73.2	0.00E+00	6777	23.0147	0.7373	0.5376	0.0151	0.875	3228	31	2773	63	3523	23	-26.1	-23.1
NG15-104_all	145	75.7	0.00E+00	8728	24.0389	0.7268	0.5583	0.0139	0.823	3270	29	2860	57	3532	26	-23.5	-20.2
NG15-03	594	251.9	4.10E-01	4709	19.2162	0.5374	0.4600	0.0103	0.800	3053	27	2439	45	3486	25	-35.9	-33.2
NG15-01	130	90.4	0.00E+00	10875	30.3554	1.2863	0.6940	0.0253	0.861	3498	42	3398	96	3556	31	-5.7	-0.4
Sample NG 13																	
NG13-07	214	33.3	0.00E+00	6300	3.2019	0.0688	0.1501	0.0031	0.97	1458	17	901	18	2399	9	-66.7	-66.2
NG13-19	82	28.5	0.00E+00	2456	10.0443	0.2187	0.3380	0.0070	0.951	2439	20	1877	34	2948	10	-41.7	-40.6
NG13-11	162	70.1	0.00E+00	5756	15.2957	0.2273	0.4217	0.0060	0.965	2834	14	2268	27	3265	6	-36	-35.4
NG13-25r all	265	111.9	0.00E+00	16899	17.0768	0.5970	0.4434	0.0153	0.99	2939	34	2366	69	3359	7	-35.2	-34.3
NG13-25r front	151	80.5	0.00E+00	10261	20.7404	0.4549	0.5325	0.0112	0.962	3127	21	2752	47	3377	9	-22.7	-21.4
NG13-03b	156	97	0.00E+00	12401	24.9194	0.4609	0.5987	0.0109	0.983	3305	18	3025	44	3480	5	-16.3	-15.6
NG13-03 end	187	111.5	0.00E+00	26704	23.5405	0.4548	0.5635	0.0107	0.98	3250	19	2881	44	3486	6	-21.4	-20.6
NG13-03 all	216	134.5	0.00E+00	19717	24.6585	0.4385	0.5886	0.0103	0.984	3295	17	2984	42	3490	5	-18.1	-17.4
NG13-29	181	106.6	0.00E+00	8664	24.5982	0.4159	0.5823	0.0095	0.96	3292	16	2958	39	3503	7	-19.3	-18.3
NG13-24 front	100	63.9	0.00E+00	7064	26.9059	0.5336	0.6351	0.0120	0.956	3380	19	3170	47	3507	9	-12.1	-10.8
NG13-25c all	190	128.1	0.00E+00	12127	28.3648	0.4471	0.6674	0.0101	0.958	3432	15	3296	39	3512	7	-7.9	-6.7
NG13-29 front	230	135.3	0.00E+00	17960	25.1243	0.4967	0.5910	0.0110	0.945	3313	19	2993	45	3513	10	-18.4	-17
NG13-25c end	251	182.9	0.00E+00	11965	30.6427	0.7092	0.7155	0.0156	0.945	3508	23	3479	59	3524	11	-1.6	
NG13-18	169	123.6	0.00E+00	12139	30.8561	0.5123	0.7165	0.0114	0.963	3514	16	3483	43	3533	7	-1.8	-0.6
NG13-27	81	55.2	0.00E+00	3407	29.4673	0.5720	0.6819	0.0128	0.965	3469	19	3352	49	3538	7	-6.7	-5.5
NG13-26	40	25.4	0.00E+00	1683	27.6445	0.5790	0.6372	0.0129	0.968	3407	21	3178	51	3544	8	-13	-11.8
NG13-28	46	30.1	0.00E+00	18924	28.3872	0.6103	0.6540	0.0136	0.969	3433	21	3244	53	3545	8	-10.8	-9.5
NG13-29 front cor	230	135.3	7.00E-02	17960	25.0690	0.4956	0.5906	0.0110	0.945	3311	19	2992	45	3510	10	-18.4	-17

Table 4.1(continued) U-Pb isotopic data for magmatic zircons from the Toggekry Formation, Nondweni greenstone belt, South Africa.

	U	²⁰⁶ Pb	²⁰⁶ Pbc ¹	²⁰⁶ Pb/ ²⁰⁴ Pb ²	²⁰⁷ Pb/ ²³⁵ U ³	1σ	²⁰⁶ Pb/ ²³⁸ U ³	1σ	ρ	²⁰⁷ Pb*/ ²³⁵ U ³	1σ	²⁰⁶ Pb*/ ²³⁸ U ³	1σ	²⁰⁷ Pb*/ ²⁰⁶ Pb* ³	1σ	Central	Min rim	
	(ppm)	(ppm)	(%)			(abs)		(abs)		age	(Ma)	age	(Ma)	age		(%)	(%)	
																		Discordance
<i>Sample NG 13</i>																		
NG13-25c all cor	190	128.1	1.70E-01	12127	28.2153	0.4449	0.6664	0.0101	0.958	3427	15	3292	39	3506	7	-7.8	-6.7	
NG13-24 corr	105	67	1.80E-01	7573	26.7773	0.5044	0.6340	0.0114	0.953	3375	18	3165	45	3502	9	-12.2	-10.8	
NG13-24 all corr	115	61.1	2.50E-01	3738	21.9576	0.7216	0.5233	0.0170	0.99	3182	32	2713	72	3492	7	-27.2	-26.4	
NG13-25r all cor	265	111.9	2.70E-01	16899	16.9135	0.5925	0.4423	0.0153	0.99	2930	34	2361	69	3348	7	-35	-34.2	
NG13-29 all corr	181	106.6	2.70E-01	8664	24.3886	0.4125	0.5809	0.0094	0.96	3284	16	2952	38	3493	7	-19.2	-18.2	
NG13-25r front cor	151	80.5	3.10E-01	10261	20.5223	0.4503	0.5310	0.0112	0.962	3116	21	2746	47	3365	9	-22.5	-21.2	
NG13-11 corr	162	70.1	4.00E-01	5756	15.0710	0.2243	0.4201	0.0060	0.965	2820	14	2261	27	3248	6	-35.9	-35.2	
NG13-05c corr	414	94	4.70E-01	5200	5.9460	0.1130	0.2174	0.0038	0.924	1968	17	1268	20	2813	11	-60.3	-59.4	
NG13-10c all	261	113.7	4.90E-01	7017	16.1055	0.2278	0.4206	0.0057	0.963	2883	14	2263	26	3350	6	-38.3	-37.6	
NG13-10c end	256	112.2	5.70E-01	7736	15.9444	0.2556	0.4212	0.0064	0.945	2873	15	2266	29	3332	8	-37.8	-36.9	
NG13-27 corr	81	55.2	5.70E-01	3407	28.9495	0.5628	0.6785	0.0127	0.965	3452	19	3339	49	3518	8	-6.5	-5.2	
NG13-14 corr	341	94.9	6.50E-01	3561	7.5736	0.1307	0.2690	0.0042	0.9	2182	15	1536	21	2860	12	-51.8	-50.8	
NG13-19 corr	82	28.5	9.10E-01	2456	9.6345	0.2111	0.3349	0.0070	0.95	2400	20	1862	34	2895	11	-40.9	-39.7	
NG13-16 corr	118	27.3	9.40E-01	2280	5.8840	0.1078	0.2213	0.0037	0.902	1959	16	1289	19	2767	12	-58.7	-57.7	
NG13-01 mid	322	120	1.10E+00	2576	10.5065	0.3125	0.3479	0.0099	0.96	2480	28	1924	48	2974	13	-40.6	-39.2	
NG13-02 corr	199	45.8	1.20E+00	3297	5.1699	0.0806	0.2173	0.0031	0.923	1848	13	1267	17	2583	10	-55.9	-55.1	
NG13-01 front	245	71.3	1.50E+00	4319	7.4329	0.2072	0.2725	0.0074	0.977	2165	25	1553	38	2808	9	-50.1	-49.2	
NG13-13 corr	81	42	1.50E+00	1857	16.2344	0.2789	0.4984	0.0083	0.971	2891	16	2607	36	3095	6	-19.1	-18.2	
NG13-01_end	281	83.5	1.60E+00	3450	8.2162	0.1741	0.2810	0.0057	0.96	2255	19	1596	29	2921	9	-51	-50.1	
NG13-08	250	35.8	1.60E+00	2799	2.7497	0.0389	0.1356	0.0017	0.91	1342	11	820	10	2312	10	-68.6	-68	
NG13-15 corr	225	47.5	1.60E+00	1920	4.9621	0.0722	0.2035	0.0028	0.934	1813	12	1194	15	2623	8	-59.5	-58.8	
NG13-18r corr	179	38.8	1.60E+00	1985	5.0900	0.0983	0.2095	0.0038	0.951	1834	16	1226	20	2618	9	-58.2	-57.4	
NG13-22 corr	198	44.2	1.60E+00	1781	6.0957	0.1000	0.2168	0.0033	0.933	1990	14	1265	18	2858	9	-61.1	-60.5	
NG13-26 corr	40	25.4	1.70E+00	1683	26.2328	0.5536	0.6279	0.0128	0.967	3355	21	3141	51	3486	8	-12.5	-11.2	
NG13-28 corr	46	30.1	1.80E+00	18924	26.8293	0.5806	0.6438	0.0135	0.97	3377	21	3204	53	3482	8	-10.1	-8.8	
NG13-06r corr	50	22.3	2.10E+00	1871	13.7001	0.3074	0.4249	0.0092	0.967	2729	21	2283	42	3079	9	-30.6	-29.5	
NG13-07 corr	214	33.3	2.20E+00	6300	2.7720	0.0604	0.1465	0.0031	0.967	1348	16	881	17	2193	9	-63.9	-63.2	

⁽¹⁾ Total common Pb in sample (inital + blank); ⁽²⁾ Raw data corrected for fractionation; ⁽³⁾ Corrected for fractionation, blank and initial common Pb; error calculated by propagating the main sources of uncertainty; initial common Pb corrected using Stacey and Kramers (1975) model Pb;

Table 4.2 U-Pb isotopic data for monazites from the Toggekry Formation, Nondweni greenstone belt, South Africa

	U	²⁰⁶ Pb	²⁰⁶ Pbc ¹	²⁰⁶ Pb/ ²⁰⁴ Pb ²	²⁰⁷ Pb/ ²³⁵ U ³	1σ	²⁰⁶ Pb/ ²³⁸ U ³	1σ	ρ	²⁰⁷ Pb*/ ²³⁵ U ³	1σ	²⁰⁶ Pb*/ ²³⁸ U ³	1σ	²⁰⁷ Pb*/ ²⁰⁶ Pb* ³	1σ	Central	Min rim
	(ppm)	(ppm)	(%)			(abs)		(abs)		(Ma)	(Ma)	(Ma)	(Ma)		(%)	(%)	
									age			age		age		Discordance	
Sample NG 3B																	
3B-01	844	458.9	0.00E+00	11454	21.9719	0.3734	0.6154	0.0100	0.960	3182	17	3092	40	3240	7	-5.8	-4.5
3B-02	371	197.5	0.00E+00	4370	21.5004	0.4893	0.6078	0.0134	0.967	3161	22	3061	54	3226	9	-6.4	-4.9
3B-03	693	417.7	0.00E+00	8696	24.0983	0.5163	0.6795	0.0139	0.958	3272	21	3342	54	3230	9	4.5	.
3B-04_uncorr	976	514.4	0.00E+00	2214	21.4668	0.4119	0.6061	0.0112	0.959	3160	19	3054	45	3228	8	-6.7	-5.3
3B-05_uncorr	570	307.1	0.00E+00	1438	21.9783	0.4576	0.6237	0.0123	0.950	3183	20	3125	49	3220	10	-3.7	-1.9
3B-06	200	119.2	0.00E+00	2343	24.8862	0.6972	0.6920	0.0192	0.988	3304	27	3390	73	3252	7	5.5	.
3B-07	381	213.5	0.00E+00	5696	22.8744	0.5825	0.6483	0.0162	0.984	3222	25	3221	64	3222	7	.	.
3B-08	278	150.6	0.00E+00	3102	22.2663	0.6387	0.6256	0.0177	0.989	3195	28	3132	70	3235	7	-4	-3
3B-09	364	208.7	0.00E+00	6031	23.6385	0.6784	0.6638	0.0188	0.988	3254	28	3282	73	3236	7	1.8	.
3B-10	465	264.7	0.00E+00	8662	23.0807	0.6748	0.6573	0.0190	0.988	3230	28	3257	74	3214	7	1.7	.
3B-11_uncorr	423	204.4	0.00E+00	1352	19.9187	0.5206	0.5602	0.0144	0.981	3087	25	2868	59	3234	8	-14	-12.8
3B-12	461	252.7	0.00E+00	16610	22.4765	0.7774	0.6326	0.0217	0.991	3205	34	3160	86	3233	7	-2.9	-1.7
3B-13	247	142.2	0.00E+00	7498	23.6629	0.8390	0.6635	0.0232	0.985	3255	35	3281	90	3239	9	1.7	.
3B-14	314	175	0.00E+00	1410	22.7883	0.9135	0.6456	0.0256	0.989	3218	39	3211	100	3222	9	-0.4	.
3B-16_uncorr	625	317.8	0.00E+00	1033	20.8647	0.7954	0.5871	0.0221	0.988	3132	37	2978	90	3233	9	-9.8	-8.4
3B-17	302	171.4	0.00E+00	1466	23.3022	0.9091	0.6549	0.0252	0.988	3240	38	3247	98	3235	9	0.5	.
3B-18	248	138.8	0.00E+00	2893	23.0918	0.9574	0.6493	0.0266	0.99	3231	40	3226	104	3234	8	-0.3	.
3B-19	707	385.1	0.00E+00	11937	22.4047	0.9470	0.6299	0.0263	0.988	3201	41	3149	104	3234	9	-3.3	-1.7

⁽¹⁾ Total common Pb in sample (inital + blank); ⁽²⁾ Raw data corrected for fractionation; ⁽³⁾ Corrected for fractionation, blank and initial common Pb; error calculated by propagating the main sources of uncertainty; initial common Pb corrected using Stacey and Kramers (1975) model Pb;

Table 4.3 Lu-Hf isotopic data for magmatic zircons from the Toggekry Formation, Nondweni greenstone belt, South Africa.

	Age (Ma)	$^{176}\text{Hf}/^{177}\text{Hf}$	1 σ (abs)	$^{176}\text{Lu}/^{177}\text{Hf}$	1 σ (abs)	$^{176}\text{Yb}/^{177}\text{Hf}$	1 σ (abs)	ϵHf	2 σ (abs)	t_{DMZ}^1 (Ga)	2 σ (abs)	t_{DMW}^2 (Ga)
<i>Sample NG 3A</i>												
NG 3A-01	3540	0.280772	0.000022	0.002223	0.000026	0.136557	0.0026	4.664356	1.442020	3.512416	0.027728	3.497601
NG 3A-03	3540	0.280727	0.000019	0.002648	0.000093	0.163165	0.0057	2.025021	0.901695	3.614713	0.017274	3.653448
NG 3A-05	3540	0.280739	0.000019	0.002559	0.000052	0.155592	0.0023	2.668399	1.101440	3.589594	0.021244	3.615500
NG 3A-06	3540	0.280712	0.000011	0.001971	0.000053	0.105366	0.0023	3.139550	0.526137	3.570825	0.009979	3.587693
NG 3A-07	3540	0.280702	0.000018	0.002596	0.000083	0.154651	0.0038	1.260974	0.879110	3.644233	0.016760	3.698479
NG 3A-12	3540	0.280663	0.000013	0.002074	0.000064	0.12795	0.0046	1.140583	0.615155	3.647356	0.011546	3.705571
NG 3A-13	3540	0.280614	0.000099	0.002327	0.000240	0.0970107	0.0038	-1.222309	-0.463330	3.738944	-0.010140	3.844575
NG 3A-14	3540	0.280730	0.000019	0.002891	0.000096	0.171022	0.0018	1.539100	0.887080	3.634219	0.017040	3.682091
NG 3A-15	3540	0.280685	0.000014	0.001745	0.000017	0.102603	0.0018	2.728023	0.915435	3.586243	0.017324	3.611981
NG 3A-16	3540	0.280679	0.000011	0.003164	0.000180	0.116512	0.0049	-0.942792	-0.092585	3.732616	-0.002777	3.828151
NG 3A-22	3540	0.280722	0.000013	0.003842	0.000140	0.13558	0.0045	-1.061331	0.244896	3.741095	0.004087	3.835117
NG 3A-28	3540	0.280651	0.000015	0.001533	0.000025	0.0908013	0.00066	2.030784	0.947764	3.612263	0.017795	3.653108
NG 3A-29	3540	0.280688	0.000014	0.002134	0.000077	0.125156	0.0066	1.887384	0.623125	3.618937	0.011740	3.661563
NG 3A-42	3540	0.280647	0.000016	0.002257	0.000061	0.133652	0.0023	0.125670	0.843682	3.686855	0.015915	3.765320
NG 3A-38	3540	0.280702	0.000017	0.002159	0.000013	0.127463	0.0014	2.324396	1.148834	3.602242	0.021986	3.635793
NG 3A-37	3540	0.280686	0.000026	0.002278	0.000060	0.132748	0.0017	1.463555	1.561594	3.635543	0.029797	3.686543
<i>Sample NJ-10-L5A</i>												
NJ -10-L5A-01	3540	0.28072	0.000019	0.00240546	0.000033	0.145805	0.0018	2.365874	1.194005	3.601062	0.022961	3.633347
<i>Sample NG 15</i>												
NG15-04	3540	0.280593	0.00001	0.00139134	0.000047	0.0765913	0.0017	0.308381	0.484064	3.676612	0.008892	3.754569
NG15-03	3540	0.280625	0.000011	0.00190052	0.000098	0.0983507	0.0023	0.208926	0.306904	3.682275	0.005441	3.760421
NG15-01	3540	0.280578	0.0000098	0.0010572	0.000035	0.0628728	0.0014	0.587538	0.528265	3.665028	0.009693	3.738138

Table 4.3 (Continued) Lu-Hf isotopic data for magmatic zircons from the Toggekry Formation, Nondweni greenstone belt, South Africa.

	Age (Ma)	$^{176}\text{Hf}/^{177}\text{Hf}$	1 σ (abs)	$^{176}\text{Lu}/^{177}\text{Hf}$	1 σ (abs)	$^{176}\text{Yb}/^{177}\text{Hf}$	1 σ (abs)	ϵHft	2 σ (abs)	t_{DMZ}^1 (Ga)	2 σ (abs)	t_{DMW}^2 (Ga)
<i>Sample NG 13</i>												
NG13-01	3530	0.280728	0.000016	0.0014	0.0000	0.0813	0.0004	4.765609	1.097119	3.500561	0.020664	3.483784
NG13-02	3530	0.280655	0.000010	0.0007	0.0000	0.0411	0.0003	3.977769	0.691164	3.530228	0.012754	3.530365
NG13-03	3530	0.280609	0.000016	0.0017	0.0001	0.0981	0.0027	-0.194328	0.834814	3.688342	0.015498	3.776366
NG13-04	3530	0.280700	0.000016	0.0016	0.0000	0.0868	0.0006	3.347884	1.072831	3.554055	0.020262	3.567578
NG13-05	3530	0.280772	0.000012	0.0017	0.0000	0.0893	0.0026	5.771202	0.748762	3.462242	0.014232	3.424270
NG13-07	3530	0.280762	0.000012	0.0017	0.0001	0.0931	0.0052	5.470236	0.447598	3.473693	0.008590	3.442089
NG13-08	3530	0.280644	0.000010	0.0008	0.0000	0.0382	0.0005	3.313709	0.659590	3.554809	0.012192	3.569596
NG13-10	3530	0.280731	0.000012	0.0023	0.0000	0.1216	0.0024	2.729728	0.714760	3.578345	0.013718	3.604073
NG13-11	3530	0.280888	0.000012	0.0045	0.0001	0.1872	0.0017	3.082225	0.535033	3.566949	0.010865	3.583265
NG13-13	3530	0.280683	0.000015	0.0021	0.0002	0.0650	0.0055	1.570989	0.000886	3.622395	-0.000533	3.672415
NG13-14	3530	0.280695	0.000018	0.0011	0.0000	0.0649	0.0005	4.314175	1.196006	3.517663	0.022334	3.510480
NG13-15	3530	0.280666	0.000015	0.0016	0.0001	0.1006	0.0036	2.083284	0.744082	3.601891	0.013906	3.642211
NG13-19	3530	0.280691	0.000012	0.0010	0.0000	0.0490	0.0019	4.642370	0.695330	3.505526	0.012935	3.491074
NG13-21	3530	0.280679	0.000013	0.0016	0.0000	0.0919	0.0027	2.699736	0.810350	3.578502	0.015253	3.605843
NG13-22	3530	0.280685	0.000016	0.0012	0.0000	0.0632	0.0007	3.805770	1.092261	3.536666	0.020420	3.540529
NG13-24	3530	0.280601	0.000009	0.0012	0.0000	0.0667	0.0010	0.936179	0.529374	3.643759	0.009773	3.709819
NG13-25	3530	0.280761	0.000022	0.0037	0.0001	0.2537	0.0059	0.487084	1.228625	3.669906	0.024214	3.736265
NG13-26rr	3530	0.280692	0.000023	0.0021	0.0000	0.1459	0.0007	1.919634	1.591863	3.609030	0.030411	3.651861
NG13-28	3530	0.280572	0.000017	0.0013	0.0000	0.0835	0.0011	-0.390562	1.110131	3.693728	0.020636	3.787909
NG13-29	3530	0.280635	0.000014	0.0015	0.0000	0.0890	0.0012	1.419548	0.915654	3.626502	0.017159	3.681341

¹ t_{DMZ} – Zircon depleted mantle model age; ² t_{DMW} – Whole-rock depleted mantle model age (protolith age): abs - absolute.

APPENDIX 5: MAPS

APPENDIX 6: PUBLICATION

PALAEOARCHAEOAN SEA-FLOOR ALTERATION AND METAMORPHISM OF PILLOW BASALTS FROM THE NONDWENI GREENSTONE BELT, SOUTHEASTERN KAAPVAAL CRATON, SOUTH AFRICA

L. SAHA

School of Agricultural, Earth and Environmental Sciences (Discipline: Geology), University of KwaZulu Natal, Private Bag X54001, 4000 Durban, South Africa
e-mail: saha.lopamudra@gmail.com

A. HOFMANN

Department of Geology, University of Johannesburg, PO Box 524, Auckland Park 2006, Johannesburg, South Africa
e-mail: ahofmann@uj.ac.za

N. JELE

School of Agricultural, Earth and Environmental Sciences (Discipline: Geology), University of KwaZulu Natal, Private Bag X54001, 4000 Durban, South Africa
e-mail: jele.nkosinathi@gmail.com

C. HARRIS

Department of Geological Sciences, University of Cape Town, Rondebosch 7701, Cape Town, South Africa
e-mail: chris.harris@uct.ac.za

© 2012 September Geological Society of South Africa

ABSTRACT

Pillow basalts from the Witkop Formation of the Nondweni granitoid-greenstone terrain preserve evidence of Palaeoarchaeoan sea-floor alteration and high-grade metamorphism. Post-depositional sea-floor alteration preferentially affected volcanic glass and led to a marked contrast in compositions and mineral assemblages of the cores and rims of the pillows. The pillow rims have elevated Al_2O_3 , TiO_2 , Fe_2O_3 , Zr, Nb, Nd, Th concentrations and lower SiO_2 , Na_2O , Sr contents, relative to pillow cores. Igneous clinopyroxene and plagioclase is preserved exclusively in pillow cores, whereas the pillow rims consist of a metamorphic mineral assemblage of garnet-hornblende-plagioclase-chlorite-quartz. The whole rock $\delta^{18}\text{O}$ values as high as 9.6‰ suggest that hydrothermal alteration of the pillow basalts initially occurred under low-temperature conditions. $\delta^{18}\text{O}$ values as low as 2.8‰ may indicate water/rock interaction at a later stage under high-temperature conditions during metamorphism. Following sea-floor alteration, the pillow basalts were deformed and metamorphosed under amphibolite facies conditions that led to formation of hornblende-defined foliation and syntectonic garnet growth in pillow rims. Garnet-hornblende-plagioclase-quartz geothermobarometry from pillow rims reveal peak metamorphic conditions of ~6.5 kbar, 600 to 650°C. P-T pseudosection analysis also confirms that contrasting mineral assemblages in pillow cores and rims developed during metamorphism principally due to the difference in major element concentrations in these domains. P-T pseudosection analysis also predicts an isobaric cooling of the basalts along an anticlockwise P-T path. The P-T estimates indicate burial to a depth of ~17 to 20 km post-tectonic to hydrothermal alterations. The occurrence of high-grade mineral assemblages in the basalts was observed only in the vicinity of the intrusive Mvunyana granodiorite. The presence of migmatitic gneiss with steeply dipping foliations at their contact indicate that metamorphism of basalts was concomitant with intrusion of the granodiorite. Hence the time-frame of metamorphism of the Witkop Formation pillow basalts can be constrained from the crystallization age of the Mvunyana granodiorite, which is ~3.29 Ga. These observations along with the high geothermal gradient (30°C/km) recorded during peak metamorphism, and the post-peak near-isobaric cooling along an anticlockwise P-T path, are consistent with a magmatic arc setting.

Introduction

Pillow basalts occur throughout the geological record. They form the uppermost part of oceanic crust, are widespread in ophiolites and are common in Archaean greenstone belts. The pillows contain rims of unstable volcanic glass and they commonly preserve evidence of the redistribution of several elements during sea-floor

alteration and/or regional metamorphism (Hart et al., 1974; Ludden and Thompson, 1979; Kerrich and Fyfe, 1981; Ludden et al., 1982; Staudigel and Hart, 1983; Alt, 1999; Gutzmer et al., 2003; Nakamura et al., 2007). The alteration processes can lead to chemical, mineralogical and isotopic differentiations between pillow cores and rims. Experimental work on basalt-

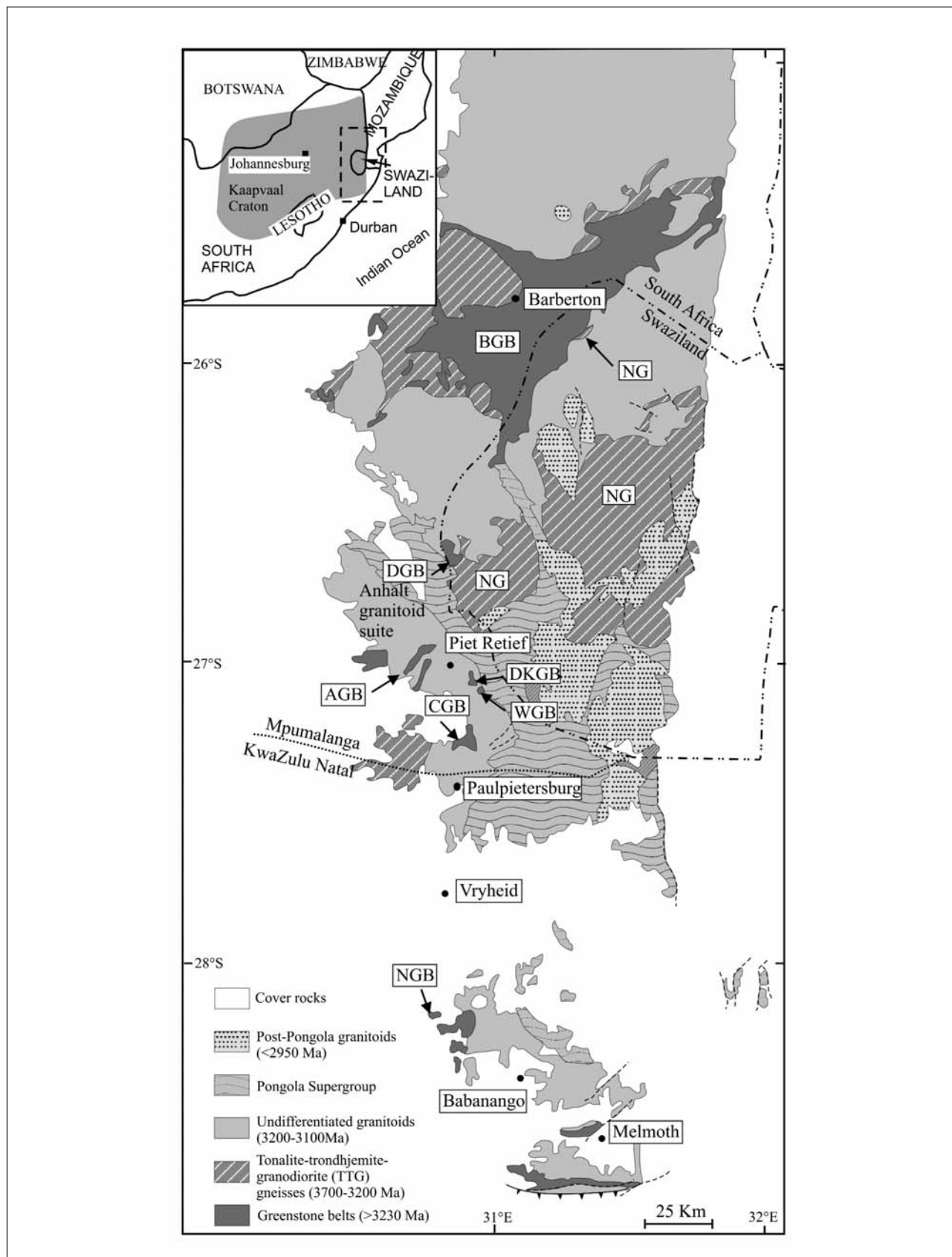


Figure 1. Geological map of the southeastern Kaapvaal craton showing distribution of the main greenstone belts (modified after Saha et al., 2010). Abbreviations: BGB (Barberton Greenstone Belt), DGB (Dwalile greenstone belt), AGB (Assegaai greenstone belt), DKGB (De Kraalen greenstone belt), CGB (Commondale greenstone belt), NGB (Nondweni greenstone belt), NG (Ngwane Gneiss). Inset map shows location of the study area and the Kaapvaal craton in southern Africa.

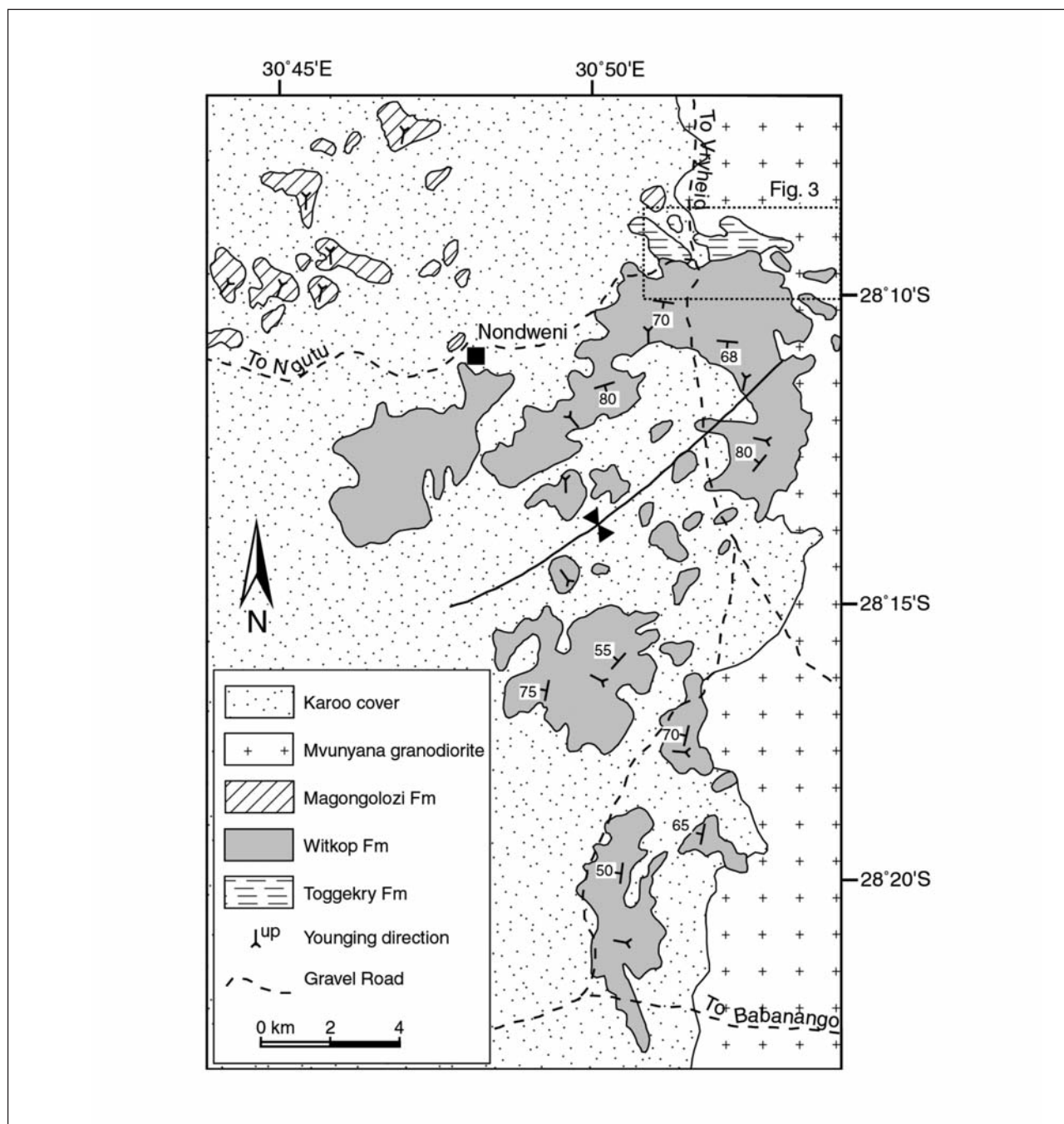


Figure 2. Geological map of the Nondweni greenstone belt showing the distribution of the Magongolozi, Toggekry and Witkop formations and their contact relationship with the intrusive Mvunyana granodiorite (modified after Wilson and Versfeld, 1994a).

seawater interaction (at high water/rock ratios) revealed that within the temperature range of 150 to 300°C, seawater, after interaction with the basalt, enriched in CaO, SiO₂, FeO, MnO, Al₂O₃, Ba and depleted in MgO, Na₂O (Menzies and Seyfried, 1979; Seyfried and Bischoff, 1979; 1981). Staudigel (2003) and German and Von Damn (2003) state that compared to other elements Fe is relatively immobile during seafloor alteration, but is enriched in hydrothermal fluids. Hofmann and Harris (2008) showed that during the Archaean, Fe was highly mobile due to the low redox potential of Archaean seawater.

In this study we show that metamorphosed pillow basalts from the c. 3.41 Ga Witkop Formation of the Nondweni greenstone belt in South Africa record sea-floor alteration. The cores and rims of pillows have contrasting trace and major element characteristics. Relict igneous mineral assemblages are preserved solely in the cores of these pillows, which are extensively replaced by amphibole. Pillow rims consist of a metamorphic mineral assemblage of garnet porphyroblasts overgrowing a hornblende-defined foliation. We present a well-constrained estimate of pressure-temperature conditions of metamorphism

of the Nondweni greenstone belt as recorded in these altered pillows.

Geology of the Nondweni Greenstone Belt

The Archaean Nondweni Greenstone Belt occurs near the southern margin of the Kaapvaal craton ~50 km north of the Natal Thrust Belt and is part of a string of Archaean greenstone belts occurring south of the Barberton Greenstone Belt. These greenstone belt fragments include those at Dwalile, Assegai, De Kraalen, Witrivier and Commondale (Figure 1). The volcano-sedimentary succession that forms the Nondweni belt is referred to as the Nondweni Group (du Toit, 1931; Linström, 1988). Based on field evidence and lithology, Versfeld (1988) subdivided the Nondweni Group into three litho-stratigraphic units (Figure 2), the Witkop, Magongolozi, and Witkop formations.

$^{207}\text{Pb}/^{206}\text{Pb}$ SHRIMP zircon ages obtained from the three formations by Xie et al. (2012) revealed that the more strongly deformed Toggekry Formation is the oldest unit (up to 3.53 Ga), whereas the Magongolozi and Witkop formations are possibly coeval (~3.43 to 3.41 Ga).

The Toggekry Formation consists of a bimodal succession of quartz-feldspar-sericite schists and variably silicified mafic schists locally showing pillow structures; the schists strike eastwest and have a near-vertical dip (Versfeld, 1988; Hofmann and Wilson, 2007). The Toggekry Formation is conformably overlain by the mafic volcanic-dominated succession of the Witkop Formation. At the eastern margin this formation is intruded by the ~3.29 Ga Mvunyana granodiorite (Matthews et al., 1989), while towards the west it is covered by Karoo sedimentary rocks.

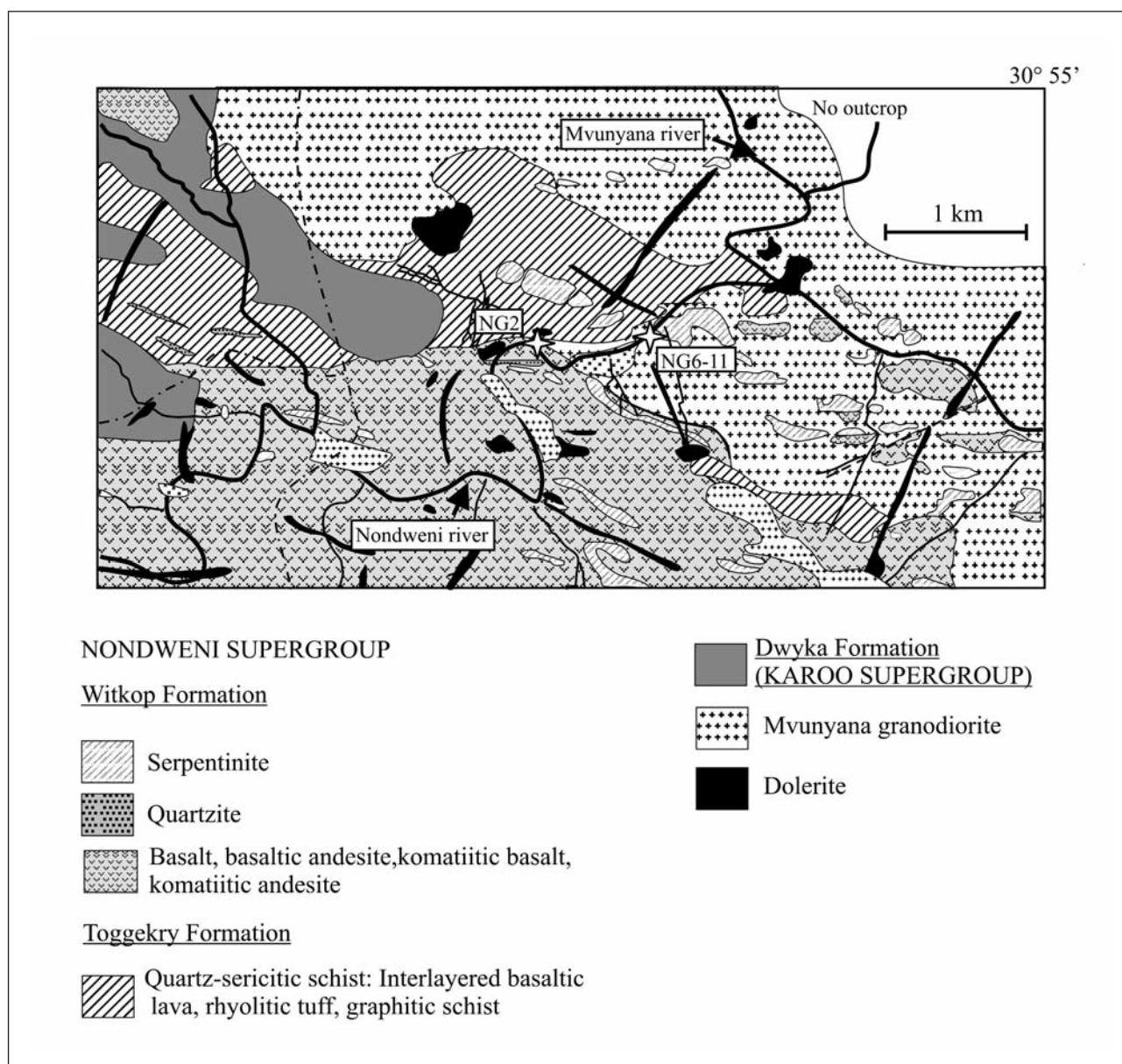


Figure 3. Geological map of the Nondweni greenstone belt in the study area, showing sample localities (modified after Versfeld, 1988).

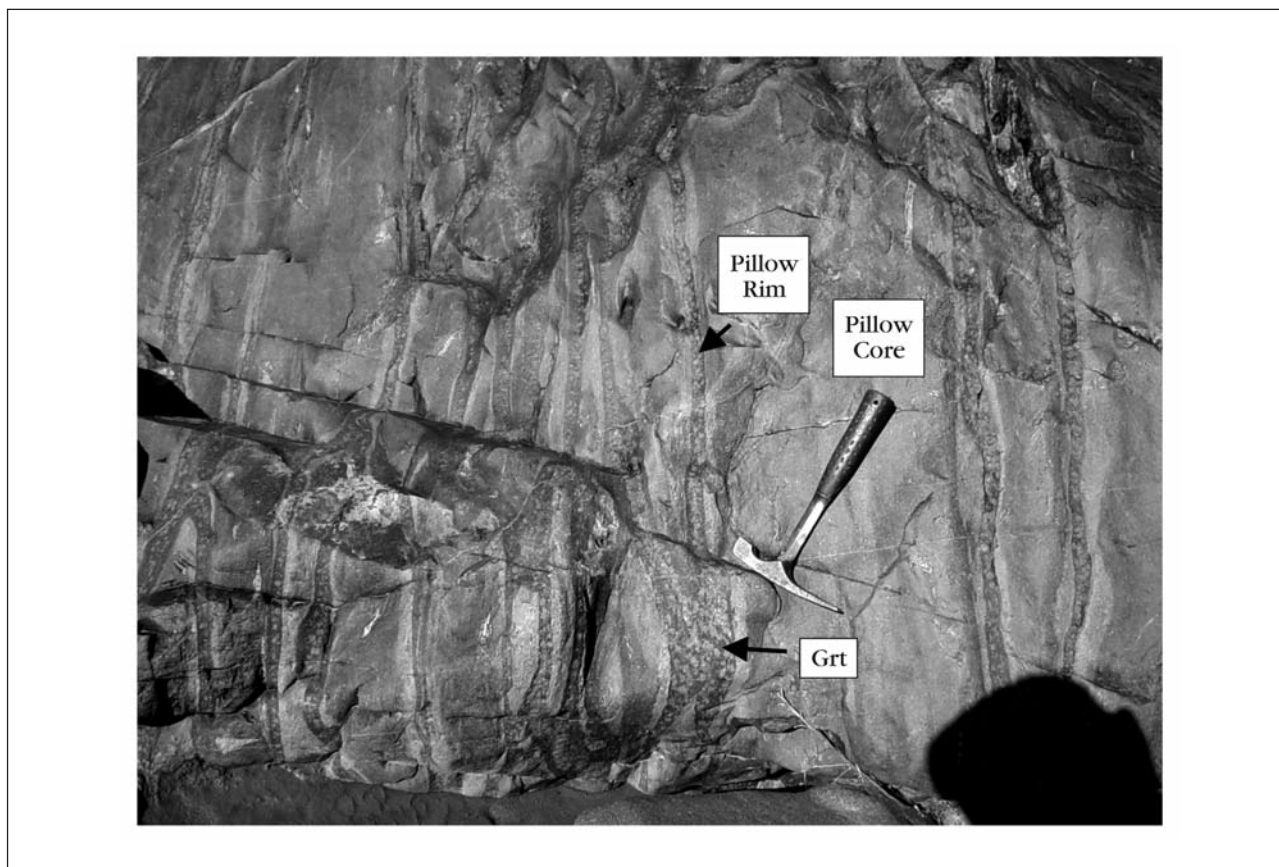


Figure 4. Field photograph of deformed pillow basalt from the Witkop Formation. Light-grey domains represent stretched pillow cores and dark-grey bands represent pillow rims. The dark-grey bands are rich in garnet porphyroblasts.

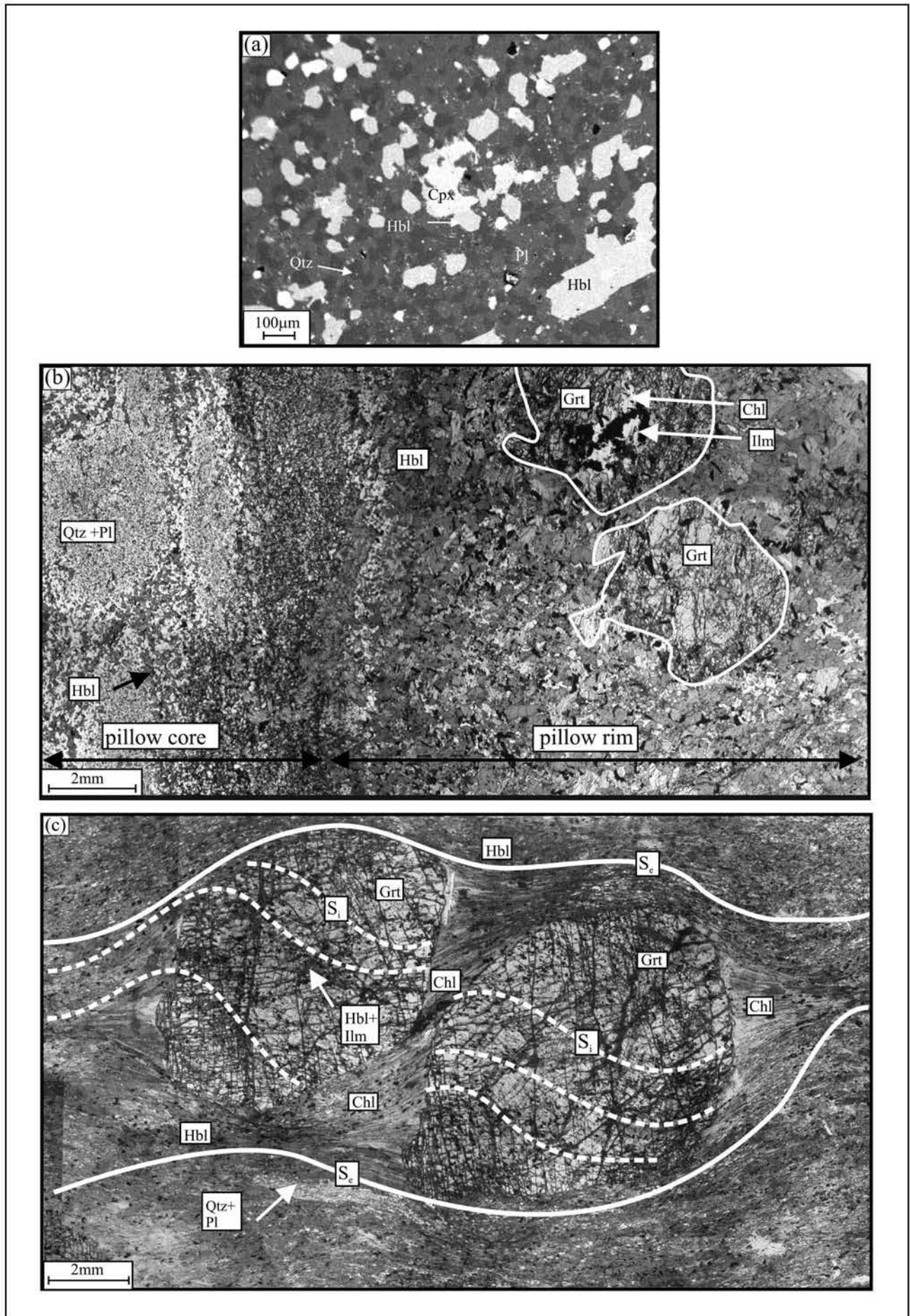
The Witkop Formation is the most extensive among the stratigraphic units of the Nondweni Group. The Witkop Formation is ~7000 m thick and mainly comprises pillowed or massive flows of basalt, komatiitic basalt and komatiite. The komatiites have a unique texture of bladed pyroxene spinifex with crystals up to 5 m in length (Wilson et al., 1989). Komatiites and basalts are commonly intercalated with bedded chert horizons (Hofmann and Wilson, 2007). Below the chert horizons, alteration zones 20 to 50 meters thick are common and are characterized by high SiO₂ contents up to 90 weight % and enrichment in K₂O (+Rb, Ba). Hofmann and Wilson (2007) concluded that these silicified zones formed by syn-depositional low-temperature (<150°C) sea-floor hydrothermal processes. Similar intercalations of mafic-ultramafic suites of rocks with chert horizons are also noted in the Onverwacht Group in the Barberton Greenstone Belt (de Wit et al., 2011). A well-preserved sedimentary succession of conglomerate, sandstone and chert (~500 m thick) occurs at the top of the Witkop Formation (Wilson and Versfeld, 1994a and b).

The Magongolozi Formation occurs as small inliers within the Phanerozoic Dwyka Group cover (Versfeld, 1988). The strike of the Magongolozi strata is mostly east to west, and dips are nearly vertical. The estimated thickness of this formation is ~7500 m. It mainly

consists of basalt, basaltic andesite and komatiitic andesite, the latter being characterized by high SiO₂ and MgO contents. These volcanic units form an interlayered sequence with locally well-preserved pillow structures and pyroxene spinifex textures (Wilson and Riganti, 1998).

The Nondweni Greenstone Belt records two major episodes of deformation (Versfeld, 1988; Matthews et al., 1989). An early deformation event (D₁) led to the development of thrust faults and associated small-scale isoclinal folds with strong penetrative axial planar cleavage, mostly recorded in the felsic schists of the Toggekry Formation. The second deformational event (D₂) led to the formation of a major synformal structure with east-northeast to west-southwest trending axial trace (Figure 2). Small-scale D₂ folds show variable plunges (near-vertical to 30°), indicating a syntectonic progressive deformation event (Versfeld, 1988). Whereas Matthews et al. (1989) considered that the D₂ folds accommodated strain related to the intrusion of the Mvunyana granodiorite; Versfeld (1988) considered the granodiorite to be post-tectonic with respect to D₂.

Versfeld (1988) suggested the regional metamorphism to be of greenschist facies as recorded by tremolite-actinolite-plagioclase-chlorite-epidote-bearing assemblages in the basalts and attributed the metamorphism to D₁. Amphibolite-facies mineral



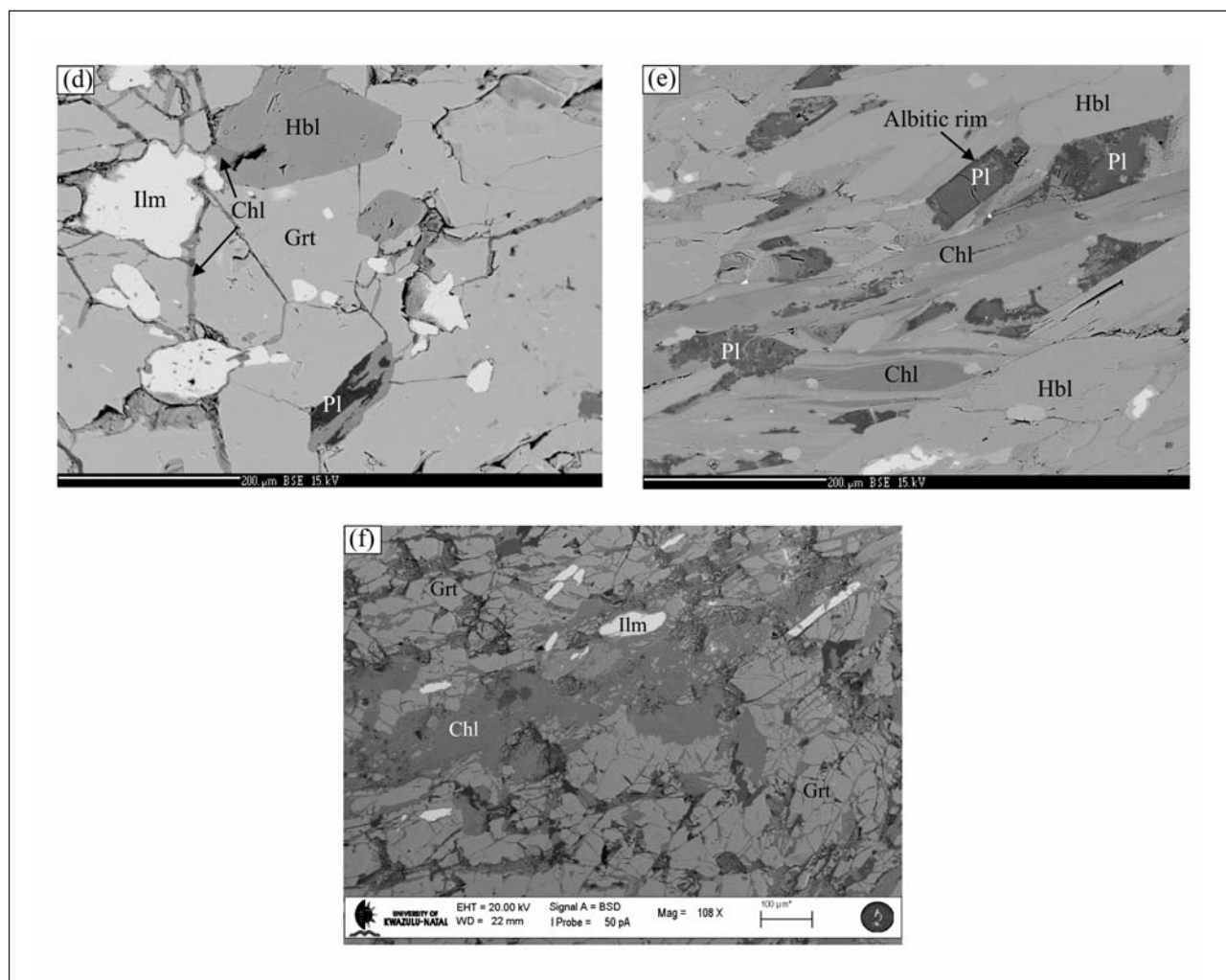


Figure 5. Back scattered electron images (**a, d-f**) and photomicrographs (**b-c**) showing textural features of pillow cores and rims. Mineral abbreviations used in the figures and tables are after Kretz (1983). (**a**) Relict clinopyroxene being replaced by hornblende at its contact with plagioclase-quartz in the core of pillow (NG10-C). Quartz and plagioclase form polygonal aggregates. (**b**) Progressive coarsening of crystal size from pillow core to rim (NG7). Note the development of hornblende-defined foliation and garnet porphyroblasts in pillow rim. (**c**) Deformed pillow rim (NG2A-R) with garnet porphyroblasts in a matrix of hornblende, plagioclase, quartz, chlorite, and ilmenite. Garnet porphyroblasts contain hornblende-ilmenite inclusion trails (S_i) and are wrapped around by hornblende-defined foliation (S_e). Chlorite replaces matrix hornblende and the margin of garnet. (**d**) Presence of hornblende-ilmenite-plagioclase inclusion in garnet porphyroblasts. Chlorite replaces garnet along fractures. (**e**) Matrix plagioclase show development of albite-rich rims around calcic cores in pillow rims (NG2-R). (**f**) Extensive replacement of garnet along its core by chlorite.

assemblages (garnet-hornblende-plagioclase) are noted mainly in basalts of the Witkop Formation at the confluence of the Mvunyana and Nondweni rivers in the north-eastern part of Nondweni greenstone belt (Figure 3; Versfeld, 1988; Mathews et al., 1989). At this locality, the Mvunyana granodiorite has extremely irregular, intrusive contacts with the supracrustal rocks, the latter containing dykes of granite and pegmatite (Figure 3). Versfeld (1988) concluded that the amphibolite-facies metamorphism occurred as a result of contact metamorphism during intrusion of the Mvunyana granodiorite. However, to date, no systematic study has been conducted to determine the exact P-T conditions of metamorphism of the Nondweni Group.

Field description of Witkop formation pillow basalts

In the study area (Figure 3), two sites have been investigated, which are characterized by the presence of stretched pillow basalts with garnet porphyroblasts in pillow rims. These sites represent the same stratigraphic level, situated close to the base of the Witkop Formation. The pillows range in size between 0.2 and 1 m and show a distinct core-rim structure (Figures 4). Contacts between pillow cores and rims are sharp. The pillow rims vary in width between 2 and 5 cm and differ from the core by being more coarse-grained, darker grey in colour and by the presence of garnet porphyroblasts (Figure 4). Garnets are characteristically absent in pillow cores.

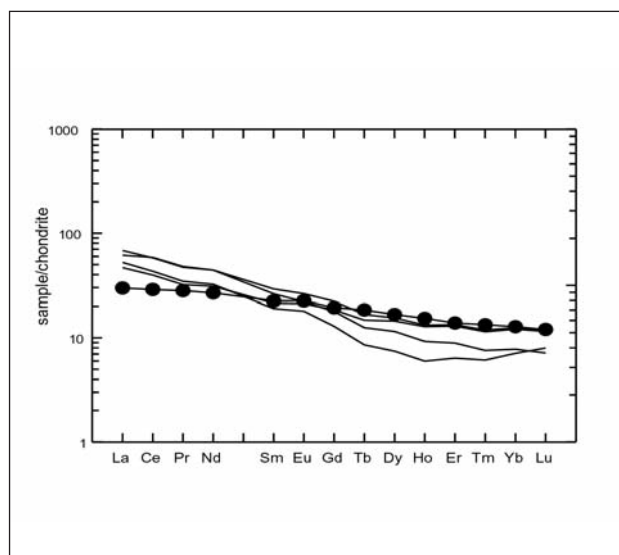


Figure 6. Chondrite-normalized REE plots of pillow cores in comparison with a sample of basaltic andesite from the Witkop Formation (filled symbol) as reported in Hofmann and Wilson (2007).

Mineralogy and texture

Pillow cores are fine-grained and mainly consist of quartz-plagioclase-hornblende-epidote±calcite with relict clinopyroxene (Figure 5a). Pillow rims are more coarse-grained compared to the cores and consist of garnet-hornblende-chlorite-plagioclase-ilmenite (Figure 5b and 5c). Hornblende defines the matrix foliation (S_e) that wraps around the garnet porphyroblasts (Figure 5c). Garnet porphyroblasts (with average diameter of ~6.4 mm) contain curved inclusion trails (S_i) defined by hornblende-ilmenite, which are continuous with the matrix foliation (Figure 5c). Plagioclase inclusions are noted at the rims of garnet porphyroblasts (Figure 5d). Plagioclase and quartz often occur in the foliation domains, plagioclase showing distinct zonation calcium-rich cores and sodic rims (Figure 5e). Garnet porphyroblasts are replaced by chlorite and epidote at their margins and along fractures (Figure 5f).

Analytical procedures

A total of 12 samples of pillow basalt were taken from two localities (Figure 3), which included six samples of pillow cores and six samples of pillow rims.

Major element concentrations were analysed by XRF spectrometry on fused glass tablets at the School of Geological Sciences, University of KwaZulu-Natal (UKZN). Trace elements were determined using a Perkin-Elmer Elan 6100 ICP-MS, also at the School of Geological Sciences, against primary standard solutions and validated against certified standard rock materials. Analytical procedures are similar to those described in Saha et al. (2010).

Oxygen isotope compositions of silicate whole rocks were determined at the University of Cape Town (UCT) using conventional extraction methods after reaction

with ClF_3 . The O_2 was converted to CO_2 using a hot platinised carbon rod. Isotope ratios were measured using a Delta XP mass spectrometer. Oxygen isotopes are expressed (Table 3) in δ -notation in per mil (‰) deviation from SMOW. The MQ internal quartz standard was analysed with every batch of samples and used to calibrate the raw data to the SMOW scale. MQ was calibrated using the value of 9.64‰ for NBS28 recommended by Coplen et al. (1983). Based on the reproducibility of MQ analysed during the course of this work, the error on a $\delta^{18}\text{O}$ determination is $\pm 0.1\text{‰}$ (1σ). Further details of the methods employed for the extraction of oxygen from silicates are given by Harris et al. (2000).

Major element mineral chemistry analyses were carried out on a JEOL (JXA 8800RL) electron microprobe at the School of Geological Sciences (UKZN). Operating conditions were 15kV with 15nA for feldspars and 20nA for other minerals. ZAF corrections were applied.

Mineral chemistry

Microprobe analyses of garnet, plagioclase, hornblende, epidote and chlorite are shown in Tables 1A, B, C and D, respectively.

In samples NG2A-R and NG2B-R, garnet porphyroblasts usually preserve compositional zoning with ~5 mol% decrease in pyrope and ~8 to 10 mol% increase in spessartine from core to rims. The resorption of garnet rims by chlorite led to lower pyrope and higher spessartine contents, however, the grossular contents remain constant from core to rim. Some of the porphyroblastic garnets in samples NG6-R, NG8-R and NG9-R are compositionally homogeneous: $\text{Prp}_{9-13}\text{Grs}_{11-17}\text{Alm}_{67-70}\text{Sps}_{3-7}$.

Plagioclase inclusions preserved in the rims of garnet porphyroblasts show anorthite content of 30 mol% (NG7-R) to 34 to 37 mol% (NG2A-R). Matrix plagioclase in samples NG2A-R and NG2B-R show depletion of anorthite contents from core (~41 to 45 mol%) to rim (~25 mol%). In sample NG7-R a significant depletion of anorthite content is noted from core (44 to 47 mol%) to rim (~7 mol%). Rims of matrix plagioclase in sample NG11-R show anorthite content of ~27 to 10 mol%. The cores of matrix plagioclase in samples NG6-R and NG11-R shows ~30 to 39 mol% of anorthite content.

Hornblende inclusions have lower X_{Mg} (0.29-0.41) than matrix hornblende (0.40-0.52). The epidotes are zoisite in composition. X_{Mg} of chlorite varies from 0.37 to 0.57.

Geochemistry

Previous studies on hydrothermal alteration of pillow basalts from the Isua Greenstone Belt (~3.6 Ga; Polat et al., 2003; andesites from Butterup Hill, Noranda, Quebec (late Archaean; Leshner et al., 1986), Zermat-Saas and Coriscan ophiolites from the Alps (Eoalpine; Bearth and Stern, 1979; Barnicoat, 1988; Miller and Cartwright, 2000; Miller et al., 2000), basalts from the Agantaufa Atoll, French Polynesia and East Pacific Rise (Schiano

et al., 1993; Schramm et al., 2005) reveal immobility of Al and Ti during such processes. Immobility of Al and Ti has also been noted during the experimental works on basalt-sea water interactions at both low and high temperatures (Seyfried et al., 1986; Berger et al., 1988). Hellman et al. (1979) also noted mobility of REE during hydrous burial metamorphism of the basalts from Maddina Volcanics, Fortescue Group, Western Australia.

In this study, major and trace element analyses were performed on 4 pairs of cores and rims from the same pillows, while only major elements were determined from the remaining samples (Table 2). The comparison between the chemical composition of cores and rims reveal marked changes, with the rims displaying compositions unlike igneous rocks, suggesting that the rims have been strongly modified during alteration processes, whereas the cores reflect more closely the primary igneous composition. Samples of pillow cores have an average SiO_2 content of 55 weight % (normalized assuming no LOI), which define them together with MgO concentrations (3.5%) and $\text{CaO}/\text{Al}_2\text{O}_3$ values (0.43) as basaltic andesites according to the scheme proposed by Wilson and Versfeld (1994b) and Riganti and Wilson (1995). However, it cannot be ascertained if the SiO_2 content of pillow cores is indeed primary, as silica content can be extremely variable in the Witkop Formation due to silicification associated with seafloor alteration (Hofmann and Wilson, 2007). Immobility element ratios of the core samples vary only slightly. For example, $\text{Al}_2\text{O}_3/\text{TiO}_2$ values have a range of

7.1 to 8.1, suggesting that the pillows were derived from compositionally similar magmas. The compositions of the pillow cores have been compared to that of the relatively unaltered basaltic andesites from the Nondweni Greenstone Belt described by Riganti and Wilson, 1995 and Hofmann and Wilson, 2007. Such comparisons indicate that the pillow cores have smooth, LREE-enriched and HREE-depleted patterns (Figure 6; $\text{La}_N/\text{Yb}_N = 3.8$ to 7.9) that are to some extent steeper than the REE patterns of the basaltic andesites.

The most striking difference in the composition of pillow rims relative to the cores are the elevated Al_2O_3 , TiO_2 and Fe_2O_3 concentrations at lower SiO_2 contents. In order to evaluate relative gains and losses of elements during alteration of the volcanic rocks, an isocon analysis was carried out (Figures 7a and 7b). Isocon analysis allows quantitative estimation of changes in mass or volume or concentrations in mass transfer processes, such as metasomatism (Grant, 1986; 2005). Altered samples of pillow rims were compared with the less altered samples of pillow cores for each core-rim pair. In an isocon diagram, if there was no change in volume during alteration, elements that show no change in concentration will fall on a line with a slope of 1, passing through the origin. A line with a slope <1 indicates an increase in the rock volume during alteration, while a slope >1 indicates a decrease in the rock volume. Elements that are enriched relative to the least altered sample will plot above this line, and those that are depleted will plot below this line (Grant, 1986; 2005).

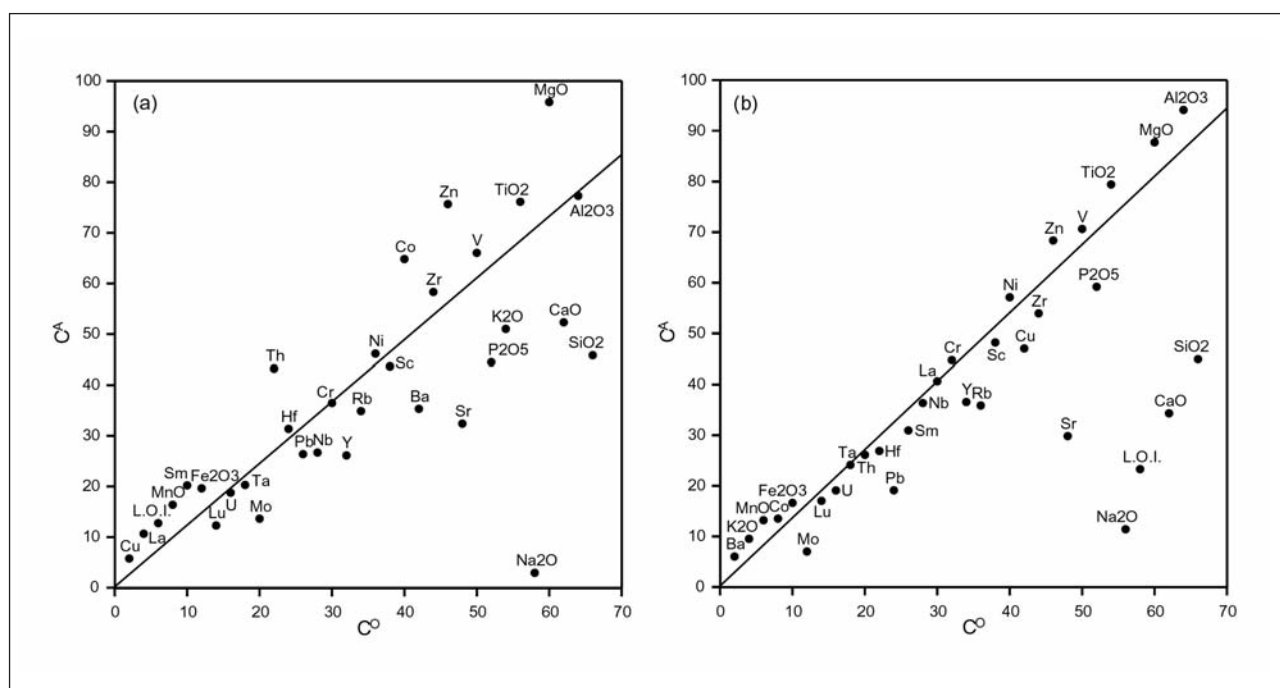


Figure 7. Isocon diagrams (Grant, 1986; 2005) for pillow cores (CO) and altered pillow rims (CA). Elements and oxides above the isocon line have been added during alteration, while those below have been depleted. (a) Core (NG6-C) vs rim (NG6-R). (b) Core (NG7-C) vs rim (NG7-R).

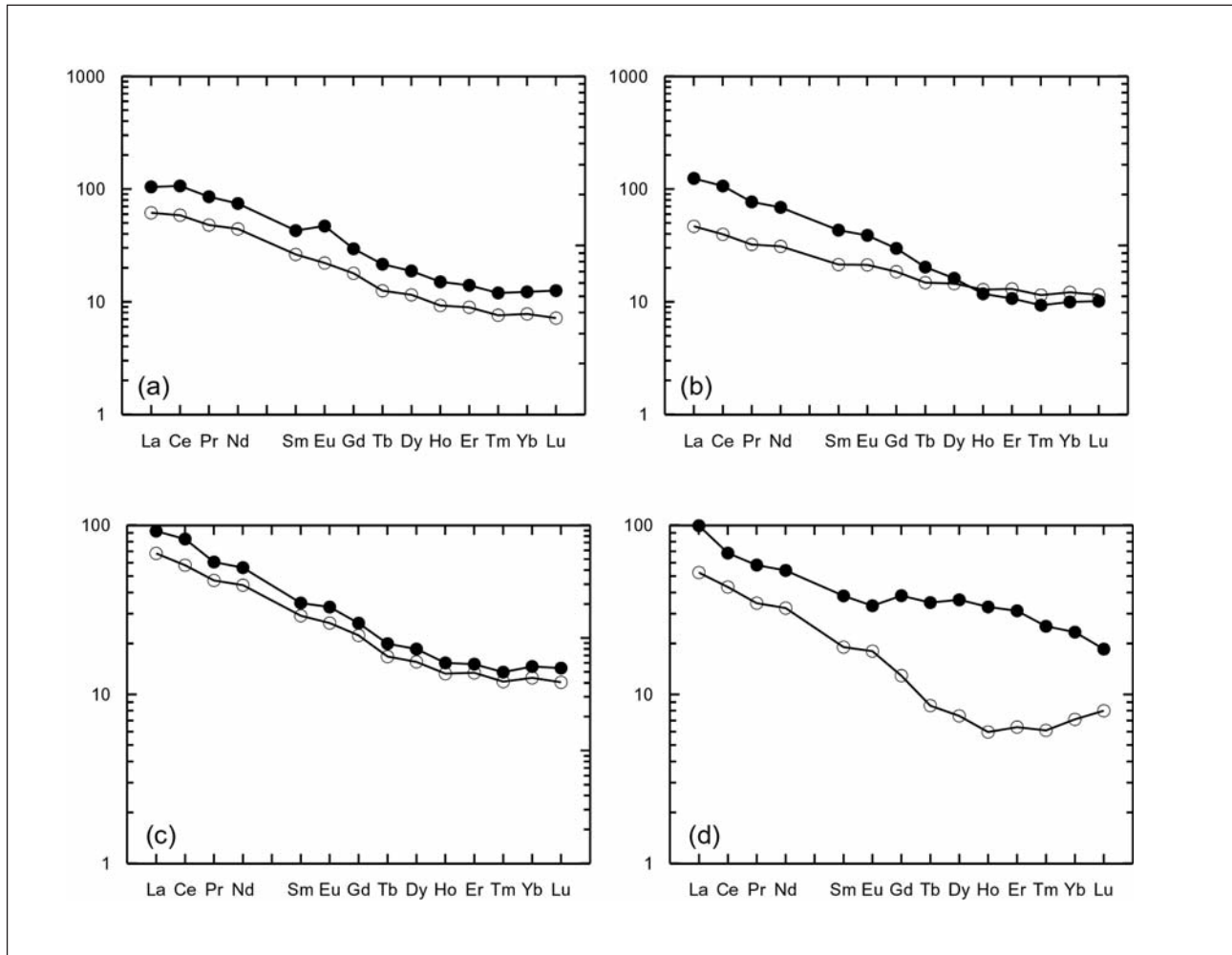


Figure 8. Chondrite-normalized REE plots of pillow cores (open symbols) vs pillow rims (filled symbol).

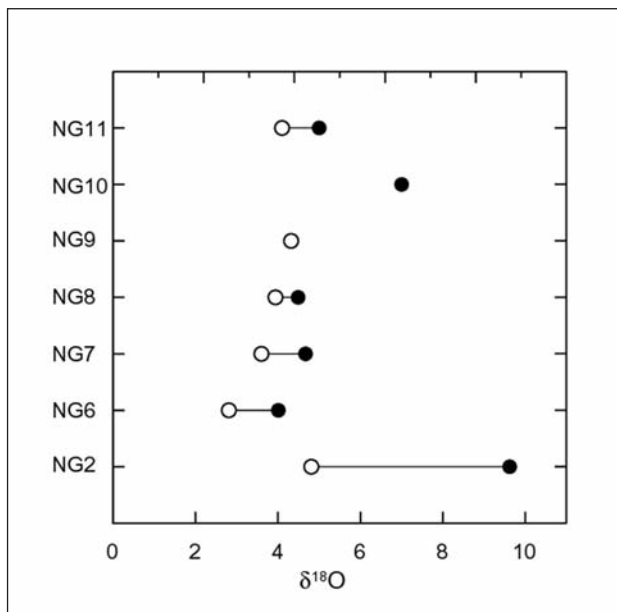


Figure 9. Oxygen isotope plot of pillow samples showing values of pillow cores (closed symbols) relative to pillow rims (open symbols). Most samples represent pairs of core and rim of the same pillow.

For four sample pairs, isocons with slopes between 1.2 and 2.4 were constructed using the relative concentrations of A_2O_3 , TiO_2 , Zr, Hf, Nb, Ta, and Sc, elements that are generally regarded to be relatively immobile during water-rock interactions. Figures 7a and 7b show isocons for two sample pairs, although isocons for the other sample pairs show similar features. The slope of the isocons > 1 indicates a decrease in the rock volume during alteration, assuming immobility of the elements used to construct the isocon. The decrease in volume can be explained by removal of specific elements during the alteration process. The isocon diagrams (Figures 7a and b) indicate that pillow rims have been affected by strong depletion of SiO_2 , Na_2O and Sr, while CaO, P_2O_5 , Mo and Pb are consistently depleted, albeit to a lesser extent. Some elements have been enriched, although to a small degree only, and these include MgO, MnO, Zn, Co, and La. All other elements were relatively immobile, or show inconsistent behaviour. For example, K_2O , together with Rb and Ba, may show large degrees of enrichment, depletion, or no change.

It is interesting to note that REE mobility during alteration gave rise to (i) an increase in the La/Yb ratio in case of NG 6 (Figure 8b) and (ii) decrease in La/Yb

Table 1A. Representative EPMA analyses of Garnet.

Sample	NG2A2-R				NG2B-R				NG6-R				NG7-R				NG8-R				NG9-R				NG11-R	
	Analyses No.	2	1	7	5	8	5	10	7	13	7	4	3	5	1	8	10	11	35	9	10	2				
Textural site	Core	Grt(P)_Core	Grt(P)_Rim*	Grt(P)_Rim*	Grt(P)_Core	Grt(P)_Rim*	Grt(P)_Rim*	Grt(P)_Chl	Grt(P)_Rim^	Grt(P)_Rim^	Grt(P)_fine	Grt(P)_fine	Grt(P)_Hbl	Grt(P)_Rim^	Grt(P)_Rim^	Grt(P)_Hbl	Grt(P)_Core	Grt(P)_Core	Grt(P)_Rim^	Grt(P)_Core	Grt(P)_Core	Grt(P)_Chl				
SiO ₂	37.50	37.93	38.11	38.54	38.12	38.12	37.91	38.19	38.53	38.08	37.60	38.35	37.98	38.02	38.46	38.24	38.02	38.38	38.20	38.05	38.67					
TiO ₂	0.17	0.08	0.03	0.01	0.04	0.04	0.06	0.04	0.04	0.03	0.01	0.10	0.02	0.03	0.00	0.03	0.01	0.06	0.07	0.05	0.07					
Al ₂ O ₃	20.68	20.90	20.71	20.92	21.06	21.06	20.60	20.88	21.05	20.59	20.72	21.08	20.75	20.92	21.46	21.21	20.82	21.09	21.03	20.80	21.16					
Cr ₂ O ₃	0.00	0.00	0.00	0.00	0.02	0.02	0.08	0.00	0.00	0.00	0.00	0.00	0.00	0.00	0.00	0.00	0.06	0.00	0.01	0.00	0.01					
FeO	29.73	31.91	31.17	32.45	31.42	31.42	30.64	32.01	32.33	30.81	29.39	30.38	32.90	32.97	31.95	30.57	32.26	32.19	30.85	30.38	30.89					
MnO	5.70	3.62	2.39	1.68	3.36	3.36	5.53	1.51	1.27	3.08	2.97	2.09	1.70	1.04	1.23	1.91	1.28	1.46	2.50	2.38	3.30					
MgO	2.04	2.27	3.29	3.59	2.71	2.71	1.91	4.25	2.99	2.08	2.22	2.44	2.66	2.82	3.57	2.83	3.16	2.81	2.44	2.48	2.67					
CaO	3.70	3.65	3.57	3.19	3.49	3.49	3.60	3.39	3.75	4.68	5.63	5.65	3.85	3.64	3.57	4.93	3.71	4.44	4.96	5.40	3.9					
Totals	99.52	100.36	99.28	100.38	100.22	100.22	100.34	100.14	99.96	99.35	98.54	100.09	99.85	99.44	100.24	99.72	99.32	100.43	100.06	99.54	100.70					
Oxygens	12	12	12	12	12	12	12	12	12	12	12	12	12	12	12	12	12	12	12	12	12					
Si	3.030	3.035	3.055	3.054	3.040	3.040	3.044	3.030	3.063	3.064	3.042	3.048	3.044	3.049	3.041	3.045	3.048	3.045	3.044	3.046	3.059					
Ti	0.010	0.005	0.002	0.000	0.002	0.002	0.003	0.001	0.002	0.002	0.001	0.006	0.001	0.002	0.000	0.002	0.001	0.003	0.004	0.003	0.004					
Al	1.970	1.971	1.957	1.954	1.980	1.980	1.950	1.992	1.973	1.954	1.977	1.975	1.960	1.978	2.000	1.991	1.968	1.973	1.976	1.964	1.974					
Cr	0.000	0.000	0.000	0.000	0.001	0.001	0.005	0.001	0.000	0.000	0.000	0.000	0.000	0.000	0.000	0.000	0.004	0.000	0.001	0.000	0.001					
Fe ²⁺	2.009	2.135	2.089	2.150	2.096	2.096	2.058	2.101	2.150	2.073	1.989	2.019	2.206	2.211	2.113	2.035	2.162	2.136	2.056	2.034	2.044					
Mn	0.390	0.245	0.162	0.113	0.227	0.227	0.376	0.100	0.085	0.210	0.204	0.141	0.115	0.071	0.082	0.129	0.087	0.098	0.169	0.161	0.221					
Mg	0.245	0.270	0.393	0.424	0.322	0.322	0.228	0.497	0.355	0.250	0.267	0.289	0.317	0.337	0.421	0.335	0.377	0.333	0.290	0.296	0.314					
Ca	0.320	0.313	0.307	0.271	0.298	0.298	0.310	0.249	0.320	0.404	0.489	0.481	0.331	0.313	0.303	0.421	0.319	0.378	0.424	0.464	0.333					
Sum	7.975	7.974	7.965	7.966	7.966	7.966	7.975	7.972	7.948	7.957	7.969	7.959	7.975	7.961	7.960	7.958	7.966	7.966	7.964	7.968	7.950					
X _{Grp}	0.08	0.09	0.13	0.14	0.11	0.11	0.08	0.17	0.12	0.09	0.09	0.10	0.11	0.11	0.14	0.11	0.13	0.11	0.10	0.10	0.11					
X _{Gr}	0.11	0.11	0.10	0.09	0.10	0.10	0.10	0.08	0.11	0.14	0.17	0.16	0.11	0.11	0.10	0.14	0.11	0.13	0.14	0.16	0.11					
X _{Alm}	0.68	0.72	0.71	0.73	0.71	0.71	0.69	0.71	0.74	0.71	0.67	0.69	0.74	0.75	0.72	0.70	0.73	0.73	0.70	0.69	0.70					
X _{Sps}	0.13	0.08	0.05	0.04	0.08	0.08	0.13	0.03	0.03	0.07	0.07	0.05	0.04	0.02	0.03	0.04	0.03	0.03	0.06	0.05	0.08					

Grt(P): Porphyroblastic garnet; ^: against; Rim*: rims containing prograde plagioclase inclusions. X_{Grp}: Mg/(Mg+Ca+Fe²⁺+Mn); X_{Gr}: Ca/(Mg+Ca+Fe²⁺+Mn); X_{Alm}: Fe²⁺/(Mg+Ca+Fe²⁺+Mn); X_{Sps}: Mn/(Mg+Ca+Fe²⁺+Mn).

Table 1B. Representative EPMA analyses of Feldspar.

Sample	NG2A-R			NG2B-R			NG6R-R			NG7-R			NG9-R			NG11-R			NG8-R							
	Analyses No.	22	24	10	24	23	27	26	8	11	7	18	20	5	8	7	18									
Textural site	Matrix	Core	Matrix	I∧Grt(P)	Matrix	Core	Matrix	Core	Matrix	Core	Matrix	Core	Matrix	Core	Matrix	Core	Matrix	Core	Matrix	Core	Matrix	Core	Matrix	Core	Matrix	Core
SiO ₂	57.88	60.27	58.63	59.03	57.17	59.37	59.06	58.58	56.89	56.74	66.83	60.75	58.86	66.27	61.00	61.02	59.55									
TiO ₂	0.04	0.06	0.02	0.07	0.00	0.06	0.00	0.01	0.00	0.00	0.00	0.01	0.01	0.00	0.04	0.05	0.02									
Al ₂ O ₃	26.07	23.13	25.38	25.8	27.26	23.82	26.40	26.23	26.23	27.33	20.59	25.16	26.01	21.38	23.53	25.24	25.40									
Cr ₂ O ₃	0.00	0.00	0.00	0.00	0.01	0.00	0.00	0.00	0.00	0.00	0.00	0.00	0.00	0.00	0.00	0.00	0.00									
FeO	0.35	0.31	0.33	0.47	0.48	0.47	0.30	0.24	0.17	0.26	0.23	0.13	0.31	0.21	0.23	0.22	0.13									
MnO	0.01	0.05	0.03	0.00	0.01	0.03	0.00	0.00	0.00	0.00	0.01	0.05	0.01	0.00	0.05	0.00	0.01									
MgO	0.00	0.00	0.00	0.00	0.00	0.00	0.00	0.00	0.00	0.00	0.00	0.00	0.00	0.00	0.00	0.00	0.00									
CaO	8.38	5.12	6.84	7.64	9.33	4.95	8.00	8.40	8.93	9.43	1.47	6.41	8.29	2.15	5.48	6.22	7.09									
Na ₂ O	6.78	8.41	6.99	7.21	6.17	4.72	7.06	6.89	6.18	5.93	10.90	8.32	7.04	10.74	8.01	8.04	7.51									
K ₂ O	0.04	0.04	0.61	0.06	0.04	5.35	0.08	0.05	0.11	0.04	0.13	0.06	0.04	0.06	0.58	0.22	0.02									
Totals	99.60	97.39	98.87	100.35	100.47	98.82	100.90	100.40	98.54	99.75	100.19	100.91	100.59	100.84	98.94	101.04	99.73									
Oxygens	8	8	8	8	8	8	8	8	8	8	8	8	8	8	8	8	8									
Si	2.602	2.745	2.648	2.629	2.553	2.716	2.615	2.610	2.586	2.550	2.928	2.682	2.618	2.891	2.741	2.688	2.660									
Ti	0.001	0.002	0.001	0.002	0.000	0.002	0.000	0.000	0.000	0.000	0.000	0.000	0.000	0.000	0.001	0.002	0.001									
Al	1.382	1.242	1.352	1.355	1.435	1.285	1.378	1.378	1.406	1.448	1.063	1.310	1.364	1.100	1.247	1.311	1.337									
Cr	0.000	0.000	0.000	0.000	0.000	0.000	0.000	0.000	0.000	0.000	0.000	0.000	0.000	0.000	0.000	0.000	0.000									
Fe ³⁺	0.013	0.012	0.013	0.018	0.018	0.018	0.011	0.009	0.007	0.010	0.009	0.005	0.011	0.008	0.009	0.008	0.005									
Fe ²⁺	0.000	0.000	0.000	0.000	0.000	0.000	0.000	0.000	0.000	0.000	0.000	0.000	0.000	0.000	0.000	0.000	0.000									
Mn	0.000	0.002	0.001	0.000	0.000	0.001	0.000	0.000	0.000	0.000	0.000	0.002	0.000	0.000	0.002	0.000	0.000									
Mg	0.000	0.000	0.000	0.000	0.000	0.000	0.000	0.000	0.000	0.000	0.000	0.000	0.000	0.000	0.000	0.000	0.000									
Ca	0.404	0.250	0.331	0.365	0.447	0.242	0.380	0.401	0.435	0.454	0.069	0.303	0.395	0.101	0.264	0.293	0.339									
Na	0.591	0.743	0.612	0.623	0.534	0.419	0.607	0.596	0.545	0.516	0.926	0.712	0.607	0.909	0.698	0.686	0.650									
K	0.002	0.002	0.035	0.003	0.002	0.313	0.005	0.003	0.006	0.002	0.007	0.003	0.002	0.003	0.033	0.013	0.001									
Sum	4.996	4.998	4.993	4.995	4.989	4.996	4.996	4.997	4.984	4.980	5.002	5.018	4.998	5.011	4.995	5.001	4.993									
X _{An}	0.41	0.25	0.34	0.37	0.45	0.25	0.38	0.40	0.44	0.47	0.07	0.30	0.39	0.10	0.27	0.30	0.34									

∧: against; I: inclusion; X_{An}: Ca/(Ca+Mg+Fe²⁺).

Table 1D. Representative EPMA analyses of chlorite, epidote.

Sample	NG2A-R				NG2B-R				NG6-R				NG7-R				NG8-R				NG11-R															
	14	25	20	19	19	21	26	15	19	21	13	26	31	33	17	38	9	14	25	20	19	21	13	26	31	33	17	38	9							
Analyses No.	Chl_	Chl/Grt_	Ep_	Chl_	Chl_	Mu_	Ep_	Ep_	Ep_	Chl_	Chl_	Chl_	Ep_	Ep_	Ep_	Ep_	Chl_	Chl_	Chl_	Chl_	Ep_	Ep_	Ep_	Chl_	Chl_	Ep_	Ep_	Ep_	Chl_	Chl_						
Textural site	Matrix	Rim	Matrix																																	
SiO ₂	26.11	26.23	41.41	25.00	25.96	46.21	40.04	38.84	26.27	25.59	27.48	39.74	40.61	39.70	25.85	25.49																				
TiO ₂	0.05	0.05	0.01	0.10	0.02	0.15	0.08	0.02	0.01	0.02	0.11	0.00	0.05	0.01	0.07	0.03																				
Al ₂ O ₃	21.77	21.26	30.41	22.16	19.86	31.19	30.96	30.32	19.34	19.83	18.25	30.11	31.10	30.45	19.91	20.05																				
Cr ₂ O ₃	0.00	0.00	0.00	0.00	0.00	0.00	0.00	0.00	0.00	0.00	0.00	0.00	0.00	0.00	0.00	0.00																				
FeO	21.91	23.34	0.87	23.44	26.31	4.96	1.76	4.93	30.16	31.19	29.27	4.11	2.19	2.98	29.68	28.84																				
MnO	0.10	0.28	0.02	0.10	0.18	0.01	0.02	0.14	0.56	0.51	0.50	0.02	0.02	0.09	0.43	0.57																				
MgO	16.36	15.54	0.00	14.99	13.30	2.65	0.00	0.00	10.89	10.21	11.69	0.00	0.00	0.00	10.95	11.06																				
CaO	0.02	0.00	22.87	0.00	0.01	0.03	24.43	21.97	0.03	0.00	0.00	24.33	23.69	24.07	0.01	0.00																				
Na ₂ O	0.01	0.00	0.21	0.00	0.00	0.02	0.00	0.03	0.00	0.01	0.00	0.00	0.12	0.02	0.02	0.00																				
K ₂ O	0.01	0.00	0.71	0.01	0.02	9.66	0.00	0.02	0.01	0.08	0.23	0.01	0.00	0.00	0.03	0.03																				
Totals	86.33	86.71	96.52	85.80	85.66	95.27	97.28	96.83	87.26	87.43	87.54	98.75	98.03	97.59	86.95	86.08																				
Oxygens	14	14	12.5	14	14	11	12.5	12.5	14	14	14	12.5	12.5	12.5	14	14																				
Si	2.735	2.76	3.185	2.664	2.816	3.107	3.078	3.012	2.857	2.797	2.963	3.031	3.085	3.050	2.815	2.797																				
Ti	0.004	0.004	0.000	0.008	0.001	0.007	0.004	0.001	0.001	0.001	0.009	0.000	0.003	0.000	0.005	0.003																				
Al	2.690	2.637	2.757	2.784	2.539	2.473	2.806	2.772	2.480	2.556	2.319	2.707	2.785	2.758	2.556	2.593																				
Cr	0.000	0.000	0.000	0.000	0.000	0.000	0.000	0.000	0.000	0.000	0.000	0.000	0.000	0.000	0.000	0.000																				
Fe ³⁺	0.000	0.000	0.000	0.000	0.000	0.195	0.000	0.317	0.000	0.000	0.000	0.251	0.138	0.160	0.000	0.000																				
Fe ²⁺	1.920	2.054	0.056	2.089	2.387	0.084	0.113	0.003	2.744	2.852	2.639	0.011	0.001	0.031	2.703	2.647																				
Mn	0.008	0.025	0.001	0.009	0.017	0.000	0.001	0.010	0.052	0.047	0.045	0.001	0.001	0.006	0.040	0.053																				
Mg	2.555	2.438	0.000	2.380	2.150	0.266	0.000	0.000	1.765	1.664	1.878	0.000	0.000	0.000	1.776	1.809																				
Ca	0.002	0.000	1.885	0.000	0.001	0.002	2.012	1.825	0.003	0.000	0.000	1.988	1.928	1.982	0.001	0.000																				
Na	0.003	0.000	0.032	0.000	0.000	0.003	0.000	0.004	0.000	0.001	0.000	0.000	0.017	0.003	0.004	0.000																				
K	0.001	0.000	0.07	0.002	0.003	0.829	0.000	0.002	0.001	0.011	0.032	0.000	0.000	0.000	0.005	0.004																				
Sum	9.917	9.918	7.987	9.937	9.915	6.967	8.015	7.945	9.903	9.929	9.885	7.990	7.959	7.992	9.906	9.906																				
X _{Mg}	0.57	0.54		0.53	0.47				0.39	0.37	0.42				0.40	0.41																				

I: Inclusion; Δ: against; X_{Mg}: Mg/(Mg+Fe²⁺).

Table 2A. Major (wt%) and trace element (ppm) concentrations of pillow basalts (cores and rims).

	NG2B-C	NG2B-R	NG6-C	NG6-R	NG7-C	NG7-R	NG8-C	NG8-R
SiO ₂	50.47	32.98	47.59	33.03	52.63	35.79	68.61	35
TiO ₂	1.99	2.91	2.03	2.76	1.88	2.77	1.59	2.83
Al ₂ O ₃	15.99	20.35	16.42	19.83	13.35	19.63	11.47	18.01
Fe ₂ O ₃	16.51	25.12	17.83	29.15	16.82	27.92	6.45	28.69
MnO	0.36	0.41	0.39	0.79	0.34	0.74	0.12	0.84
MgO	3.88	7.58	4.19	6.69	4.05	5.92	1.58	6.49
CaO	5.67	6.36	6.39	5.39	7.14	3.95	5.06	7.24
Na ₂ O	3.40	1.58	3.57	0.18	2.95	0.60	3.98	0.40
K ₂ O	0.49	0.89	0.90	0.85	0.56	1.33	0.09	0.20
P ₂ O ₅	0.56	0.88	0.62	0.53	0.58	0.66	0.53	0.58
Total	99.31	99.06	99.93	99.20	100.30	99.31	99.49	100.27
L.O.I.	0.05	2.98	2.01	4.27	3.44	1.38	0.91	2.61
Sc	17	32	35	40	31	40	27	39
V	113	238	265	350	244	345	194	334
Cr	188	323	25	30	24	33	15	20
Co	35	72	45	73	42	71	36	57
Ni	93	151	33	42	32	45	22	36
Cu	61	12	88	252	55	61	35	26
Zn	74	310	181	297	149	221	189	251
Rb	5.10	51.20	28.00	28.70	25.80	25.70	25.10	6.20
Sr	328.10	111.10	195.50	132.00	209.60	130.10	166.20	92.70
Y	17.70	27.50	26.00	21.20	25.20	27.10	11.20	59.00
Zr	120.40	276.10	121.90	161.60	143.00	175.30	53.50	186.60
Nb	12.12	20.62	9.59	9.14	8.78	11.39	5.65	18.38
Mo	0.49	1.18	0.59	0.40	0.29	0.17	0.36	0.14
Ba	10.20	137.10	112.30	94.50	96.90	290.70	75.10	16.80
La	19.01	32.31	14.42	38.38	21.09	28.55	16.24	30.73
Ce	47.21	85.79	31.96	85.65	46.79	66.83	34.75	55.16
Pr	5.82	10.39	3.92	9.35	5.74	7.38	4.22	7.08
Nd	26.48	44.54	18.53	41.12	26.47	33.61	19.38	32.33
Sm	5.11	8.32	4.15	8.39	5.68	6.75	3.70	7.44
Eu	1.62	3.44	1.56	2.85	1.94	2.41	1.32	2.45
Gd	4.62	7.62	4.77	7.68	5.76	6.81	3.33	9.91
Tb	0.59	1.02	0.70	0.96	0.79	0.94	0.41	1.65
Dy	3.70	6.03	4.65	5.18	5.00	5.95	2.40	11.64
Ho	0.66	1.08	0.92	0.84	0.95	1.10	0.43	2.36
Er	1.87	2.93	2.73	2.24	2.81	3.16	1.34	6.54
Tm	0.25	0.39	0.37	0.30	0.38	0.44	0.20	0.82
Yb	1.63	2.55	2.53	2.08	2.61	3.05	1.48	4.87
Lu	0.23	0.40	0.37	0.33	0.38	0.46	0.26	0.60
Hf	2.54	5.63	2.57	3.36	2.99	3.65	1.30	3.89
Ta	0.65	1.11	0.54	0.61	0.51	0.68	0.47	0.78
Pb	4.53	3.97	4.69	4.76	4.68	3.72	11.07	4.00
Th	1.64	2.85	1.49	2.92	1.93	2.52	1.74	2.76
U	0.43	0.73	0.48	0.56	0.46	0.55	0.35	0.57
$\delta^{18}\text{O}_{\text{SMOW}}$	9.6	4.8	4.0	2.8	4.7	3.6	4.5	3.9

Table 2B. Major element (wt%) concentrations of pillow basalts (cores and rims).

	NG10-C	NG9-R	NG11-C	NG11-R
SiO ₂	61.51	42.81	51.03	44.7
TiO ₂	1.72	2.08	1.43	1.76
Al ₂ O ₃	13.53	17.03	16.08	14.97
Fe ₂ O ₃	9.22	20.34	13.6	20.61
MnO	0.23	0.49	0.40	0.43
MgO	2.36	4.58	4.72	6.16
CaO	6.62	8.21	8.42	8.09
Na ₂ O	4.10	2.08	3.11	1.70
K ₂ O	0.36	0.99	1.26	1.21
P ₂ O ₅	0.59	0.66	0.37	0.48
Total	100.25	99.27	100.42	100.11
L.O.I.	0.25	1.33	1.66	2.39
$\delta^{18}\text{O}_{\text{SMOW}}$	7.0	4.3	5.0	4.1

ratio in case of NG8 (Figures 8d) probably due to the addition of La and other LREE. One sample shows a depletion of HREE in the core. This depletion is mirrored probably by addition of HREE in the pillow rim (Figures 8a-d) or may reflect palagonitisation, a phenomenon described by Pauly et al., (2011).

Oxygen isotope analysis

In each analyzed pillow, the rims have lower $\delta^{18}\text{O}$ values than the cores (Figure 9). Whereas 4 sample pairs show very similar values for core ($4.5 \pm 0.4\text{‰}$) and rim ($3.6 \pm 0.6\text{‰}$), one sample pair has higher values for both core (9.6‰) and rim (4.8‰). There are no correlations between oxygen isotope values and major or trace element concentrations. A weak negative correlation ($R^2 = 0.48$), however, exists between $\delta^{18}\text{O}$ values and loss on ignition. Similar values ($\delta^{18}\text{O} \sim 7.8\text{‰}$) have also been made from the cores of the pillow basalts in the Isua Greenstone Belt by Furnes et al. (2007).

Metamorphism

Evolution of mineral assemblages in the cores and rims of the pillows

In the pillow cores, primary clinopyroxene and plagioclase are replaced at their margins by hornblende and epidote (Figure 5a), indicating that metamorphism of the pillows occurred under amphibolite facies conditions under H₂O-present condition. Coarse quartz grains with wavy grain boundaries are present in the pillow cores (Figure 5b). Hornblende forms a foliation in the cores of deformed pillows (Figure 5b).

The pillow rims are characterized by a coarsening of crystal size and the presence of a hornblende foliation overgrown by garnet, the latter containing plagioclase-hornblende-quartz-ilmenite inclusions (Figures 5c and d). Continuity of inclusion trails in garnet porphyroblasts with matrix foliation indicates syntectonic growth (Figure 5c). The presence of hornblende-plagioclase-quartz inclusions in garnet indicates the following reaction in the pillow rims during peak metamorphism:



The reaction (equation 1) proceeds with an increase in pressure (Štípská et al., 2006), which indicates that the basalts were subjected to burial during garnet formation (peak metamorphism). The increase in 5 to 8 mol% of pyrope from core to rim of the garnet porphyroblasts (Table 1A) indicates a slight increase in temperature during garnet growth. Decrease in pyrope content of the garnet (Table 1A) at its rims against chlorite-epidote indicates post-peak cooling. Since grossular contents of garnets do not show any change from core to rim, it can be concluded that post-peak cooling occurred at isobaric conditions.

Geothermobarometry

To determine the P-T conditions of metamorphism of the pillow basalts average P-T have been calculated from the garnet-hornblende-plagioclase-quartz assemblage in the pillow rims using the internally consistent thermodynamic dataset of Holland and Powell (1998) and THERMOCALC ver. 3.25 (Table 3). The results are shown in Table 4. In sample NG2A-R garnet rims with plagioclase and hornblende inclusions in textural equilibrium yield P-T conditions of 5.9 kbar, 660°C. In samples NG8-R and NG9-R, garnet and matrix plagioclase-hornblende at textural equilibrium yield P-T conditions of 6 to 6.5 kbar, 600 to 640°C. It can be concluded that during garnet formation at the expense of hornblende and plagioclase, the basalts were subjected to P-T conditions of ~6.5 kbar and 650°C.

Pseudosections

T-X, P-X and P-T pseudosections (temperature-composition and pressure-composition) have been constructed to further constrain the mineralogical evolutions of the pillow basalts. For the T-X and P-X pseudosections, the pressure and temperature were fixed from thermobarometry (see geothermobarometry section). Sample NG8 shows the most pronounced contrast in the major element contents of pillow core (NG8-C) rim (NG8-R) as compared to other samples (Table 2). The bulk compositions of NG8-C and NG8-R have, therefore, been used to construct the T-X and P-X pseudosections in order to demonstrate generation of different mineral assemblages at pillow core and rim with respect to changing pressure and temperature. The pseudosections have been constructed in the system Na₂O-CaO-FeO-MgO-Al₂O₃-SiO₂-H₂O (Figures 10a and b). MnO has been excluded from the bulk composition during calculations due to its low proportion (~0.11 mol% in pillow core and 0.74 mol% in pillow rim). TiO₂ has been excluded as ilmenite is the only titanium-bearing phase and the titanium content of hornblende is very low (~0.03 wt%) in the sample. H₂O contents of the bulk compositions have been determined from the loss on ignition. The pseudosections were constructed using the *People_X* software (Connolly, 2005). The mixing

Table 3. Results of geothermobarometry (average P-T, THERMOCALC).

Sample No.	Average Pressure (THERMOCALC) (Kbar)	Average Temperature (THERMOCALC) (°C)
Grt _{porphyroblast(rim)} -Pl (inclusion)- Hbl (inclusion)		
NG2A-R	5.9 ± 2.6	658 ± 105
NG6-R	5.9 ± 1.2	625 ± 73
NG8-R	6.0 ± 1.6	640 ± 93
NG9-R	6.5 ± 2.7	596 ± 142

properties of minerals used in the pseudosections are based on the following models: garnet (Holland and Powell, 1998), chlorite (Holland et al., 1998), amphibole (Dale et al., 2000), clinopyroxene (Holland and Powell, 1996) and plagioclase (Newton et al., 1980).

As the pressure estimates of peak metamorphism of the pillow basalts are tightly constrained (~6 to 6.5 kbar) from the average P-T calculations (Table 3), an isobaric T-X (composition) pseudosection (Figure 10a) has been constructed at ~6.5 kbar to study the topology of the stable mineral assemblages with change in temperature for the composition ranging from the pillow core (C₁) and rim (C₂). The T-X pseudosection reveals that clinopyroxene is stable at lower temperatures (475 to 600°C) in the pillow core, which indicates that with hydration of the pillow core and progressive increase in temperature, clinopyroxene been replaced by amphibole. This observation explains textural features like replacement of clinopyroxene by hornblende and development of hornblende foliation in the cores of deformed pillows during prograde metamorphism (Figures 5a and b). With progressive change in bulk composition from C₁ (pillow core) to C₂ (pillow rim), garnet modes increase, while plagioclase modes decrease (Figure 10b). Within bulk composition range X(C₂) = 0.9 to 1 (pillow rim, Figure 10b), the amphibole mode decreases with increase in garnet mode. Such modal distribution of garnet, plagioclase and amphibole supports the textural observation of garnet growth by breakdown of plagioclase and amphibole at pillow rims. Garnet modes are parallel to the temperature axis except in the field chlorite-amphibole-plagioclase-garnet-vapour that stretches for a small temperature range (~50°C), indicating that garnet formation is not dependent on temperature. Figure 10c shows the detailed T-X pseudosection for bulk compositions close to that of pillow rim (X(C₂) = 0.8 to 1) at 6.5 kbar. In this pseudosection, anorthite isopleths show shallow positive slopes at lower temperature ~475°C and anorthite content of plagioclase decreases rapidly within a small temperature range, with the appearance of zoisite. Thus zoisite formation led to depletion in calcium content of plagioclase along the isobaric cooling path, supported by development of albitic rims in matrix plagioclase (Figure 5b). Along this isobaric cooling path,

garnet X_{Mg} isopleths show decrease in values with progressive increase in chlorite modes, a fact supported by decrease in X_{Mg} content of garnet along the rims at contact with chlorite (Table 1A).

An isothermal P-X pseudosection (Figure 11a) was constructed at 600°C (estimated from the thermometry) to determine the variation of phase topology in the pillow core (C₁) to pillow rim (C₂) with change in pressure. Clinopyroxene is replaced by amphibole as the bulk composition change from that of the pillow core to that of the pillow rim. Garnet modal isopleths (Figure 11b) have positive slopes at lower pressures (2 to 4 kbar), while their slopes become negative at higher pressures (4 to 10 kbar). Garnet modes increase with progressive change in bulk composition from pillow core towards rim. Plagioclase modal isopleths have negative slopes along bulk composition range of X(C₂) = 0 to 0.8 and show continuous decrease from pillow core towards rim (Figure 11b). At bulk composition closer to pillow rim (X(C₂) = 0.8 to 1), plagioclase modal isopleths become parallel to the composition axis and show a continuous decrease in values with increase in pressure. The slopes of amphibole modal isopleths become steeply negative for this bulk composition range and decrease with increase in pressure (Figure 11b). Such distribution of modal isopleths of garnet, amphibole and plagioclase at pillow rim indicates formation of garnet by breakdown of amphibole and plagioclase with progressive increase in pressure. Figure 11c shows the distribution of modal isopleths of anorthite and grossular along the P-X pseudosection (at 600°C) for X(C₂) = 0.8 to 1. With increase in pressure, anorthite content of plagioclase decreases, while grossular content of garnet increases.

A P-T pseudosection (Figure 12) has been constructed with the whole rock bulk composition of the pillow rim (NG8-R). Garnet is stable throughout the P-T range of 5.5 to 7 kbar and 500 to 650°C. The field for peak metamorphic mineral assemblage containing garnet-amphibole-plagioclase-chlorite-quartz-vapour (H₂O) extends for a pressure-temperature range of 5.5 to 7 kbar and ~600°C. Within this field, garnet modal isopleths have steep negative slopes with garnet mode increasing with pressure. Modal isopleths of amphibole and plagioclase intersect the garnet modal isopleths at high angles and both plagioclase and amphibole modes decrease with increasing pressure within this field, supporting formation of garnet from breakdown of plagioclase and amphibole. Chlorite modal isopleths are parallel to the temperature axis and increase with lowering of temperature. Zoisite is stable at lower temperature. Such observations specify formation of zoisite and chlorite by breakdown of garnet during near-isobaric cooling, which also supports textural observations (Figures 5d and f). Star represents average P-T for peak metamorphism obtained from rim composition of the garnet porphyroblasts (Table 3) in different samples of the pillow basalts by THERMOCALC.

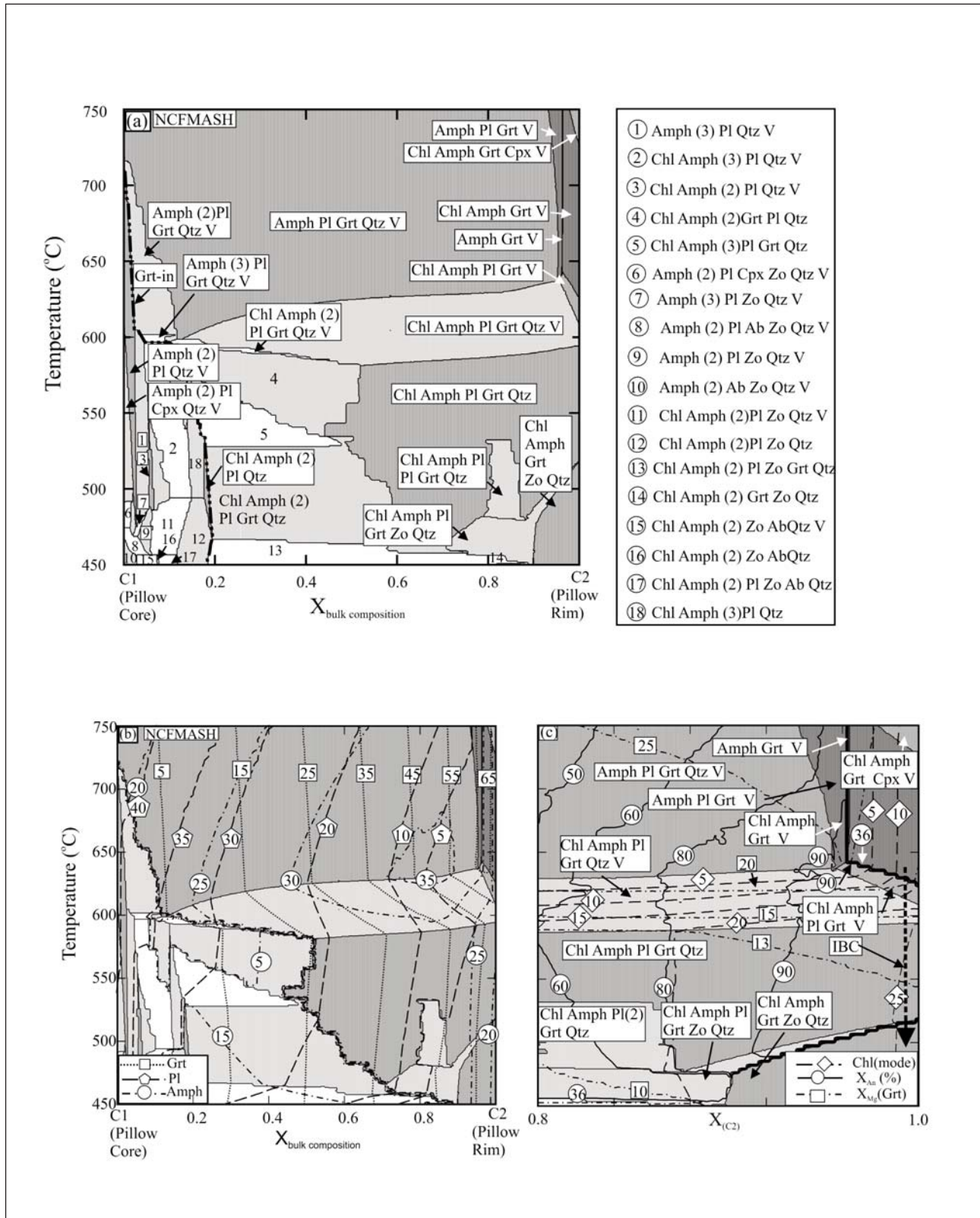


Figure 10. NCFMASH isobaric T-X pseudosections (a-c) at 6.5 kbar, where X represents bulk composition (XRF, NG8) variations between pillow core (C₁) and rim (C₂). The salient features of the compositional vector X are increase in Al₂O₃, FeO, MgO, CaO, H₂O and decrease in SiO₂, Na₂O from pillow core to rim. C1 and C2 in terms of molar proportions of SiO₂ : Al₂O₃ : FeO : MgO : CaO : Na₂O : H₂O are, respectively, 73.68 : 7.26 : 3.92 : 2.64 : 5.03 : 4.21 : 3.26 and 38.21 : 11.59 : 21.23 : 11.33 : 7.58 : 0.56 : 9.50. (a) T-X pseudosection showing the topology of different mineral assemblages. (b) T-X pseudosection showing the modal distribution of garnet, plagioclase and amphibole. (c) T-X pseudosection for X_{C2} = 0.8 to 1, showing isopleths of chlorite modes, X_{An} in plagioclase and X_{Mg} in garnet. See text for details. (The numbers in parentheses indicate total number of immiscible phases).

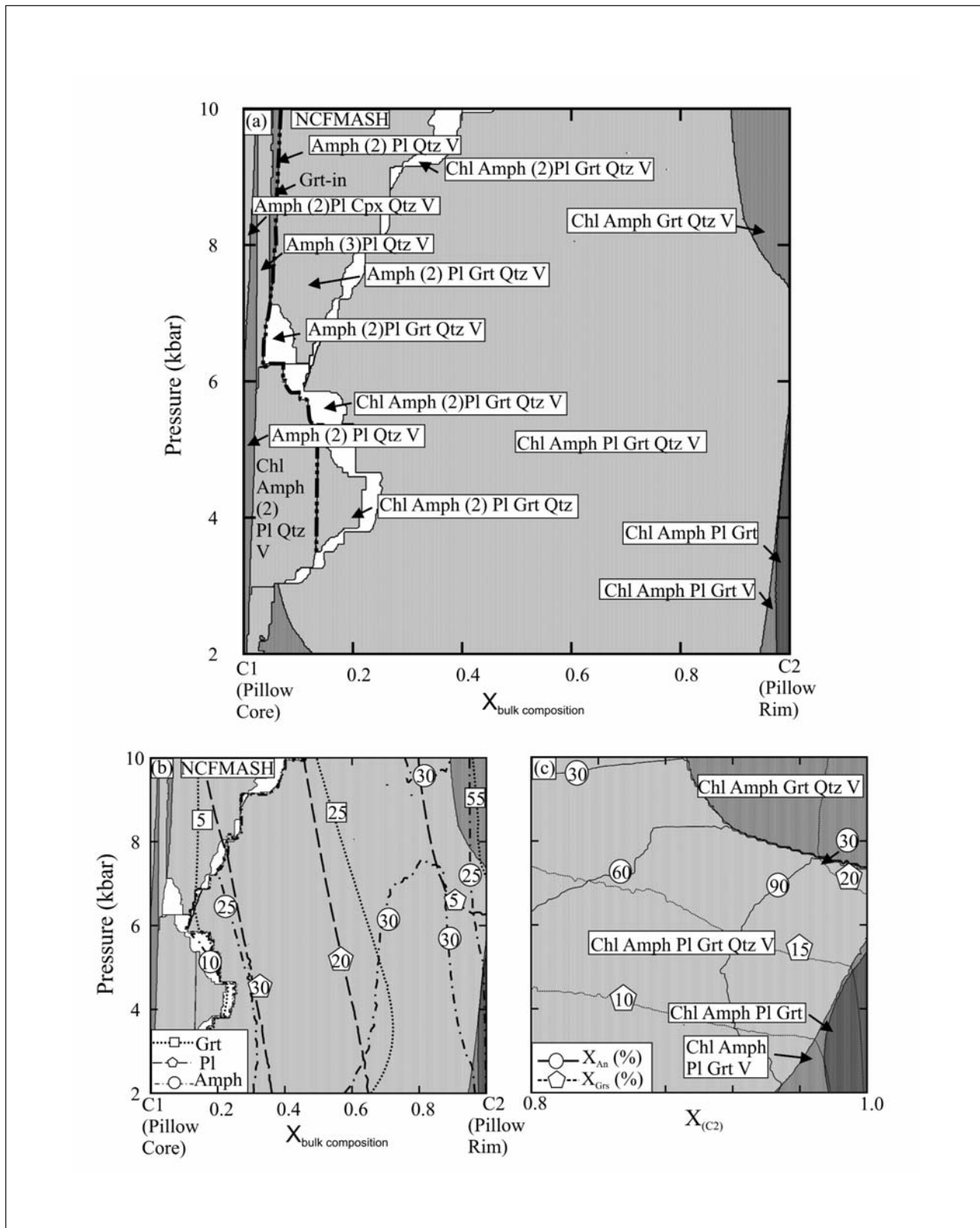


Figure 11. NCFMASH isothermal P-X pseudosections (a-c) at 600°C, where X axis shows same variation in bulk composition as in Figure 10. See text for details.

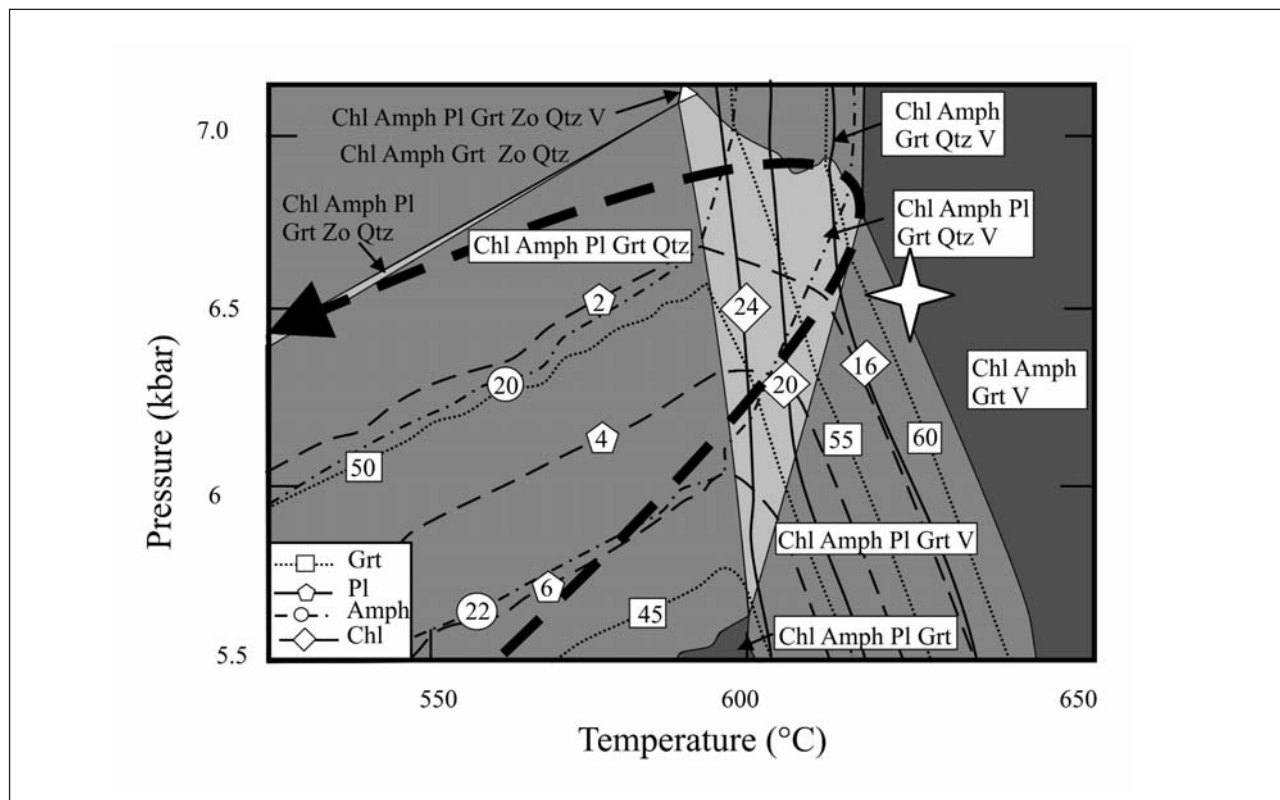


Figure 12. NCFMASH P-T pseudosection for the pillow rim, that shows modes of garnet, plagioclase, amphibole, chlorite. Also shown is the estimate of P-T condition of peak metamorphism as calculated by THERMOCALC.

Thus it can be concluded that post sea-floor alteration, pressure and temperature of the pillow basalts were increased to ~6 to 6.5 kbar, 600 to 650°C during peak metamorphism, which was followed by near-isobaric cooling along an anti-clockwise P-T path (Figure 12).

Discussion

The pillows consist of a secondary mineral assemblage that formed during regional metamorphism of the Witkop Formation. The most striking difference between the pillow cores and rims is the presence of garnet in the latter. The restricted growth of garnet in the rims can be explained by compositionally controlled growth, due to higher Al_2O_3 contents. Differences in chemical composition are likely the result of seafloor alteration that preceded the amphibolite facies metamorphic overprint.

Submarine alteration of basaltic rocks is a characteristic feature of modern oceanic crust. Two types of alteration are generally distinguished: low-temperature (<~150°C) basalt-seawater interaction, which preferentially affects the uppermost few hundred metres of oceanic crust, and high-temperature (>~150°C) hydrothermal alteration related to hydrothermal systems near areas of magmatic activity, such as along mid-ocean ridges (Staudigel, 2003; German and von Damm, 2003). Alkali metals, such as K, are released from basalts at temperatures of 150°C and above (Seyfried, 1987),

whereas the solubility of most other metals increases significantly only at temperatures above 350°C (Seewald and Seyfried, 1990). Most metals are leached from basalt during high-temperature hydrothermal alteration and interaction with up to ~400°C fluids, whereas Mg and sometimes Na are added. In contrast, low-temperature alteration generally results in a gain of alkali metals. However, element fluxes can be variable at different depths in crustal sections (Staudigel et al., 1996).

Hofmann and Wilson (2007) presented a detailed study of sea floor alteration characterized by silicification that is widespread in the Nondweni greenstone belt. Alteration zones are 20 to 50 metres thick, are characterized by intense silicification and minor carbonatization of volcanic rocks and are developed below silicified sea floor sediments represented by chert. SiO_2 contents increase with degree of alteration, from the original igneous value up to c. 90%. Silicification is associated with a depletion of most elements commonly mobile during water-rock interaction, while K_2O , Rb and Ba are enriched in these zones. Metals such as Cu and Zn were depleted in the underlying volcanic rocks during alteration. The element depletion-enrichment patterns have been interpreted to reflect low-temperature (100 to 150°C) hydrothermal processes for the silicification of the volcanic rocks (Hofmann and Wilson, 2007).

The changes in the concentration of various elements observed in this study are distinct to low-temperature

silicification. Although depletion of Na_2O , CaO , P_2O_5 , and Sr is commonly associated with silicification of Palaeoarchaean greenstone successions, a depletion of Fe and Mg is also typically observed (Duchac and Hanor, 1987; Hofmann and Wilson, 2007; Hofmann and Harris, 2008). The lack of K metasomatism and the enrichment of Mg could suggest that hydrothermal processes were operating at relatively high temperatures above $\sim 150^\circ\text{C}$ (Seyfried, 1987; Staudigel, 2003). The oxygen isotope data may shed some light on this question. Smith et al. (1984) suggested on the basis of the oxygen isotope composition of orthopyroxene separates from Barberton komatiites that the magma had a $\delta^{18}\text{O}$ value of c. 5.7‰ at the time of crystallisation, which is in the range of the isotopic composition of present day mantle-derived magmas (Ito et al., 1987). Low-temperature alteration during basalt-seawater interaction increases the $\delta^{18}\text{O}$ value of seafloor rocks, whereas high-temperature alteration causes lowering of the $\delta^{18}\text{O}$ value (Muehlenbachs and Clayton, 1972; Alt et al., 1986). The pillow samples in this study show values both higher and lower than the likely primary $\delta^{18}\text{O}$ value of c. 5.7‰. The elevated value of core sample NG2 (9.6‰) may suggest low-temperature alteration. The rim, by contrast, has a much lower value (4.8‰), suggesting isotopic exchange between basalt and a fluid at higher temperatures. It is possible that all samples originally had experienced low-temperature alteration with a concomitant increase in O isotope values, but that isotopic exchange at higher temperatures at a later stage gave rise to lowering of the isotope values. A similar observation has been made from amphibolite facies komatiites from the Schapenburg greenstone belt near Barberton. Lecuyer et al. (1994) inferred the lowering of $\delta^{18}\text{O}$ values by metamorphic fluids (with initial $\delta^{18}\text{O}$ values of +5 to +7) to between +3.2‰ and +5.0‰ at high temperature (450°C) under high water/rock ratios.

The element enrichment-depletion patterns observed here are very similar to those reported by Polat et al. (2003; 2005), who investigated metamorphosed pillow basalts from the Isua greenstone belt that experienced seafloor alteration prior to an amphibolite facies metamorphic overprint. Some differences do exist, such as steepening of the REE patterns of pillow rims relative to cores in the Nondweni pillows, whereas Polat et al. (2005) observed a flattening of the REE patterns. In both cases, this can be attributed to the mobility of LREE during alteration. Hofmann and Harris (2008) observed an increase in $\text{La}_\text{N}/\text{Yb}_\text{N}$ ratios during silicification of volcanic rocks from the Barberton greenstone belt and attributed it to enrichment of LREE relative to the HREE. The same explanation is probably valid for the pillows investigated here. Although LREE are generally regarded to be more mobile during water-rock interaction due to their larger ionic radii, alteration of the pillow basalts did result in remobilisation of HREE, as indicated by a relative depletion of the HREE in a pillow core and the enrichment in the pillow margin (Figure 8d).

Subsequent to hydrothermal alteration processes on the sea-floor, the pillow basalts were buried to a depth of ~ 20 to 25 km. The increased pressure, accompanied by increase in temperature, possibly by intrusion of the Mvunyana granodiorite, led to metamorphism of the basalts under amphibolites facies conditions, where they were metamorphosed under P-T conditions of ~ 6.5 kbar and 600 to 650°C . Under the peak metamorphic conditions, garnet porphyroblasts formed in pillow rims by the breakdown of hornblende-plagioclase. The basalts then underwent isobaric cooling to $\sim 450^\circ\text{C}$ when the chlorite-albite-epidote-bearing assemblage was formed. Thus the pillow basalts followed an anticlockwise P-T path. Isobaric cooling also indicates that the pillow basalts resided at the depth of burial for a considerable time, before being exposed to the surface.

In the study area, the ~ 3.29 Ga Mvunyana granodiorite is only weakly foliated and cuts the foliation in the supracrustal rocks. It contains abundant enclaves of the supracrustal rocks, the latter ranging from centimetre-size to rafts of ~ 0.5 km in diameter. These enclaves include quartz-sericite schist, amphibolite, metachert, and serpentinite. Migmatitic gneisses with enclaves of amphibolite have also been observed within the Mvunyana granodiorite; anatexis has been associated with granitoid emplacement (Matthews et al., 1989). These observations, together with evidence for syn-tectonic garnet growth indicate that intrusion of the Mvunyana granodiorite was late syn-tectonic, and concomitant with the amphibolite facies metamorphism of the supracrustal rocks of the Nondweni greenstone belt.

Isobaric cooling along anticlockwise P-T paths has so far been reported mainly from the medium-pressure granulites in (1) the Adirondacks, (2) the Archaean (~ 3.1 Ga) Napier Complex, Enderby Land, Antarctica, (3) the Palaeoproterozoic (~ 2.5 Ga) Jiao-Liao-Ji Belt and Jining Complex, North China Craton (Stoddard, 1976; Harley, 1985; Ehrhard, 1986; Seal, 1986; Bohlen, 1987; Zhao, 2007; Santosh et al., 2009). In the Adirondacks, such P-T paths have also been recorded from the garnetiferous amphibolites with peak P-T ~ 6.5 kbar and $\sim 650^\circ\text{C}$ (Stoddard, 1976; Ehrhard, 1986; Seal, 1986; Bohlen, 1987). Inferences have been made that such metamorphic P-T paths are indicative of extensional tectonic regimes such as: magmatic and back-arc settings (Bohlen, 1987; 1991; Brown, 2006), intracontinental rifts (Sandiford and Powell, 1986) or intracontinental mantle plumes (Zhao et al., 1999). The peak P-T conditions of ~ 6 to 6.5 kbar, 600 to 650°C and the near isobaric cooling recorded in the pillow basalts of Nondweni greenstone belt are similar to that recorded in the amphibolites of the Adirondacks, latter being formed in a magmatic-arc setting (Stoddard, 1976; Ehrhard, 1986; Seal, 1986; Bohlen, 1987).

The geothermal gradient recorded during peak metamorphism of the Nondweni pillow basalts is

~30°C/km. According to the numerical modeling conducted from the batholiths at continental magmatic arc settings by Rothstein and Manning (2003), shield geothermal gradients in such terrains get elevated to ~30°C/km, during plutonic intrusions at depths of ~17 to 20 km. Kisters et al. (2010) also concluded that such high geothermal gradients recorded from the amphibolite facies rocks of the Schapenburg schist belt at the contact of the Badplaas pluton indicate a magmatic arc setting. Since formation of high-grade mineral assemblages in the Nondweni pillow basalts are found only at the contact of intrusive Mvunyana granodiorite, it is possible that the high temperature attained by these rocks during peak metamorphism resulted from intrusion of the granodiorite in a magmatic arc setting. Such inference is also supported by the anticlockwise P-T paths recorded within these basalts, which are comparable with that from the amphibolites in the Adirondacks.

The age of the intrusive Mvunyana granodiorite (~3.29 Ga) indicates that peak metamorphism of the Nondweni greenstone belt occurred well before that of the 3.23 and 3.20 Ga metamorphic events recorded respectively from the Barberton and De Kraalen-Assegaai greenstone belts (Dziggel et al., 2002; Diener et al., 2005; Moyen et al., 2006; Saha et al., 2010). Hence it is possible that southern part of southeastern Kaapvaal craton was stabilised prior to the northern part.

Conclusions

Lithofacies of the sedimentary sequences of Nondweni Greenstone Belts indicate their deposition in a rift-related basin at continental margin setting (Wilson and Versfeld, 1994a). Presence of cross-laminations in the chert and lapilli tuff horizons associated with the Witkop pillow basalts have been interpreted to be results of fluvial and coastal reworking (Riganti and Wilson, 1995). Hofmann and Wilson (2007) stated that the silicification of the Witkop pillow basalts took place due to low-temperature alterations beneath Archaean sea-floor by heated sea water that moved in shallow sea-floor convection cells most likely driven by regional heat flow. The present study also reveals that the pillow basalts from the Witkop Formation in contact with the Mvunyana granodiorite show evidence of Palaeoarchaean sea-floor alteration. A combination of $\delta^{18}\text{O}$ values that are significantly above and below the expected value for unaltered oceanic crust (5.7‰, Ito et al., 1987) can be explained if the pillows experienced low-temperature hydrothermal alteration followed by higher-temperature alteration during metamorphism, as observed in the Schapenburg greenstone belt komatiites by Lecuyer et al (1994). The alteration processes led to significant depletion of SiO_2 , Na_2O , Sr, CaO, P_2O_5 , Mo and Pb and enrichment in MgO, MnO, Zn, Co, and LREE. Metamorphism of the pillows took place at P-T conditions of ~6 to 6.5 kbar, 600 to 650°C, which marked syn-tectonic garnet growth in pillow rims. Subsequent to peak metamorphism, the

pillows underwent isobaric cooling to ~450°C along an anticlockwise P-T path. The late syntectonic intrusion of the Mvunyana granodiorite into the supracrustal rocks and the presence of migmatites near the contact indicate that peak metamorphism of the Witkop basalts occurred at ~3.29 Ga. The high geothermal gradient recorded during peak metamorphism of these rocks and the anticlockwise P-T path support a magmatic setting. Thus it can be concluded that this part of southeastern Kaapvaal craton attained stability prior to that of its northern part as recorded in the granitoid-greenstone terrains of Barberton, De Kraalen, Witrivier and Assegaai.

Acknowledgements

LS acknowledges University of KwaZulu-Natal for a Competitive Research Grant, that partially supported the project. AH acknowledges support by the National Research Foundation (NRF) of South Africa. NJ was supported by an NRF bursary and a grant from the GSSA Research, Education and Investment (REI) Fund. Fayroza Rawoot assisted with the O-isotope analyses. The authors thank Peter Schiffman and Harald Furnes for helpful reviews that improved the manuscript.

References

- Alt, J.C., 1999. Hydrothermal alteration and mineralization of oceanic crust: mineralogy, geochemistry and processes. In: C.T. Barrie and M.D. Hannington (Editors), *Volcanic-associated Massive Sulphide Deposits: Processes and Examples in Modern and Ancient Settings*, Reviews in Economic Geology, 133-155.
- Alt, J.C., Muehlenbachs, K., and Honnorez, J., 1986. An oxygen isotopic profile through the upper kilometer of the oceanic crust, DSDP Hole 504B. *Earth and Planetary Science Letters*, 80, 217-229.
- Barnicoat, A.C., 1988. Zoned high-pressure assemblages in pillow lavas of the Zermatt-Saas ophiolite zone, Switzerland. the scale of isotopic resetting is relatively small, *Lithos*, 21, 227-236.
- Beath, P. and Stern, W., 1979. Zur Geochemie von Metapillows der Region Zermatt-Saas. *Schweizerische Mineralogische und Petrographische Mitteilungen*, 59, 349-373.
- Berger, G., Schott, J. and Guy, C., 1988. Behavior of Li, Rb and Cs during basalt glass and olivine dissolution and chlorite, smectite and zeolite precipitation from seawater: Experimental investigations and modelization between 50° and 300°C. *Chemical Geology*, 71, 297-312.
- Bohlen, S.R., 1987. Pressure-temperature-time paths and a tectonic model for the evolution of granulites. *Journal of Geology*, 95, 617-632.
- Bohlen, S.R., 1991. On the formation of granulites. *Journal of Metamorphic Geology*, 9, 223-229.
- Brown, M., 2006. Duality of thermal regimes is the distinctive characteristic of plate tectonics since the Neoproterozoic. *Geology*, 34, 961-964.
- Connolly, J.A.D., 2005. Computation of phase equilibria by linear programming: a tool for geodynamic modeling and its application to subduction zone decarbonation. *Earth and Planetary Science Letters*, 236, 524-541.
- Coplen, T.B., Kendall, C. and Hopple, J., 1983. Comparison of stable isotope reference samples. *Nature*, 302, 236-238.
- Dale, J., Holland, T. and Powell, R., 2000. Hornblende-garnet-plagioclase thermobarometry: a natural assemblage calibration of the thermodynamics of hornblende. *Contributions to Mineralogy and Petrology*, 140, 353-362.
- de Wit, M.J., Furnes, H. and Robins, B., 2011. Geology and tectonostratigraphy of the Onverwacht Suite, Barberton Greenstone Belt, South Africa. *Precambrian Research*, 186, 1-27.
- Diener, J.F.A., Stevens, G., Kisters, A.F.M. and Poujol, M., 2005. Metamorphism and exhumation of the basal parts of the Barberton greenstone belt, South Africa: Constraining the rates of Mesoproterozoic tectonism. *Precambrian Research*, 143, 87-112.

- Du Toit, A.L., 1931. The geology of the country surrounding Nkandhla, Natal. Explanation Sheet: 109, Geological Survey of South Africa, 111p.
- Duchac, K.C. and Hanor, J.S., 1987. Origin and timing of metasomatic silicification of an early Archean komatiite sequence, Barberton Mountain Land, South Africa. *Precambrian Research*, 37, 125-146.
- Dziggel, A., Stevens, G., Poujol, M., Anhaeusser, C.R. and Armstrong, R.A., 2002. Metamorphism of the granite-greenstone terrane south of the Barberton greenstone belt, South Africa: an insight into the tectono-thermal evolution of the 'lower' portions of the Onverwacht Group. *Precambrian Research*, 114, 221-247.
- Ehrhard, L.E., 1986. Low activities of H₂O at the amphibolite – granulite transition, northwest Adirondacks: Evidence for pre-Grenville melting and dehydration. Unpublished MSc thesis, State University of New York at Stony Brook, New York, U.S.A., 64p.
- Furnes, H., de Wit, M., Staudigel, H., Rosing, M. and Muehlenbachs, K., 2007. A vestige of Earth's oldest ophiolite. *Science*, 315, 1704-1707.
- Furnes, H., Robins, B. and de Wit, M.J., 2012. Geochemistry and petrology of lavas in the upper Onverwacht Suite, Barberton Mountain Land, South Africa. *South African Journal of Geology*, 115, 171-210.
- German, C.R. and von Damm, K.L., 2003. Hydrothermal processes. *Treatise on Geochemistry*, 6, 181-222.
- Grant, J.A., 1986. The isocon diagram: a simple solution to Gresen's equation for metasomatic alteration. *Economic Geology*, 81, 1976-1982.
- Grant, J.A., 2005. Isocon analysis: A brief review of the method and applications. *Physics and Chemistry of the Earth*, 30, 997-1004.
- Gutzmer, J., Banks, D.A., Luders, V., Hoefs, J., Beukes, N.J. and von Benzig, K.L., 2003. Ancient sub-seafloor alteration of basaltic andesites of the Ongeluk Formation, South Africa: implications for the chemistry of Paleoproterozoic seawater. *Chemical Geology*, 201, 37-53.
- Harley, S.L., 1985. Garnet-orthopyroxene-bearing granulites from Enderby Land, Antarctica: Metamorphic pressure-temperature-time evolution of the Archaean Napier Complex. *Journal of Petrology*, 26, 819-856.
- Harris C., Smith S. and le Roex, A.P., 2000. Oxygen isotope composition of phenocrysts from Tristan da Cunha Gough Island lavas: variation with fractional crystallisation and evidence for assimilation. *Contribution to Mineralogy and Petrology*, 138, 164-175.
- Hart, S.R., Erlank, A.J. and Kable, E.J.D., 1974. Sea-floor basalt alteration: Some chemical and isotopic effects. *Contributions to Mineralogy and Petrology*, 44, 219-230.
- Hellman, P.L., Smith, R.E. and Henderson, P., 1979. The mobility of the rare earth elements: evidence and implications from selected terrains affected by burial metamorphism. *Contributions to Mineralogy and Petrology*, 71, 23-44.
- Hofmann, A. and Harris, C., 2008. Silica alteration zones in the Barberton greenstone belt: A window into subseafloor processes 3.5-3.3 Ga ago. *Chemical Geology*, 257, 221-239.
- Hofmann, A. and Wilson, A.H., 2007. Silicified basalts, bedded cherts and other sea floor alteration phenomena of the 3.4 Ga Nondweni greenstone belt, South Africa. *Developments in Precambrian Geology*, 15, 571-609.
- Holland T.J.B. and Powell, R., 1996. Thermodynamics of order-disorder in minerals; II, Symmetric formalism applied to solid solutions. *American Mineralogist*, 81, 1425-1437.
- Holland, T.J.B. and Powell, R., 1998. An internally consistent thermodynamic data set for phases of petrological interest. *Journal of Metamorphic Geology*, 16, 309-343.
- Holland, T.J.B., Baker, J. and Powell, R., 1998. Mixing properties and activity-composition relationships of chlorites in the system MgO-FeO-Al₂O₃-SiO₂-H₂O. *European Journal of Mineralogy*, 10, 395-406.
- Ito, E., White, W.M. and Gopel, C., 1987. The O, Sr, Nd, and Pb isotope geochemistry of MORB. *Chemical Geology*, 62, 157-176.
- Kerrick, R. and Fyfe, W. S., 1981. The gold-carbonate association: source of CO₂ and CO₂ fixation reactions in Archaean lode gold deposits. *Chemical Geology*, 33, 265-293.
- Kisters, A.F.M., Belcher, R.W., Poujol, M. and Dziggel, A., 2010. Continental growth and convergence-related arc plutonism in the Mesoarchaen: Evidence from the Barberton granitoid-greenstone terrain, South Africa. *Precambrian Research*, 178, 15-26.
- Kretz, R., 1983. Symbols of rock-forming minerals. *American Mineralogist*, 68, 277-279.
- Lecuyer, C., Gruau, G., Anhaeusser, C.R. and Fourcade, S., 1994. The origin of fluids and the effects of metamorphism on the primary chemical compositions of Barberton komatiites: New evidence from geochemical (REE) and isotopic (Nd, O, H, ³⁹Ar/⁴⁰Ar) data. *Geochimica et Cosmochimica Acta*, 58, 969-984.
- Leshner, C.M., Gibson, H.L. and Campbell, I.H., 1986. Composition-volume changes during hydrothermal alteration of andesite at Buttercup Hill, Noranda District, Quebec. *Geochimica et Cosmochimica Acta*, 50, 2705-2893.
- Linstrom, W., 1988. The Geology of the Dundee area. Explanation Sheet: 2830 (1:250000), Geological Survey of South Africa, 136p.
- Ludden, J.N., Gelinias, L. and Trudel, P., 1982. Archaean metavolcanics from the Rouy-Noranda district, Abitibi greenstone belt, Quebec. 2. Mobility of trace elements and petrogenetic constraints. *Canadian Journal of Earth Sciences*, 19, 2276-2287.
- Ludden, J.N. and Thompson, G., 1979. An evaluation of the behavior of the rare earth elements during the weathering of sea-floor basalts. *Earth and Planetary Science Letters*, 43, 85-92.
- Matthews, P.E., Charlesworth, E.G., Eglington, A.A. and Harmer, R.E., 1989. A minimum 3.29 Ga age for the Nondweni greenstone complex in the south-eastern Kaapvaal Craton. *South African Journal of Geology*, 92, 272-278.
- Menzies, M., and Seyfried, W.E., 1979. Basalt-seawater interaction: Trace element and strontium isotopic variations in experimentally altered glassy basalt. *Earth and Planetary Science Letters*, 44, 463-472.
- Miller, J.A., Buick, I.S. and Cartwright, I., 2000. Textural implications of high-pressure fluid flow controlled by pre-subduction deformation and alteration patterns, *Journal of Geochemical Exploration*, 69-70, 551-555.
- Miller, J.A. and Cartwright, I., 2000. Distinguishing between seafloor alteration and fluid flow during subduction using stable isotope geochemistry: examples from Tethyan ophiolites in the Western Alps. *Journal of Metamorphic Geology*, 18, 467-482.
- Moyen, J.-F., Stevens, G., and Kisters, A.F.M., 2006. Record of mid-Archaen subduction from metamorphism in the Barberton terrain, South Africa: *Nature*, 442, 559-562.
- Muehlenbachs, K. and Clayton, R.N., 1972. Oxygen isotope studies of fresh and weathered submarine basalts: *Canadian Journal of Earth Sciences*, 9, 172-184.
- Nakamura, K., Kato, Y., Tamaki, K. and Ishii, T., 2007. Geochemistry of hydrothermally altered basaltic rocks from the Southwest Indian Ridge near the Rodriguez Triple junction. *Marine Geology*, 239, 125-141.
- Newton, R.C., Charlu, T.V. and Kleppa, O.J., 1980. Thermochemistry of the high structural state plagioclases. *Geochimica Cosmochimica Acta*, 44, 933-941.
- Pauly, B.D., Schiffman, P. and Zierenberg, R.A. 2011. Environmental and chemical controls on palagonitization. *Geochemistry Geophysics Geosystems*, 12, doi: 10.1029/2011GC003639.
- Polat, A., Hofmann, A.W., Münker, C., Regelous, M. and Appel, P.W.U., 2003. Contrasting geochemical patterns in the 3.7-3.8 Ga basalt cores and rims, Isua greenstone belt, Southwest Greenland: Implications for postmagmatic alteration processes. *Geochimica et Cosmochimica Acta*, 67, 441-457.
- Polat, A., Kusky, T.M., Li, J.H., Fryer, B., Kerrich, R., and Patrick, K., 2005. Geochemistry of Neoproterozoic (ca. 2.55-2.50 Ga) volcanic and ophiolitic rocks in the Wutaishan Greenstone Belt, Central Orogenic Belt, North China Craton: Implications for geodynamic setting and continental growth. *Geological Society of America Bulletin*, 117, 1387-1399.
- Riganti, A. and Wilson, A.H., 1995. Geochemistry of the mafic/ultramafic volcanic associations of the Nondweni greenstone belt, South Africa, and constraints on their petrogenesis. *Lithos*, 34, 235-252.
- Rothstein, D.A. and Manning, C.E., 2003. Geothermal gradients in continental magmatic arcs: Constraints from the eastern Peninsular Ranges batholiths. Baja California, Mexico. *Geological Society of America Special Paper*, 374, 337-354.
- Saha, L., Hofmann, A., Xie, H., Hegner, E., Wilson, A., Wan, Y., Liu, D. and Kröner, A., 2010. Zircon ages and metamorphic evolution of the Archaean Assegai-De Kraalen granitoid-greenstone terrain, Southeastern Kaapvaal Craton, *American Journal of Science*, 310, 1384-1420.

- Sandiford, M. and Powell, R., 1986. Deep crustal metamorphism during continental extension: modern and ancient examples. *Earth and Planetary Science Letters*, 79, 151-158.
- Santosh, M., Sajeev, K., Li, J.H., Liu, S.J. and Itaya, T., 2009. Counterclockwise exhumation of a hot orogen: The Paleoproterozoic ultrahigh-temperature granulites in the North China Craton. *Lithos*, 110, 140-152.
- Schiano, P., Dupre, B. and Lewin, E., 1993. Application of element concentration variability to the study of basalt alteration (Fangataufa atoll, French Polynesia). *Chemical Geology*, 104, 99-124.
- Schramm, B., Devey, C.W., Gillis, K.M. and Lackschewitz, K., 2005. Quantitative assessment of chemical and mineralogical changes due to progressive low temperature alteration of East Pacific Rise basalts from 0 to 9 Ma. *Chemical Geology*, 218, 281-313.
- Seal, T.L., 1986. Pre-Genville dehydration metamorphism in the Adirondack Mountains, New York. Unpublished M.S. thesis, State University of New York, Stony Brook, U.S.A., 1-84.
- Seewald, J.S. and Seyfried, W.E., 1990. The effect of temperature on metal mobility in subseafloor hydrothermal systems: constraints from basalt alteration experiments. *Earth and Planetary Science Letters*, 101, 388-403.
- Seyfried, W.E. Jr., 1987. Experimental and theoretical constraints on hydrothermal alteration processes at mid-ocean ridges. *Annual Reviews of Earth and Planetary Sciences*, 15, 31-335.
- Seyfried, W.E., and Bischoff, J.L., 1979. Low temperature basalt alteration by seawater: An experimental study at 70°C and 150°C. *Geochimica et Cosmochimica Acta*, 43, 1937-1947.
- Seyfried, W.E., and Bischoff, J.L., 1981. Experimental seawater-basalt interaction at 300°C, 500 bars, chemical exchange, secondary mineral formation and implications for the transport of heavy metals. *Geochimica et Cosmochimica Acta*, 45, 135-147.
- Seyfried, W.E. Jr, Berndt, M. and Janecky, D.R., 1986. Chloride depletions and enrichments in seafloor hydrothermal fluids: Constraints from experimental basalt alteration studies. *Geochimica et Cosmochimica Acta*, 50, 469-475.
- Smith, H.S., O Neil, J.R. and Erlank, A.J., 1984. Oxygen isotope compositions of minerals and rocks and chemical alteration patterns in pillow lavas from the Barberton greenstone belt, South Africa. In: A. Kröner, G.N. Hanson and A.M. Goodwin, (Editors), *Archaean Geochemistry*, Springer, Berlin, 115-137.
- Staudigel, H., 2003. Hydrothermal alteration processes in the oceanic crust. *Treatise on Geochemistry*, 3, 511-535.
- Staudigel, H. and Hart, S.R., 1983. Alteration of basaltic glass: Mechanisms and significance for the oceanic crust-sea water budget. *Geochimica et Cosmochimica Acta*, 47, 337-350.
- Staudigel, H., Plank, T., White, W. and Schmincke, H.-U., 1996. Geochemical fluxes during seafloor alteration of the basaltic upper oceanic crust: DSDP sites 417 and 418. In: G. Bebout, D.W. Scholl, S.H. Kirby and J.P. Platt (Editors), *Subduction: Top to Bottom*. Geophysical Monograph, 96, 19-37.
- Stoddard, E.F., 1976. Granulite facies metamorphism in the Colton-Rainbow Falls area, Northwest Adirondacks, New York. Unpublished Ph.D. Thesis, University of California, Los Angeles, U.S.A., 267p.
- Štípská, P., Pitra, P. and Powell, R., 2006. Separate or shared metamorphic histories of eclogites and surrounding rocks? An example from the Bohemian Massif. *Journal of Metamorphic Geology*, 24, 219-240.
- Versfeld, J.A., 1988. The geology of the Nondweni greenstone belt. Unpublished Ph.D. Thesis, University of Natal, Pietermaritzburg, South Africa, 298p.
- Wilson, A.H. and Riganti, A., 1998. A fractionated komatiitic basalt lava lake sequence in the Nondweni greenstone belt. In: International Volcanological Conference, IAVCEI, Cape Town, South Africa, 70p.
- Wilson, A.H. and Versfeld, J.A., 1994a. The early Archaean Nondweni greenstone belt, southern Kaapvaal Craton, South Africa, Part 1. Stratigraphy, sedimentology, mineralization and depositional environment. *Precambrian Research*, 67, 243-276.
- Wilson, A.H. and Versfeld, J.A., 1994b. The early Archaean Nondweni greenstone belt, southern Kaapvaal Craton, South Africa, Part 2. Characteristics of the volcanic rocks and constraints on magma genesis. *Precambrian Research*, 67, 277-320.
- Wilson, A.H., Versfeld, J.A. and Hunter, D.R., 1989. Emplacement, crystallization and alteration of spinifex-textured komatiitic basalt flows in the Archaean Nondweni greenstone belt, southern Kaapvaal Craton, South Africa. *Contributions to Mineralogy and Petrology*, 101, 310-317.
- Xie, H., Hofmann, A., Hegner, E., Wilson, A., Wan, Y., Liu, D. 2012. Zircon SHRIMP dating confirms a Palaeo- to Mesoarchaean supracrustal terrain in the Kaapvaal craton, southern Africa. *Gondwana Research*, 21, 818-828.
- Zhao, G.C., 2007. When Did Plate Tectonics Begin on the North China Craton? Insights from Metamorphism. *Earth Science Frontiers*, 14, 19-32.
- Zhao, G.C., Wilde, S.A., Cawood, P.A. and Lu, L.Z., 1999. Thermal evolution of two types of mafic granulites from the North China Craton: implications for both mantle plume and collisional tectonics. *Geological Magazine*, 136, 223-240.

Editorial handling: L.D. Ashwal.